Universidade do Algarve

# Soft-computing techniques applied to artificial tissue temperature estimation

César Alexandre Domingues Teixeira

Doutoramento em Engenharia Electrónica e Computação,

especialidade de Processamento de sinal

**2008**

Universidade do Algarve

# Soft-computing techniques applied to artificial tissue temperature estimation

César Alexandre Domingues Teixeira

**Tese orientada por:**
Maria da Graça Cristo dos Santos Lopes Ruano
e
António Eduardo de Barros Ruano

Doutoramento em Engenharia Electrónica e Computação,
especialidade de Processamento de sinal

**2008**

# Resumo

Desde tempos remotos que a variação (aumento ou redução) da temperatura dos tecidos humanos tem sido usada no tratamento de determinadas doenças. Os primeiros registos dos benefícios das chamadas terapias térmicas remontam aos tempos de Hipócrates, na Grécia antiga, por volta de 500 a.C.. Por outro lado, as antigas práticas termais da civilização Romana chegaram aos tempos actuais, com elevado mérito no tratamento de inúmeras doenças.

Actualmente, as terapias térmicas são extensivamente utilizadas em fisioterapia, nomeadamente no tratamento de problemas relacionados com o sistema músculo-esquelético. Mais recentemente, o aumento da temperatura para tratamento de problemas oncológicos tem recebido elevada atenção dos cientistas. A chamada hipertermia oncológica é uma técnica que consiste na elevação da temperatura de tumores a níveis citotóxicos, de forma a estancar ou regredir o seu crescimento. Neste campo, o principal objectivo da hipertermia é manter a temperatura do tumor entre 43 e 45 $^{o}$C. A hipertermia pode ser aplicada por si só, ou em conjunto com as conhecidas radioterapia e quimioterapia. A temperatura corporal pode ser elevada de uma forma geral, normalmente por imersão do doente numa banheira de água quente, ou mais de acordo com a região em tratamento. A elevação localizada pode ser conseguida, não-invasivamente, usando por exemplo: feixes de micro-ondas, ou ultra-som (focalizado ou não) a médias ou a altas intensidades. Nas últimas décadas tem-se investigado muito sobre a aplicação de ultra-som focalizado de alta

intensidade, mais conhecido por HIFU (High Intensity Focused Ultrasound), em hipertermia.

Um aspecto importante no que respeita à aplicação das terapias térmicas é a monitorização da temperatura ao longo do tempo, na região sob tratamento. O conhecimento quantitativo preciso da temperatura é essencial, quer por questões de segurança do paciente, quer para garantir a eficácia da terapia. A forma mais intuitiva de obter esse conhecimento é através de medição directa na região de interesse, ou seja invasivamente. Esta modalidade sofre de problemas graves, tais como: o reduzido número de pontos onde a temperatura pode ser monitorizada, uma vez que o tecido é danificado pela inserção dos sensores e também porque pode existir dificuldade no posicionamento dos sensores em algumas situações; os sensores funcionam como espalhadores indesejados (no caso de ultra-som), onde pontos de elevada temperatura podem ocorrer; os sensores podem permitir a condução térmica para regiões onde o aquecimento não é desejado; a cavitação ultra-sónica pode também ocorrer no caminho deixado pela passagem dos sensores: a limitação no número de sensores pode resultar numa cobertura espacial insuficiente. Devido aos problemas atrás referidos, a opção seria a obtenção da temperatura na região espaço-temporal de interesse de forma não invasiva. Isto implica que a temperatura não é medida mas sim estimada. A utopia das terapias térmicas é ter um sistema completo composto por: uma fonte de aquecimento não invasiva e simultâneamente um estimador espaço-temporal de temperatura preciso. A existência de uma metodologia precisa de estimação da temperatura possibilitaria um controlo correcto da instrumentação de aquecimento, levando a uma eficaz deposição da energia nos tecidos e consequentemente a um padrão de aquecimento desejado e pré-definido.

Diversos trabalhos em estimação não invasiva de temperatura já foram publicados. Estes trabalhos relatam métodos baseados em: tomografia de impedância eléctrica (EIT) [1], termometria de micro-ondas [2], ressonância magnética nuclear

(MRI) [3], e ultra-som retro-espalhado (BSU) [4]. Em [5] é referido que actualmente somente os métodos baseados em MRI conseguem atingir a resolução necessária para hipertermia/diatermia, resolução essa que corresponde a um erro máximo absoluto de 0,5 $^{o}$C em 1 cm$^3$. No entanto há a ressaltar que a instrumentação de MRI é dispendiosa, e algumas práticas terapêuticas são difíceis de aplicar no espaço ambiental do equipamento de MRI, o que leva a tomar em consideração outras alternativas. O uso de BSU pode trazer algumas vantagens, tais como: instrumentação menos dispendiosa; os equipamentos de ultra-som têm a capacidade de processamento e aquisição em tempo-real, permitindo a visualização funcional do paciente; as ondas ultra-sonoras atingem zonas profundas (uma das principais limitações da tomografia de impedância eléctrica); o processamento dos sinais de BSU requer ferramentas simples; e por fim a vantagem de se poder usar a mesma forma de energia para aquecer o meio e para estimar a temperatura, quando é usado ultra-som de terapia. Baseado em BSU diversas metodologias para estimação não invasiva foram publicadas, diferindo entre si na característica dependente da temperatura extraída dos sinais. Podem ser apontados quatro tipos de metodologias: as que usam o atraso temporal entre ecos [4], as que calculam desvios nas posições das componentes espectrais [6], as que seguem mudanças no coeficiente de atenuação [7] e as que se baseiam nas mudanças da energia retro-espalhada [8]. O atraso temporal e as variações nas componentes espectrais ocorrem porque existem mudanças na velocidade do som e no espaçamento médio entre partículas. Por outro lado, a absorção do meio também varia afectando o coeficiente de atenuação e a energia que retorna ao transdutor. Estas metodologias aplicam relações lineares entre a característica extraída e a temperatura a estimar. A relação linear é sustentada por uma constante de proporcionalidade que é obtida a-priori. Métodos como os publicados em [4] e [6] calculam uma única constante para um meio homogéneo, o que os torna inaplicáveis a meios não homogéneos multi-camada, como é o caso da maior parte das estruturas

presentes no corpo humano. Apesar de os modelos físicos apresentados nestas publicações assentarem em princípios físicos bem definidos, estes são obtidos através de simplificações que num ambiente real não têm representatividade. A validação do desempenho dos métodos propostos foi feita de uma forma muito restritiva, ou seja somente em 3 pontos e para uma única intensidade do equipamento de terapia.

O trabalho desenvolvido nesta tese baseia-se essencialmente no cálculo de características dos sinais BSU (à excepção do primeiro experimento que envolve uma estimação invasiva), quando os diferentes meios estudados são irradiados com ultrasom de terapia. Aplicaram-se novas técnicas para relacionar as características com a temperatura, técnicas essas designadas por "Soft-Computing". Neste trabalho aplicaram-se os algoritmos genéticos, as redes neuronais e os sistemas difusos. A escolha destas técnicas baseou-se no facto das mesmas serem apontadas como úteis para a resolução de problemas complexos do mundo real, para os quais as técnicas tradicionais são incapazes de retornar uma solução completa a baixo custo computacional.

Nesta tese, diversos arranjos experimentais foram realizados e construíram-se modelos para estimar a temperatura invasiva e não-invasivamente. Primeiramente foi desenvolvido um arranjo experimental para teste dos modelos num ambiente de estimação invasivo, num meio líquido e num só ponto. O experimento desenvolvido consistia num tanque de glicerina, aquecido com um aparelho de ultra-som comummente usado em fisioterapia. Foram medidos (a cada 10 segundos) sinais de intensidade e de temperatura com um hidrofone e um termopar, respectivamente. Cada experiência consistia em 60 minutos de aquecimento e a aproximadamente outros 60 de arrefecimento. O meio foi aquecido usando três intensidades diferentes (1,0; 1,5 e 2,0 $W/cm^2$ ). Para cada sinal de intensidade medido foi calculado o espectro, e a amplitude de algumas das suas componentes monitorizadas durante a evolução da experiência. Foram testados 3 tipos de metodologias: uma linear

com busca iterativa da estrutura, outra baseada em redes neuronais de base radial (RBFNNs), e ainda outra que englobou redes neuronais de base radial com entradas lineares (RBFLICs). Nas duas últimas metodologias a estrutura dos modelos foi optimizada usando o algoritmo genético multi-objectivo (MOGA) [9] [10] [11]. Da análise dos resultados pode-se concluir que é inviável estimar a temperatura nas condições experimentais consideradas através de modelos lineares, tendo-se verificado a existência de um erro máximo absoluto de 2.1 ºC. Nas metodologias que envolveram modelos não lineares, um erro máximo absoluto de 0.09 ºC e 0.12 ºC foi obtido no caso das RBFNNs e RBFLICs, respectivamente.

Tendo em mente a estimação não invasiva, foi desenvolvido outro arranjo experimental para estimação mono-ponto e bi-ponto de temperatura, em meio líquido. Três esferas foram imersas num tanque de glicerina e o meio aquecido com ultra-som de fisioterapia. Por forma a possibilitar uma estimação não invasiva, foi colocado um outro transdutor de ultra-som (de imagem) a funcionar em pulso-eco, que insonorizou as três esferas que funcionaram como espalhadores de ultra-som. Foi introduzido um termopar na esfera central e a cada 10 segundos foram registados o sinal de BSU e o valor de temperatura fornecidos pelo transdutor de imagem e pelo termopar, respectivamente. Tal como no experimento desenvolvido para estimação invasiva, o meio foi aquecido durante os primeiros 60 minutos, usando as mesmas três intensidades (1,0; 1,5 e 2,0 $W/cm^2$ ), e deixado arrefecer o sistema durante os últimos 60 minutos. Dos sinais de BSU medidos, calcularam-se sete características dependentes da temperatura. Entre elas, seis foram extraídas do espectro e uma extraída directamente no domínio do tempo. Usando estas características, duas metodologias foram testadas, uma envolvendo de novo as RBFNNs e outra centrada num modelo linear. Ambas as estruturas foram optimizadas usando o MOGA, possibilitando uma comparação mais fidedigna do que a comparação realizada para estimação invasiva. As RBFNNs foram usadas para estimação mono-ponto e bi-ponto. Dos

resultados obtidos foi possível verificar que as RBFNNs obtiveram um erro máximo absoluto inferior a 0,5 ºC. Mais uma vez o modelo linear, mesmo com estrutura optimizada pelo MOGA não conseguiu apresentar a performance standard, salientando a superioridade das RBFNNs para os ambientes de estimação propostos.

Tendo em vista a evolução para uma estimação não-invasiva e multi-paramétrica, isto é, em múltiplas intensidades e em múltiplos pontos, foi desenvolvido um outro arranjo experimental que envolvia um meio solido homogéneo ("phantom"), que simulou as propriedades acústicas de um tecido do tipo muscular. O meio desenvolvido é composto por uma mistura de água (86,5%), glicerina (11%) e agar-agar (2,5%). No interior do "phantom" foram colocados 5 termopares, que passaram a definir a região de estudo. As extremidades dos termopares encontravam-se contidas num plano paralelo e à distância de 60 mm da face do transdutor de terapia. Também neste arranjo experimental foi considerado um transdutor de imagem que recolheu os sinais de BSU, a serem posteriormente utilizados para estimação. Cada medição compreendeu 5 minutos de espera, 15 de aquecimento (com ultra-som de fisioterapia) e 15 de arrefecimento. Foram aplicadas quatro intensidades de aquecimento (0,5; 1,0; 1,5 e 2,0 $W/cm^2$ ). Para cada sinal de BSU foi calculado o atraso temporal entre ecos (induzido pelas variações de temperatura) ao longo de cada experimento. Usando esses atrasos foram construídos modelos baseados em RBFNNs treinados com o algoritmo "orthogonal least squares" (OLS); modelos baseados em RBFNNs com estrutura optimizada pelo MOGA; e modelos baseados em estruturas difusas do tipo ANFIS, com entradas seleccionadas pelo MOGA. Foi possível observar que para o ambiente de estimação considerado, a metodologia baseada em RBFNNs com estrutura optimizada pelo MOGA foi a que conseguiu obter níveis satisfatórios de erro e complexidade computacional. A metodologia baseada em RBFNNs com estrutura escolhida pelo OLS retornou um erro máximo absoluto de 6.6 ºC, tornando-a inapropriada para estimação nas presentes condições experimen-

tais. Esta ineficácia pode ser explicada pela simplicidade do algoritmo. Por outro lado, a metodologia baseada em ANFIS com entradas escolhidas pelo MOGA não conseguiu satisfazer o desempenho desejado em termos de erro, devido à elevada complexidade computacional das estruturas ANFIS. É possível depreender que a metodologia baseada em RBFNNs com estrutura optimizada pelo MOGA é uma solução intermédia (nem muito complexa nem muito simples) que consegue estimar a temperatura com a qualidade requerida. A capacidade de generalização dos modelos, isto é a capacidade dos modelos operarem sobre situações novas foi também estudada. Para tal os modelos foram construídos considerando apenas algumas das intensidades e dos pontos espaciais, no entanto, na sua validação foram consideradas todas as situações medidas, isto é, os 5 pontos e as 4 intensidades, ou seja 20 pontos de operação.

Em busca de ambientes de estimação mais ambiciosos, foi construído um "phantom" de três camadas, tendo em vista o estudo da evolução da temperatura num meio não homogéneo. Foram colocados cinco termopares ao longo do eixo do transdutor de terapia, com um espaçamento de 5 mm entre si. A temperatura foi medida em cada camada e nas interfaces entre elas. Mais uma vez foi considerado um transdutor de imagem para capturar os sinais BSU, e permitir uma estimação não invasiva. Para se conseguir obter informação da região onde foram colocados os termopares, o transdutor de imagem foi colocado face-a-face com o transdutor de terapia. Esta disposição obrigou ao desenvolvimento de um protocolo de sincronização, dado que a alta intensidade emitida pelo transdutor de terapia saturava o de imagem, destruindo a informação útil presente nos sinais BSU. Desta forma foi colocado o transdutor de terapia a funcionar em modo pulsado, e o transdutor de imagem a adquirir os sinais BSU durante os tempos "mortos" do feixe de terapia. Cada experimento durou 35 minutos, onde foram considerados 5 minutos de espera inicial, 15 minutos de aquecimento e 15 minutos de arrefecimento. Para aquecer o

meio foram usadas oito intensidades (0,3; 0,5; 0,7; 1,0; 1,3; 1,5; 1,7 e 2,0 $W/cm^2$ ) do aparelho de terapia. Através do processamento dos sinais BSU, foi mais uma vez extraído o atraso temporal entre os ecos ao longo de cada experimento. Usando esses atrasos foram desenvolvidos modelos baseados em RBFNNs com estrutura optimizada pelo MOGA. Um erro máximo absoluto inferior a 0,5 °C foi obtido em todas as posições espaciais (internas e interfaces) e para todas as intensidades. Como foram consideradas cinco posições espaciais e oito intensidades, os modelos foram testados em 40 pontos de operação. Alguns destes pontos de operação não foram usados na construção dos modelos, reafirmando a capacidade de generalização dos modelos desenvolvidos.

As redes neuronais de funções de base radial, com estrutura optimizada pelo algoritmo genético multi-objectivo, foram comparadas com modelos lineares e com outros modelos não lineares. Pode-se observar que este tipo de modelos conseguiu superar em termos de erro e complexidade as outras abordagens testadas, quer fossem elas lineares ou não.

Nesta tese foi possível observar que a melhor metodologia aplicada, isto é RBFNNs com estrutura optimizada pelo MOGA, obteve erros máximos absolutos melhores ou comparáveis com os métodos de referência, nomeadamente os publicados em [4] e [6]. Um aspecto importante a ter em conta nesta tese, é o facto dos parâmetros dos modelos e a sua estrutura serem obtidos a partir dos dados, evitando a determinação da constante do meio, assim como as "pseudo-simplificações" que eram forçosas nas metodologias apresentadas em [4] e [6]. Como os modelos aplicados são completamente construídos a partir dos dados, a sua aplicabilidade não é restrita a meios homogéneos, podendo portanto ser aplicada em meios não homogéneos multi-camada. Isto sucede porque o conhecimento da evolução da temperatura em cada camada é conseguido através de um processo de aprendizagem, pela observação de situações semelhantes, descartando a determinação de constantes do meio. Os mo-

delos desenvolvidos foram testados em ambientes mais abrangentes, incluindo um máximo de 40 pontos de operação num meio não homogéneo, ao contrário do modelo proposto em [4], onde a qualidade da estimação foi somente avaliada em 3 pontos de operação. Esta validação extensiva indica que os modelos apresentados nesta tese são mais versáteis e, portanto, com características melhores para aplicações reais. Valores de erro baixos e ao mesmo tempo com complexidade computacional reduzida foram aspectos fulcrais tidos em conta na optimização das estruturas dos modelos (usando o MOGA). Tal significa que, os modelos foram aperfeiçoados por forma a obter boa performance com carga computacional reduzida, como desejado em aplicações de tempo-real. Pode-se então concluir que a metodologia aplicada supera as que haviam sido propostas nos artigos científicos internacionais da especialidade, em termos de desempenho e aplicabilidade a situações reais, estendendo a validação a multi-ponto e multi-intensidade, e permitindo a sua aplicabilidade a meios multi-camada. Este tipo de cenário, no melhor do nosso conhecimento, nunca foi desenvolvido para estimação não-invasiva de temperatura, usando ultrasom retro-espalhado.

A principal limitação da metodologia proposta é a sua alta dependência nos dados, visto que ambos os parâmetros e a estrutura são definidos a partir dos mesmos. Isto implica que os dados usados na construção dos modelos devem ser representativos, ou seja, devem englobar o maior número de situações passíveis de ocorrência no ambiente de estimação. Um erro nos dados pode comprometer todo o processo de modelação e levar à obtenção de modelos com uma má capacidade de generalização. Outro aspecto a ter em conta é o facto de a aplicação real em humanos estar dependente do desenvolvimento de "phantoms" que consigam "imitar" a evolução da temperatura em tecidos biológicos vivos, uma vez que é inconcebível a medição invasiva em pacientes, para posteriormente se desenvolver modelos de temperatura. Este problema também é visível nos métodos propostos no estado da arte, uma vez

que estes também dependem de constantes do meio que tem que ser determinadas à priori.

Como trabalho futuro aponta-se o teste dos modelos em tecidos biológicos in-vitro e posteriormente em animais. Uma vez dispondo da instrumentação adequada, pretende-se estender a estimação a duas e três dimensões. O desenvolvimento de "phantoms" que aproximem as propriedades térmicas e acústicas dos tecidos humanos também devem ser objectos de estudo. O teste de outros tipos de modelos que possam vir a facilitar o controlo da instrumentação de terapia é também apontado como linha de investigação futura.

**Palavras-chave**: Estimação de temperatura, técnicas de "Soft-computing", Redes neuronais de base radial, algoritmos genéticos multi-objectivo, terapias térmicas.

# Abstract

Safety and efficiency of thermal therapies strongly rely on the ability to quantify temperature evolution in the treatment region. Research has been developed in this field, and both invasive and non-invasive technologies have been reported. Till now, only the magnetic resonance imaging (MRI) achieved the hyperthermia/diathermia gold standard value of temperature resolution of 0.5°C in $1cm^3$, in an in-vivo scenario. However, besides the cost of MRI technology, it does not enable a broad-range therapy application due to its complex environment. Alternatively, backscattered ultrasound (BSU) seems a promising tool for thermal therapy, but till now its performance was only quantitatively tested on homogeneous media and on single-intensity and three-point assessment have been reported.

This thesis reports the research performed on the evaluation of time-spatial-temperature evolution based mainly on BSU signals within artificial tissues. Extensive operating conditions were tested on several experimental setups based on dedicated phantoms. Four and eight clinical ultrasound intensities, up to five spatial points, homogeneous and heterogeneous multi-layered phantoms were considered. Spectral and temporal temperature-dependent BSU features were extracted, and applied as invasive and non-invasive methodologies input information. Soft-computing methodologies have been used for temperature estimation. From linear iterative model structure models, to multi-objective genetic algorithms (MOGA) model structure optimisation for linear models, radial basis functions neural net-

works (RBFNNs), RBFNNs with linear inputs (RBFLICs), and for the adaptive-network-based fuzzy inference system (ANFIS) have been used to estimate the temperature induced on the phantoms. The MOGA+RBFNN methodology, fed with completely data-driven information, estimated temperature with maximum absolute errors less than 0.5°C within two spatial axes.

The proposed MOGA+RBFNN methodology applied to non-invasive estimation on multi-layered media, is a innovative approach, as far as known, and enabled a step forward on the therapeutic temperature characterisation, motivating future instrumentation temperature control.

**Keywords**: Temperature estimation, Soft-computing techniques, Radial basis functions neural networks, Multi-objective genetic algorithms, Thermal therapies.

# Agradecimentos

Primeiramente queria agradecer aos meus orientadores Prof. Doutora Maria da Graça Cristo dos Santos Lopes Ruano e Prof. Doutor António Eduardo de Barros Ruano, pelo convite inicial e pelo apoio e amizade ao longo deste doutoramento.

Agradecimentos a todos os elementos do laboratório de controlo, em especial ao Engenheiro Sérgio Silva, Mestre Eduardo Crispim e Doutor Pedro Frazão, pela ajuda e camaradagem na resolução de inúmeros problemas relacionados com esta tese.

Especial reconhecimento ao Doutor Wagner Coelho de Albuquerque e Pereira, pelas inúmeras ajudas financeiras que permitiram o desenvolvimento inicial desta tese, pela camaradagem e pelas inúmeras discussões construtivas que permitiram o desenvolvimento deste trabalho. Agradecimentos também à equipa do Laboratório de Ultra-som em Medicina (LUS) do Programa de Engenharia Biomédica, COPPE-Universidade Federal do Rio de Janeiro, em especial ao Doutor André Victor Alvarenga e ao Dr. Luís Eduardo Maggi, pela camaradagem e ajuda nas visitas realizadas.

Agradecimentos à equipa de investigação do Laboratorio de Acústica Ultrasonora (Facultad de Ciencias, Universidad de la República, Montevideo, Uruguay) em especial ao Doutor Carlos Negreira, Mestre Guilhermo Cortella e Engenheiro Hector Gomez pelo acolhimento e ajuda na aquisição dos primeiros dados experimentais, sem os quais esta tese não seria tão completa.

Agradecimentos pela ajuda financeira da Fundação para a Ciência e a Tecnologia, através da bolsa SFRH/BD/14061/2003 e do projecto POSC/EEA-SRI/61809/2004, fundamentais para tornarem esta tese possível. Igualmente de reconhecer ajuda financeira do Conselho Nacional de Desenvolvimento Científico e Tecnológico (CNPq), através do projecto "Determinacíon de patrones ultrasónicos eficaces para terapia segura mediante control de radiacíon pulsada distribuída (PULSETS)".

Por fim queria agradecer à minha companheira Nádia pela sua compreensão, amizade e carinho durante o desenvolvimento deste trabalho. Especiais agradecimentos aos meus pais pelo incentivo ao estudo, desde "tenra" idade.

# Contents

# List of Figures

# List of Tables

# Chapter 1

# Introduction

## 1.1 Motivation

Thermal therapies have been applied since ancient times, such as in the thermal practices of the Romans. Nowadays thermal therapies are extensively applied in physiotherapy, for the treatment of muscle-skeletal problems. Recently the application in oncology has received an increasing attention by the scientists. Oncologic hyperthermia is a technique where the temperature of tumours is raised to values between 43 and 45 °C. Hyperthermia can be applied alone or in conjunction with traditional methods, such as radiotherapy and chemotherapy [16]. Hyperthermia can also be applied in a general or localised fashion. The general version is normally applied by immersion in a water bath, aiming to obtain a moderate heating and a broader effect. On the other side, the localised applications aim at interacting only with the tumour, preventing from undesired effects on other body regions. Localised heating can be obtained by using, for example, microwaves or ultrasound at moderate and high intensities. In the last decades the application of high intensity focused ultrasound (HIFU) has been investigated.

A main aspect concerning the application of thermal therapies is the monitoring

of temperature in the time and space sense, during treatment. A quantitative assessment of temperature is of extreme relevance for both patient security, and for the efficacy of the therapy. Previous approaches ([17], [18], and [19]) were based on the assessment of temperature directly at the treatment site, i.e. by invasive measurement. Although it is a precise temperature measurement (the quality of the measurement is highly dependent on the sensor accuracy), this modality suffers from serious problems. Only a limited number of sensors can be placed because there is tissue damage at each sensor placement and in even certain regions it is impossible to place sensors. An insufficient number of sensors can result in a poor spatial resolution. In addition, the sensors act like undesired scatterers where dangerous hot-spots can occur, thermal conduction can occur through the sensors cables to undesired regions, and the sensors placement can increase the formation of acoustic cavitation. These problems turn inviable the application of invasive assessment, leading to the evaluation of the possibility of estimating temperature by non-invasive means. The main goal for a thermal therapy system is to have a non-invasive heating source, and simultaneously a precise and effective time-spatial non-invasive temperature estimator. Reliable temperature estimators would enable an efficient therapy control, which would then result in the correct application of pre-defined heating patterns, preventing undesired effects and improving effectiveness. The existence of such a system would increase the acceptability of thermal therapies, in particular those where high temperature changes are desired, such as in the application of high intensity focused ultrasound (HIFU) for non-invasive therapy and surgery.

Several works on non-invasive temperature estimation have been published. Those based on electrical impedance tomography (EIT) [1], microwave thermometry [2], magnetic resonance imaging (MRI) [3], and backscattered ultrasound (BSU)[4]. It has also been pointed that only the methods based on MRI reached the desired resolution for hyperthermia till now. The referred resolution is a maximum absolute

error of 0.5 °C in 1-cm$^3$ [5]. However, there are some therapies that are impossible to apply together with a MRI device, and the MRI instrumentation is very expensive as compared to other technologies. On the other hand, ultrasound instrumentation is relatively cheap, ultrasound waves can reach deep regions inside the body, BSU signals require simpler signal processing requirements as ultrasound imaging systems can process and display imaging features in real-time. Another positive point is the possibility of using the same form of energy for estimation and heating, when therapeutic ultrasound is applied. The application of BSU for temperature estimation is reported in several research papers, based on the extraction of temporal-echo shifts [4], frequency shifts [6], changes on the attenuation coefficient [7] and changes on the backscattered energy[8]. In [4] and [6], the proposed methodologies consider only linear relations between the extracted feature and temperature. In [4], the accuracy of the method is only tested at one intensity in three points inside a homogeneous rubber phantom. Estimators for in-vivo application must be tested in more real media such as multilayered phantoms, and under several operating situations.

## 1.2 Proposed goals

The main goal of this thesis was to develop a computational system that aim to improve the efficacy and security of the thermal therapies, by:

- identifying temperature-dependent signal and ultrasonic system features, to enable a quantitative temperature evaluation;
- creating neural models based on the identified features, aiming at temperature estimate on the region of interest, i.e. in the time and space;
- if possible, using the developed models to control the therapeutic instrumentation.

## 1.3 Thesis outline

This chapter describes the motivation of the work based on main background readings, the proposed goals and summary of the main contributions of this thesis.

In Chapter, 2, the applied soft-computing techniques background is described. Special attention is given to radial-basis-functions neural networks (RBFNNs), which are part of a significant number of developed models. The adaptive neuro-fuzzy inference system (ANFIS) was also applied for non-invasive temperature estimation, and used for comparison with the extensively applied RBFNN models. The chapter ends with a description of genetic algorithms and in particular the multi-objective genetic algorithm (MOGA), which was used to search for appropriate model structures.

Chapter 3 reports the fundamental aspects of ultrasound, and its principal applications in therapy. Attention is also given to ultrasonic phantoms, which are essential in this work.

Background and the state of the art on temperature assessment on health environment is given in Chapter 4. Primarily, invasive temperature estimation is addressed. Secondly, methods and technologies so far applied for non-invasive estimation are explained. Emphasis is given to temperature estimation using backscattered ultrasound (BSU), i.e. the "technology" used in this thesis.

The different experimental setups used to create and validate the different models are described in Chapter 5. A gradual increasing in the experiments' complexity was performed along the duration of the work. Thus this chapter starts by describing a simple experiment for invasive temperature estimation, then more complex setups involving non-invasive estimation are planed, finishing with an experimental arrangement for multilayer non-invasive estimation.

In Chapter 6, the model structures applied in the different phases of the work are presented, as well as the extracted features from the collected ultrasound signals.

The way how these features were computed, and the associated pos-processing (filtering and normalisation) are also presented. The applied model structures ranged from the simple autoregressive model with exogenous inputs (ARX) to the complex radial-basis-functions neural networks with linear input connections (RBFLIC) and ANFIS structures. In this chapter, a subdivision is implemented between models for single-point (Section 6.2) and for non-invasive estimation in the time and space (Section 6.3).

The results and related discussions in each phase of the work are presented in Chapter 7. The results obtained are presented and discussed according to the different experimental setups developed, starting by invasive estimation to non-invasive estimation on multilayered media. At the end of this chapter an overall view of the results obtained is presented, and comparisons with published reference results are also performed.

Overall concluding remarks, as well as indication of future research lines are referred in Chapter 8.

## 1.4 Main contributions

This thesis reports the development of a new methodology for non-invasive temperature estimation using backscattered ultrasound, characterised by:

- presenting the first solution for non-invasive estimation in multilayered media (as far as known);
- being based on the application of soft-computing methodologies, enabling as so the application of non-linear approaches, which leads to greater processing power than the methods reported till now in the literature;
- being tested in different situations, ranging from simple invasive environments

to more complex multilayered phantoms. The models were evaluated at multiple intensities and multiple spatial positions (up to 40 operating points), presenting maximum absolute errors inferior to the internationally accepted threshold for hyperthermia;

- in addition to the extensive testing, the models show appropriateness for real-time control implementations, since their performance was very good when evaluated in operating situations (regarding space and ultrasound intensities) never applied during their construction;

- presenting models that are entirely extracted from data (data-driven models), i.e. both model structure and parameters were found using the measured data. Thus, discarding mathematical simplifications and physical constants determination, necessary for the modelling approaches presented in the state of the art.

This thesis contributed with the following publications:

- **Papers in national and international scientific periodicals with referees**

  1. C. A. Teixeira, G. Cortela, H. Gomez, M. G. Ruano, A. E. Ruano, C. Negreira, and W. C. A. Pereira, "Temperature models of a homogeneous medium under therapeutic ultrasound", *Brazilian Journal of Biomedical Engineering*, vol. 20, no. 2-3, pp. 97–101, 2004.

  2. C. A. Teixeira, A. E. Ruano, M. G. Ruano, W. C. A. Pereira, and C. Negreira, "Non-invasive temperature prediction of in-vitro therapeutic ultrasound signals using neural networks", *Medical and Biological Engineering and Computing*, vol. 44, no. 1-2, pp. 111–116, 2006.

3. C. A. Teixeira, M. Graça Ruano, W. C. A. Pereira, A. E. Ruano, and C. Negreira, "Linear versus non-linear non-invasive temperature predictors in a homogeneous medium subjected to physiotherapeutic ultrasound", *Brazilian Journal of Biomedical Engineering*, vol. 22, no. 2, pp 131–141, 2006.

4. C. A. Teixeira, A. E. Ruano, M. Graça Ruano, and W. C. A. Pereira, "Generalization assessment of non-invasive data-driven temperature estimators from therapeutic ultrasound", *Brazilian Journal of Biomedical Engineering*, vol. 23, no. 2, pp. 143–151, 2007.

5. C. A. Teixeira, M. Graça Ruano, A. E. Ruano, and W. C. A. Pereira, "A soft-computing methodology for non-invasive time-spatial temperature estimation", *IEEE Transactions on Biomedical Engineering*, vol. 55, no. 2, pp. 572–580, 2008.

- C. A. Teixeira, M. Graça Ruano, A. E. Ruano, and W. C. A. Pereira, "Neuro-genetic non-invasive temperature estimation: intensity and spatial prediction", *Artificial Intelligence in Medicine*, 2008 (*submitted*).

- **Papers in conference proceedings**

1. C. A. Teixeira, G. Cortela, H. Gomez, M. G. Ruano, A. E. Ruano, C. Negreira, and W. C. A. Pereira, "Modelos de temperatura de um meio homogéneo sob ultrassom de terapia", in *IFMBE Proceedings Series (III Latin-American Congress on Biomedical Engineering)*, J. Nadal, L. V. Batista and J. J. A. Ferreira, Eds., João Pessoa, Paraiba, Brasil, September 2004, vol. 5, In CD-Rom. (Third prize in the IFMBE Student Paper Competition, during the III Latin-American Congress on Biomedical Engineering)

2. C. A. Teixeira, W. C. A. Pereira, A. E. Ruano, and M. Graça Ruano,

"Multi-objective genetic algorithm applied to the structure selection of rbfnn temperature estimators", in *proc. 7th International Conference on Adaptive and Natural Computing Algorithms (ICANNGA'05)*, B. Ribeiro, R. F. Albrecht, A. Dobnikar, D. W. Pearson and N. C. Steele, Eds., Coimbra, Portugal, March 2005, pp. 506–509.

3. C. A. Teixeira, M. Graça Ruano, W. C. A. Pereira, and A. E. Ruano, "Temperature modelling of an homogeneous medium using genetically selected rbf(lic)", in *proc. of the 16th IFAC World Congress*, P. Piztek, Eds., Prague, Czech Republic, July 2005, Elsevier.

4. C. A. Teixeira, W. C. A. Pereira, A. E. Ruano, C. Negreira, and M. Graça Ruano, "Neural network models for non-invasive two-point temperature monitoring in a homogeneous medium irradiated by therapeutic ultrasound", in *IFMBE Proceedings Series (3rd European Medical and Biological Engineering Conference (EMBEC'05))*, Peter Kneppo and Jiří Hozman, Eds., Prague, Czech Republic, November 2005, vol. 11, Paper # 2473.

5. C. A. Teixeira, M. Graça Ruano, A. E. Ruano, W. C. A. Pereira, and C. Negreira, "Single black-box models for two-point non-invasive temperature prediction", in *Proc. of the 6th IFAC Symposium on Modelling and Control in Biomedical Systems(MCBMS'06)*, D. D. Feng, O. Dubios, J. Zaytoon, and E. Carson, Eds., Reims, France, September 2006, pp. 135–140, Elsevier.

6. C. A. Teixeira, M. Graça Ruano, A. E. Ruano, and W. C. A. Pereira, "Non-invasive time-spatial temperature simulation using neural networks", in *Proc. 7th Portuguese Conference on Automatic Control (Controlo 2006)*, M. A. Botto, Eds., Lisbon, Portugal, September 2006, Paper #92.

7. C. A. Teixeira, M. Graça Ruano, A. E. Ruano, and W. C. A. Pereira, "Non-invasive tissue temperature evaluation during application of therapeutic ultrasound: precise time-spatial non-linear modelling", in *IFMBE Proceedings-WC 2006 "World Congress on Medical Physics and Biomedical Engineering*, S. I. Kim and T. S. Suh Seoul, Eds., Korea, August 2006, pp. 70–73.

8. C. A. Teixeira, A. E. Ruano, M. Graça Ruano and W. C. A. Pereira, "Noninvasive black-box temperature simulation: precise spatial generalisation", in *Proc. of the XX Brasilian Congress on Biomedical Engineering-XX CBEB*, S. S. Mühlen, Eds., São Paulo, Brasil, October 2006, pp. 229–232.

9. C. A. Teixeira, M. Graça Ruano, A. E. Ruano, and W. C. A. Pereira, "Open source data sensing software for ultrasonic non-invasive temperature estimation", in *Proc. of 5th Ibero-American congress on Sensors - Ibersensor 2006*, H. Gomez, Eds., Montevideo, Uruguay, September 2006, Paper # 36.

10. C. A. Teixeira, M. Graça Ruano, A. E. Ruano, and W. C. A. Pereira, "A soft-computing approach for non-invasive temperature estimation", in *Proc. of the Global Educational Technology Symposium*, Faro, Portugal, July 2006, Paper #14.

11. C. A. Teixeira, W. C. A. Pereira, A. E. Ruano, and M. Graça Ruano, "NARX structures for non-invasive temperature estimation in non-homogeneous media", *IEEE International Symposium on Intelligent Signal Processing (WISP 2007)*, Alcalá de Henares, Spain, October 2007.

12. C. A. Teixeira, M. Graça Ruano, A. E. Ruano, and W. C. A. Pereira, "A neuro-genetic approach to non-invasive temperature estimation in mul-

tilayered media under ultrasound therapy", *19$^{th}$ International Congress on Acoustics (ICA'07)*, Madrid, Spain, September 2007.

- **Patents**

  - C. A. Teixeira, M. Graça Ruano, Plataforma de aquisição de dados para a estimação não invasiva de temperatura, Patente nacional nº 103530 (*submitted*)

# Chapter 2

# Soft-computing methodologies

## 2.1 Introduction

Soft-computing refers to a set of techniques inspired by natural computation, in contrast to the traditional algorithmical-based methods. These techniques aim to exploit tolerance for imprecision, uncertainty and partial truth, in an attempt to solve highly complex problems, for which more conventional methods cannot yield a low cost and complete solution. Soft-computing includes techniques from computer science, artificial intelligence, machine learning and some engineering areas, such as: neural networks, fuzzy systems, evolutionary algorithms, Bayesian networks, chaos theory.

In this chapter, the soft-computing techniques applied during the research work are exposed. In Section 2.2 radial-basis-functions neural networks (RBFNNs), as well as their standard training and structure selection schemes are presented. The adaptive network based on a fuzzy inference system (ANFIS), applied for comparison with the RBFNN, is explained in 2.3. Emphasis is given to the genetic algorithms and in particular to the multi-objective genetic algorithm (MOGA) in Section 2.4.

## 2.2 Radial basis functions neural networks

Radial-basis-functions neural networks (RBFNNs) were in first place applied for high-dimensional interpolation [20], and were introduced as an artificial neural network by [21]. A RBFNN is composed by three layers, as it can be seen in Figure 2.1. The first one is a set of inputs which interfaces the network with its environment.

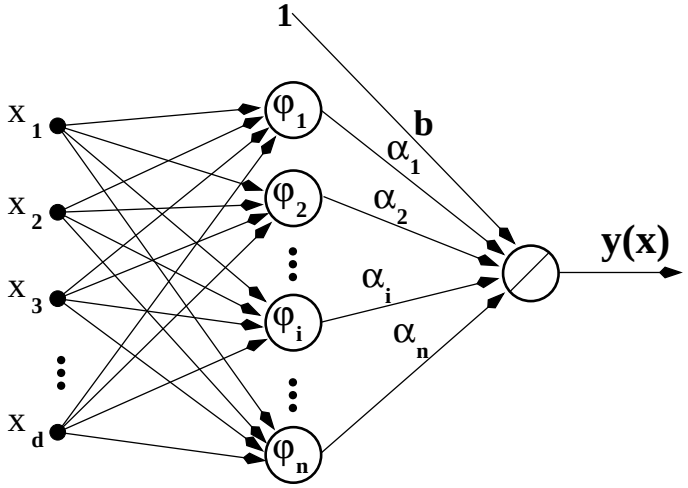


**Figure 2.1:** *Radial basis function neural network structure.*

The second layer, the unique hidden layer, performs a non-linear transformation from the input space to a hidden space, that in the majority of the cases is of high dimensionality. The third layer, combines linearly the output of the hidden layer to obtain the overall network output. The hidden layer is formed by a set of processing elements, called neurons. Each hidden neuron is expressed by a radial basis function, given as:

$$\varphi_i(\mathbf{x}) = \gamma(|\mathbf{c}_i - \mathbf{x}|), \tag{2.1}$$

where $\gamma$ represents a transformation (usually non-linear), $\mathbf{c}_i \in \mathbf{R}^d$ (where $d$ is the number of network inputs) is the function centre and $\mathbf{x} \in \mathbf{R}^d$ is the point where the function is evaluated. To note that $\mathbf{R}^d$ represents the real space with dimension

equal to the number of network inputs ($d$). Possible basis functions are:

$$\begin{aligned}
\varphi_i(\mathbf{x}) &= |\mathbf{c}_i - \mathbf{x}| && \text{radial linear function} \\
\varphi_i(\mathbf{x}) &= |\mathbf{c}_i - \mathbf{x}|^3 && \text{radial cubic function} \\
\varphi_i(\mathbf{x}) &= e^{-\frac{|\mathbf{c}_i - \mathbf{x}|^2}{2\sigma^2}} && \text{Gaussian function} \\
\varphi_i(\mathbf{x}) &= |\mathbf{c}_i - \mathbf{x}|^2 \log |\mathbf{c}_i - \mathbf{x}| && \text{thin plate spline function} \\
\varphi_i(\mathbf{x}) &= \sqrt{|\mathbf{c}_i - \mathbf{x}|^2 + \sigma^2} && \text{multi-quadratic function} \\
\varphi_i(\mathbf{x}) &= \frac{1}{\sqrt{|\mathbf{c}_i - \mathbf{x}|^2 + \sigma^2}} && \text{inverse multi-quadratic function} \\
\varphi_i(\mathbf{x}) &= \log |\mathbf{c}_i - \mathbf{x}|^2 + \sigma^2 && \text{shifted logarithm function}
\end{aligned} \tag{2.2}$$

Among those functions, the mostly applied is the Gaussian function, in conjunction with the Euclidean norm:

$$\varphi_i(\mathbf{x}) = e^{-\frac{||\mathbf{c}_i - \mathbf{x}||_2^2}{2\sigma_i^2}}, \tag{2.3}$$

where $\sigma_i$ is the function spread. As an example, in Figure 2.2 two Gaussian functions are represented in $\mathbf{R}^2$ (the space defined by "I1" and "I2"). The functions centres are [-5,-5] and [5,5], their spread being 2.5. The Gaussian function has some interesting properties, such as: its multivariate version can be written as a product of univariate functions, its derivative is also a Gaussian function, and is a localised function (i.e. as the distance from the centre increases the function approaches zero).

Taking into account the linear combination at the last network layer, the overall network output is given by:

$$y(\mathbf{x}) = b + \sum_{i=1}^{n} \alpha_i e^{-\frac{||\mathbf{c}_i - \mathbf{x}||_2^2}{2\sigma_i^2}}, \tag{2.4}$$

where $\{\alpha_i\}_{i=1}^n$ are the network linear weights, $n$ the number of neurons and $b$ is a bias term. The bias term enables the possibility to increase or decrease the network

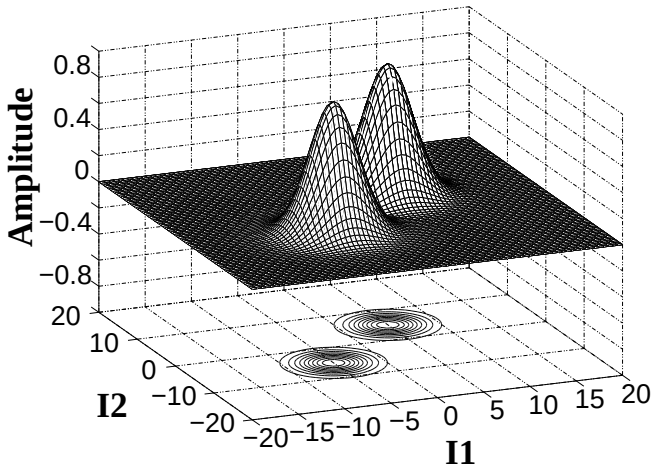


**Figure 2.2:** *Two Gaussian radial-basis functions defined in* $\mathbf{R}^2$*. The functions centres are [-5,-5] and [5,5], and their spread is 2.5.*

output by a constant. Figure 2.3 presents an example of a simple RBFNN mapping

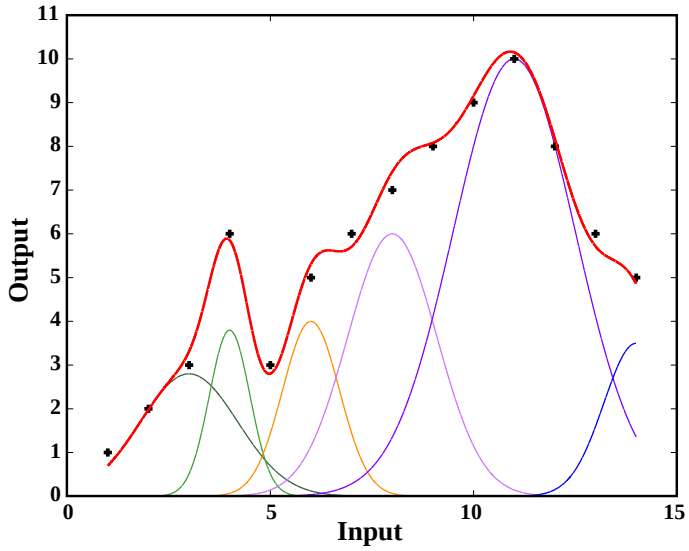


**Figure 2.3:** *Example of an one-dimensional RBFNN mapping. The black points represent the desired discrete output (i.e. the data observed from the environment). The red line represents the obtained RBFNN output for the defined parametrisation. The different weighted basis functions are also represented in different colours.*

($\mathbf{R} \rightarrow \mathbf{R}$). The network was created taking into account discrete input/output data presented in Table 2.1. The desired target output (t) is represented by the black points, while the red line represents the output supplied by the "hand tuned"

**Table 2.1:** *Synthetic data used for a simple RBFNN one-dimensional mapping.*

| Input (x) | 1 | 2 | 3 | 4 | 5 | 6 | 7 | 8 | 9 | 10 | 11 | 12 | 13 | 14 |
|---|---|---|---|---|---|---|---|---|---|---|---|---|---|---|
| Output (t) | 1 | 2 | 3 | 6 | 3 | 5 | 6 | 7 | 8 | 9 | 10 | 8 | 6 | 5 |

RBFNN. The six weighted radial-basis functions are also presented in this figure. Taking into account Equation 2.4, the mathematical expression that provides this mapping is:

$$y(x) = \sum_{i=1}^{6} \alpha_i e^{-\frac{|c_i - x|^2}{2\sigma_i^2}} = 2.8e^{-\frac{|(3-x)|^2}{2*(1.2)^2}} + 3.8e^{-\frac{|(4-x)|^2}{2*(0.5)^2}} + \tag{2.5}$$
$$4e^{-\frac{|(6-x)|^2}{2*(0.7)^2}} + 6e^{-\frac{|(8-x)|^2}{2*(1.1)^2}} + 10e^{-\frac{|(11-x)|^2}{2*(1.5)^2}} + 3.5e^{-\frac{|(14-x)|^2}{2*(0.8)^2}}.$$

The network represented by the above equation has centres $\{c_i\}_{i=1}^{6} = [3, 4, 6, 8, 11, 14]$, spreads $\{\sigma_i\}_{i=1}^{6} = [1.2, 0.5, 0.7, 1.1, 1.5, 0.8]$, and linear weights $\{\alpha_i\}_{i=1}^{6} = [2.8, 3.8, 4, 6, 10, 3.5]$ (to note that in this case the bias term is zero). The above parameters were set manually, aiming an exemplification of how RBFNNs operates over the data. In practice the problem of RBFNNs training is more complex, given that larger data sets are involved. Automatic determination of parameters is then necessary by using one of the training strategies presented later on this chapter.

RBFNNs, as the well known multilayer perceptrons neural networks (MLPNNs) [22] [23] have the propriety of universal approximation [24] [25] [26]. This means that the networks can accomplish any arbitrary mapping, given that a sufficiently number of hidden units are available. However, RBFNNs possess also the best approximation propriety, which is not present in MLPNNs [27]. The best approximation propriety means that there is always a RBFNN that provides the minimum error for the function to be approximated. Unlike the standard MLPNN, the RBFNN basis-functions can have local behaviour, meaning that a change in one basis functions does not affect the behaviour of the network in other areas of the space, enabling a

more efficient and independent use of the neurons. The disadvantages of this local behaviour is that training becomes slower and the adaptation can be caught in local minima[12]. It is referred in [12] that RBFNNs training is very efficient, once the centres are determined, since the error is then linear in weights. This means that the weights at the output layer can be optimally set in one iteration by, for example, a linear least squares operation. This characteristic originated a new training schema, based on the separability of the parameters into linear and nonlinear [28], as it will be explained latter on this chapter (Sub-section 2.2.1, Hybrid Training).

### 2.2.1 Training schemes

In the early beginning, RBFNNs training was just the placement of a basis function at each data point. This way, a RBFNN was an interpolator, where the goal was to force the function to pass exactly through all of the training points. This strategy suffered from the increase in complexity with the data size, leading to ill-conditioned networks quite often. To solve this problem, RBFNNs should be regarded as approximators instead of interpolators, meaning that the centres do not coincide and are less than the data points.

#### Fixed centres selected at random

The simplest way to construct a RBFNN approximator is by selecting the centres randomly. Alternatively, the centres can be randomly selected from the training set. When this strategy is used the spreads are normally taken as [29]:

$$\sigma = \frac{d_{max}}{\sqrt{2n}}, \tag{2.6}$$

where $d_{max}$ is the maximum Euclidean distance between centres and $n$ is the number of centres, in the $\mathbf{R}^d$ space. Equation 2.6 ensured that each basis function is not

too peaky or too flat; both of these extreme conditions should be avoided [29]. The linear weights ($\mathbf{u} = [\alpha_1, \cdots, \alpha_n, b]$) are then found by:

$$\hat{\mathbf{u}} = \mathbf{\Phi}^{+}\mathbf{t}, \tag{2.7}$$

where $\mathbf{\Phi}^{+}$ is the pseudo-inverse matrix of the hidden neurons output with dimensions $P \times n$, being $P$ the number of patterns or points. The vector $\mathbf{t}$ represents the target or desired network output, which has dimensions $P \times 1$.

### Self-organised selection of centres

The problem with the above training scheme is that it may require a large training set and several different random initialisations to reach the desired performance. Alternatively a two stage framework can be employed. First of all the centres and spreads $\{c_i, \sigma_i\}_{i=1}^{n}$ are found using a data clustering method. The second stage encompasses the determination of the linear parameters, which can be found by applying a linear least-squares strategy. The most popular data clustering method is the K-means clustering algorithm (see algorithm 1)[30]. The k-means clustering algorithm iterates until no significant changes are visible in the centres. This is a special case of a competitive learning process known as the *self-organising map*. The above algorithm can only achieve local optimum solutions that depend on the initial centre values. The solution to this limitation was proposed in [31], where an algorithm based on a cluster variation-weighted measure, is proposed, enabling the above algorithm to converge to an optimum or near-optimum, independently of the initial centre values [29]. This enhanced *K-means algorithm* was called the *optimal adaptive k-means clustering algorithm* (OAKM).

The spreads of the basis functions can be found using Equation 2.6, or using other strategies such as:

**Algorithm 1** k-means clustering algorithm

1: Initialisation – Choose different random values for the centres, and keep their Euclidean norm small;
$j = 1$
2: **while** go_on **do**
3: Sampling – Find a sample vector $x(j)$ from the input matrix
4: Similarity matching – Find the centre (out of $m_1$) closest to $x(j)$. Let its index be

$$k(x) : k(x) = \arg\min_i ||\mathbf{x}(j) - \mathbf{c}_i||_2, \quad i = 1, ..., n$$

5: Updating – Adjust the centres according to:

$$\mathbf{c}_i[j+1] = \begin{cases} \mathbf{c}_i[j] + \eta(\mathbf{x}(k) - \mathbf{c}_i), & i = k(x) \\ \mathbf{c}_i[j], & \text{otherwise} \end{cases}$$

where $\eta$ is a learning-rate parameter that assumes values between 0 and 1.
6: $j = j + 1$
7: **end while**

- the *k-nearest neighbours heuristic*, defined as:

$$\sigma_i = \frac{\sum_{j=1}^{k} ||\mathbf{c}_i - \mathbf{c}_j||_2}{k\sqrt{2}}, \tag{2.8}$$

being $k$ a user-defined percentage of the closest centre to $\mathbf{c}_i$;

- the *empirical standard deviation*, given by:

$$\sigma_i = \sum_{i=1}^{l} \sqrt{\frac{||\mathbf{c}_i - \mathbf{x}_j||_2^2}{n}}, \tag{2.9}$$

where $n$ represents the number of patterns (training figures) associated with cluster $i$;

- maximum distance between patterns, defined as:

$$\sigma_i = \frac{max_{i,j=1,...,p}||\mathbf{x}_i - \mathbf{x}_j||}{2\sqrt{2}}, \tag{2.10}$$

where $p$ is the number of training patterns.

### Supervised selection of RBFNNs parameters

In this learning scheme all the network parameters ($\mathbf{c}_i$, $\sigma_i$ and $\mathbf{u}$) are free parameters that are found by a supervised learning process[1], which can be performed by a gradient descent algorithm, such as the well known Back-propagation (BP) algorithm [22] [23]. Of course, the application of a gradient-based algorithm implies that the network is differentiable in their parameters.

The BP algorithm has the following parameter update rule:

$$\mathbf{w}[k+1] = \mathbf{w}[k] - \eta \mathbf{g}[k], \tag{2.11}$$

where $\mathbf{w}$ is the vector representing the model parameters, $\eta$ the learning rate, and $\mathbf{g} = d\Omega/d\mathbf{w}$ is the gradient vector. Usually, the error criterion applied is based on the sum of the squared errors:

$$\Omega(\mathbf{w}, \mathbf{x}) = \sum_{i=1}^{P} \frac{(t_i - y(\mathbf{w}, \mathbf{x}_i))^2}{2} = \frac{||\mathbf{t} - \mathbf{y}(\mathbf{w})||_2^2}{2} = \frac{||\mathbf{e}||_2^2}{2}, \tag{2.12}$$

where $\mathbf{t}$ is the desired output, $\mathbf{y}$ is the network output obtained, $P$ is the number of training patterns, $\mathbf{x}_i$ is the ith input vector and $\mathbf{e}$ is the error vector. For the remaining of this section, the input vector $\mathbf{x}_i$ will be omitted, since it is always constant for the off-line training schemas presented. The BP is computationally efficient, but since it implements the steepest descent method, its convergence rate can be slow. In addition, it is difficult to select the appropriate learning rate.

[1]Supervised learning is a paradigm where input and the desired output patterns are always present. In an iterative fashion, the response of the networks is assessed and compared with the desired one. The difference between the desired and attained response (error) is then used to adjust the network parameters, according to some criterion. Usually, this process is repeated until a desired error level is attained. Supervised learning is recognised as powerful paradigm for the design of artificial neural network [29].

In the field of unconstrained non-linear optimisation, some alternatives to the BP algorithm, can be pointed as follow:

- Conjugate gradient– Is a similar approach to the *steepest descent* one, but including a momentum term. The momentum is not obtained at an *ad-hoc* fashion, but is found at each iteration to produce conjugate search directions. The parameter update rule for this approach is:

$$\mathbf{w}[k+1] = \mathbf{w}[k] - \eta\mathbf{g}[k] + \beta[k]\Delta\mathbf{w}[k-1]. \tag{2.13}$$

  In the same way, $\eta$ is the learning rate, $\mathbf{g}[k]$ the gradient vector, and $\Delta\mathbf{w}[k-1] = \mathbf{w}[k] - \mathbf{w}[k-1]$. The parameter $\beta$[k] could be determined in different ways, but probably, the most accepted one is[13]:

$$\beta[k] = \frac{\mathbf{g}^T[k]\mathbf{g}[k]}{\mathbf{g}^T[k-1]\mathbf{g}[k-1]}. \tag{2.14}$$

- Quasi-Newton– This class of methods employ an approximation of the inverse of the Hessian matrix ($\mathbf{H}$), which is the inverse of the matrix of the second derivatives of $\Omega(\mathbf{w}, \mathbf{x})$ (from Equation 2.12). The update rule for this kind of methods is:

$$\mathbf{w}[k+1] = \mathbf{w}[k] - \eta[k]\mathbf{H}[k]\mathbf{g}[k]. \tag{2.15}$$

  It is reported in [13] that the most frequently used approximation to $\mathbf{H}[k]$ is the Broyden, Fletcher, Goldfarb and Shanno (BFGS) approach.

- Levenberg-Marquardt (LM)– This method was initially proposed by Kenneth Levenberg in [32], and rediscovered by Donald W. Marquardt [33]. This method uses the Gauss-Newton method to approximate the Hessian ($\mathbf{G}$). Con-

sidering the error criterion given by equation 2.12, the gradient is:

$$\mathbf{g}(\mathbf{w}) = \nabla\Omega(\mathbf{w}) = \mathbf{J}^T(\mathbf{w})\mathbf{e}(\mathbf{w}), \tag{2.16}$$

where $\nabla$ is the gradient operator ($\nabla\Omega(\mathbf{w}) = \left[\frac{\partial\Omega(\mathbf{w})}{\partial w_1}, \ldots, \frac{\partial\Omega(\mathbf{w})}{\partial w_n}\right]^T$, being $n$ the number of weights), and $\mathbf{J}$ is the Jacobean matrix given by:

$$\mathbf{J}(\mathbf{w}) = \begin{pmatrix} \frac{\partial e_1(\mathbf{w})}{\partial w_1} & \cdots & \frac{\partial e_1(\mathbf{w})}{\partial w_n} \\ \vdots & \ddots & \vdots \\ \frac{\partial e_P(\mathbf{w})}{\partial w_1} & \cdots & \frac{\partial e_P(\mathbf{w})}{\partial w_n} \end{pmatrix}, \tag{2.17}$$

where $e_i$ is the instantaneous error for the i-th pattern, $P$ is the number of patterns, and $n$ again the number of network weights. The Hessian matrix is given by:

$$\mathbf{G}(\mathbf{w}) = \nabla^2\Omega(\mathbf{w}) = \mathbf{J}(\mathbf{w})^T\mathbf{J}(\mathbf{w}) + \mathbf{S}(\mathbf{w}), \tag{2.18}$$

where $\nabla^2$ is the Laplacian operator, and:

$$\mathbf{S}(\mathbf{w}) = \sum_{i=1}^{P} \mathbf{e}(\mathbf{w})\nabla^2 e_i(\mathbf{w}). \tag{2.19}$$

Assuming that $\mathbf{S}(\mathbf{w})$ is small, then the Hessian is approximated by:

$$\mathbf{G} \approx \mathbf{J}(\mathbf{w})^T\mathbf{J}(\mathbf{w}). \tag{2.20}$$

The LM parameter update for iteration $k$ is given as the solution of:

$$(\mathbf{J}(\mathbf{w}[k])^T\mathbf{J}(\mathbf{w}[k]) + \nu[k]\mathbf{I})\Delta\mathbf{w}[k] = -\mathbf{J}(\mathbf{w}[k])\mathbf{e}(\mathbf{w}[k]), \tag{2.21}$$

where $\mathbf{I}$ represents the identity matrix, and $\nu[k]$ a regularisation parameter, which is detailed afterwards. The LM is of the "trust-region" or "restricted

step" type, meaning that the method tries to identify a neighbourhood where the quadratic function model agrees with the actual error function in some sense. This algorithm ensures that the convergence to a local minimum is guaranteed, even when the Jacobean matrix is rank-deficient. The radius of the neighbourhood is controlled by the parameter $\nu[k]$, where its update should then reflect how well the actual error function is represented by a quadratic one. Using this approach, the predicted criterion reduction ($\Delta\Omega^p(\mathbf{w}[k])$) is:

$$\Delta\Omega^p(\mathbf{w}[k]) = \Omega(\mathbf{w}[k]) - \frac{(\mathbf{e}^p(\mathbf{w}[k]))^T(\mathbf{e}^p(\mathbf{w}[k]))}{2}, \tag{2.22}$$

being:

$$\mathbf{e}^p(\mathbf{w}[k]) = \mathbf{e}(\mathbf{w}[k]) - \mathbf{J}(\mathbf{w}[k])\Delta\mathbf{w}[k]. \tag{2.23}$$

The actual criterion reduction is:

$$\Delta\Omega(\mathbf{w}[k]) = \Omega(\mathbf{w}[k]) - \Omega(\mathbf{w}[k] + \Delta\mathbf{w}[k]). \tag{2.24}$$

The ration between the actual and the predicted criterion reduction ($r[k] = \frac{\Delta\Omega(\mathbf{w}[k])}{\Delta\Omega^p(\mathbf{w}[k]}$) is used to update the regularisation parameter ($\nu$). Normally the following update rule is employed [13]:

$$\nu[k+1] = \begin{cases} \frac{\nu[k]}{2}, & r[k] > \frac{3}{4} \\ 4\nu[k], & r[k] < \frac{1}{4} \\ \nu[k], & others. \end{cases} \tag{2.25}$$

For negative values of $r[k]$ only the regularisation parameter is updated, not the network parameters.

One important aspect related with gradient-descent algorithms is the stopping criterion employed. Two classes of stopping criterions can be identified:

- Stopping based on the training error – The simplest way to stop training is by considering a pre-defined number of iterations to adapt the parameters. The unique advantage on this technique is the simplicity, given that it does not use any information of how well the parameters are adapted to the training data. When the pre-defined number of iterations is reached there is no guarantee that the parameters are close to the optimal ones. To avoid these problems, training is normally stopped when a desired resolution is attained. The commonly used termination criterion in non-linear optimisation is[13]:

$$\Omega[k-1] - \Omega[k] < \tau_f \cdot (1 + \Omega[k]), \tag{2.26}$$

$$||\mathbf{w}[k-1] - \mathbf{w}[k]|| < \sqrt{\tau_f} \cdot (1 + ||\mathbf{w}[k]||), \tag{2.27}$$

$$||\mathbf{g}[k]|| < \sqrt[3]{\tau_f} \cdot (1 + |\Omega[k]|), \tag{2.28}$$

  where $\tau_f$ is a measure of the desired number of correct digits in the training criterion. Training stops when all the three conditions are met.

- Stopping based on generalisation – The preceding procedure guarantees that the trained model is well-fitted for the training data, but there exists no information about how well the model performs in fresh data, that is, no information about the generalisation capacity of the model. The model may become so specialised in the training data, that looses the ability to follow unseen data. The solution to this problem is to stop training taking into account the performance of the network with new data. It is referred in [12] that it is experimentally verified that the training error always decreases with the number of iterations, for a sufficiently large network. On the other hand, the error in fresh data initially decreases but eventually starts to increase (see Figure 2.4). The training algorithm should then stop when the error in fresh data begins to increase, as shown in Figure 2.4. This stopping modality is called the

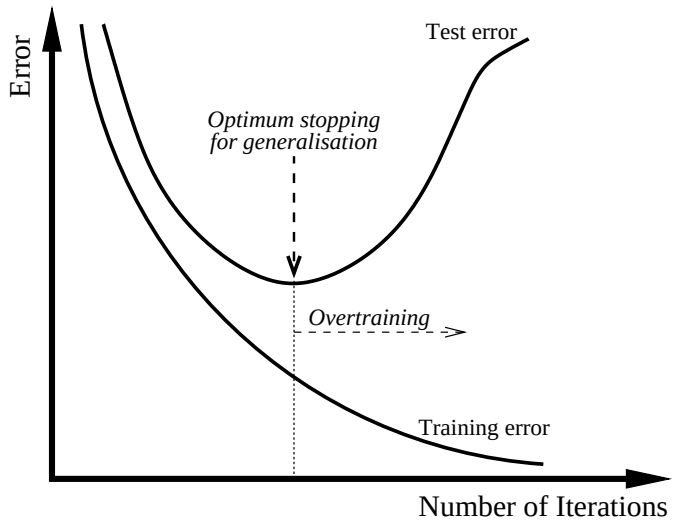


**Figure 2.4:** *Variation of the training and test errors, with the number of iterations. The Early-stopping criterion assesses the point of maximum generalisation to stop training and prevent overtraining. (Figure adapted from [12]).*

*early-stopping* technique. This procedure implies that the available training data must be subdivided in two sets: one training set used to find the model parameters, and a fresh data set called test-set used for establishment of the *early-stopping* criterion. The main disadvantage of this technique is requiring two sets of data (training and test), which, for scarce data environments, may result on a limitation of its applicability. The " early-stopping" is referred as the recommended stopping criterion for real-world applications [12], thus is applied in this thesis.

### Regularisation

RBFNNs can also be trained using the regularisation theory proposed in [34]. The regularisation theory was introduced in the context of approximation theory to deal with ill-posed problems, and was introduced in the neural network field by [35]. A possible training criterion used in regularisation is:

$$\phi = \frac{||\mathbf{t} - \mathbf{y}||_2^2 + \lambda||\mathbf{u}||_2^2}{2}, \tag{2.29}$$

where $\mathbf{t}$ is the target output vector, $\mathbf{y}$ is the network output vector, $\mathbf{u}$ is the linear weights vector, and $\lambda$ is the regularisation parameter (which is set in a trial-and-error schema). To note that the possible values of the non-linear parameters (centres and spreads in the RBFNN case) are related with the range of the input data (which is bounded). This means that the ill-posed problem only occurs in the linear parameters ($\mathbf{u}$), enabling the non-linearly transformed input data to fit the most close as possible the desired output ($\mathbf{t}$). The norm of the linear weights can assume a very high value, resulting in overtraining and consequently in bad generalisation. The above criterion incorporates a term which measures the value of the weights, meaning that during training not just the error but also the weights norm are taken into account. The regularisation presented above is called the *zero-order regularisation*. The application of high-order procedures is also possible, as explained in [13].

### Hybrid training

Some of the above techniques can be combined to improve training. The centres can be initialised using the unsupervised optimal adaptive k-means clustering algorithm (OAKM), and then a supervised gradient-based training approach can be used to improve the adjustment of the parameters. In this thesis the combination of the OAKM algorithm and a strategy that involves the Levenberg-Marquardt (LM) algorithm is extensively applied for RBFNN training.

To mention that a RBFNN has two types of parameters ($\mathbf{w} = [\mathbf{v}, \mathbf{u}]^T$) that must be found, the non-linear ($\mathbf{v} = [\mathbf{c}_1, \cdots, \mathbf{c}_n, \sigma_1 \cdots, \sigma_n]^T$) and the linear ones ($\mathbf{u} = [\alpha_1, \cdots, \alpha_n, b]^T$). The network output can be expressed as:

$$\mathbf{y} = \mathbf{\Phi}(\mathbf{v})\mathbf{u}, \tag{2.30}$$

where $\mathbf{\Phi}$ is the matrix of the hidden neurons outputs, with a column of ones to

account for the bias term ($b$). Considering the error criterion presented in equation 2.12:

$$\Omega(\mathbf{v}, \mathbf{u}) = \frac{||\mathbf{t} - \mathbf{y}||_2^2}{2} = \frac{||\mathbf{t} - \mathbf{\Phi}(\mathbf{v})\mathbf{u}||_2^2}{2}. \tag{2.31}$$

For any value of $\mathbf{v}$, the optimum value of $\Omega$ with respect to $\mathbf{u}$ can be found using the linear least-squares solution, which can be determined using the pseudo-inverse of $\mathbf{\Phi}$ ($\mathbf{\Phi}(\mathbf{v})^+$):

$$\hat{\mathbf{u}} = \mathbf{\Phi}(\mathbf{v})^+\mathbf{t}. \tag{2.32}$$

Replacing the above equation in 2.31, a new training criterion arises:

$$\psi(\mathbf{v}) = \frac{||\mathbf{t} - \mathbf{\Phi}(\mathbf{v})\mathbf{\Phi}(\mathbf{v})^+\mathbf{t}||_2^2}{2}. \tag{2.33}$$

This new criterion was proposed in [28]. It depends only on the non-linear parameters and improves the performance of the training algorithms by exploiting the separability of the parameters[28].

In [28] and [36] it is proven that the gradient of $\psi$ can be determined, computing first the optimal value of $\mathbf{u}$ and then performing the normal gradient computation, considering only the partition related with the non-linear parameters. The same procedure can be applied to compute the Jacobean matrix. The application of criterion 2.33 instead of 2.12 can bring some advantages [13]:

- the dimension of the problem is reduced;
- when the LM is used, each iteration is computationally cheaper;
- usually a smaller number of iterations are required to obtain convergence to a local minimum.

In this thesis the LM algorithm (as presented previously) was used to minimise the criterion presented in Equation 2.33, that is to found the non-linear parameters

($\mathbf{v} = [\mathbf{c}_1, \cdots, \mathbf{c}_n, \sigma_1 \cdots, \sigma_n]^T$); while the linear weights ($\mathbf{u} = [\alpha_1, \cdots, \alpha_n, b]^T$) were found at each training iteration by using the linear least-squares method.

### 2.2.2 Structure selection schemes

The most popular structure selection method for RBFNNs is the orthogonal least squares (OLS) algorithm [37]. This algorithm chooses the centres one by one in an iterative fashion, until a desired performance level is attained. By using an orthogonalisation process a subset of centres are chosen from a larger set previously determined. The linear weights of the network are found using the linear least-squares strategy.

Another approach to select RBFNNs centres is to use the resource allocation network (RAN) method proposed in [38]. This method adds a neuron to the network when the error or the distance between the current pattern and its neighbour exceeds pre-defined thresholds. As the network construction is performed in a pattern-by-pattern basis, this method is suitable for on-line applications.

The above structure selection methods deal exclusively with the selection of the number of hidden neurons. However, there exist situations where multiple variables are available as inputs, and the selection of the relevant ones is also important. The selection of both the relevant inputs and the number of neurons can be a high-time consuming task, due to the enormous number of possible combinations. A suitable way to search for proper solutions from large search spaces is by means of evolutionary algorithms. Normally, more than one model feature is relevant for the final application. For example, low-error and also low-complex models are desired, and the structure selection problem should be formulated as a multi-objective optimisation procedure, using multi-objective evolutionary algorithms (MOEAs). In the particular case of RBFNN the multi-objective genetic algorithm (MOGA) [10] was extensively applied for greenhouse climate prediction [39], prediction of building's

temperature [40], and in non-invasive temperature estimation [41].

## 2.3 ANFIS models

The development of fuzzy systems [42] [43] [44] was originally motivated by the need of using human reasoning to solve problems . A mathematical model which in some way uses fuzzy systems is called a fuzzy model. In fuzzy systems, relationships are represented explicitly in the form of if-then rules with fuzzy predicates, such as "if door is open then temperature is low". To make a fuzzy model operational, the terms "open" and "low" must be defined more precisely. This is done by using fuzzy sets, which refer to sets where the membership is changing gradually rather than in an abrupt way. Fuzzy sets are defined by their membership functions, which defines the degree of membership of particular elements to the related set. These functions assume values between 0 and 1. The extreme values 0 and 1 denote non-membership or complete membership, respectively. The values between 0 and 1 represent partial membership in the fuzzy set. An element can simultaneously belong to more than one set with different degrees of membership. Depending on the structure of the if–then rules, two types of fuzzy models can be pointed: the Mamdani, also called the linguistic model; and the Takagi–Sugeno model.

### 2.3.1 Mamdani model

The Mamdani model [43] considers fuzzy propositions for both the "if" (antecedent) part and "then" (consequent) part of the rules:

$$\mathcal{R}_i : \text{if } \mathbf{x} \text{ is } A_i \text{ then } y \text{ is } C_i, \quad i = 1, 2, \cdots, K. \tag{2.34}$$

$K$ is the number of rules, and $A_i$ and $C_i$ are the antecedent and consequent

linguistic terms, such as “slow”, “fast’, which are represented by fuzzy sets. The Mamdani model is more suited for qualitative purposes, although it can be applied also for quantitative applications. Data–driven techniques can be applied to adapt the membership functions to a desired input–output map [45].

### 2.3.2 Takagi–Sugeno model

While the Mamdani model has been mostly applied to represent qualitative expert knowledge, the Takagi–Sugeno (TS) model [44] was extensively used for quantitative applications, such as data–driven identification. This model consider rules with an antecedent part like the Mamdani model, and a consequent part formed by an affine linear function of the input variables:

$$\mathcal{R}_i : \text{if } \mathbf{x} \text{ is } A_i \text{ then } y_i = \mathbf{a}_i^T \mathbf{x} + b_i, \quad i = 1, 2, \cdots, K, \tag{2.35}$$

where $\mathbf{a}_i$ is a vector of consequent parameters and $\{b_i\}_{i=1}^K$ is a bias term for the i-th rule. The TS model combines a linguistic description with standard functional regression. The antecedent part describes regions in the input space where the consequent functions are valid. The overall input/output relation for this model is:

$$y = \frac{\sum_{i=1}^K \beta_i(\mathbf{x}) y_i}{\sum_{i=1}^K \beta_i(\mathbf{x})} = \frac{\sum_{i=1}^K \beta_i(\mathbf{x})(\mathbf{a}_i^T \mathbf{x} + b_i)}{\sum_{i=1}^K \beta_i(\mathbf{x})}, \tag{2.36}$$

where $\beta_i(\mathbf{x})$ is the degree of fulfilment of the i-th rule. If only the bias ($\{b_i\}_{i=1}^K$) terms are considered (i.e. the consequent part is formed by zero–order polynomials) the input/output relation is given by:

$$y = \frac{\sum_{i=1}^K \beta_i(\mathbf{x}) b_i}{\sum_{i=1}^K \beta_i(\mathbf{x})}. \tag{2.37}$$

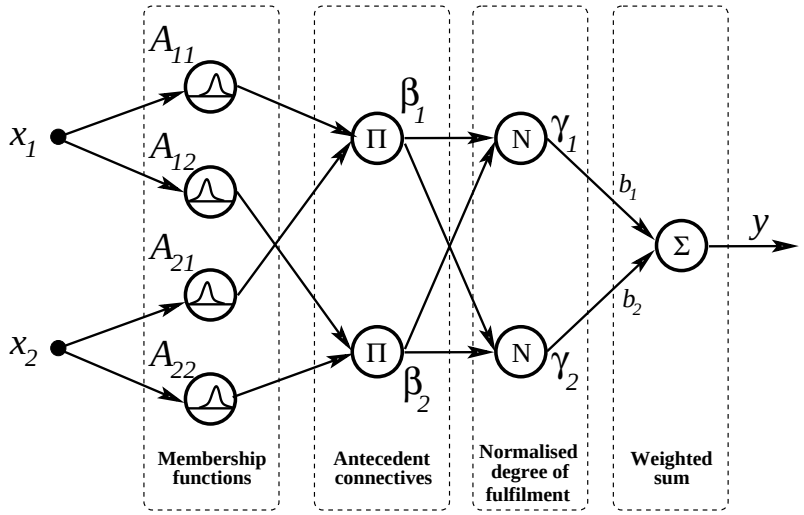


**Figure 2.5:** *ANFIS structure representing a two rule zero–order Takagi–Sugeno fuzzy model (adapted from Figure 1.4 in [13]).*

This simplified TS model is a special case of a Mamdani model, where the consequent fuzzy sets are singletons (real numbers).

### 2.3.3 ANFIS system

Fuzzy systems can be viewed as structures similar to radial-basis-functions neural networks [13]. In this way, the standard training algorithms applied to neural networks can be used for fuzzy systems. This is commonly known as neuro-fuzzy modelling.

Considering the zero-order TS model with two rules:

$$\begin{cases} \text{if } x_1 \text{ is } A_{11} \text{ and } x_2 \text{ is } A_{21} \text{ then } y = b_1 \\ \text{if } x_1 \text{ is } A_{12} \text{ and } x_2 \text{ is } A_{22} \text{ then } y = b_2 \end{cases}$$

These rules can be represented as a feed–forward network, as is shown in Figure 2.5. The first layer compute the membership degree of inputs in the antecedent fuzzy sets. The second layer is formed by a set of product nodes, acting like the antecedent connective “and” in the rules. A third layer performs a normalisation on

the *degree of fulfilment* ($\beta_1$ and $\beta_2$ ) of each rule. The overall output is obtained at the fourth layer by applying a wighted sum to the normalised *degree of fulfilment*. This structure is the Adaptive Neuro–Fuzzy Inference System (ANFIS) and was first introduced by J.-S. R. Jang on [46]. The input/output relation of a zero–order ANFIS model is:

$$y = \sum_{i=1}^{K} \gamma_i(\mathbf{x}) b_i, \tag{2.38}$$

where:

$$\gamma_i(\mathbf{x}) = \frac{\prod_{j=1}^{p} \mu A_{i,j}(x_j)}{\sum_{i=1}^{K} \prod_{j=1}^{p} \mu A_{i,j}(x_j)}, \tag{2.39}$$

where $p$ is the number of inputs on the system, $K$ the number of rules, and $\mu A_{i,j}(x_j)$ is the antecedent membership function related with the i-th rule and with the j-th input. It is pointed in [13] that smooth functions, such as Gaussian functions, are normally employed. In the same way as for the zero-order TS model, the first–order version can also be represented as an ANFIS structure. A first–order TS model with two rules is represented by:

$$\begin{cases} \text{if } x_1 \text{ is } A_{11} \text{ and } x_2 \text{ is } A_{21} \text{ then } y_1 = a_{11}x_1 + a_{12}x_2 + b_1 \\ \text{if } x_1 \text{ is } A_{12} \text{ and } x_2 \text{ is } A_{22} \text{ then } y_2 = a_{21}x_1 + a_{22}x_2 + b_2 \end{cases}$$

The corresponding ANFIS structure is presented in Figure 2.6. The input/output relation of a general first–order network is:

$$y = \sum_{i=1}^{K} \gamma_i(\mathbf{x})(\mathbf{a}_i^T \mathbf{x} + b_i), \tag{2.40}$$

being $\gamma_i(\mathbf{x})$ the same as for the zero–order structure.

As for the the neural networks, gradient-descent rules can be derived for the ANFIS structure, and the commonly used training algorithms employed. In addition, the ANFIS parameters can also be separated in non-linear (the parameters on the

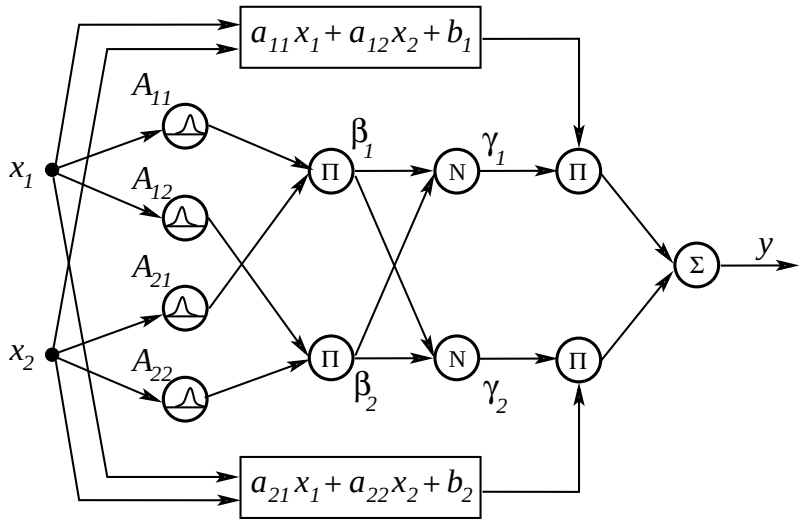


**Figure 2.6:** *ANFIS structure representing a two rule first–order Takagi–Sugeno fuzzy model (adapted from Figure 1.5 in [13]).*

antecedent part, related with the membership functions) and linear (the parameters on the consequent part, related with the affine linear functions), as for the RBFNNs. This means that a hybrid learning technique can be employed. As explained for the RBFNNs the linear parameters can be obtained with the linear-least-squares strategy, while the non-linear ones are found using the standard training algorithms, such as the Back-propagation or the Levenberg Marquardt methods.

## 2.4 Multi-objective genetic algorithms

### 2.4.1 Foundations of genetic algorithms

Genetic algorithms (GAs) introduced by Holland in [47] and popularised by Goldberg in [48], are a subset of a larger set called evolutionary algorithms (EAs). This kind of algorithms is based on natural evolution and survival of the fittest notion. GAs evolve a population of individuals (potential problem solutions), meaning that multiple points in the search space are investigated simultaneously. This parallel search behaviour enables GAs to search for global optimum, instead of local op-

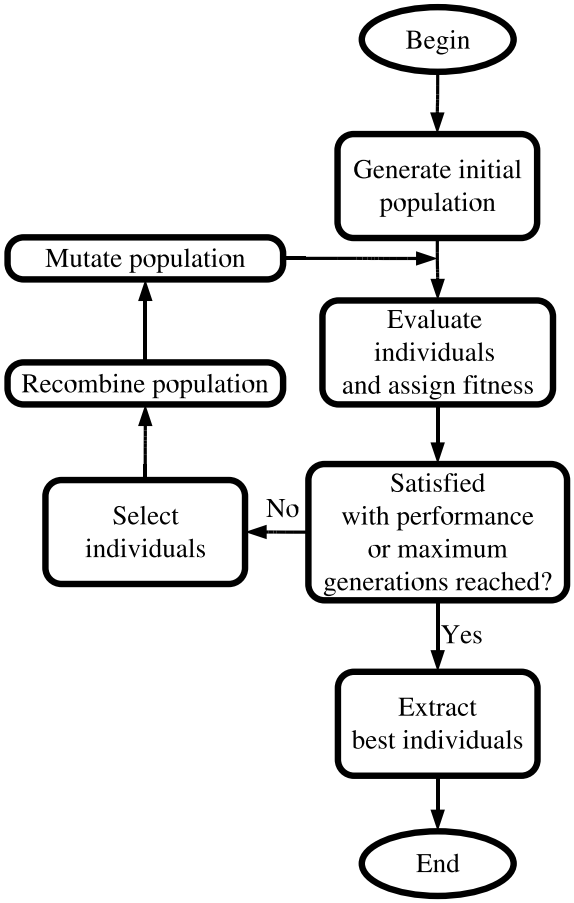


**Figure 2.7:** *Genetic algorithm flowchart.*

timum solution, which is provided by other evolutionary algorithms, such as the evolutionary strategies (ESs) [49] [50]. The individuals compete between each other for survival, and each one can be defined at two levels: the *phenotypic* level and the *genotypic* level. An individual's *phenotype* is its value in the domain where the objective function is defined. The individual's *genotype* is a representation of its *phenotype* at a lower level, which is manipulated by the GA to evolve the population. In analogy, the *phenotype* is for example the hair colour, or the height in a human being; while the *genotype* corresponds to the genetic sequences in biological chromosomes [9]. In the original GA, the chromosomes are *bit* strings encoding the individuals features. However, other data structures can be used to encode the individuals, such as matrices, trees, etc.[9]. At each iteration (see Figure 2.7) the in-

dividuals must be evaluated in order to assess their appropriateness to the problem, and then to improve the reproduction of the fittest. The individuals are evaluated considering an objective function which defines the problem. After the evaluation, each individual has an associated cost (considering a minimisation problem), and the *fitness* of each one is a function of its cost, assigned taking into account the other individuals. The cost is a problem-dependent measure which is not changeable, and that can assume values in any ordered set. On the other hand, fitness is related to the selection process and can be customisable, for a given optimisation strategy. The cost-to-fitness mapping should be monotonic onto $\mathbf{R}^+$. The two main types of fitness assignment strategies are: scaling, where fitness is computed as a linear or non-linear function of the cost; and ranking, where the population is sorted by cost and then the fitness values are assigned according to the position (ranking) of the individuals in the population. The functions used to translate between rank and fitness are usually linear or exponential. It is said in [9] (page 14), that the main difference between exponential and linear fitness assignment is that the first one does not penalise so much the worst individuals, and assign to the middle-rank individuals fitness values slightly less than the average. It is also stated in [9] that the exponential ranking generally contributes to a more diverse search. Ranking strategies eliminates the scale dependence, controlling the excessive reproduction of the so called "super" individuals, which could happen during the standard scaling approach. In this situation, an individual can assume high fitness values and through selection rapidly dominate the population. The difference between the other individuals in the population can be so minimal that the search process could become stagnant. Even when the individuals are similar, ranking enables that the best one is always preferred to the rest of the population.

If the stopping criterion is not met then individuals from the population must be selected to generate the new population. In the GA the selection process has

stochastic behaviour (to avoid systematic errors), and the probability of an individual being selected is determined by its fitness value. Obviously the fittest individuals are those with greater probability of being selected. There are three standard selection schemas: *Roulette Wheel Selection* (RWS) proposed by Goldberg's [48], *Stochastic Universal Sampling*[51] (SUS), and *Tournament Selection*[52]. RWS or sampling with replacement consists of a sequence of independent selection trials. The probability of one individual being selected at each trial remains constant and equal to its normalised fitness. On the other hand, SUS consists of a single selection event, where a single random value is used to sample all the individuals by choosing them at uniformly spaced intervals. *Tournament selection* is based on a different concept. In this selection schema at least two individuals are randomly picked from the population and then are compared (compete) among each other and the fittest one (the winner) is selected. Tournament selection is useful when it is easier to compare the individuals, such as in genetic programming approaches. It was reported in [9] that RWS originates large selection errors, while using SUS the expected number of offspring of an individual corresponds to its fitness, and the selection errors remain as small as possible. Tournament selection , like RWS, originates also large selection errors.

After selection the chosen individuals should be modified, using variation operators (*genetic operators*), in order to search for best performance and to introduce some novelty to the evolutionary process. Two main categories of genetic operators exist: recombination or crossover and mutation operators. The recombination operators implies the presence of at least two individuals. One or more points are selected in the individuals chromosome, then they are broken and subsequent genetic material exchanged between parents. In Figure 2.8 *single-point crossover* involving two individuals represented by binary strings is shown.

Crossover aims to attain superior performance based on the known solutions.

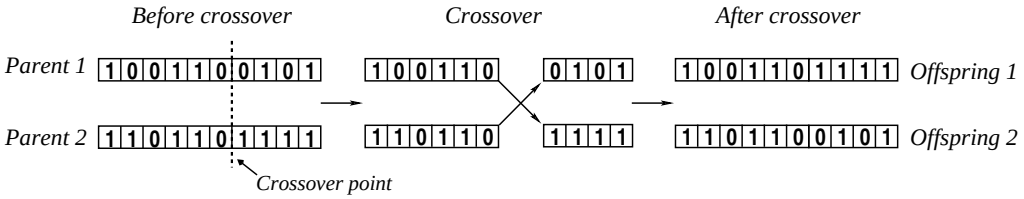


**Figure 2.8:** *Binary single-point crossover.*

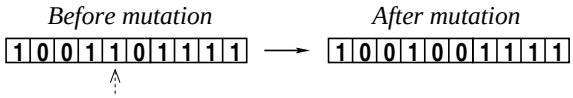


**Figure 2.9:** *Binary mutation.*

Mutate an individual means that its genotype representation will suffer a small change, according to a specific probabilistic rule. Figure 2.9 exemplifies using a binary string the mutation of an individual. A bit in the chromosome is identified and then changed by its opposite value. Mutation aims to explore new areas in the search space, having in mind the attainment of better performance which by recombination probably could not be reached. The variation operators above presented have stochastic behaviour and accept parameters that define the probability and nature of a particular application. The choice of these parameters is an important aspect to the success of the optimisation process. More information on the selection of the mutation rate is exposed in [9], in pages 23 and 24.

After crossover and mutation the generated offspring must be inserted into the population. The original genetic algorithm implements a generational replacement model, where the old population is all unconditionally replaced by the new one. Some other strategies propose that the offspring should have the possibility to compete with at least some of their parents. In [9] the different approaches to select the parents to replace, the different ways to reinsert, and additional considerations on this topic are reported.

### 2.4.2 Multi-objective optimisation using genetic algorithms

In engineering most of the problems need the attainment of multiple criterions/objectives. These objectives may be such that improving one may deteriorate the other (conflicting objectives). On these situations the problem presents a set of solutions rather than a single optimal one, the so called Pareto-optimal set [53]. A solution is said non-dominated or Pareto-optimal if among the whole set of solutions, there is no better solution, regarding all the objectives. The purpose of a multi-objective optimiser is to move the front surface formed by the non-dominated solutions as close as possible to the origin of the objective space (point "O" in Figure 2.10), assuming a minimisation problem and non-negative objectives.

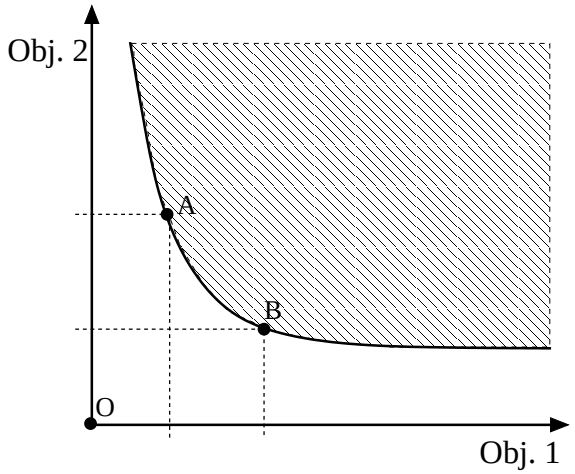


**Figure 2.10:** *Bi-objective minimisation problem. The solid line represents the non-dominated solutions, and the dominated ones are located on the shaded region.*

The solid line in Figure 2.10 represents the non-dominated solutions of the overall solution set (considering a two-objective minimisation problem), being A and B two Pareto-optimal solutions. The dominated solutions are located on the shaded area. Visualisation of the non-dominated solutions, like the one above presented, is only possible when a maximum of three objectives is considered. Otherwise, the method of parallel coordinates is commonly applied [9]. In this method an integer index is associated to each objective, and then each non-dominated solution is represented by

a line which connects the points defined by the associated index and the normalised objective value (see Figure 2.11).

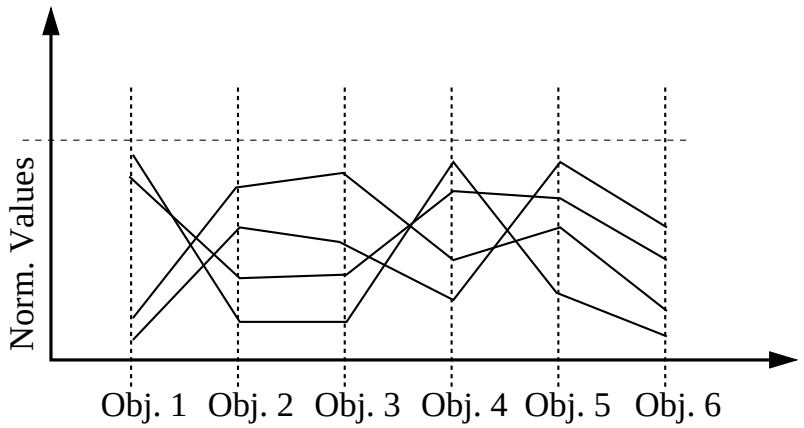


**Figure 2.11:** *Multi-objective minimisation problem. Parallel coordinates representation of a problem involving multiple objectives.*

In this representation if the lines of objectives with consecutive indexes crosse between each other, then the objectives are competitive (for example Obj. 1 and 2 in Figure 2.11). On the other hand, non-competing consecutive index objectives result in non-crossing lines (as Obj. 5 and 6 in Figure 2.11).

GAs were recognised to be well-suited for multi-objective optimisation [9]. Its population-based behaviour results in a parallel search, which provides results for a number of points within the space defined by the objectives. With a single run, a set of solutions is provided, instead of just one. Also the potential to handle complex problems, such as the ones involving noisy functions evaluation, discontinuities, multi-modality and disjoint feasible spaces, reinforce their potential for multi-objective optimisation. The standard GA proposed by Goldberg [48] can be extrapolated to handle multi-objective problems. The main challenge is the cost assignment problem. In a multi-objective problem different cost descriptors exist, and must be aggregated in some way to produce a single cost value for each individual. Once this single cost value is defined the evolutionary procedure can be the same as in a single objective problem. The simplest way to assign the cost is by using the

weighted sum approach. In this technique a weight is associated to each objective prior to the search procedure. The weights define the relative importance among objectives. This approach suffer from some problems: inappropriate weights may result in a wrong search; in most of the practical applications it is only possible to select the appropriate weights after search, meaning that multiple optimiser runs may be necessary to find the appropriate weights; small variation in the weights may result in large changes in the objective vectors, being the opposite also possible; as said in [9] and [13] this approach cannot assess non-convex regions of the search space. The Pareto dominance notion can be employed to assign cost to the individuals, and to automatically assign fitness by ranking. This schema was implemented in the Multi-objective Genetic Algorithm (MOGA) proposed by Fonseca and Fleming [10], and extensively used in this thesis for radial basis function neural network structure optimisation. This Pareto-based ranking enables the assessment of all the search space, including convex and non-convex regions. The individuals are ranked according to the number of individuals by which they are dominated. If an individual is non-dominated then its rank is 0 (the best one). However, if an individual is dominated by two other individuals then its rank is 2 and so on. In Figure 2.12 it is visualised how the individuals are ranked. The rank of a particular individual is the number of individuals that lie in the rectangle formed between its position and the origin of the objective space.

In real-world applications some individual features (objectives) should be defined as goals to be met by the optimiser, in order to obtain feasible individuals. In addition there should exist objectives which are preferable than others. The definition of goals and priorities for the objectives imply that the ranking technique presented above has to be modified. In Figure 2.13 the ranking of individuals considering the goals **g1** and **g2** and the same (a) and different (b) priorities for the objectives is presented. In Figure 2.13 a) the individuals who met the goals are assigned with a

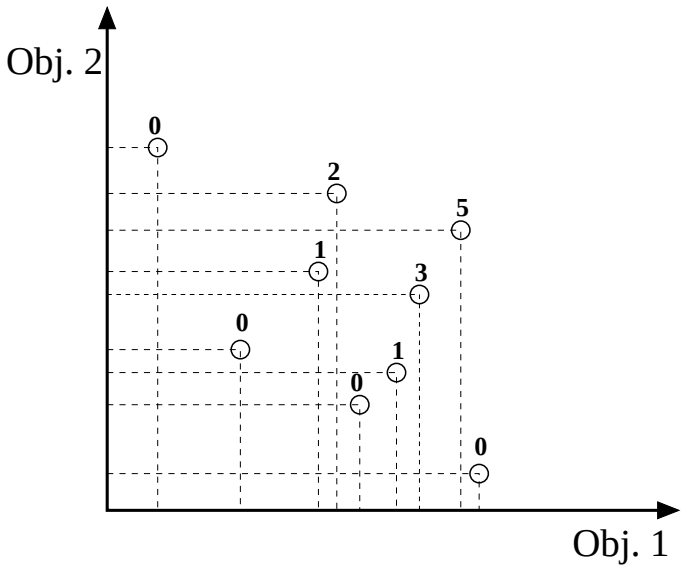


**Figure 2.12:** *Pareto ranking as implemented by the MOGA (minimisation).(Adapted from [9])*

rank equal to the number of individuals by which they are dominated. On the other hand, the individuals that not met the goals are penalised by having the assignation of a higher rank. When the objectives have different priorities the individuals that meet the higher priority goal are less penalised than the others that do not meet it.

After ranking, the fitness or the number of offspring that an individual is expected to produce through selection, must be assigned. The MOGA implements a slightly different version of the standard rank-fitness assignment strategy. Primarily, the population is sorted according to rank. Secondly fitness is assigned by interpolating from the best individual to the worst, using in general a linear or exponential function. After this, the fitness assigned to individuals with the same rank are averaged and assigned to them. In this way the individuals with the same rank have the same probability of being selected. This averaging operation enables that global population fitness to keep constant across generations [9].

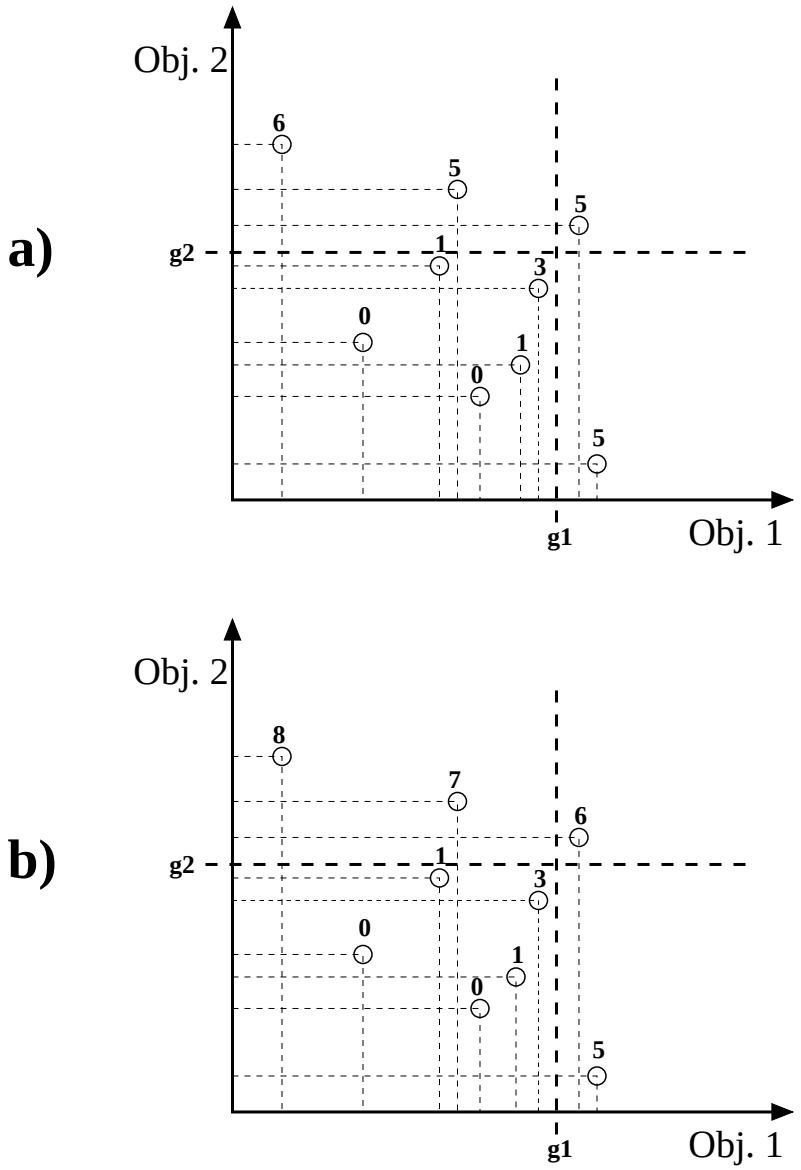


**Figure 2.13:** *Pareto ranking considering objectives and priorities (minimisation). a) equal priorities, and b) Obj. 2 has great priority. (Adapted from [9]).*

# Chapter 3

# Medical ultrasound

## 3.1 Introduction

Ultrasound are mechanical waves, with frequencies above 20 kHz, that is at frequencies that humans cannot hear. Ultrasound as well as the audible sounds are the same form of energy, and thus present the same physical properties and interaction with matter.

Ultrasound is used in medicine for both diagnostic and therapy and nowadays is an indispensable tool for non-invasive imaging and Doppler blood flow studies. Commercial ultrasound equipments now have frequencies ranging from 1 to 10 MHz [54] and can aggregate both imaging and Doppler capabilities. Thus, anatomic structures, as well as, blood flow information from a particular vessel position can be viewed simultaneously. Recent development in hardware and software enable foetal visualisation in three and four dimensions (3D plus movement). Ultrasound at higher frequencies is used for specialised imaging applications, such as in the eye and skin or for acoustic microscopy [55]. Research in new imaging techniques is an active field, which can widen even more the application of diagnostic ultrasound. The most recent ultrasound imaging techniques are based on harmonic emission and

elastography imaging. Harmonic imaging is based on the non-linear propagation of ultrasound, induced by micro-bubbles (used as contrast-agents) but also from isonated tissue. Acoustic impedance mismatch is the main phenomenon that enables the use of ultrasound for imaging. One of the problems of the conventional ultrasonic imaging is the impossibility to differentiate between two media with similar acoustic impedance. Ultrasonic echoes are formed at boundaries between media. On an ideal homogeneous medium no echoes are produced. Ultrasonic elastographic images are formed by estimating the elastic constants of the medium. In this rising imaging method, the key factor is the difference between the elastic medium properties, rather than the acoustic impedance. This makes that interfaces originated by media with similar acoustic impedance but with different elastic properties become visible.

Ultrasound enabled the development of a variety of non-invasive therapies in medicine. According to the clinical application, therapeutic ultrasound may be classified into two classes: one corresponding to applications where low intensity levels are required (0.125–3 $W/cm^2$ ) and another related with high intensity ultrasound($\geq$ 5 $W/cm^2$ ). Low intensity ultrasound aims at the stimulation of normal physiological processes, such as, drug delivery through the skin or moderate heating of tissues. On the other side, application of ultrasound at high intensities aims at destroying pathologic tissue regions, in a controlled manner. Interaction of ultrasound with tissue may be divided into thermal and non-thermal one. However, it is difficult to assign a particular biological effect as being produced by a thermal or non-thermal effect, since it can be produced by both [16]. Different positive points have been assigned to the thermal effect, such as: increase in extensibility of collagenous structures (like tendons and scar tissue); decrease in joint stiffness, pain relief, changes in blood flow, decrease in muscle spasm, and for selective tissue heating using high intensity focused ultrasound (HIFU) [16]. However, the lack of accurate temperature distribution maps and the definition of rigorous dosimetry raise many issues

about the real benefits and safety of heating therapies with ultrasound. The non-thermal effects produced by ultrasound can be of cyclic or non-cyclic nature. The periodic behaviour of the ultrasonic waves can originate micro-massages. The main non-cyclic effect is related to acoustic streaming, due to stable cavitation or due to radiation forces in intra or extra cellular fluids. It is reported that streaming can modify the local environment of a cell, changing the concentration gradients in the vicinity of an extracellular membrane. This change on the concentration gradients affects the diffusion of ions and molecules across the membrane, producing a change on calcium and potassium content of the cells which is vital for life maintenance [16]. Cavitation refers to the interaction of a sound field with a gas bubble (naturally generated from gas molecules dissolved inside biological tissues). Stable cavitation describes a repetitive oscillation of a bubble over many sound wave cycles. Another type of cavitation, called transient cavitation, describes the rapid growth and collapse of bubbles, when high intensity ultrasound is applied. The bubble collapse can induce high temperatures and pressures, which can lead to the formation of free radicals [54]. Transient cavitation, is normally an undesired phenomenon, while stable cavitation is desired for therapeutic and imaging purposes.

Real-time, non-ionising, cost-effective, and portability behaviour are characteristics that make ultrasound very attractive for the development of new approaches. The application of both diagnostic and therapeutic ultrasound, the first for heating and the second as a tool for non-invasive temperature estimation is the main point of this thesis.

Primarily, this chapter exposes the basic physics, necessary to understand both therapeutic and imaging ultrasound. In second place, a brief description of some therapeutic modalities will be exposed. The chapter ends with an explanation about tissue mimic phantoms, which are extensively applied in this work.

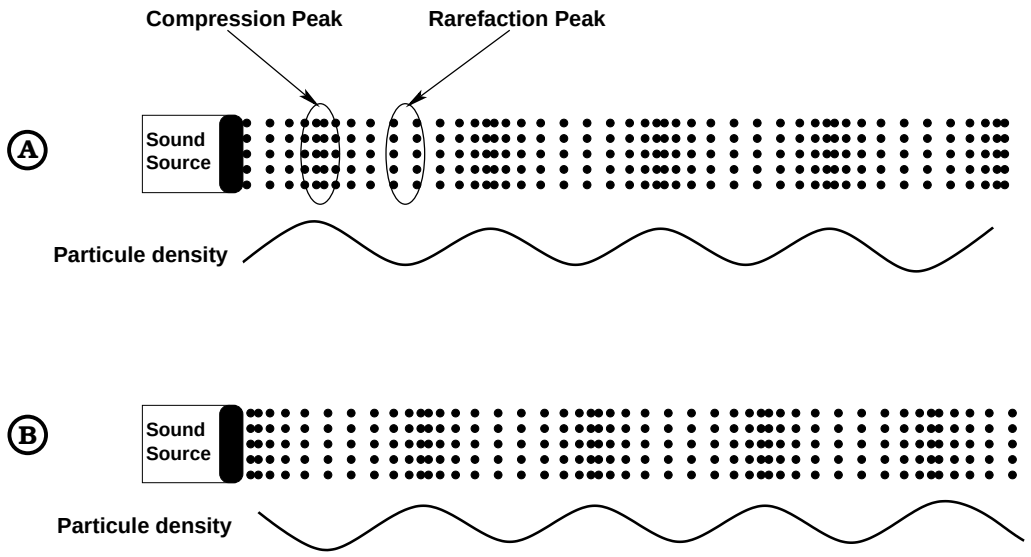


**Figure 3.1:** *Variation of particles density along the propagation path with time.* **A-** *Initial observation.* **B-** *after a short time it is possible to analyse that the compression and rarefaction changed in place (wave propagation). (Adapted from Figure 1-5 in [14])*

## 3.2 Basic ultrasound physics

Ultrasound is characterised by pressure or mechanical waves which travel in a given medium. Wave propagation is due to the relative movement of the particles of a medium from its resting position, which creates compression and rarefaction zones. A compression zone is a region of high pressure, i.e. a region where particles are pushed together. A rarefaction zone is characterised by low molecular density, i.e. a low pressure zone. Compression zones alternate with rarefaction zones, giving rise to the sound wave propagation. Between adjacent rarefaction areas, particle density increases to a maximum in the compression zone and then decreases back towards the minimum (again in the rarefaction zone). Figure 3.1 exemplifies the propagation of a sound wave, showing the alternating compression and rarefaction areas in two different time instants. One important aspect to retain is that, the propagation of a sound wave from two points results from the interaction between adjacent particles, and not from the net movement of particles between these two points [14].

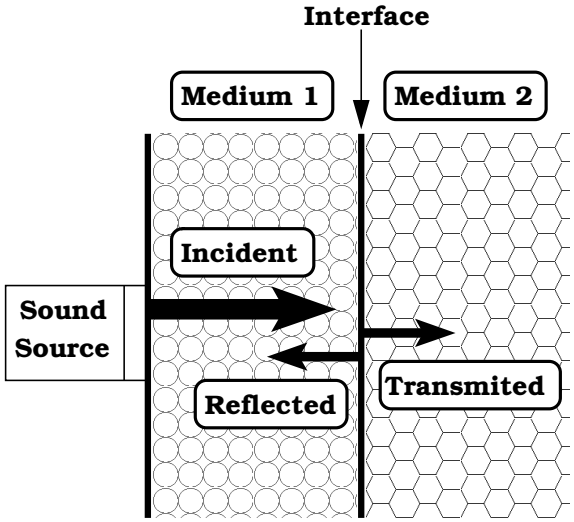


**Figure 3.2:** *Reflection of an incident sound wave that hits perpendicularly a large and smooth interface. (Adapted from Figure 1-10 in [14])*

Ultrasound waves in biological tissue are mostly longitudinal that is, particle motion is in the same direction where propagation occurs, as shown in Figure 3.1. In contrast, for example sea waves can be transversal, as particles movements can be perpendicular to the wave propagation.

Ultrasound interacts with media by means of: reflection, refraction, scattering, diffraction, divergence, interference, and absorption. All of these interactions with exception of interference decrease the intensity of the ultrasound beam (attenuation). Without reflection diagnostic ultrasound could not exist. When a sound beam is directed normally to an interface larger than the beam width, some of the transmitted energy is transmitted forward, and other part is reflected back to the source. An exemplification of reflection is presented in Figure 3.2. The returned energy is processed and used for the formation of images by considering the time-of-arrival of the echoes, and assuming that the mean speed of sound in soft tissue is 1450 m/s[14]. The resistance that a medium offers to the passing of a sound wave is accounted by a quantity called acoustic impedance ($Z$), given as:

$$Z = \rho c. \tag{3.1}$$

Where $\rho$ is the medium density (in kg/m$^3$) and $c$ is the speed-of-sound in the medium (in m/s). This quantity is analogous to the momentum in classical mechanics, which is equal to mass times velocity. In ultrasound, mass is substituted by density and velocity by speed-of-sound in the medium. Acoustic impedance is expressed as kilograms per square meter per second (kg/m$^2$/s), and also given in *rayl* in the MKS system.

The reflection of ultrasound at an interface is due to the difference in acoustic impedance between the two media. If the two media present the same acoustic impedance, then no reflection exists and it is not possible to use ultrasound for imaging purposes. The percentage of energy that is reflected at an interface is:

$$\%R = \left(\frac{Z_2 - Z_1}{Z_2 + Z_1}\right)^2 \times 100, \tag{3.2}$$

where $Z_1$ and $Z_2$ are the acoustic impedances of medium 1 and 2, respectively. Assuming no losses, the percentage of transmitted energy is given by:

$$\%T = 100 - \%R = \left(\frac{4Z_2Z_1}{(Z_2 + Z_1)^2}\right) \times 100. \tag{3.3}$$

Another important interaction of ultrasound with tissue is named scattering, and is responsible for providing information about the internal texture of organs. Scattering occurs when a sound beam hits interfaces smaller than the wavelength. In this situation each interface acts as a separate sound source, "emitting" in all directions.

When an ultrasound beam strikes an interface at an angle of 90 degrees, the transmitted beam direction follows the incident direction. However, when the incident angle is not 90 degrees the direction of the transmitted beam is not the same as the incident one. The relation between the incident and transmitted angle is given

by the Snell's law:

$$\frac{\sin(\phi_i)}{\sin(\phi_t)} = \frac{c_i}{c_t}. \tag{3.4}$$

Where $c_i$ and $c_t$ are the speeds-of-sound in the incident and transmitted medium, respectively. In the same way, $\phi_i$ and $\phi_t$ are the incident and transmitted angles, respectively. These angles are measured between an imaginary line normal to the interface, and the direction of the beams.

Diffraction causes the ultrasound beam to diverge as the distance from the source increases. As the diameter of the source decreases, the rate of divergence increases. Diffraction also occurs when a beam passes through a small aperture on the order of one wavelength. The aperture acts as a small source, with small diameter, thus producing a rapidly diverging beam.

Ultrasound waves also can interfere between each other. Interference can contribute to an increasing or decreasing in amplitude. If waves with the same frequency and in phase interfere, the resulting wave has amplitude greater than the original wave (constructive interference). On the other and, if the waves with the same frequency but out of phase interfere a destructive effect is obtained. In the extreme case of 180 degrees out of phase, a completely destructive interference can be registered. The interference of waves with different frequencies results in a multi-frequency wave.

Absorption is one process where sound energy is converted in other energy form, usually in heat. The transformation of the mechanical energy in heat enables the application of ultrasound for therapy. The absorption rate is related with two media properties and to the frequency of the applied ultrasound beam. The reported medium properties that affect absorption are viscosity and relaxation time. The relaxation time describes the rate at which particles return to their resting position, after being displaced. In short relaxation-time media, the particles return to the rest position before the next compression arrives. On the other hand, in a long

relaxation-time medium, the particles may be moving back to the resting position as the compression wave reaches again. In this situation more energy is necessary to stop and reverse the direction of the particles, resulting in production of more heating. The viscosity of a medium is the ability of its particles to move past from each other. A viscous medium imposes a great resistance to molecular flow (high friction), and then more energy is dissipated resulting in more heat. The frequency of the beam is related to absorption, because it affects the time given to the particles to return to the rest position. Taking in account the relaxation time, the compression wave may strike the particles before the rest position and more energy is necessary to stop and redirect them, increasing absorption. If frequency is increased the particles go forward and backward more times per unit of time, then more heat is generated from the drag caused by friction (viscosity). It is reported that the rate of absorption is directly proportional to frequency [14].

The physical parameter that discriminates the amount of ultrasonic energy flowing through a given area per unity of time is named as acoustic intensity. The intensity is directly related to the density of particles in the compression zone, i.e. an increase in intensity means that the distribution of particles becomes more dense. A change in intensity also means a change in the peak acoustic pressure, change in the length of particle oscillation, and a change of the maximum particle velocity. Intensity is usually given in Watt per centimetre square ($W/cm^2$ ), and theoretically the intensity of an ultrasonic beam is reduced in an exponential fashion as it travels through a medium:

$$I(z) = I_0 e^{-\mu z}, \tag{3.5}$$

where $z$ is the independent variable related with distance, $I_0$ is the intensity at $z = 0$ (in $W/cm^2$ ), $I(z)$ is the intensity at distance $z$ from the origin, and $\mu$ is the attenuation coefficient (in Nepper/cm). The attenuation is basically produced by two processes: scattering and absorption. In this way, $\mu$ can be represented by

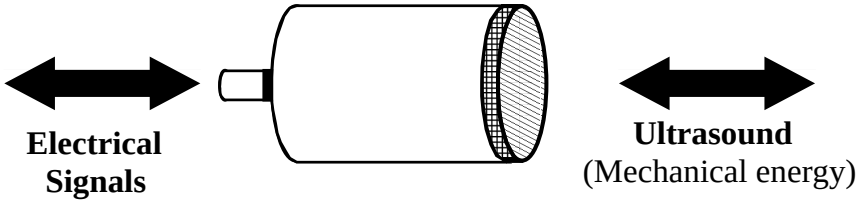


**Figure 3.3:** *Piston-like transducer, commonly applied in physiotherapy.*

$\mu = \alpha + u$, being $\alpha$ the absorption coefficient and $u$ the scattering coefficient. It is referred in [16] that the absorption accounts for 60–80% of the total attenuation, thus it can be considered that $\mu \approx \alpha$. The rate at which temperature rises is given by $\alpha I/\rho C$ [16], being $\rho$ the medium density (in kg/m$^3$) and $C$ its heat capacity (in J/cm$^3$/°C). As an example, if liver is the medium to be considered, a temperature rise of 0.14 °C/$s$ is obtained if ultrasound at 3 MHz and with intensity 1 $W/cm^2$ is applied.

## 3.3 Therapeutic modalities

### 3.3.1 Physiotherapy

The early application of ultrasound in physiotherapy was for diathermia. The main applications of ultrasound in physiotherapy are: soft tissue injuries treatment, to accelerate bone and wound healing, and to decrease joint stiffness. Typically, physiotherapeutic ultrasound devices use piston-like transducers, as shown if Figure 3.3. Theoretically, all the points in the face of a piston-like transducer move backwards and forwards exactly in phase and with the same amplitude. An example of the beam shape produced by this type of transducer is presented in Figure 3.4a. The beam can be divided in two parts: the near and the far field. For circular-shaped transducers, the near field is cylindrical in shape and has approximately the same diameter as the transducer. On the other hand, the far field diameter is greater than the transducer diameter, as the concentrated energy in near field diverges (at

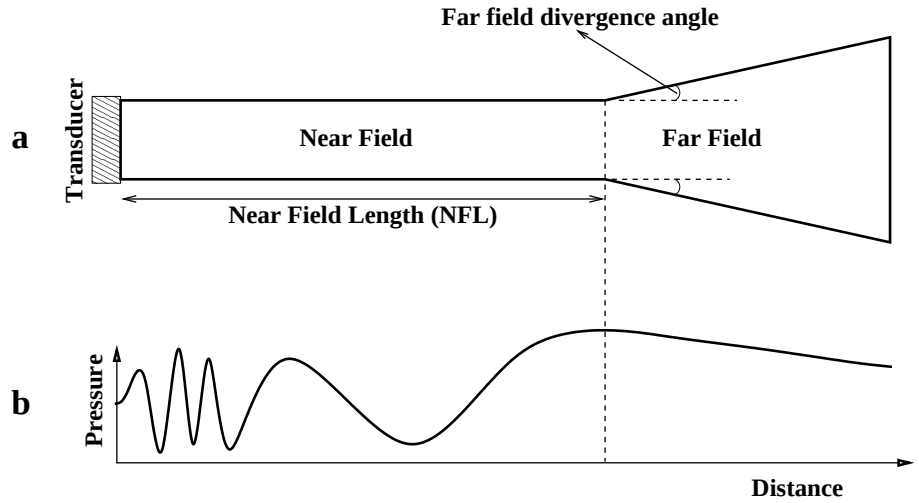


**Figure 3.4:** *Ultrasound beam form a piston-like transducer. a) Beam shape, discriminating near and far field, as well as the near field length and far field divergence angle. b) Pressure (or intensity) profile across the axis of the transducer.*

a given angle) in the far field. Figure 3.4b represents the pressure profile across the transducer axis. The axial distance between the transducer face and the spatial point where the last maximum pressure appears is the near field length (NFL), and mathematically is given by:

$$NFL = \frac{r^2}{\lambda}, \tag{3.6}$$

where $r$ is the radius of the transducer, and $\lambda$ the wavelength. The far field divergence angle can be obtained by solving:

$$\sin(\theta) = 0.61\left(\frac{\lambda}{r}\right), \tag{3.7}$$

where $\theta$ is the divergence angle. Based in the previous equations one can say that when the radius of the transducer is small compared to the wavelength, the near field is short and the divergence angle in the far field is large. Therefore, when the wavelength is small as compared with the radius, the near field is long and there is a little divergence in the far field.

The frequency used in physiotherapy ranges from 0.75–5 MHz, and the spatial

average intensities applied are less than 3 $W/cm^2$ . The choice of the frequency depends on how deep the treatment is intended to be applied, due to the frequency dependence of the ultrasonic attenuation. Deeper regions require lower frequencies. The beam can also be pulsed or continuous. Pulsed beams are used to reduce the thermal effect and to amplify the non-thermal ones.

### 3.3.2 Hyperthermia

The more promising application of therapeutic ultrasound is for hyperthermic cancer treatment [16]. Ultrasound for hyperthermia can be applied solely, or in conjunction with other standard technique, such as radiotherapy or chemotherapy. The principal objective of a hyperthermic treatment is to maintain the tumour region at about 43–45 °C during 60 min, while keeping the surrounding normal tissue at physiologically safe levels [16]. This achievement is only possible by using focused ultrasound beams. These beams can be produced by normal ultrasound transducers with lens, curved transducers, mirror systems and phased array transducers. The principal problem with hyperthermia is the safety of the surrounding healthy tissue. If the therapeutic focus is not well placed, injuries in the healthy tissue can occur. This rises the problem of real-time non-invasive temperature feedback. An accurate feedback would enable an appropriate focus placement and also a precise temperature evaluation, preventing undesired effects.

### 3.3.3 Other applications

#### Non-invasive surgery

The use of ultrasound for surgery involves the application of very high intensities (approximately spatial peak intensities of 1 k$W/cm^2$ ), in order to reach temperatures of about 60 °C at the region of interest, during 1–2s. As in hyperthermia,

focused ultrasound systems are used to destroy the desired target, maintaining the surrounding tissue. In this procedure, security issues play an important role, and consequently the need of accurate temperature feedback. Ultrasound was used to selectively destroy tissue volumes in the brain. Studies for the treatment of *Parkinson's* disease were also performed. Applications on the opthalmologic field, with reduced acceptance, were reported. HIFU was also used for blood flow interruption, and in the treatment of the *Menière's* disease (the disease of the inner ear which causes attacks of vertigo)[16].

#### Lithotripsy

Lithotripsy is a medical procedure used to treat gallstones and kidney stones. In this procedure, high-amplitude acoustic shock waves are generated outside the body and directed to the stone position. Lithotripters typically have a high focusing gain so that high pressures hit the stone (approximately 1000 bar) but substantially lower pressures arrives at the surrounding tissue [56]. The shock wave breaks the stones apart, and its fragments are expelled throughout the urinary system. The major problem is the stone motion due to breathing. If the shock waves miss the stone severe injuries may occur in the surrounding tissue. Focusing based on ultrasound acoustic time-reversal was proposed to dynamically point the focus to the stone [56].

## 3.4 Ultrasonic Phantoms

Ultrasonic phantoms are structures (objects) formed by tissue mimicking materials that try to simulate some acoustic properties of biological tissues or organs. They can be used for different purposes: training/demonstration, quality assurance programs, and for the research and development of ultrasound equipment and methods. Tissue mimicking phantoms and test objects were developed to evaluate and cali-

brate commercial ultrasound scanners. The norms IEC 1390 [57] and AIUM (1990 e 1995)[58] [59] specify the values of the acoustical properties of the soft-tissues, as well as phantom models to evaluate different quality imaging parameters. More realistic phantoms simulating cysts and other structures were also developed to analyse the scanners capabilities [60]. The main acoustic properties to be mimicked by materials are speed-of-sound and acoustic attenuation, which in average are 1540 $\pm$ 6 m/s and 0.7 $\pm$ 0.05 dB.cm$^{-1}$.MHz$^{-0.83}$, respectively [57].

In what concerns therapeutic ultrasound, phantoms take another role as they are used to evaluate temperature induced by ultrasound. Therapeutic ultrasound apply high intensity to the medium, and hazardous effects can be induced in the tissue. So, phantoms are required to be used as a first step when new transducers are designed or when a new method for temperature estimation is developed. Commercial tissue mimicking phantoms exist for HIFU heating. Crystal clear synthetic gels where developed, so that lesions induced by HIFU transducers can be viewed as white regions within the phantom. These regions correspond (in position, size and shape) to lesions that will be produced in real tissue if subjected to the same heating source. In the research environment, several tissues mimicking phantoms were developed for testing new transducers and also for the construction and accuracy assessment of temperature estimations methods. In [4] a phantom composed by rubber with microspheres was developed for non-invasive temperature estimation when the medium was heated by a HIFU transducer. In this thesis liquid phantoms, as well as homogeneous and multilayered gel-based phantoms were developed for construction and assessment of the proposed models. In Chapter 5 the developed phantoms are described for each experimental setup.

# Chapter 4

# Temperature assessment on health environment

## 4.1 Introduction

The assessment of temperature during a therapy should be considered a mandatory issue, concerning safety in first place and then effectiveness. In acoustic hyperthermia and surgery only a delimited area is treated, and care must be taken to avoid undesired effects on the surrounding tissue. Thus, therapy guidance methods are then necessary to measure/estimate temperature at both time and space. Invasive temperature estimation faces some problems, such as: very limited number of points can be monitored, as tissue is damaged due to sensors insertion and also due to difficulties on placing sensors in many clinical situations; sensors act like undesired scatterers and unsafe hot-spots can occur. In addition, thermal conduction and cavitation along the track originated by the sensors placement can occur. The limitation on the number of sensors can result in less spatial information than the necessary for a correct therapy guidance. Nevertheless, invasive measurements are necessary for laboratory measurements, and for the construction and calibration of

non-invasive methods[17].

Non-invasive thermometry is a fundamental aspect, aiming to solve invasive temperature measurement problems, and then improve thermal therapies. The "holly grail" of thermal therapies is to have a completely non-invasive heating method, and at the same time a non-invasive and accurate time-spatial temperature estimation method. The feed-back provided non-invasively would then be used to improve the correct *in-situ* power deposition.

## 4.2 Invasive thermometry

Temperature measurements have been performed by small wire thermocouples, being the method of choice for temperature measurement in tissue [17]. Other sensor types, such as, fibre-optic probes and thermistors have also been applied. However, the acoustic absorption of the plastic that encases some fibre sensors can induce artifacts, reducing their appropriateness. Thermistors suffer from two intrinsic problems: their size and non-linearity. Metal thermocouples experience also two problems: heat conduction and viscous heating. The primary can be minimised by using small-diameter and low-thermal conductivity wires. The second, so called "viscous heating", is due to the friction of the wires in the medium irradiated by therapeutic ultrasound. The solution to this phenomenon encompasses the application of correction methods. Another type of sensors, called thin-film thermocouples (TFT) seem to solve the problems of conduction and viscous heating, since the film avoids the relative movements of the thermocouple junction. The film also reduces conduction distortions, because the thin cross-section ensures that the electrodes are in thermal equilibrium with the medium. However, due to their their small-size and shape, fine-wire thermocouples are preferable for *in-vivo* applications, in place of

TFT. Another problem of TFT is the possibility of standing waves[1] generation, due to the flat TFT membrane when using ultrasound for heating. This problem can be solved by ensuring that the TFT is not exactly perpendicular to the ultrasonic beam axis. To note that, standing waves can induce regions of very high pressure fields, where dangerous hot-spots can occur.

Both acoustic and temperature feed-back were investigated for therapy guidance. In-situ measurement of acoustic intensity and temperature were used for dynamic focusing of HIFU transducers. This feed-back was obtained using invasive hydrophones and thermocouples in the form of needles[18][19].

## 4.3 Non-invasive temperature estimation

In the past decades, several methods based on electrical impedance tomography (EIT) [1], microwave radiometry [2], magnetic resonance imaging (MRI) [3], and backscattered ultrasound (BSU) [4] were reported for non-invasive temperature estimation. They will be briefly explained in the next sections and special attention will be given to the ultrasound method, which is the one used in this work.

### 4.3.1 EIT thermometry

Electrical impedance tomography (EIT) is an imaging technique based on the measurement of electrical conductivity (or resistivity) of tissues. It is reported that there exist a large resistivity difference (in the order of 200:1) among the different tissue types in the body [61], and thus, turning possible the formation of conductivity maps, which are related with the different tissue types, or within the same tissue but under different conditions (for example, different temperatures). This technique injects a continuous current into the medium (excitation), and then the

[1] A standing wave is generated when two waves (in this case acoustic waves), travel in opposite directions. Their interference originates a third wave, which is always in the same position.

induced voltages are measured by a set of adjacent electrodes. The measurement process is repeated for all the electrode pairs, used to inject the reference current, and the other electrodes used to measure the voltages. To obtain reasonable images, at least one hundred, and preferably several thousand, of such measurements must be made. The spatial accuracy of an EIT system is then dependent on the number of electrodes. After the measurement stage, the image formation is the solution of an inverse problem. The conductivity changes with the temperature, turning possible to visualise non-invasively temperature differences within tissues, by using the EIT technique. In [62] an *in-vitro* and *in-vivo* assessment of EIT capability for non-invasive thermometry, during hyperthermia, was investigated. The medium was heated by using a microwave diathermia applicator. It was found that a temperature resolution better that 1 $^{o}$C was possible for the *in-vitro* experiment. In the *in-vivo* trial many image artifacts were registered, probably due to patient movement, blood flow effects, and electrode contact degradation. More recently Paulsen *et. al* ([1]) tested an EIT system also for hyperthermia temperature estimation, in two humans and one animal. Accuracies of approximately 1.5 $^{o}$C were reported. However large errors, more than 5 $^{o}$C, were also registered. It is referred that EIT has potential for hyperthermia temperature feed-back, but the relationship between temperature and tissue impedance is complex. The direct (linear) relation between temperature and tissue impedance, in both the referred papers ([62] and [1]) seems to be not sufficient for the attainment of desired temperature resolutions. Compared with techniques like computerised X-ray tomography, positron emission tomography or magnetic resonance imaging, EIT requires cheaper instrumentation, applies no ionising radiation, and has real-time capabilities. Their limitations are low spatial resolution, and large variability of images between individuals.

### 4.3.2 Microwave thermometry

Microwaves are electromagnetic waves with wavelengths between 1 dm and 1 mm, and with frequencies in the range 3–300 GHz. Medical microwave tomography is based on the different dielectric properties of the tissues. For example, most tumours have 10–20% difference in dielectric properties than normal tissue [63]. The dielectric properties vary with temperature, and by monitoring them during thermal therapy, estimations of the induced temperature field can be obtained, using difference imaging techniques [2]. In EIT, a pair of sources emit current to the medium, and a set of adjacent sensors measure the induced voltage. In microwave tomography (MWT) a source antenna emits electromagnetic waves into the medium, and a set of receiving antennas senses the received radiation. The image formation is again the solution of an inverse problem. Reconstruction algorithms are then used to obtain an image from the information recorded by the different antennas. Temperature accuracy is dependent on the reconstruction algorithm employed. In [64], a resolution of 1.0 °C in simulation, and 1.6 °C in phantoms were presented. Recent advances in the reconstruction algorithms pointed an accuracy of 0.2 °C in phantoms and where electrical properties vary linearly with temperature over a range relevant to hyperthermic cancer therapy [65].The strong dependence of dielectric properties on temperature are exploited to reconstruct accurate temperature maps. However, this technique is more suitable for regions near the tissue surface, due to the strong attenuation of the microwaves through tissues.

### 4.3.3 MRI thermometry

Magnetic resonance imaging (MRI) has also been applied for thermal therapy guidance. With or without administration of intravenous contrast agents most of the lesions to be treated are visible, allowing good localisation for therapy[3]. The

monitoring of certain temperature sensitive MRI parameters, can be used to quantitatively assess the temperature elevation. Possible parameters are: relaxation time, diffusion coefficient (D) or proton resonance frequency of tissue water (PRF). The sensitivity, temporal and spatial resolutions depend on the chosen parameter. It is reported in [66] that concerning temporal resolution, the PRF parameter returns satisfying results. In terms of sensibility, the application of temperature-sensitive contrast agents resulted also in improved results. Both relaxation time, diffusion coefficient and PRF are appropriate for the attainment of a suitable spatial resolution. In [67], it is referred that in phantoms, the previously referred MRI parameters provide the information necessary to attain resolutions between 0.5–1.0 °C. In *in-vivo* situations, only methods based on PRF are suitable for thermometry [68], being possible to reach resolutions of 0.5 °C for pelvic and lower extremity region, under optimal conditions (target movements relatively limited) [67].

### 4.3.4 Backscattered ultrasound thermometry

Four main research lines that apply backscattered ultrasound (BSU) for non-invasive temperature estimation can be pointed. Each research line is assigned with one or more effects of temperature change on the medium. There are methods based on:

- temporal echo-shifts, due to changes in speed of sound and medium expansion [4];
- tracking the frequency variation of the echoes components in the spectral domain, also due to medium expansion and changes on speed of sound [69];
- changes on the attenuation coefficient [7];
- and those based in changes in the backscattered energy [8].

Methods based in echo-shifts and frequency-shifts have been preferred for estimation in temperature fields induced by HIFU transducers. The following text explains how the temperature-dependent features so far listed, in special temporal echo-shifts and frequency-shifts, are applied for temperature estimation.

### Temporal echo-shifts

The description of how temporal echo-shifts are used for non-invasive temperature estimation in one dimension, was introduced in [70]. In [4] it is presented a theoretic description of the physical model used for non-invasive temperature estimation. The authors start by considering that temperature is constant and equal to $T_0$ at initial time $t = 0$. If only the effect of speed of sound is considered, the time delay ($td_c$) of an echo originated at depth $z$ is given by:

$$td_c(z) = 2\int_0^z \frac{1}{c(\zeta, T(\zeta))} d\zeta, \tag{4.1}$$

where $T(\zeta) = T_0 + \delta T(\zeta)$ is the temperature at depth $\zeta$, $c(\zeta, T(\zeta))$ is the speed of sound at depth $\zeta$ and at temperature $T(\zeta)$. In order to account for thermal expansion $d\zeta$ is substitute by $(1+\alpha(\zeta)\delta T(\zeta))d\zeta$. The parameter $\alpha(\zeta)$ is the thermal expansion coefficient at depth $\zeta$. In this way, the time delay ($td$) accounting for both speed of sound and thermal expansion is given by:

$$td(z) = 2\int_0^z \frac{(1 + \alpha(\zeta)\delta T(\zeta))}{c(\zeta, T(\zeta))} d\zeta. \tag{4.2}$$

At $t = 0$, the echo time delay is:

$$td_0(z) = 2\int_0^z \frac{1}{c(\zeta, T_0)} d\zeta, \tag{4.3}$$

and as temperature changes, a cumulative time-shift is observed in the echo originated at depth $z$:

$$\delta td(z) = td(z) - td_0(z) = 2\int_0^z \left(\frac{(1+\alpha(\zeta)\delta T(\zeta))}{c(\zeta, T(\zeta))} - \frac{1}{c(\zeta, T_0)}\right) d\zeta. \tag{4.4}$$

Differentiating the previous equation with respect to the depth $z$:

$$\frac{\partial}{\partial z}(\delta td(z)) = 2\left(\frac{(1+\alpha(z)\delta T(z))}{c(\zeta, T(z))} - \frac{1}{c(z, T_0)}\right). \tag{4.5}$$

In [4] it is considered that the variation of the medium speed of sound is approximately linear with temperature, for the range of interest (hyperthermia range), and equal to:

$$c(z, T(z)) = c(z, T_0)(1 + \beta(z)\delta T(z)), \tag{4.6}$$

where $\beta(z) = \frac{1}{c(z,T_0)}\frac{\partial c(z,T(z))}{T(z)}\Big|_{T=T_0}$. Substituting the previous equation in 4.5, and considering $|\beta(z)\delta T(z)| << 1$, the temperature change at a depth $z$ is given by:

$$\delta T(z) = \frac{c(z, T_0)}{2}\left(\frac{1}{\alpha(z) - \beta(z)}\right)\frac{\partial}{\partial z}(\delta td(z)). \tag{4.7}$$

In [4], [70] and in other works that apply the previously described temperature estimation, $c(z, T_0)$, $\alpha(z)$ and $\beta(z)$ were considered invariant with respect to the depth $z$. In this way, temperature estimation can be described by:

$$\delta T(z) = K\frac{\partial}{\partial z}(\delta td(z)), \tag{4.8}$$

being:

$$K = \frac{c(T_0)}{2}\left(\frac{1}{\alpha - \beta}\right). \tag{4.9}$$

The medium-dependent proportionality constant $K$ must be determined in first place, in order to proceed with the time-shift-based estimations. Obtaining a-priory

knowledge of such constant is not an easy task for in *in-vivo* situations. The speed of sound can vary greatly in different type of tissues. In fact, it can vary in different directions with the same temperature change. The speed of sound in lipid tissue decreases with increase in temperature, and in aqueous media the speed-of-sound increases with temperature increase [5]. As the previous model considers only one constant, it can not be applied in multi-layered non-homogeneous media, in which it would be necessary one constant $K$ for each layer.

In [70] an error inferior or equal to 0.5 °C was reported in a homogeneous rubber phantom. The work reported in [4] is an extension of the work presented in [70] for the two dimensional case. A maximum absolute error of 0.44 °C was reported as the best results obtained, when observing three control points near two focuses of a HIFU transducer. More recently this approach was extended to three dimensions [71]. An accuracy of 0.24 °C was reported, while a homogeneous phantom was heated invasively using a nichrome heating wire instead of HIFU heating.

### Frequency-shifts

Most biological tissues can be viewed as a semi-regular lattice of discrete scatterers, separated by an average distance $d$. As temperature changes, this distance changes too, i.e. the medium expands or contracts. This phenomenon can be described by defining a coefficient of linear expansion ($\alpha$) of a particular medium. It was observed that the spectrum of a backscattered ultrasound signal presents harmonically related frequencies when originated by a medium with scatters uniformly spaced. These harmonics are closely related with the temperature-dependent average scatterer spacing $d(T)$ [6]:

$$f_k(T) = \frac{kc(T)}{2d(T)}, \tag{4.10}$$

where $c(T)$ is the temperature-dependent speed-of-sound, and $k$ is the index of the considered harmonic. Usually the imaging transducers have impulse responses

that are Gaussian shaped, which means that only the harmonics of $f_1$ present in the passband are visible. It was reported in [6] that direct determination of $f_1$ is difficult, because it is out of the passband of typical transducers. The solution for this problem is to determine it as a difference between two adjacent harmonics:

$$f_1 = f_{k+1} - f_k. \tag{4.11}$$

The change on $f_k$ by temperature change is given by:

$$\frac{\partial f_k(T)}{\partial T} = \frac{k}{2}\left(\frac{\partial c(T)}{\partial T}\frac{1}{d(T)} - \frac{\partial d(T)}{\partial T}\frac{c(T)}{d^2(T)}\right). \tag{4.12}$$

Discretising the previous equation, using the forward difference operator, at a given temperature $T_0$, the following relation arises:

$$\Delta f_k(T) \approx \frac{k}{2}\left(\frac{\partial c(T)}{\partial T}\frac{1}{d(T)}\bigg|_{T=T_0} - \frac{\partial d(T)}{\partial T}\frac{c(T)}{d^2(T)}\bigg|_{T=T_0}\right). \tag{4.13}$$

Considering that the average scatterer spacing is given by:

$$d(T) = d_0(1 + \alpha\Delta T), \tag{4.14}$$

where $d_0$ is the mean scatterer spacing at baseline temperature ($T_0$), and $\alpha$ is the thermal expansion coefficient. Replacing the above equation in 4.12, the relation between $f_k$ and $\Delta T$ is reduced to:

$$\Delta f_k(T) \approx k\Gamma\Delta T, \tag{4.15}$$

where:

$$\Gamma = \frac{1}{2d_0}\left(\frac{\partial c(T)}{\partial T}\bigg|_{T=T_0} - \alpha c_0\right). \tag{4.16}$$

The coefficient $c_0$ is the speed of sound at baseline temperature ($T_0$). To note that the constant $\Gamma$ accounts for both changes in speed of sound and medium expansion. It is referred in [69] that $\Gamma$ is considered constant for temperature increments up to 15 °C from the normal human body temperature. Above 20 °C the methods based on echo ultrasound are likely to fail.

In [6] the previously described method was applied for uni-dimensional temperature estimation, when applying HIFU and a waterbath for heating. Experiments were performed in a rubber phantom, *in-vitro* and *in-vivo*. An error standard deviation of 0.4 °C and a spatial resolution of 3 mm were claimed for the rubber phantom experiment. In the *in-vitro* (chicken liver tissue sample) and *in-vivo* (dog thigh tissue sample) experiments error standard deviations errors of 0.5 °C were pointed with the same spatial resolution. To mention that the accuracies in the phantom and in-vitro where obtained using a waterbath heating experiment, instead of the HIFU transducer. In [6] the determination of the backscattered ultrasound signals spectrum was performed by autoregressive models. The Levinson-Durbin algorithm was used for solving the Yule-Walker equation.

In [69] the same temperature estimation model was applied in two spatial dimensions. It is mentioned that although the autoregressive method, applied in [6] is able for temperature estimation, their bias and variance turns difficult to develop a robust algorithm for temperature estimation. In [69] a high-resolution spectral estimation algorithm was used to estimate the frequency shifts. This algorithm is based on a new formalism, where generalised second-order statistics were derived from data. In [69] a temperature resolution compared with the one presented in [4] was achieved. It is pointed that the frequency-shift method is more appropriate for quantitative temperature estimation, given that it is based on the scatterer lattice of a particular medium. However, its success is dependent on the existence of regular (or quasi-regular) spaced scatters, i.e. the ones that produce harmonics. Both echo-

and frequency-shifts methods suffer from a problem called the *thermo-acoustic lens effect*, which is explained in [4]. This effect occurs because local changes in speed of sound (due to temperature change) act like phase aberators for the imaging device, which then produce ripple in the temperature estimates. In [72] an imaging technique known as "ultrasonic spatial compound imaging" was applied to reduce this effect.

### Attenuation

An ultrasonic wave experiences attenuation as it travels throughout a medium. The attenuation coefficient also changes with temperature, thus it can be used for non-invasive estimation. It is reported in [5] that although the attenuation varies with temperature, it appears to be more pronounced at temperatures above 50 °C. This temperature range is not suitable for hyperthermia and diathermia, being only useful for surgery purposes. This fact probably contributed to a reduced interest in methods based in attenuation. In [7] the frequency dependent attenuation was assessed, and a temperature resolution of 2 °C was reported in two dimensions.

### Backscattered energy

In [73] it was proposed that the ultrasonic backscattered energy from individual scatters changed monotonically with temperature. In addition, this variation is visible in the temperature range accepted for hyperthermia. In [73] it was theoretically simulated that the backscattered energy could change 5 dB over the temperature range 37–50 °C. It was also found that it varies in different ways, depending on the medium type (in aqueous media it decreases, while in lipid media it increases). In [74] it was demonstrated that, for the same medium, the backscattered energy could also vary in opposite directions, depending on the region where it is computed. As backscattered energy varies monotonically with temperature it is suggested as a

suitable parameter for non-invasive thermometry. However its accuracy and spatial resolution have not been determined yet [5].

## 4.4 Final remarks

Magnetic resonance imaging (MRI) has been extensively studied for non-invasive thermometry. Their enhanced imaging capabilities enable a superior identification of the target region, and subsequent identification of the area under heating. By monitoring one or more temperature dependent parameters, quantitative temperature estimates can be obtained. It is reported that the unique technology that could provide temperature accuracies of 0.5 $^{o}$C in 1 $cm^3$ is the MRI. This accuracy is also referred as an optimal threshold for hyperthermia/diathermia purposes [5]. At the moment, MRI is the most advanced clinical tool for non-invasive temperature estimation. More precisely, the treatment of uterine fibroid using HIFU and MRI is now offered as a clinical service. The main drawback with MRI for thermometry is the time required (depending on the MRI parameter) to perform one estimation. This problem is amplified when HIFU is to be applied for high temperature thermal ablation, where temperature >50 $^{o}$C in 5–6 min are induced. This therapeutic modality requires a rapid refresh rate with high spatial (in the order of mm's) and moderate temperature resolution. In addition, MRI devices are very expensive (depending on the strength of the magnetic field) and some therapeutic modalities are unpractical, due to the physical space left inside this device.

On the other hand, ultrasound instrumentation is much cheaper and more portable than MRI. Ultrasound devices enable real-time acquisition and processing capabilities (approximately 30 frames per second). The ultrasound waves can penetrate deeper inside the body, which is the main limitation of microwave thermometry. Another advantages are the good temporal and spatial resolution (the main limitation

of EIT), and the compatibility with the therapeutic ultrasound instrumentation. The application of ultrasound for thermometry was successful applied in homogeneous phantoms, and in *in-vitro* (errors less than 0.5 °C with spatial resolutions of 3 mm). The *in-vivo* application was limited to some experiments in animals. The main limitation is that different tissues have different sound speed–temperature relations, turning the already developed models inappropriate. In addition, this relation is assumed to be linear up to 10 °C above the normal body temperature. For each medium, a proportionality constant has to be determined, and only homogeneous media can be characterised, since only one constant is considered. These limitations suggest that the current models are not sufficiently powerful for the attainment of comparable results with the MRI technique. The accuracy of models, such as the ones proposed in [4] and in [69], were only evaluated in a very restrictive environment, i.e. only for one intensity and for three discrete points. More extensive validations should be performed (for example multi-intensity and in multilayered media). New modelling schemas should be applied in conjunction with the emergent ultrasound instrumentation, in order to enable real clinical applications.

Given this scenario, invasive feedback, even with its disadvantages, is still the unique way to reach appropriate temperature and temporal accuracies. In addition, the development on non-invasive methods is dependent on calibration values, which must be obtained invasively.

# Chapter 5

# Experimental setup

## 5.1 Introduction

The construction and validation of the proposed data-driven models required the development of a sequence of experimental setups, which increased in complexity along the work. At the beginning only single-point invasive and non-invasive experiments were developed in a glycerine tank, considering only three intensities. Multi-point and up to eight intensities were applied in gel-based phantoms, at the final stage of this thesis. Homogeneous and non-homogeneous phantoms were considered. This increase in complexity aimed the assessment of the proposed methodology performance in a gradual fashion. The first experimental setup developed is presented in Section 5.2, and was developed for initial tests on invasive estimation. Temperature and acoustic intensity signals were measured from a glycerine tank at the point where temperature was to be estimated. The evolution of the experimental setup in Section 5.2, for non-invasive temperature estimation is presented in Section 5.3. In this experimental setup the hydrophone, used to measure the acoustic intensity, was removed and replaced by an imaging ultrasound transducer. This transducer sends ultrasound bursts to the medium, which are then reflected by three spheres

placed along the imaging beam direction. The backscattered ultrasound energy is then sensed by the imaging transducer, and afterwards processed for non-invasive temperature estimation. In Section 5.4 an experimental setup based on a homogeneous gel-based phantom is presented. The data collected with this experiment enabled the development of non-invasive time-spatial estimators. The last experimental setup (presented in Section 5.5) is the more realistic one, enabling the development and validation of estimators for non-invasive temperature evaluation in multilayered media.

A common point in all the developed experimental setups is the heating modality. The studied media were all heated using therapeutic ultrasound (TUS), commonly applied in physiotherapy. The device used was the Sonopulse Generation 2000 (Ibramed, São Paulo, Brazil). This device has a transducer with two faces, i.e. two nominal effective radiation areas (ERAs) can be applied, one has 1.0 $cm^2$ and other 3.5 $cm^2$. When using the bigger face, frequencies of 1 and 3 MHz can be applied, the smaller face only allows the application of 1 MHz. Intensities from 0 to 2 $W/cm^2$ with increments of 0.1 $W/cm^2$ can be transmitted to the media, using any of the transducer faces. In this thesis the face with ERA of 1.0 $cm^2$ was not applied, given that its heating region is very small, and just allowed the application of ultrasound at 1 MHz. In all the experiments, except the first (for invasive test), the frequency applied was 1 MHz, because at 3 MHz a smaller penetration is achieved (i.e. heating is just obtained near the transducer face). For the 1-MHz setups the pressure field was measured in water in order to have an idea about the distribution of the ultrasound energy in the regions under study. The pressure profile along the axis of the transducer is presented in Figure 5.1. It is possible to analyse that the transducer has it natural focus at 42 mm, i.e. its near field length (NFL) is 42 mm.

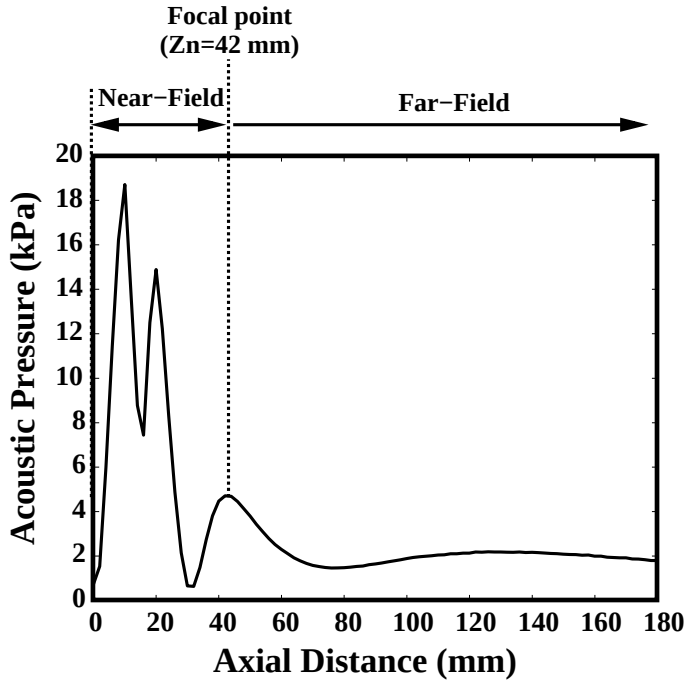


**Figure 5.1:** *Pressure profile across the axis of the therapeutic transducer.*

## 5.2 Invasive temperature estimation

The experimental setup used to collect data for the first set of tests, for invasive temperature estimation is presented in Figure 5.2.

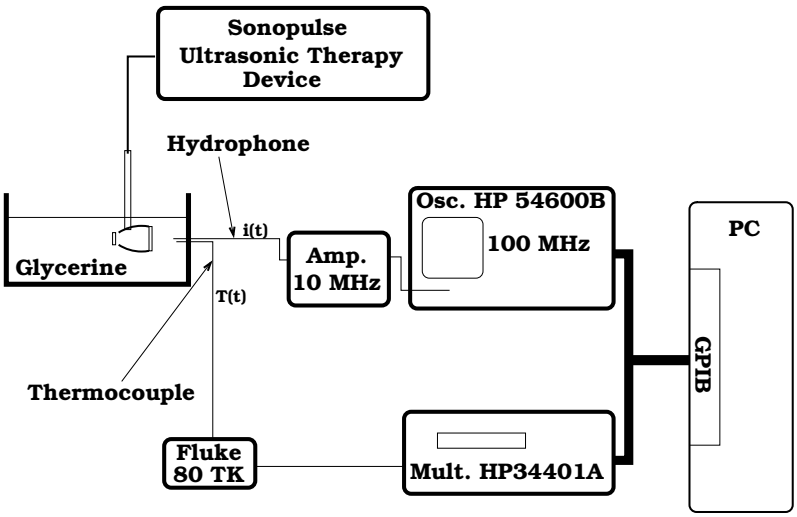


**Figure 5.2:** *Experimental setup used to collect the signals for the invasive temperature estimation trial.*

The phantom applied was a glycerine reservoir (liquid medium). The data collected were temperature and acoustic intensity signals, in a point 48-mm distant (axial distance) from the TUS transducer. Temperature at the point under study was measured using a type-K thermocouple, connected to a compensation module (80TK, Fluke, Everett, WA, USA). This module amplifies the voltage at the thermocouple terminals and then applies a cold junction compensation. This module is then connected to a digital multimeter (34401A, Agilent, Santa Clara, CA, USA), which digitalises the temperature and makes it available to a general purpose PC. The acoustic intensity signals were in first place measured with a hydrophone. The hydrophone output was amplified and then digitalised by an oscilloscope (54600B, Agilent, Santa Clara, CA, USA). At each 10 s one digitalised acoustic intensity signal was transferred to the PC via GPIB bus, as well as one temperature value. Each experiment lasted approximately 110 min, where the first 60 min were used for heating and the last 50 min to allow the system to cool down. Each acquired acoustic intensity signal lasted 5 $\mu$s and was formed by 2000 samples. Three sets of signals were acquired, each one corresponding to a therapeutic device intensity. During these experiments, the medium was heated using continuous waves, with frequency of 3 MHz and intensities of 1.0, 1.5 and 2.0 $W/cm^2$ . An example of the measured signals is presented in Figure 5.3.

## 5.3 Non-invasive temperature estimation: liquid medium

The transition from an invasive temperature estimation environment to a non-invasive one required the development of a new experimental setup, which is presented in Figure 5.4.

In the experimental setup presented for invasive estimation (Section 5.2) the hy-

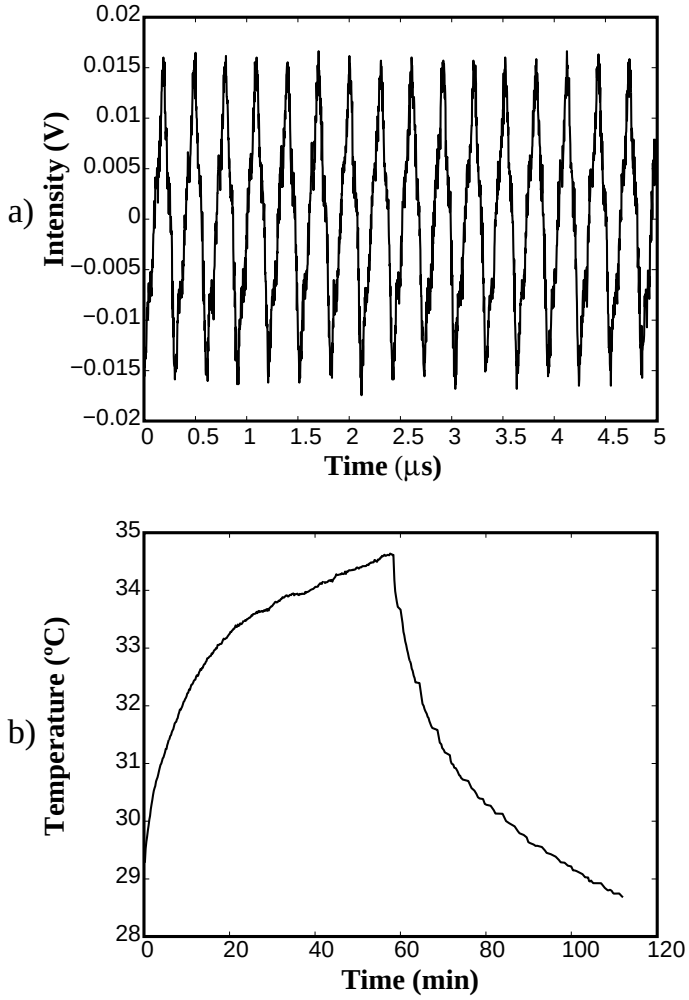


**Figure 5.3:** *Measured signals from the experimental setup used for invasive temperature estimation. a) Intensity and b) temperature. To note that in a) the values in the vertical axis (that are related with the intensity) are the values measured in the oscilloscope and are in Volt.*

drophone was replaced by an imaging ultrasound (IUS) transducer (Sonic, USA). This transducer enabled non-invasive temperature estimation by processing the acquired backscattered ultrasound (BSU) signals. The reservoir was filled with 1,400-ml of glycerine, and three lead spheres (3-mm radius) were included inside it. The spheres were supported by nylon wires, as presented in Figure 5.5, and they were necessary to obtain acoustic information from the liquid homogeneous medium, i.e. they act as the scatterers that produced the echoes to be used for temperature estimation. As it can be seen in Figure 5.5, the spheres were separated by 10 mm. The

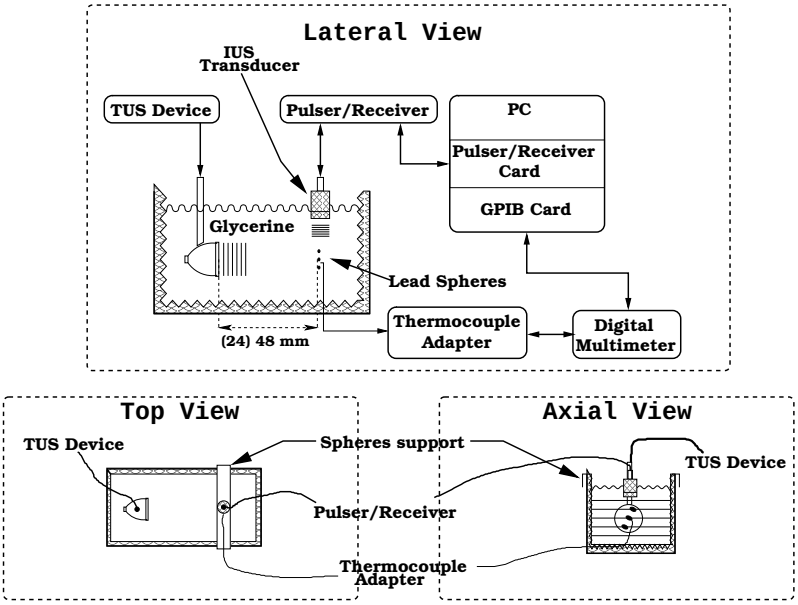


**Figure 5.4:** *Experimental setup used for non-invasive temperature estimation in liquid medium, viewed from different perspectives: lateral view, top view and axial view.*

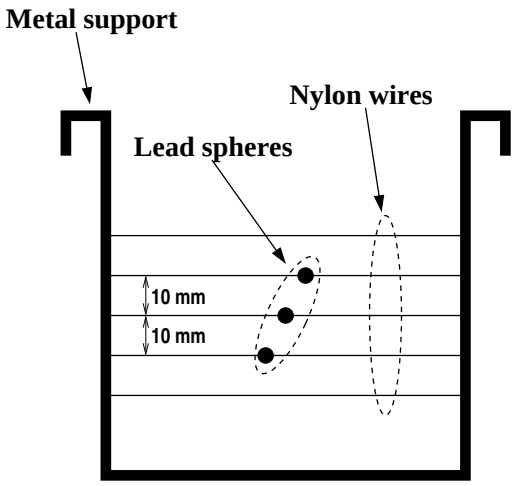


**Figure 5.5:** *System developed to support the spheres in liquid medium.*

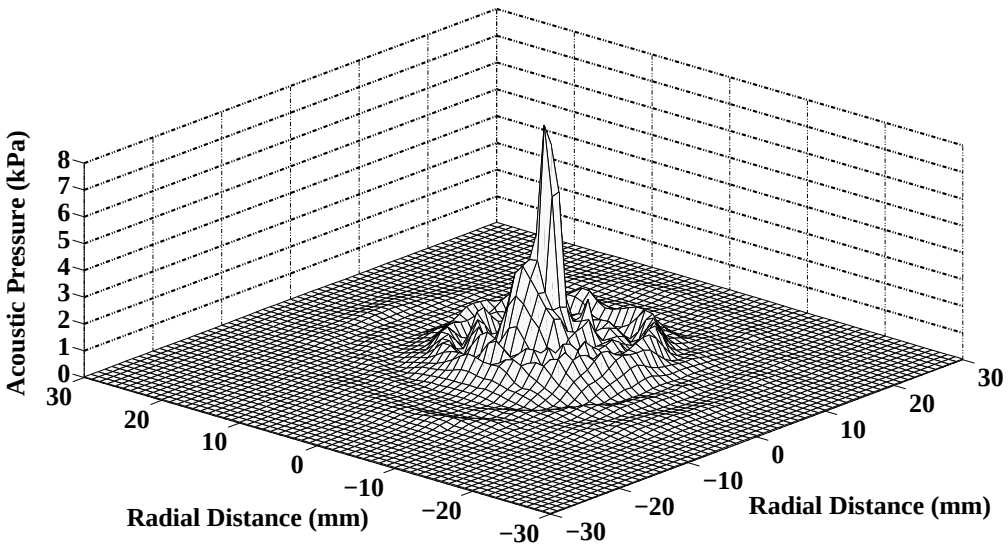


**Figure 5.6:** *Pressure field of the therapeutic transducer measured in a plan parallel to the face and at 24-mm distance.*

central one was placed 24- or 48-mm distant from the therapeutic transducer face, so that two axial distances were considered. The pressure fields measured in water and at a plan 24- or 48-mm distant from the TUS transducer face are presented in Figure 5.6 and 5.7, respectively. These figures show that at 24 mm the ultrasound energy is more concentrated in the region coincident with the centre of the transducer. At 48 mm the energy is more distributed and less abrupt changes occurs as distance from the central region increases. This is because 48 mm is already in the transducer far-field, while 24 mm is within the transducer near-field (as it can be observed in Figure 5.1). A type-K thermocouple was placed in the central sphere, where the temperature was to be estimated. The medium was heated at three different TUS intensities (1.0, 1.5, and 2.0 $W/cm^2$ ). The TUS transducer propagated a continuous mode wave (frequency of 1 MHz) towards the spheres. The spheres were in a plan perpendicular to the direction of the TUS beam. To prevent the formation of standing waves, the inside of reservoir walls was covered with a scattering material (polyurethane foam). As the temperature in the medium changed, the 5-MHz

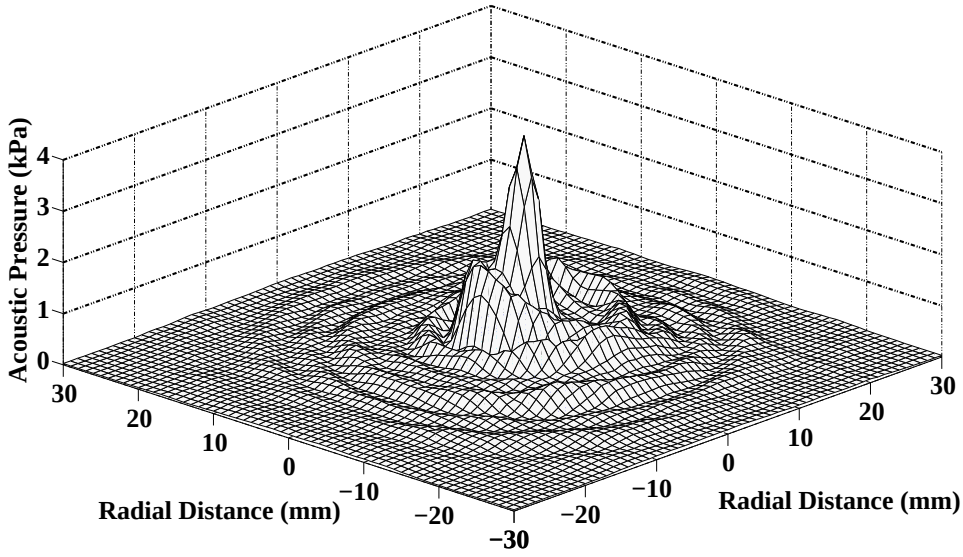


**Figure 5.7:** *Pressure field of the therapeutic transducer measured in a plan parallel to the face and at 48-mm distance.*

non-focused IUS transducer collected acoustic information from the medium. This transducer was driven by a pulser/receiver (Corelec, France), which was connected to the PC through a dedicated card. The imaging beam was perpendicular to the therapeutic beam in order to minimise the acoustic interference between each other. If the beams are not perpendicular, the relatively high intensity TUS beam could saturate the imaging transducer, making impossible the extraction of temperature-dependent features from the BSU signals. At each 10 s a digitalised BSU signal was saved as well as the temperature value measured by the thermocouple. Each digitalised BSU is composed by 2048 samples, obtained at a sample rate of 40 MHz. The temperature sensing by the thermocouple results in a voltage, which was then amplified and cold junction compensated by the 80TK module. In the same way as for the previous experiment, the module was connected to a digital multimeter, which interfaces with a general purpose PC through a GPIB bus. Each experiment lasted approximately 2 hours, at an acquisition rate of 10 s. This means that a total of 720 temperature values/BSU signal pairs were obtained in each measurement.

For each axial distance (24 mm or 48 mm) three experimental trials (corresponding to the three TUS intensities) were performed, meaning that 6 files containing 720 temperature values/BSU signal pairs were collected. An example of the measured signals is presented in Figure 5.8. Looking at Figure 5.8a it can be seen the therapeutic beam interference on the imaging transducer. Although the transducers were perpendicular to each other, in practice a small interference could be observed.

## 5.4 Non-invasive temperature estimation: homogeneous gel-based phantom

Towards more ambitious estimations environments, an experimental setup for multi-point and multi-intensity temperature estimation was developed. The medium used was a homogeneous gel-based phantom. The phantom was prepared by adding (in % of weight): 86.5% of degassed water, 11% of glycerine, and 2.5 % of agar-agar [75]. It has dimensions 120×60×120 mm, and its speed-of-sound at approximately 22 $^{o}$C was measured as approximately 1600 m/s, which is equal to the one reported for muscle, and is close to the mean speed-of-sound assumed for the soft-tissues, which is 1540 m/s. The speed-of-sound was measured by considering the two-way travel-time between two reference points, where the relative distance is known. The phantom contains five thermocouples (as it will be explained later on this section) spaced by 5 mm. Analysing one acquired BSU signal it is possible to extract the two-way travel time between adjacent thermocouples. After this, the computation of the speed-of-sound is given by:

$$c = \frac{2d}{t} = \frac{2 \times 0.005m}{6.23E-6s} \approx 1600m/s, \tag{5.1}$$

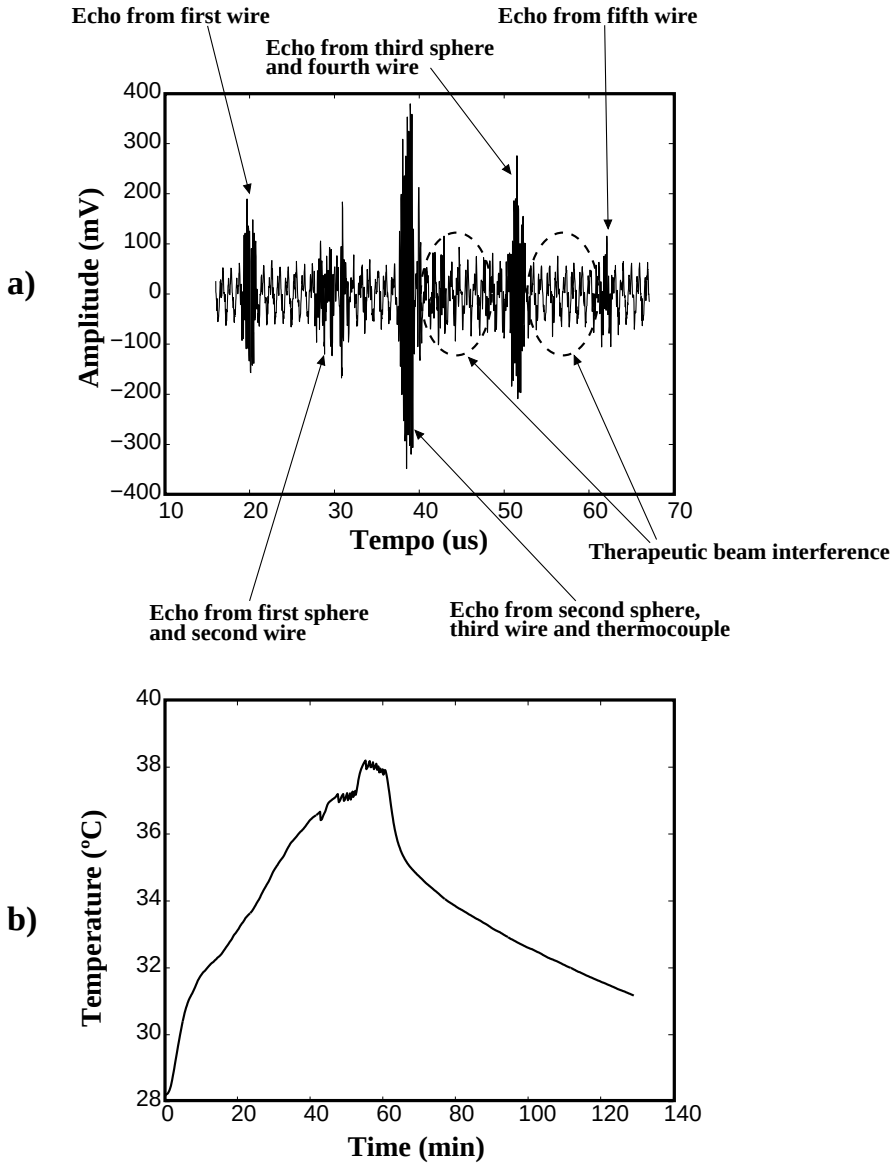


**Figure 5.8:** *Measured signals from the experimental setup used for non-invasive estimation in liquid media. a) one measured backscattered ultrasound signal and b) temperature for a complete heating and cooling event.*

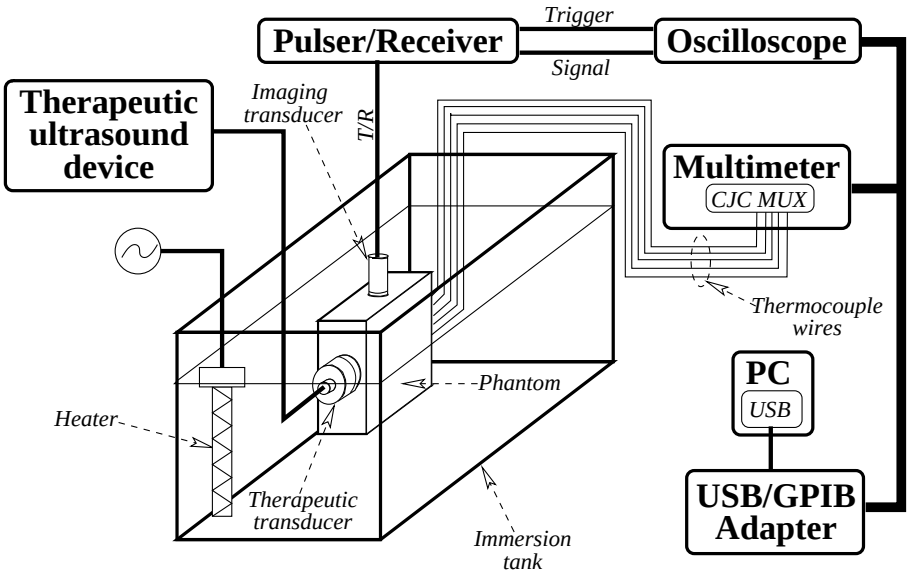


**Figure 5.9:** *Experimental setup developed for multi-intensity and multi-point estimation in a homogeneous gel-based phantom.*

where $c$ is the speed-of-sound, $d$ is the known distance between reference points, and $t$ is the two-way travel time measured from the BSU signals.

In the same way as in the other experimental setups, the phantom was heated using therapeutic ultrasound (TUS). As it can be seen in Figure 5.9, the TUS device heated the medium by emitting 1-MHz continuous ultrasound waves, at four different intensities (0.5, 1.0, 1.5 and 2.0 $W/cm^2$ ).

The phantom was immersed in a degassed water tank (with size $200 \times 200 \times 400mm$) having in mind an efficient coupling between the transducers and the medium, and to discard abrupt room temperature changes. The water tank temperature was maintained at approximately 22 $^o$C by using a 75-W aquarium heater with integrated thermostat. The backscattered ultrasound (BSU) signals were collected using a 5-MHz imaging ultrasound (IUS) transducer (V310SU, Panametrics-NDT, Waltham, MA, USA) with 6-mm of diameter, and working in pulse-echo mode. The IUS transducer was driven by a computer controlled pulser/receiver (5800PR, Panametrics-NDT, Waltham, MA, USA) which returned the analogue BSU signals to an oscilloscope. The oscilloscope (TDS2024, Tektronix, Beaverton, OR, USA)

digitalised the backscattered ultrasound signals at 50 MHz, being each digital signal composed by 2500 samples. The sample frequency was dependent on the time-scale defined. This was because the TDS2024 oscilloscope can only return a maximum of 2500 samples from the current waveform. In order to reach a sample frequency of 50 MHz, the time scale was defined as 5 $\mu$s/division. If a larger time scale was defined the sample frequency decreases, resulting in a poor resolution. A trade-off exists between the extension of the phantom region that is possible to view (with the IUS transducer) and the sample frequency. Higher sample rates mean that a smaller region inside the phantom can be viewed. The oscilloscope was connected to a general purpose personal computer (PC) where the digital BSU signals were saved for future use. The PC receives data and controls the instruments by sending commands through a GPIB bus. A USB/GPIB adapter (GPIB-USB-B, National Instruments, Austin, TX, USA) was used to enable instrument control by using a standard PC USB port. The temperature measurements at the points under study were accomplished by five thermocouples (type K), as shown in Figure 5.10. The strong acoustic impedance mismatch gel/thermocouples generated five echoes (Figure 5.12a), and can be viewed as a simulation of soft-tissue/bone interfaces, where significant heating may occur. The thermocouples were 5-mm spaced across the axial line of the imaging transducer, being distributed between the centre line and edge line of the TUS transducer, and at 60-mm apart form its face. The pressure field in a plan parallel and 60-mm distant from the TUS transducer face was measured and is presented in Figure 5.11. This figure shows that at 60 mm the beam geometry is more well-behaved than at 48 mm (Figure 5.7), given as the axial distance increases (in the far-field) the energy is more and more spread. As it can be viewed in Figure 5.10, the IUS and TUS beams were perpendicular to each other, as in the experimental setup presented in Section 5.3, in order to reduce acoustic interference. The thermocouples were connected to a digital multimeter (2700/7700, Keithley, Cleve-

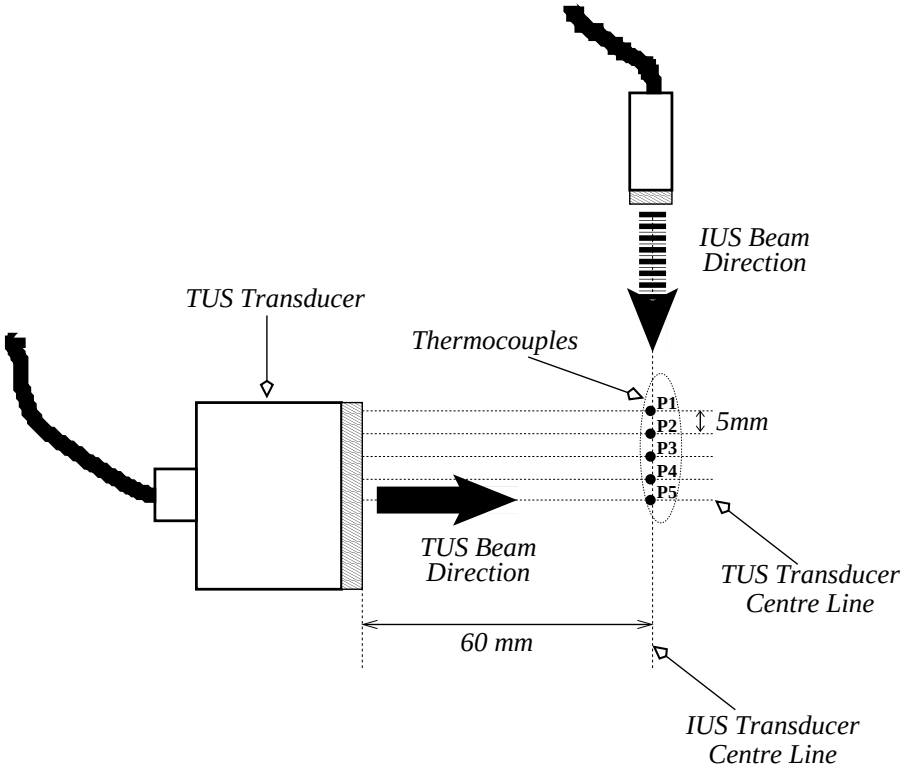


**Figure 5.10:** *Thermocouple location in relation to the therapeutic and imaging beams.*

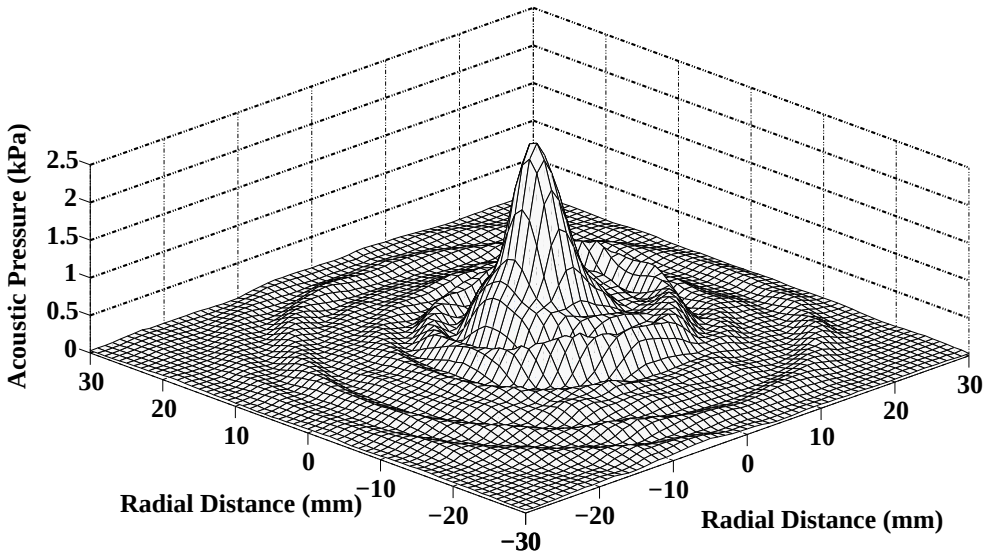


**Figure 5.11:** *Pressure field of the therapeutic transducer measured in a plan parallel to the face and at 60-mm distance.*

land, OH, USA), via a cold junction compensation multiplexer (CJC MUX). The temperature values were then transferred to the PC via the GPIB bus. At each 10 s a BSU signal was collected from the medium, as well as the five temperature values. Each measurement trial (correspondent to one data file) was composed by 5-min base-line temperature, 15-min heating, and 15-min cooling, meaning that each experiment lasted 35 min. For each TUS intensity 6 trials were performed, meaning that a total of 24 data files were collected. An example of the collected BSU and temperature signals throughout one experiment is presented in Figure 5.12. Looking at this figure it is possible to say that a higher temperature is reached at P5, which is located under the TUS transducer centre line. The maximum of the temperature decreases from P5 to P1, i.e. as the distance from the central axis of the TUS transducer increases, as expected by observing Figure 5.11.

### 5.4.1 Dedicated acquisition software

One fundamental aspect concerning the development and validation of data-driven models is the quality of the data acquired from the environment. In this way, the development of dedicated data acquisition systems is a fundamental step. For this thesis a data acquisition system based on Open-Source software was developed. Open-source software refers to computer applications available with its source code, and under an open-source license. The license allows anyone to study, change, tune and also distribute the modified software. Programmers may want to publish their software with an open-source licence, so that anybody may develop the same software, study it and probably contribute with improvements. In the present case a software based on the Linux-GPIB package [76] was developed. In Figure 5.13, the software stack employed is presented. The Linux GPIB package contains drivers and user-space libraries written in C and with Guile, Perl, PHP, Python$^{TM}$ and TCL bindings [76]. Linux and other operating systems (OS) control hardware by means

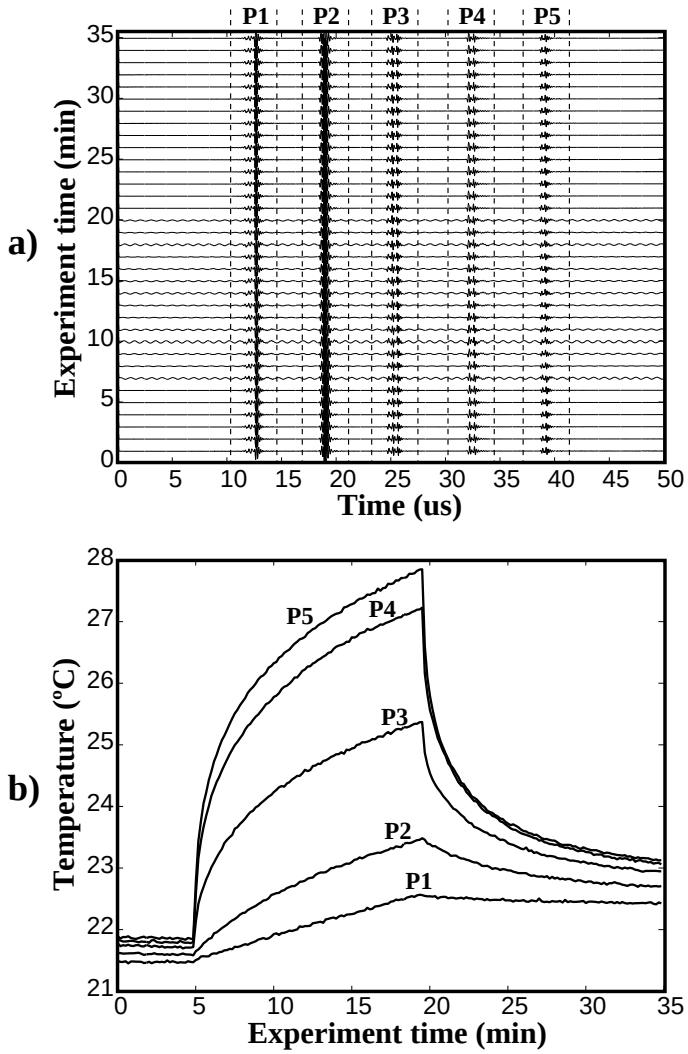


**Figure 5.12:** *Signals collected from the homogeneous gel-based phantom. a) Examples of backscattered ultrasound signals, collected throughout one experiment, and b) correspondent temperature signals for the different spatial points (P1, P2, P3, P4 and P5 in Figure 5.10).*

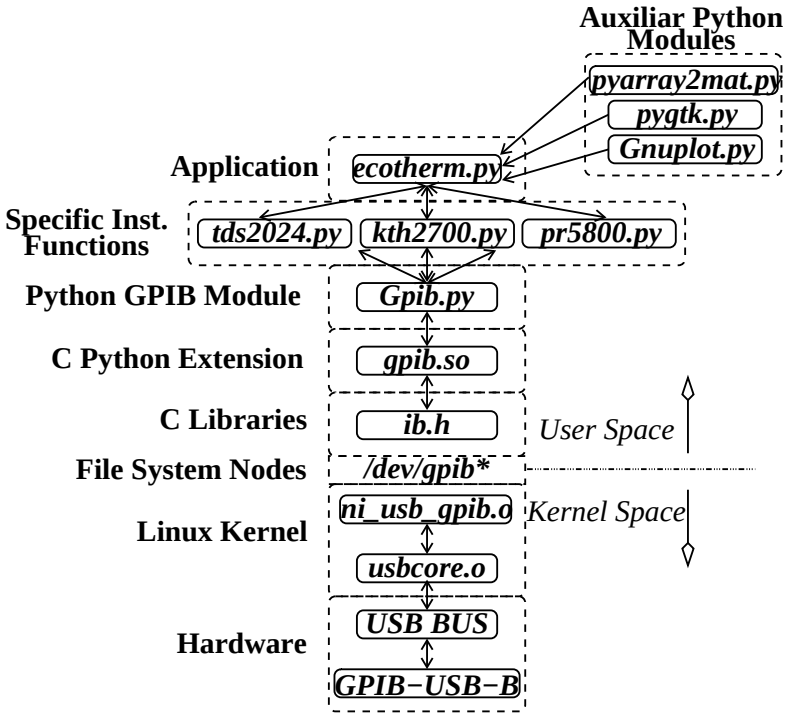


**Figure 5.13:** *Software interconnexion.*

of a software routine called device driver. In Linux, these drivers are called "kernel modules" and can be dynamically loaded at run-time. In the developed application the PC USB bus and consequently the USB/GPIB adaptor (NI GPIB-USB-B) are controlled by the "usbcore.o", which is the general USB driver. In order to introduce specific controls to the GPIB adaptor, there exists a specific module, called "ni_usb_gpib.o", which interacts with the general USB driver. The fundamental device-driver rule is to enable user-space programs (user applications) to interact with the hardware. This interaction is attained in Linux, like in other UNIX derived operating systems, by implementing hardware abstraction by means of a file. The device-driver maps system-calls like "open", "read", and "write" to perform specific operations in the hardware. These files are known as "file system nodes", and in the case of the GPIB modules, are named as "/dev/gpib0", "/dev/gpib1", etc. A user program can open these nodes as a normal file and control the hardware by means of the system-calls which are mapped in the driver. The C libraries

of the Linux GPIB package implement abstraction mechanisms that control the acquisition devices, by interacting with the file system nodes. Aiming a fast and intuitive software development, the Python language [77] was chosen to interface the C libraries. This interaction is accomplished by means of a C–Python extension module (gpib.so), which enables Python programs to use the C functions. This module is imported in a general Python module called "Gpib.py", which defines a general GPIB instrument class. The developed software is composed of three specific instrument modules, one for the oscilloscope ("tds2024.py"), other for the multimeter ("kth2700.py"), and other for the pulser/receiver ("pr5800.py"). These modules define three classes which inherit the methods of the general GPIB class, and create specific methods for specific instruments. The principal modules used by the developed application ("ecotherm.py") are: the previously reported instrument specific modules; the "pyarray2mat.py" module; the "pygtk.py" module and the "Gnuplot.py" module. The "pyarray2mat.py" was created to convert Python arrays to Matlab [78] arrays and save them in Mat-Files, enabling data processing and analysis by a large number of Matlab toolboxes. The "pygtk.py" module is part of the PyGTK [79] package, which provides a convenient wrapper for the GTK+ library for use in Python programs. GTK+ is a graphical user interface (GUI) toolkit for developing graphical applications that run on OSs such as Linux, Windows and MacOS X [79]. For easy and intuitive software manipulation, it is always required a well-designed GUI, which can liberate the user from learning complex command syntaxes. The "Gnuplot.py" [80] is a Python$^{TM}$ module that interfaces to gnuplot [81], the popular open-source plotting program. It allows the call of gnuplot from Python$^{TM}$ to plot data arrays from memory, data files, or mathematical functions. This module is used in the "ecotherm.py" application to plot the acquired temperature signals in real-time.

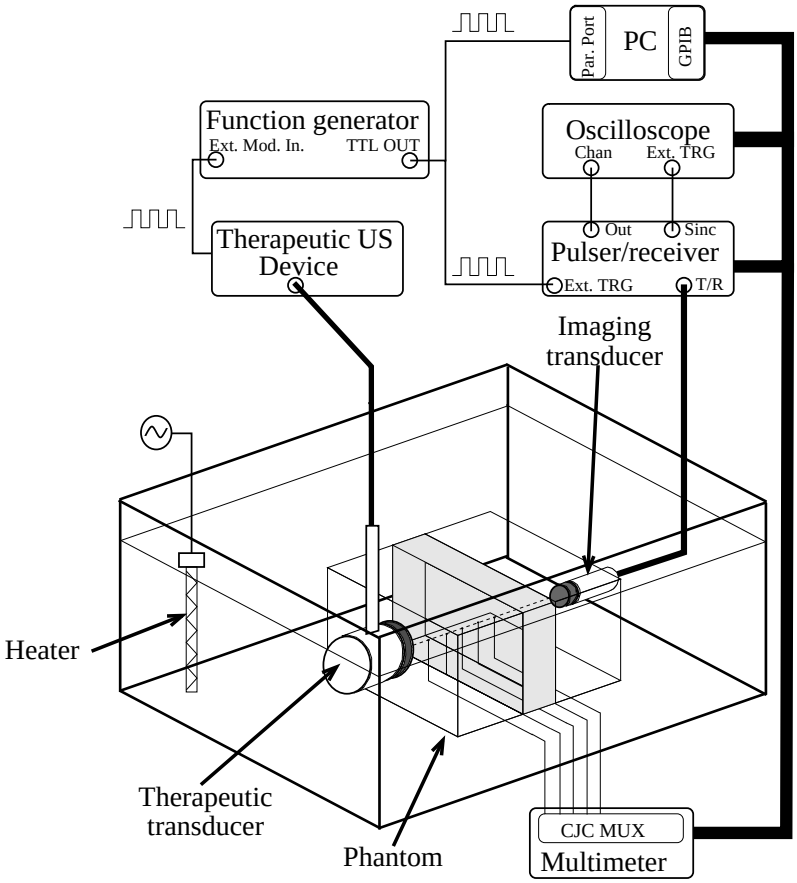


**Figure 5.14:** *Experimental setup applied for estimation in multilayered media. The pulsed nature of the therapeutic beam enabled the acquisition of the backscattered ultrasound signals during its off-cycles, thus preventing form TUS interference in the imaging transducer, being possible to locate the transducers face-to-face.*

## 5.5 Non-invasive temperature estimation: multi-layer gel-based phantom

The test and analysis of the proposed non-invasive estimation methodology in more realistic environments, required data acquisition from multilayered non-homogeneous media. The experimental setup used for data acquisition is presented in Figure 5.14. The gel-based phantom built had three layers, two of them composed by (in % weight): 86.5 % of degassed water, 11 % glycerine, and 2.5 % of agar-agar. The intermediate layer (with graphite) was obtained by adding 2 % of the water weight, in graphite powder to the above composition.

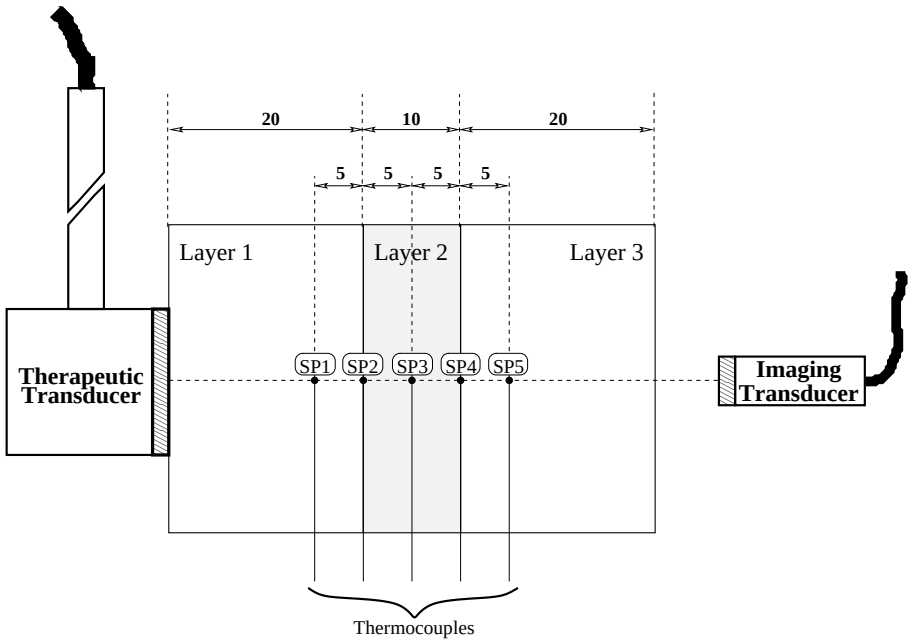


**Figure 5.15:** *Transducers and thermocouples deposition used for the multilayer gel-based phantom experiment. The transducers were face-to-face, and the thermocouples located along the axial line of both transducers. (All length units are in mm)*

As it can be seen in Figure 5.15, five thermocouples (5-mm spaced) were placed along the axis of the therapeutic transducer, one inside each layer and two at the interfaces. This thermocouple disposition enabled the temperature measurement at the different regions of the phantom where the maximum heating occurs (axis of the therapeutic beam). The pressure field across the axial and radial dimensions of the TUS transducer is presented in Figure 5.16. It is possible to realise by Figures 5.1, 5.15, and 5.16 that the spatial locations under study are all contained in the TUS transducer near-field, where the beam assumes more irregular geometries. The phantom was immersed in a degassed water tank, and heated by the therapeutic ultrasound (TUS) transducer at eight different intensities (0.3, 0.5, 0.7, 1.0, 1.3, 1.5, 1.7 and 2.0 $W/cm^2$). The water was maintained at approximately 21 $^{o}$C by using a 75-$W$ aquarium heater. In this experimental setup, the TUS device heated the medium by emitting 1-MHz bursts of ultrasound waves (0.5 of duty-cycle) at 100 Hz pulse repetition frequency, i.e. it works in pulsed mode. The pulsed nature

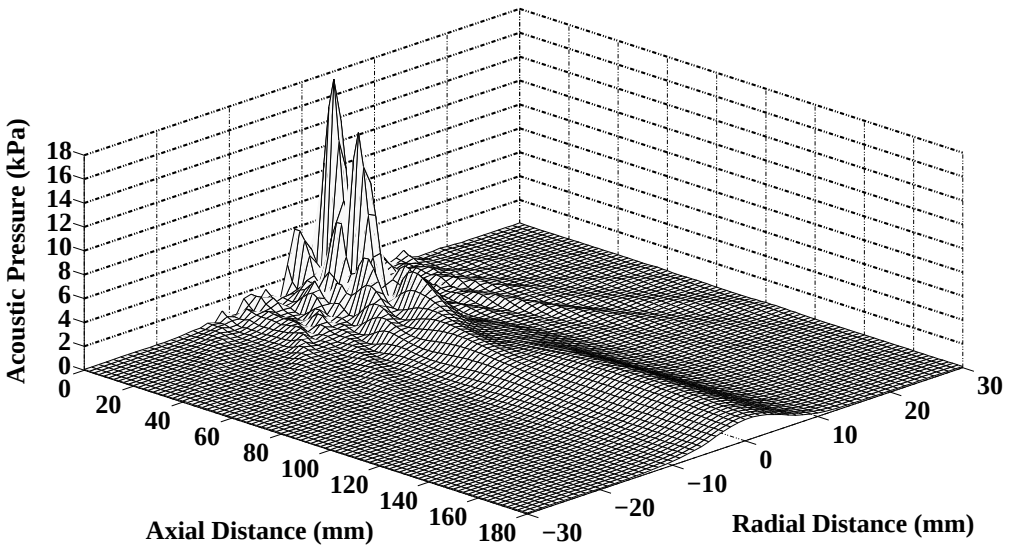


**Figure 5.16:** *Pressure field of the therapeutic transducer measured along the axial and radial dimensions.*

of the therapeutic beam enabled the acquisition of the backscattered ultrasound signals (BSU) during its off-cycles. In this way, the TUS beam does not interfere with the imaging transducer, being possible to locate the transducers as presented in Figure 5.15. The signal used to modulate the continuous TUS wave at the therapeutic device was presented to the external modulation input of a function generator (33220A, Agilent, Santa Clara, CA, USA). Then the function generator produced a TTL signal with the same frequency, but out of phase, as shown in Figure 5.17. The originated signal was then used to trigger the pulser/receiver (5800PR, Panametrics-NDT, Waltham, MA, USA) to drive the imaging ultrasound (IUS) transducer. Then a BSU signal was acquired during the off-cycle of the therapeutic beam. As in Section 5.4, the IUS transducer (V310SU, Panametrics-NDT, Waltham, MA, USA) has 5-MHz of central frequency and 6-mm of diameter. The analogue BSU signals collected by the pulser/receiver were digitalised at 50 MHz using a digital oscilloscope (TDS2024, Tektronix, Beaverton, OR, USA). The acquisition of temperature at the five points under study was accomplished by a 20-channel multiplexer, with

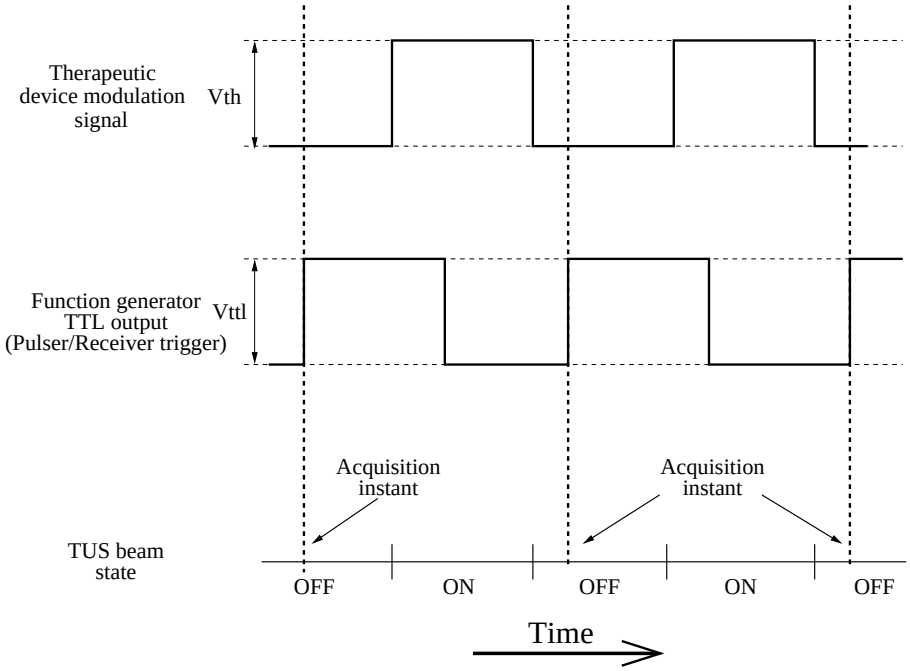


**Figure 5.17:** *Synchronisation signals, and exemplification were acquisition of the BSU signals take place by the pulser receiver.*

integrated cold junction compensation (CJC). This multiplexer is part of a digital multimeter (2700/7700, Keithley, Cleveland, OH, USA). At each 10 s, the temperature values and one digitalised BSU signal were transferred from the multimeter and oscilloscope to the PC via a GPIB bus. Each experimental trial lasted 35 min, being composed by 5-min baseline temperature acquisition, 15-min heating and 15-min to allow the system to cool down. In the first 5-min, the TUS device was inactive and no modulation signal existed. In this situation the pulser/receiver must be driven by an internal trigger signal. When heating begins (TUS device active), the pulser/receiver trigger mode must changed from internal to external, in order to avoid acoustic interference between transducers. During the cooling time, the TUS device was again inactive and the trigger mode of the pulser/receiver must be again internal. The switch between trigger modes was performed by the PC via the GPIB bus. The trigger signal produced by the function generator was supplied to the PC parallel port. When this signal was maintained at 0V then the TUS device was

inactive and the pulser/receiver trigger mode must be set as internal. On the other way, the trigger must be set as external. The software developed to change the pulser/receiver trigger mode, was also developed in Python$^{TM}$. This software has two parts: one C-Python extension module that enables direct reading and writing from the parallel port; and a Python$^{TM}$ function that analyses if the therapeutic device is "ON" or "OFF". This Python$^{TM}$ function decides which trigger mode to apply, by sending a command to the pulser/receiver via GPIB. The trigger mode must be changed as the therapeutic device state changes, in order to ensure that in the next acquisition action the trigger mode was correct. This monitoring software should run independently of the acquisition cycle. In this way, it was launched as a Python$^{TM}$ thread which ran parallel to the acquisition software reported in sub-section 5.4.1. Threads are sequences of instructions (procedures) that can run independently from the main program. Unlike a normal OS process, threads duplicate from the parents only the essential resources that enable them to exist as executable code. Threads in the same process may share resources, and read or write to the same memory positions. This means that any change in one is visible by all the other threads, improving communication.

Six repetitions of the same measurement trial, that is, using the same TUS intensity, were performed. This means that 48 measurement trials were performed, corresponding each one to 210 BSU signals and to 210 temperature values per spatial point (SP1, SP2, SP3, SP4 and SP5). In Figure 5.18a some examples of the collected backscattered ultrasound signals along one experiment trial are presented. Figure 5.18b provides a detailed view of the echo produced at SP3. The red line indicates that as temperature increases the echo comes sooner, meaning that the speed of sound has increased. In the same way, as temperature decreases the speed of sound also decreases. The temperature waveforms at the different spatial positions are presented in Figure 5.18c.

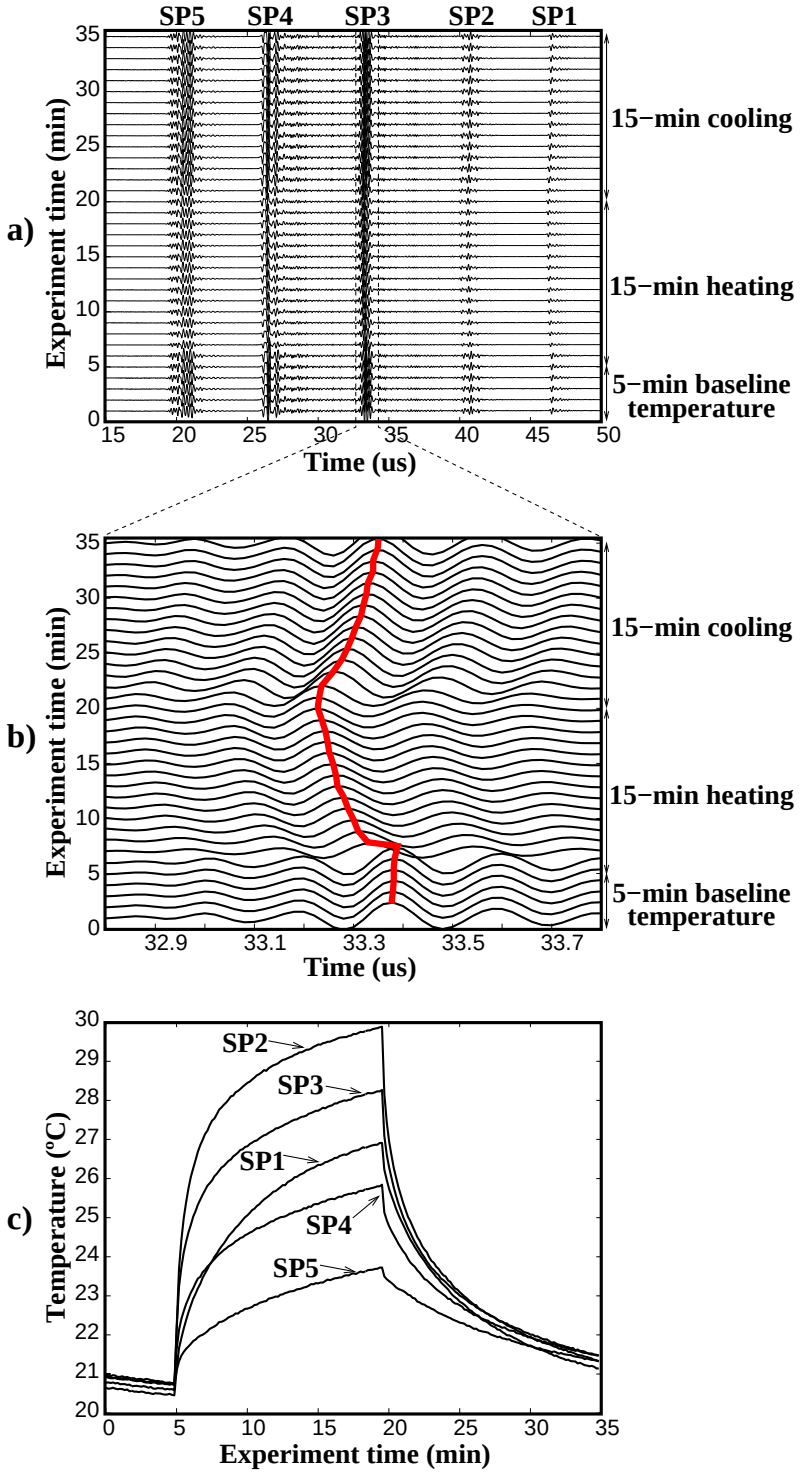


**Figure 5.18:** *Signals collected for non-invasive temperature estimation in multilayered media. a) backscattered ultrasound signals; b) detailed view of the echo originated at SP3, the red line enhances the visual perception of the change on time-of-arrival due to temperature; c) temperatures at the different spatial positions.*

# Chapter 6

# Applied estimation models

## 6.1 Introduction

This chapter describes the different temperature estimation model structures applied in this thesis. All the previous processing required for the development of such models, as well as their training and structure optimisation are also reported. The pre-processing encompasses: a feature extraction phase, features processing, and data selection. Among the different estimation trials spectral and temporal features were computed and then prepared for model's construction. The preparation usually encompasses a filtering and normalisation process. The overall pre-processing ends with data selection for the different model construction phases, i.e. training, test and validation. Training refers to the computation of the model parameters, test is the phase where the models are evaluated in fresh data during the structure optimisation cycle. Validation is the final step where the best optimised structures are tested in fresh data, in order to evaluate the real generalisation performance. Non-invasive temperature estimation needs proper models for multi-step-ahead operation, i.e. models where only the initial temperature is supplied, and then they can estimate temperature over a predefined prediction horizon. This is possible by feeding-back

the past estimated temperatures. This required multi-step-ahead behaviour defines the way as the data were selected for training, test and validation. When only one-step-ahead operation is required, all the data sets can be joined together, and then spared patterns can be randomly selected for the different model's construction phases. This procedure aims to achieve a wide coverage of the estimation space. In multi-step-ahead estimation, during the model's training and structure selection, the long-term error must be assessed and then minimised. The computation of this error implies the availability of the entire waveforms (and not isolated randomly selected patterns) in the test data. In validation it is also desired entire waveforms in order to evaluate the models's multi-step-ahead behaviour. In situations where data are scarce (as reported in Sub-section 6.2.2), the training set can be obtained by random selection of patterns from all of the available data, but the test and validation sets should encompass complete signals.

The applied structures were based on radial-basis-functions neural networks (RBFNNs), linear models, and adaptive-network-based fuzzy inference system (ANFIS). For RBFNN-based structures, the multi-objective genetic algorithm (MOGA) was extensively applied. However, the standard orthogonal least squares (OLS) was also applied for comparison proposes. MOGA was also applied for linear and ANFIS-based structure optimisation. The RBFNNs were trained using the schema explained in Sub-section 2.2.1. This schema involves the Levenberg-Marquardt algorithm (LM) to optimise the non-linear parameters, and the least squares strategy to compute the linear parameters. The training was stopped by taking into account the "early–stopping" criterion (see Figure 2.4 in Sub-section 2.2.1). The linear-based structures were trained in one iteration using a linear least-squares strategy. The ANFIS structures were trained using a similar schema to the one applied for the RBFNNs structures, the difference being that the backpropagation algorithm was employed instead of the LM. During the MOGA different model features (perfor-

mance descriptors) were computed in order to select the best ones for matting. The performance descriptors employed can be divided in three groups: model errors, model complexity and model-validity tests. In what concerns the errors, one-step-ahead training error, one- and multi-step-ahead test errors were considered. The complexity descriptors considered were the linear weights norm and the number of parameters. The model-validity tests were explained in [82], and involve the computation of first and higher order correlations between model inputs, output and residuals.

The generic MOGA-based framework employed for structure optimisation and validation is presented in Figure 6.1. First of all the MOGA parameters should be defined. These parameters are: the number of generations employed, the population size, the objectives (performance descriptors) and related goals and priorities, crossover and mutation probabilities, percentage of random immigrants and structure restrictions. The number of generations, population size, objectives and associated goals and priorities, and structure restrictions were set according to the estimation environment considered. These parameters are pointed in the next section for each one of the applications considered. The crossover probability was set for all MOGA runs as 0.7. This value was set after several attempts considering other values, and was found to be appropriate. The mutation probability was set as 0.5 for all the runs. This value was computed as the inverse of the selection pressure[1], considering a selection pressure of 2, then the mutation probability is 0.5. This rule was applied successfully in other MOGA applications. The percentage of random immigrants was set as 10%. Random immigrants are randomly generated individuals (like the ones in the initial generation) that substitute individuals in the population at each generation, improving population diversity. Another reason is to speed-up the algorithm. It is assumed that the last individuals in a given generation

[1]The number of offspring's that the best individual is expected to produce

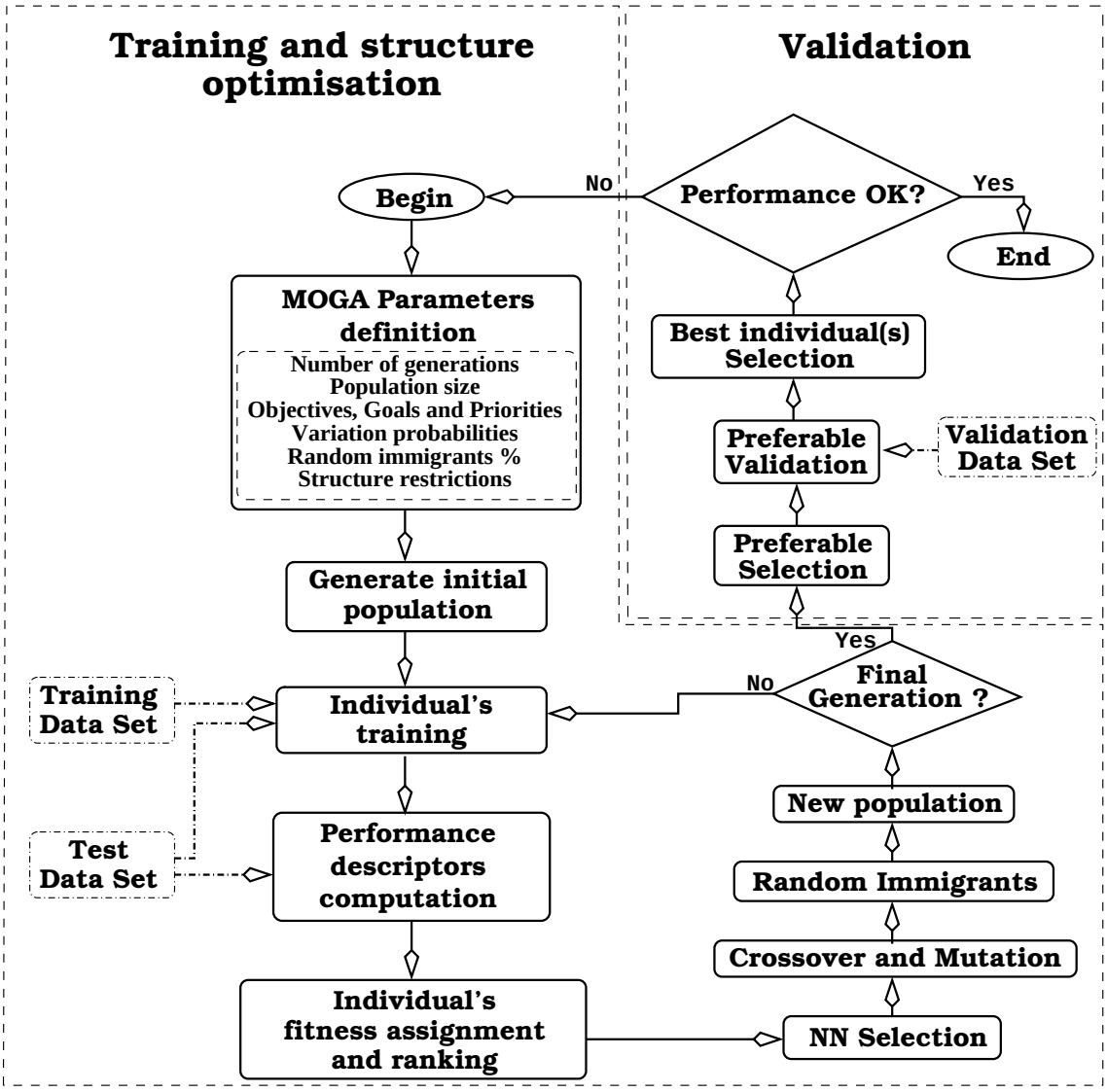


**Figure 6.1:** *Flowchart describing the generic structure optimisation and validation process employed.*

are not fitted, then are not evaluated, i.e. time is not spent with them and they are substituted by the immigrants. It was found that 10 % of random immigrants was a proper value.

The structure restrictions define possible values for the structure parameters. In the RBFNN case, the structure limitations are the maximum number of inputs, the minimum and maximum number of neurons, and the maximum lag for the input variables. After the initial definition of the parameters, an initial population is randomly generated and trained. The training needs two data sets. The training set to optimise the parameters, and the test set to stop training by using the "early-stopping" criterion. This means that the model under training is evaluated in fresh data (test), and training is stopped at the point of maximum generalisation. After training, the performance descriptors were computed. Among these descriptors there were those related with the generalisation performance, and consequently the test set is needed at this time. The performance descriptors computed were viewed as objectives to minimise. As explained in Sub-section 2.4.2, all individuals in the population were ranked, taking into account the goals and priorities defined for the objectives. Using the rank information a fitness value was assigned to each individual. Afterwards, the individuals were selected for matting, according to their fitness. According to a given probability they undergo or not crossover and (or) mutation. A quantity of random immigrants substitutes some of the individuals, and a new population is obtained. If the number of generations was not attained, a new cycle would take place. Otherwise, the structure optimisation stops, and the preferable individuals picked up from all the generations. These individuals are the best ones, concerning the goals and priorities defined. These individuals are analysed in fresh data (validation data), and if their generalisation performance is appropriate, the overall optimisation process ends. Otherwise, the MOGA parameters should be reviewed (population size, objectives goals and priorities, and structure restrictions),

the data employed should be also analysed and changed if necessary. The changes on data are for example: deletion or addition of a new variable (temperature-dependent feature).

The following sections report the different structures employed for each case-study, and the parametrisation for the structure optimisation process. First of all, the structures for single-point estimation are presented is Section 6.2. Among these structures some were developed for invasive estimation, while others were concerned with non-invasive estimation. In Section 6.3, the developed structures for non-invasive estimation on the time-space domain are explained. Separation is made between structures for single and for multiple intensities.

## 6.2 Models for single-point estimation

### 6.2.1 Invasive estimation

The development of temperature estimators requires the extraction of temperature–dependent features from the collected signals. For invasive temperature estimation experiments spectral features were extracted from the collected intensity signals. The magnitude spectrum of one collected intensity signal (like the one presented in Figure 5.3 a)) is presented in Figure 6.2. In this spectrum it is possible to see four spectral components. The first one is located at approximately 3 MHz, which is the working frequency of the TUS transducer. The other three are harmonics of this principal component. It was found that the amplitude of the spectral components varies with temperature, being possible to use these variations for estimation. The amplitude of the different spectral components along the experiments is presented in Figure 6.3. To note that three experiments were performed for each one of the applied TUS intensities (1.0, 1.5, and 2.0 $W/cm^2$ ). Using these features four model structures were applied. First of all, only the amplitude of the fundamental

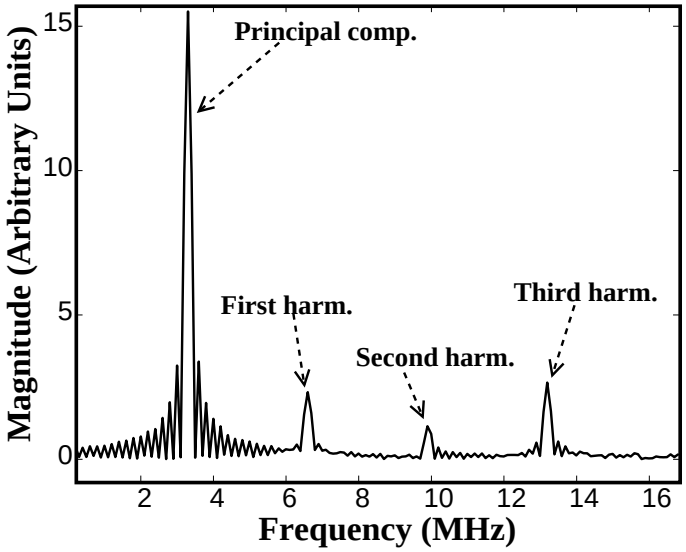


**Figure 6.2:** *Magnitude spectrum of one intensity signal collected with the experimental setup developed for invasive estimation.*

harmonic was considered, and the capabilities of the RBFNN were analysed against the performance of a simple autoregressive model with exogenous inputs (ARX). The third and fourth model structures employed were obtained by considering in addition to the amplitude of the principal component, the amplitude of the first and second harmonics. One of these structures was formed by a normal RBFNN while the others consisted in a RBFNN with additional linear input connections (RBFLIC). The explanation of how these models were set up is given afterwards. The third harmonic was not considered because, as it can be seen in Figure 6.3, its amplitude is practically constant and similar for 1.5 $W/cm^2$ and 2.0 $W/cm^2$ .

### RBFNN and ARX based on the amplitude of the principal component

Usually in data-driven modelling approaches, data are filtered in order to remove noise and then to enable a better training. In addition, if the different variables present different scales, a normalisation process must be employed. Looking at Figure 5.3b and Figure 6.3, it can be noticed that both the computed amplitude of the principal spectrum component and the measured temperature present low noise

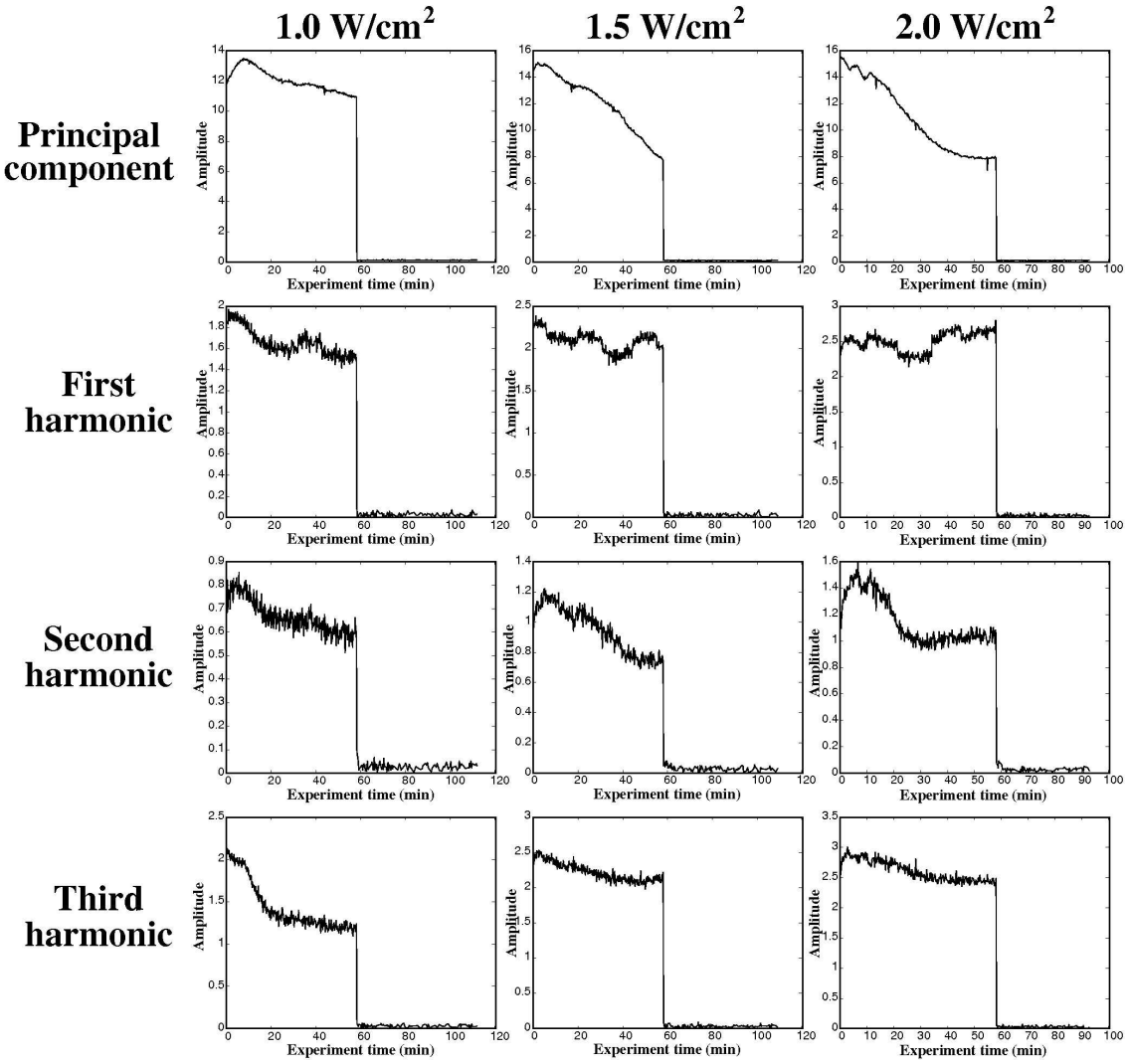


**Figure 6.3:** *Variation of the amplitude of the spectral components presented in the spectrum of the collected intensity signals. Three intensities were considered, and four components can be observed.*

levels, thus the filtering phase was discarded. As the amplitude of the principal component and the temperature have different scales, normalisation in amplitude to values between 0 and 1 was employed to both variables. It was assumed that the normalised amplitude of the principal component, and the normalised temperature are represented as $A_{pc}$ and $T$, respectively.

For this initial invasive estimation approach, the data collected at 1.0 $W/cm^2$ was selected for training, the data collected at 1.5 $W/cm^2$ for test, and the validation was performed with the data collected at 2.0 $W/cm^2$ .

Selection of appropriate structures for a particular estimation environment can be a hard task due to the enormous number of possible solutions. For a structure involving RBFNNs, the relevant inputs and the number of neurons should be determined simultaneously. The possible inputs are lags of the assumed input variables. This introduces external dynamics to the static RBFNN structure. In this preliminary test it was assumed that the maximum lag for the input variables ($A_{pc}$ and $T$) was 48, the number of inputs was an integer in the interval [2, 30], and the number of neurons was an integer in the interval [2, 15]. The applied generic structure based on RBFNN is presented in Figure 6.4. With simple calculations, the number of possible structures, taking in account the previously referred structure limitations, can be found:

- the number of input variables is $NV = 2$ ($A_{pc}$ and $T$);
- the total number of input terms is $IT = NV \times 48 = 2 \times 48 = 96$;
- taking in account the limitations on the number of inputs, the total number of input combinations is $IC = \sum_{n=2}^{30} {}^{IT}C_n = \sum_{n=2}^{30} {}^{96}C_n \approx 1.21E25$;
- considering the limitation on the number of neurons the total number of possible structures is $(15 - 1) \times IC \approx 1.70E26$

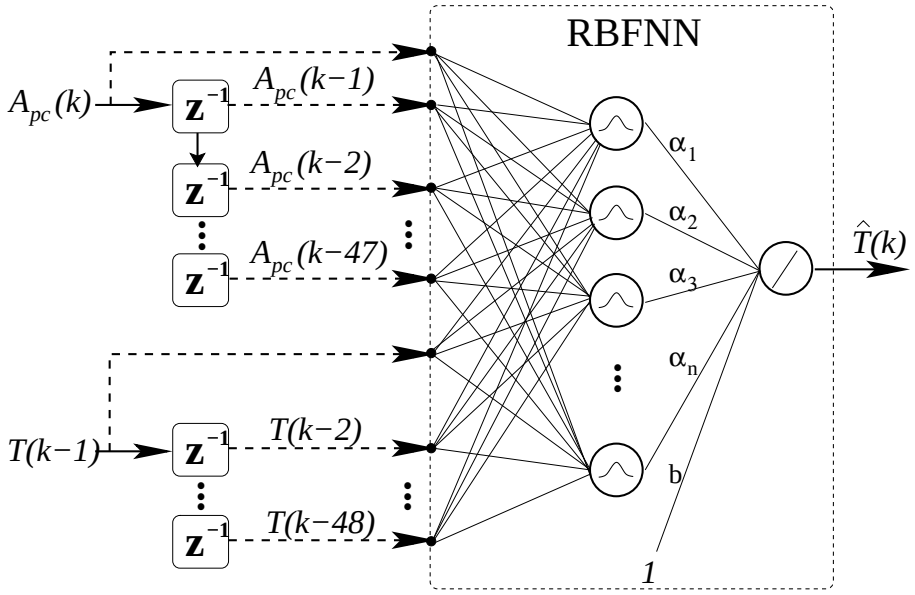


**Figure 6.4:** *Generic structure based on RBFNN, applied for invasive temperature estimation. The dashed arrows represent inputs that are to be selected. The symbol* $\mathbf{z}^{-1}$ *represents the ideal unit-delay operator.*

Such a high number turns impossible the training and validation of all the possible structures. For large search spaces evolutionary computing approaches, such as genetic algorithms (GAs), can be used to search for suitable solutions. In some engineering applications not just the minimisation (or maximisation) of one objective is important for the final application. Multi-objectives must be addressed simultaneously, enabling a multi-objective optimisation process. The structure optimisation of models such as the one presented in Figure 6.4 can also be formulated as a multi-objective optimisation problem. Given the enormous number of solutions, the multi-objective genetic algorithm (MOGA) [10] can be used to address this problem. In order to apply this genetic search, the model structure must be codified, i.e. a chromosome must be assigned to each solution in the population. A straightforward way to represent the model structure presented in Figure 6.4 is by considering a chromosome where the first locus is the number of neurons, and the other loci are indexes to the available input terms. The set of input term indexes in each chromosome is a subset of the total set of possible input term indexes.

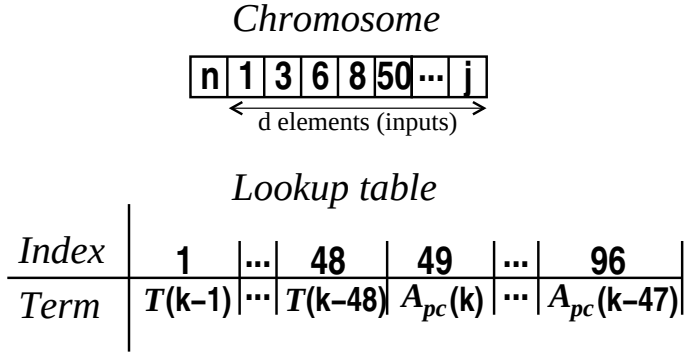


**Figure 6.5:** *Model's chromosome and terms lookup table for the invasive estimation trial.* **d** *is the number of inputs in a particular structure.*

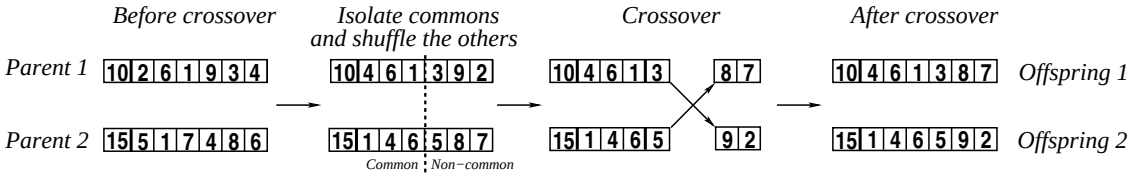


**Figure 6.6:** *Full identity preserving crossover.*

This input term selection was applied in [9] for system identification purposes, using nonlinear autoregressive moving-average with extra inputs (NARMAX) structures. The length of the chromosome is variable, according to the number of inputs in a correspondent structure. The available input terms are related to the indexes using a lookup table. In Figure 6.5 the chromosome representation, as well as the lookup table are presented for this particular structure. A change on the representation means that the genetic operators must also be changed. In the case of RBFNNs the crossover operator must recombine strings of input term indexes, instead of binary strings (such as presented in Figure 2.8). The crossover operator applied to subset representations must ensure that the parents with common elements do not produce offspring with repeated elements, and that the maximum chromosome length is respected without loss of input terms. This type of recombination is called "full identity preserving crossover" and works as presented in Figure 6.6. Primarily, the common term indexes are isolated, secondly the other terms are shuffled, and finally normal crossover is performed in the non-common part of the chromosomes.

The mutation operator to subset representations is implemented by three basic operations: substitution, deletion and addition of one element. Each element in the chromosome is tested, and with a given probability is replaced by other input term not present in the model, or deleted. The mutation can end with the addition of a new term. Care must be taken in order to prevent term repetition and the pre-defined boundaries. The number of neurons is mutated with a given probability by adding or subtracting one neuron to the model; of course care must also be taken to keep the pre-defined boundaries.

The MOGA needs the computation of model features, in order to evaluate their capacity for the proposed estimation environment. These model features are viewed as objectives to minimise, and are used by the MOGA engine to compute a cost and then assign fitness values, which are then used to select the best individuals for mating. In this preliminary work, the objectives considered were: the root mean square error in the training set ($RMSE_{TR}$), root mean square error in the test set ($RMSE_{TE}$), maximum of the auto-correlation of the errors ($R_{ee}$) and maximum of the cross-correlation between the inputs and the error ($R_{ue}$). The last two objectives are part of the set of conditions called "model-validity tests" which are explained in detail in [82]. These tests involve the computation of first and high-order correlations between models inputs, outputs and errors. The total set of these tests encloses eight conditions. A model is considered adequate (with 95% of confidence) if the computed correlation tests are inferior to a confidence interval defined as:

$$CI = \frac{1.96}{\sqrt{P}}, \tag{6.1}$$

where $P$ is the number of training patterns.

In order to impose some level of accuracy, the objective related with the error in new data (i.e. the $\mathrm{RMSE_{TE}}$) was assigned with a goal value of 0.003. For the

objectives related with the model-validity tests ($R_{ee}$ and $R_{ue}$), a goal value equal to $CI$ was assigned. As the number of training patterns for this preliminary test is 377, then $CI$ is approximately 0.1.

For the MOGA, the population of structures like the generic one presented in Figure 6.4 must be trained, in order to compute the previously referred objectives. The training was accomplished by a methodology that involves the Levenberg Marquardt algorithm (LM) and the minimisation of the criterion presented in Equation 2.33. This criterion exploits the separability of the RBFNN parameters into linear and non-linear, improving the performance of the training [13]. The LM optimised only the centre and spreads ($\mathbf{v} = [\mathbf{c}_1, \cdots, \mathbf{c}_n, \sigma_1 \cdots, \sigma_n]^T$), while the linear weights ($\mathbf{u} = [\alpha_1, \cdots, \alpha_n, b]^T$) were found using the linear least squares strategy, given by Equation 2.32. As reported in Sub-section 2.2.1, this training methodology brings some advantages, thus being applied in this thesis. One important aspect is the setup of the initial values of the centres and spreads, used by the LM to start the search for the "optimum" values. In all the experiments performed, the initial value of the centres were found using a enhanced version of the K-means clustering algorithm (Algorithm 1 in Sub-section 2.2.1). The initial value of the spreads was obtained using:

$$\sigma_i = \frac{d_{\max}}{\sqrt{2n}}, i = 1, \cdots, n, \tag{6.2}$$

where $d_{\max}$ is the maximum distance between centres and $n$ is the number of centres.

The training process was stopped by using the "early–stopping" criterion. As explained in Sub-section 2.2.1, this criterion stops training based on the generalisation performance. When the performance on the test data (in this first case-study the data collected at 1.5 $W/cm^2$ ) begins to deteriorate the training is stopped. This deterioration indicates that the network begins to be specialised on the training data, i.e. overtrained. The "early–stopping" is recognised as the ideal stopping criterion

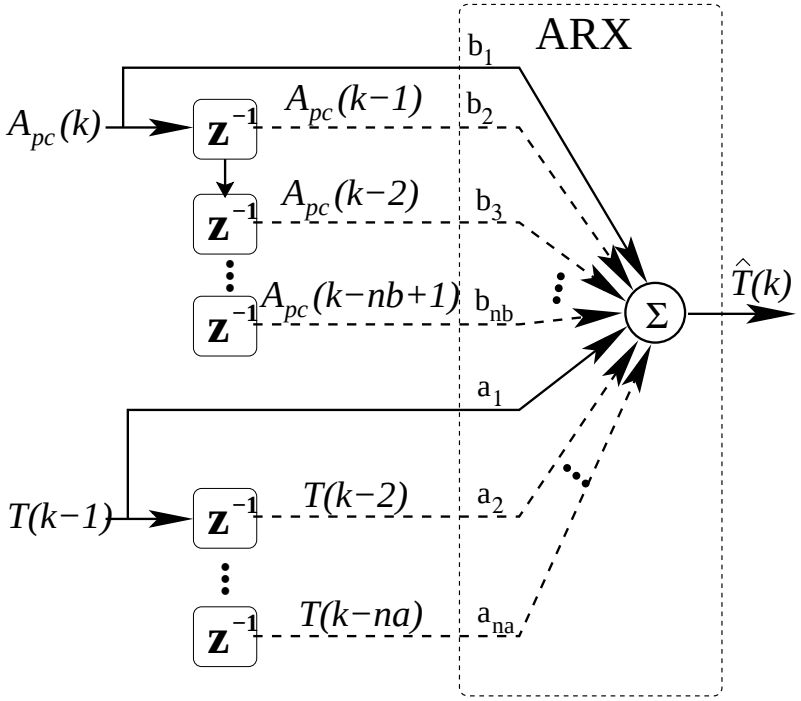


**Figure 6.7:** *Generic structure based on ARX, applied for invasive temperature estimation. The dashed arrows represent inputs that should be selected. The symbol* $\mathbf{z}^{-1}$ *represents the ideal unit-delay operator.*

for real world applications.

The ARX structure employed for comparison with the RBFNN-based structure is presented in Figure 6.7. In the same way, as for the RBFNN-based structure, the input information considered was the past 48 lags of the measured temperature and the amplitude of the principal component of the intensity signals spectrum. As the inputs are directly related with the output, the model parameters can be found using the linear least squares method, as the linear parameters in the RBFNN-based structure. The search for proper ARX-based structures was performed iteratively, i.e. by performing a scanning among the possible inputs, as exposed in Algorithm 2.

**Algorithm 2** ARX structure selection

1: Initialisation
   • Training the ARX structure with inputs $\{A_{pc}(k),\, T(k-1)\}$
   • Analyse performance of the trained ARX structure on the validation data
   • Save performance
2: **for** $nb = 2$ to 48 **do**
3:  **for** $na = 2$ to 48 **do**
4:  • Training the ARX structure with inputs $\{A_{pc}(k),\cdots,\, A_{pc}(k-nb+1),$ $T(k-1),\cdots,T(k-na)\}$
   • Analyse performance of the trained ARX structure on the validation data
   • Save performance
5:  **end for**
6: **end for**
7: • Analyse saved performance and choose best

### RBFNN and RBFLIC based on the amplitude of the principal component and in the amplitude of the first and second harmonics

Using the same experimental data employed for the previously reported structures, two other model structures were applied for single-point invasive temperature estimation. For these structures, in addition to the amplitude of the principal component of the spectrum of the intensity signals, the amplitude of the related first and second harmonics was also considered.

The amplitude variation of the principal component and related harmonics is presented in Figure 6.3. For the previous two structures the filtering process was discarded because the amplitude of the fundamental component and the temperature presented low noise levels. For the structures considering the amplitudes of the harmonics, it was assumed and then verified that the noise presented by these variables does not affect the final estimation performance. In this way, as in the previous structures, only a normalisation to values between 0 and 1 was performed. For the remaining text, the convention used is:

- Normalised amplitude of the principal component–$A_{pc}$;
- Normalised amplitude of the first harmonic–$A_{1h}$;

- Normalised amplitude of the second harmonic–$A_{2h}$;
- Normalised temperature–$T$.

In the same way as for the structures that consider only the principal component, the training was performed with data collected at 1 $W/cm^2$ . Data collected at 1.5 $W/cm^2$ and at 2.0 $W/cm^2$ were applied for test and validation, respectively.

The structure limitations considered were: a number of inputs between [2, 20], a number of neurons between [2,15], and a maximum lag for the input variables of 20. The model structure involving the standard RBFNN is presented in Figure 6.8.

A radial-basis-function neural network with linear input connections (RBFLIC) is a normal RBFNN but with inputs directly connected to the third layer. This way, the inputs can contribute both linearly and non-linearly for the overall network output. The input/output relation for a RBFLIC is:

$$y(\mathbf{x}, \mathbf{x}_l) = b + \sum_{i=1}^{n} \alpha_i \varphi \left( ||\mathbf{x} - \mathbf{c}_i|| \right) + \mathbf{x}_l \lambda, \tag{6.3}$$

where $\mathbf{x}$ is an input pattern vector with dimension $1 \times d$, being $d$ the number of non-linear inputs. The vector $\mathbf{c}_i$ and the scalar $\alpha_i$ represent the centre coordinates and the linear weight of the i-th basis function, respectively. The number of non-linear neurons is represented by $n$, and $b$ is a bias term. The vector $\mathbf{x}_l$ is an input pattern vector related to the linear inputs and has dimensions $1 \times m$, $m$ being the number of linear inputs. The vector $\lambda$ represents the weights related to the linear inputs and has dimensions $m \times 1$.

For the proposed invasive estimation environment, the same inputs applied in the previous RBFNN-based structure were considered for the structure involving the RBFLIC. In addition, these inputs were considered to contribute both non-linearly and linearly to the estimated temperature. The number of non-linear and linear inputs was considered as an integer in the interval [2,20]. For the number of non-

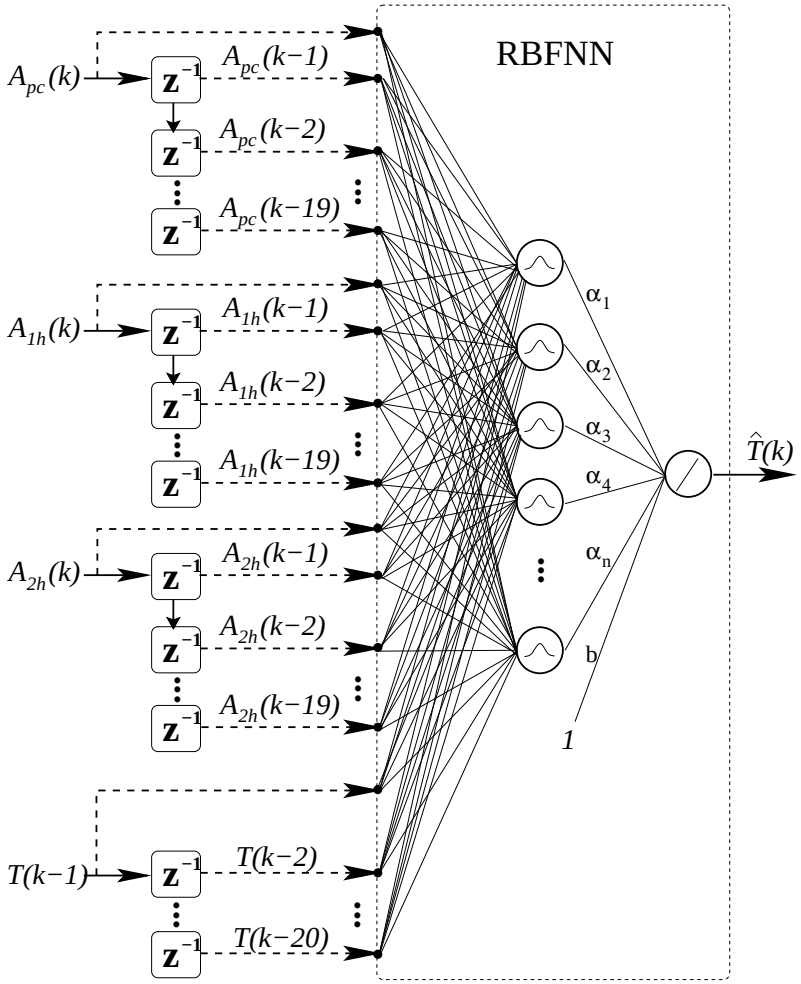


**Figure 6.8:** *Generic structure based on RBFNN, applied for invasive temperature estimation, considering as inputs both the information of the amplitude of the fundamental component and the amplitude of the first and second harmonics. The dashed arrows represent inputs that should be selected. The symbol* $\mathbf{z}^{-1}$ *represents the ideal unit-delay operator.*

linear neurons, the same range defined for the structure presented in Figure 6.8, was considered. The applied structure based on RBFLIC is presented in Figure 6.9. Considering the previous limits, the number of possible structures was 7.28E19 when considering the standard RBFNN, and 3.78E38 when considering the RBFLIC. This difference is because in the RBFLIC case, both the linear and non-linear inputs contribute to the number of possible combinations. These numbers indicate the impossibility for analysing each structure individually. In this way, a search by means of the multi-objective genetic algorithm (MOGA) was also applied to obtain proper structures. The genetic codification of the structure composed by the RBFNN is the same as presented in Figure 6.5. On the other hand, the RBFLIC chromosome is composed by two sub-chromosomes: one related to the non-linear function and the other related to the linear behaviour. As presented in Figure 6.10, the first part is the same as the chromosome of a normal RBFNN, as presented in Figure 6.5. The first sub-chromosome is composed by a first position related to the number of neurons, and the other positions are indexes to the available input terms. The sub-chromosome related to the linear behaviour is composed only by indexes to the available input terms. The lookup table is presented in Figure 6.11. The crossover and mutation operators are the same explained previously. These operators were applied independently to each part of the chromosome, as the non-linear and linear inputs must be selected independently. Obviously, for the linear part, the place associated to the number of neurons does not exist and the crossover and mutation involve only operations with the indexes to the available input terms.

The model performance descriptors considered for these two structures were:

- root mean square error in training–$RMSE_{TR}$;
- root mean square error in test–$RMSE_{TE}$;
- model-validity tests;

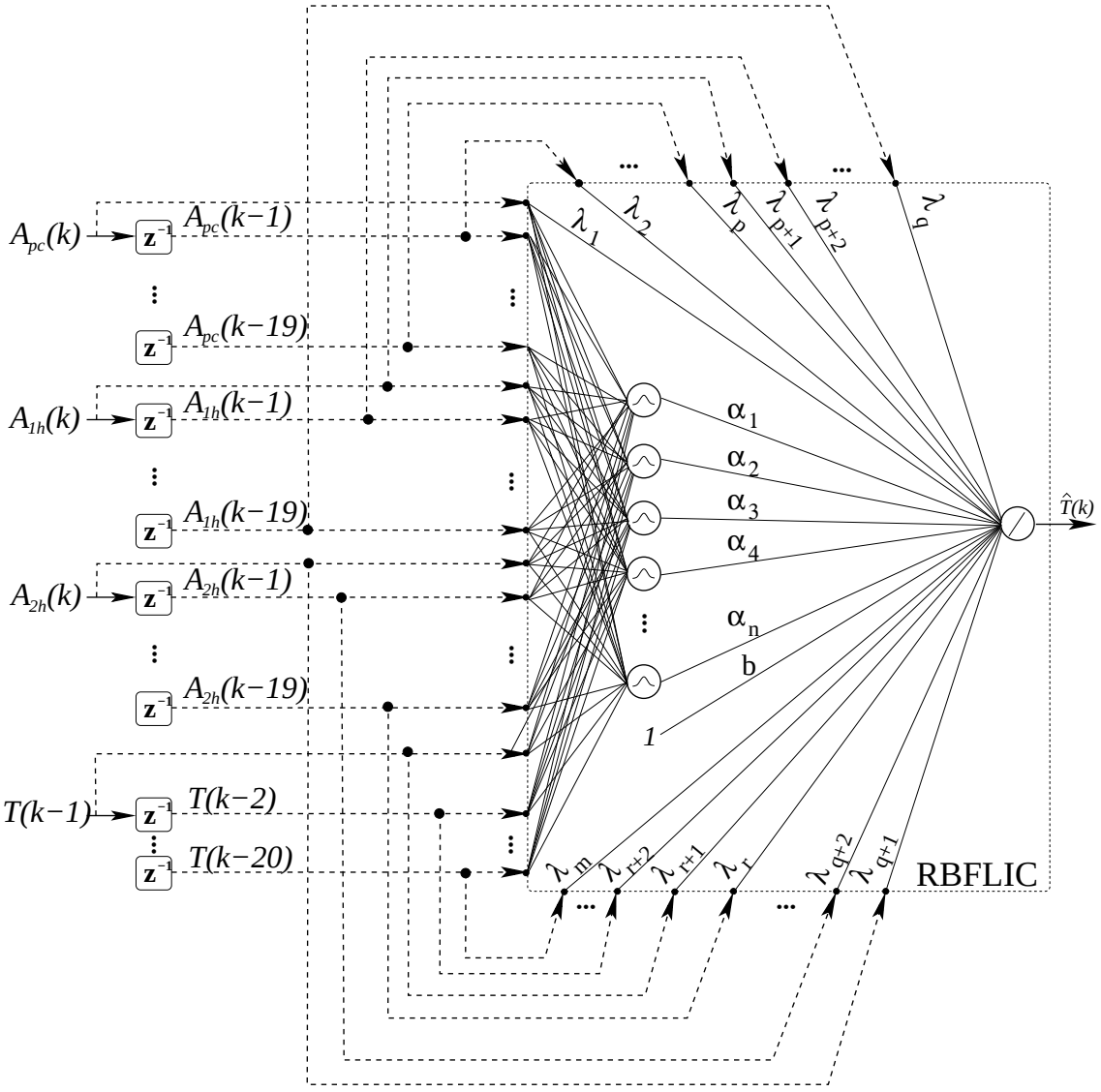


**Figure 6.9:** *Generic structure based on RBFLIC, applied for invasive temperature estimation, considering as inputs the information of the amplitude of the fundamental component and the amplitude of the first and second harmonics. The dashed arrows represent inputs that are to be selected. The symbol* $\mathbf{z}^{-1}$ *represents the ideal unit-delay operator. The indexes associated to the linear weights are such that:* $0<p<q<r<m$.

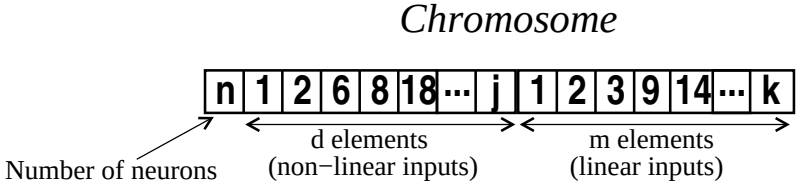


**Figure 6.10:** *Chromosome assigned to each structure based on RBFLIC.* **d** *is the number of non-linear inputs while* **m** *is the number of linear inputs in a particular structure.*

*Lookup table*

| *Index* | 1 | ... | 20 | 21 | ... | 40 | 41 | ... | 60 | 61 | ... | 80 |
|---|---|---|---|---|---|---|---|---|---|---|---|---|
| *Term* | $T$(k–1) | ... | $T$(k–20) | $A_{pc}$(k) | ... | $A_{pc}$(k–19) | $A_{1h}$(k) | ... | $A_{1h}$(k–19) | $A_{2h}$(k) | ... | $A_{2h}$(k–19) |

**Figure 6.11:** *Lookup table for invasive estimation considering the principal component and the first two harmonics of the spectrum of the intensity signals.*

- number of model parameters (complexity)–$NP$.

In the previously referred structures (RBFNN and ARX structures based only on $A_{pc}$ and $T$) only two model-validity tests were applied ($R_{ee}$ and $R_{ue}$). For the new structures the total set of model-validity tests was considered. As said previously and described in [82], these tests involve the computation of first-order and higher-order correlations between model inputs, outputs and errors. Theoretically a model is considered adequate if the set of eight conditions is satisfied. The conditions are:

$$\begin{aligned} R_{ee}(\tau) &= \delta(\tau) \\ R_{ue}(\tau) &= 0 \quad ,\forall\tau \\ R_{u^2e}(\tau) &= 0 \quad ,\forall\tau \\ R_{u^2e^2}(\tau) &= 0 \quad ,\forall\tau \\ R_{e(eu)}(\tau) &= 0 \quad ,\tau \geq 0 \\ R_{e^2e^2}(\tau) &= \delta(\tau) \\ R_{(ye)e^2}(\tau) &= k\delta(\tau) \\ R_{(ye)u^2}(\tau) &= 0 \quad ,\forall\tau \end{aligned} \tag{6.4}$$

In practice, the correlations will never be equal to zero for all lags. In this way, the condition is considered satisfied if the normalised correlation functions lie within the 95% interval defined by Equation 6.1. In the same way, the auto-correlations are never exactly equal to the delta function, but the conditions are considered satisfied

if the normalised functions lie within the 95% interval before lag one. In this thesis, the maximum absolute values of these correlation functions were considered as model performance descriptors and then assumed by the MOGA engine as objectives to minimise. In real world implementations, the criterion of small error models is not the only one to be considered. A model may be so complex as to turn its practical implementation impossible. Therefore, the minimisation of both the error and the computational complexity is a fundamental aspect. So for the structure based on RBFNN and RBFLIC, the number of model parameters was considered as an objective to be minimised. The number of parameters is defined as:

$$NP = NC \times NI + NS + NW, \tag{6.5}$$

where $NC$ is the number of centres, $NI$ is the number of non-linear inputs, $NS$ is the number of spreads, and $NW$ is the number of linear weights. For the RBFNN $NW = n + 1$, while for the RBFLIC is $NW = n + 1 + m$, being $n$ the number of neurons and $m$ the number of parameters related with the linear inputs.

From the MOGA point of view, the previously referred model features were objectives to minimise. In order to define feasibility constrains, goals were assigned to some of the objectives. Another important aspect is the relative relevance among the different objectives. Some of them should be considered more relevant for the final application than the others, and MOGA allows the definition of priorities for them. The goals and priorities for the different objectives are presented in Table 6.1, where it can be seen that the error related to the generalisation performance, i.e. the $RMSE_{TE}$, was defined with the highest priority. This is because the main goal is to achieve models with good performance in data different from the one applied for training. The value defined for this objective was 0.003. The maximum of the correlation tests was defined with a goal value of $CI = 1.96/\sqrt{429 - 20} \approx 0.097$,

**Table 6.1:** *Goals and priorities defined for the objectives applied in the optimisation of RBFNN- and RBFLIC-based structures.*

| Objective | Goal | Priority |
|---|---|---|
| $RMSE_{TR}$ | - | 0 |
| $RMSE_{TE}$ | 0.003 | 2 |
| $NP$ | 70 | 1 |
| $R_{ee}$ | 0.097 | 1 |
| $R_{e^2e^2}$ | 0.097 | 1 |
| $R_{(ye)e^2}$ | 0.097 | 1 |
| $R_{(ye)u^2}$ | 0.097 | 1 |
| $R_{ue}$ | 0.097 | 1 |
| $R_{u^2e^2}$ | 0.097 | 1 |
| $R_{u^2e}$ | 0.097 | 1 |
| $R_{e(eu)}$ | 0.097 | 1 |

and with priority 1. For the number of parameters a goal value of 70 and a priority 1 were assigned. This goal value was defined by taking in account the maximum possible value for $NP$, and by realising that it was possible to attain proper models with $NP$ inferior or equal to 70. The absence of goal and priority values for the $RMSE_{TR}$ means that the MOGA is allowed to just minimise this objective (priority 0), having no restriction to take into account.

The training of each RBFNN- and RBFLIC-based structures was performed by using the training methodology presented previously. That is, the non-linear parameters were found using the Levenberg Marquardt (LM) algorithm by minimising the criterion presented in Equation 2.33. In both structures, the linear parameters were found using the linear least squares strategy, and the training stops by taking in account the "early stopping" criterion.

### 6.2.2 Non-invasive estimation

As referred in Chapter 4, invasive temperature estimation presents some inherent problems. For the safety and effectiveness of the thermal therapies, temperature should be assessed non-invasively. The first tests of the proposed estimation me-

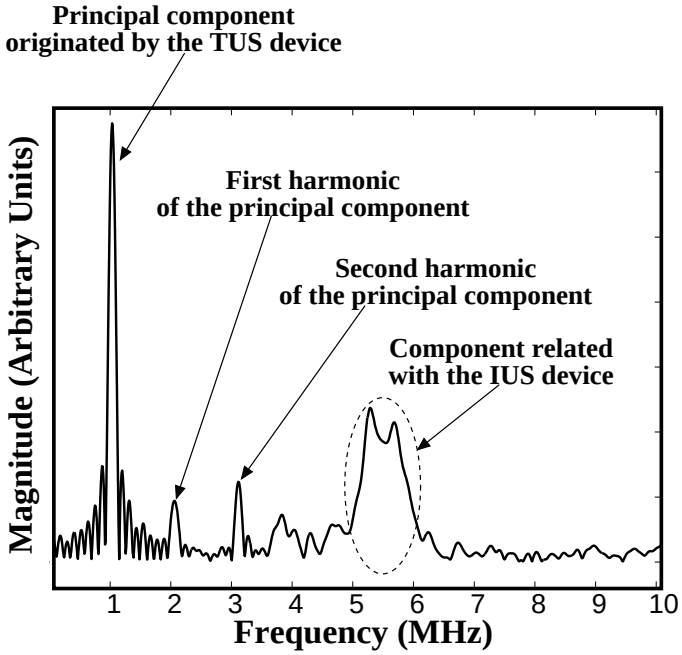


**Figure 6.12:** *Magnitude spectrum of echo originated by the central sphere and by the thermocouple.*

thodology, for non-invasive thermometry were performed using the signals collected from the experimental setup presented in Section 5.3 which are backscattered ultrasound (BSU) signals and the temperature. The temperature was measured in a central sphere, where single-point non-invasive estimation was performed. Two distances (24 mm and 48 mm) from the therapeutic ultrasound transducer to this central sphere were considered. As temperature was to be estimated in this central point, features extraction was solely performed in the echo originated by the central sphere in conjunction with the thermocouple. This was done in order to discard information originated by other scatterers outside the region of interest. After a rectangular window application, the echo of interest was isolated and spectral features extracted during each experimental trial. An example of the magnitude spectrum of the echo of interest is presented in Figure 6.12. The spectral features monitored were: the amplitude of the principal component related to the therapeutic ultrasound (TUS) device; the amplitude of the first and second harmonic of this

principal component; the amplitude , bandwidth (-6 dB) and central frequency of the component related to the imaging ultrasound (IUS) device. In addition to these spectral features, one temporal feature was also considered: the time position of the echo of interest. This temporal position was found by computing the envelope of the complete BSU signal, and then selecting the peak correspondent to the echo of interest. Mathematically, the envelope can be obtained as follow, considering the Hilbert transform of the BSU signal $b(t)$ as:

$$\hat{b}(t) = \mathcal{H}\{b(t)\} = \frac{1}{\pi}\int_{-\infty}^{\infty}\frac{b(\tau)}{t-\tau}d\tau, \tag{6.6}$$

being $\hat{b}(t)$ the Hilbert transform of $b(t)$. The analytic signal of $b(t)$ is given by:

$$b_+(t) = b(t) + j\hat{b}(t). \tag{6.7}$$

The envelope of the complete BSU signals is:

$$\tilde{b}(t) = |b_+(t)| = \sqrt{b^2(t) + \hat{b}^2(t)} \tag{6.8}$$

Finally, the envelope was smoothed by applying a low-pass Butterworth digital filter with order 2 and cut-off frequency of 1/20 of the Nyquist frequency. An example of the computed envelope is presented in Figure 6.13. This figure also shows the peak of interest, and how the time position is assessed. The choice of this method for computing the changes on temporal position (i.e. the time-of-arrival), instead of a standard correlation-based method is due to the interference of the TUS beam. This interference is shown in Figure 5.8a and can induce considerable temporal variations between consequent BSU signals. Such a noise in the computed temporal position makes the temperature induced variation impossible to be assessed. The method based on the envelope extraction reduces this noise, enabling the use of this feature

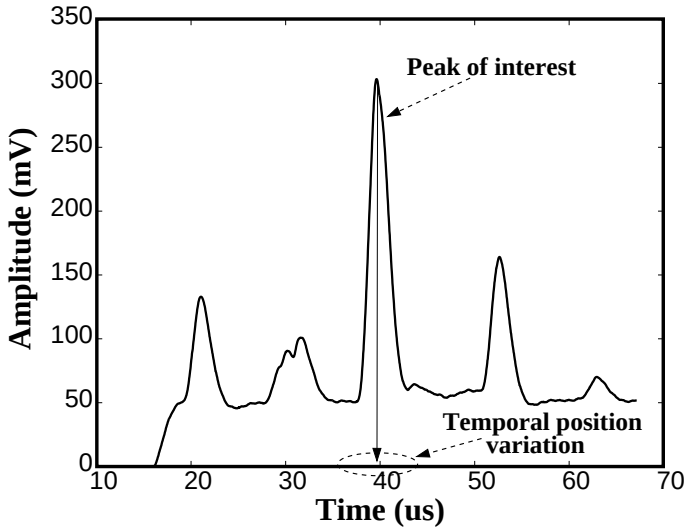


**Figure 6.13:** *Computed envelope of a measured BSU signal. The peak of interest, i.e. the one correspondent to the echo originated by the central sphere and the thermocouple, is pointed.*

for temperature estimation.

Some of the computed features present considerable noise levels, thus a filtering process was applied to the features and measured temperature. As they have different scales, a normalisation to values between 0 and 1 was employed. For this estimation environment, the following convention was used:

- filtered and normalised amplitude of the principal component originated by the TUS device–$AF_{TUS}$;
- filtered and normalised amplitude of the first and second harmonic of principal component originated by the TUS device–$AH1_{TUS}$ and $AH2_{TUS}$;
- filtered and normalised amplitude, bandwidth, and central frequency of the component related with the IUS transducer–$A_{IUS}$, $BW_{IUS}$, and $F_{IUS}$;
- filtered and normalised temporal position–$TP$;
- filtered and normalised temperature–$T$.

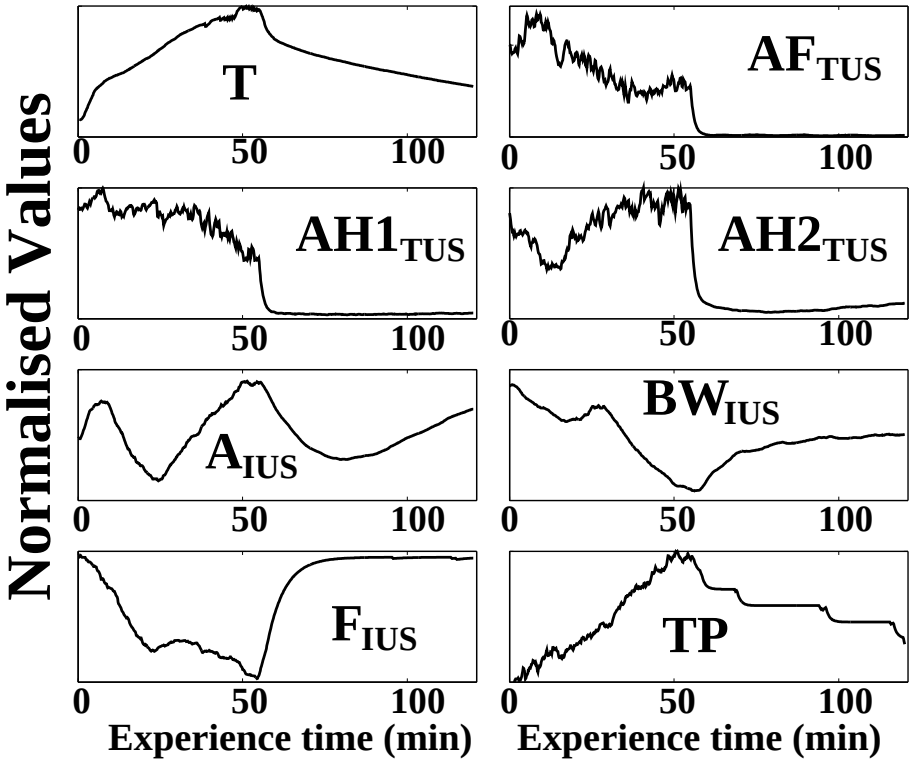


**Figure 6.14:** *Extracted features as compared with the measured temperature for 2.0-$W/cm^2$ TUS intensity, and considering a spacing between the therapeutic transducer and the central sphere of 48 mm.*

An example of the filtered and normalised features and temperatures for 2.0 $W/cm^2$ TUS intensity, is presented in Figure 6.14. Looking at this figure, it can be said that only $TP$, $BW_{IUS}$ and $F_{IUS}$ present some small linearity with the temperature. The other features can only be related to the temperature by non-linear models.

Using these features, two model structures were applied: one based on RBFNN, and another on a linear model, similar to the ARX presented previously. In fact, this linear structure can become an ARX structure, depending if the past temperature values are or not considered as inputs. The difference between these two structures and the first ones developed for invasive temperature estimation is that new non-invasive features were considered, and these new model structures were designed for multi-step-ahead estimation. This means that instead of the past measured temperature values, the past estimated ones were considered. This operation mode is

essential for a completely non-invasive estimation approach, given that in practice the temperature cannot be measured. In addition, the linear structures were optimised in the same way as the RBFNN-based structure, using the multi-objective genetic algorithm (MOGA), enabling more trustworthy comparisons. Of course, the training of both non-linear and linear structures was performed in a one-step-ahead fashion, that is considering the measured temperature values. Then in the test and validation phases, the performance of the trained structures was assessed for multi-step-ahead estimation. The estimated temperature values at the output were supplied at the inputs, meaning that a complete temperature waveform was estimated along one complete experiment, based only on the initial temperature.

For these structure types, the training data were obtained by randomly selecting patterns from the three measured sets (1/3 from each set) for each distance, in order to consider data from the three intensities. The test data were obtained from the complete data sequences measured at 1.5 $W/cm^2$ . At the end of the structure selection process, the models performance was assessed using the complete data sequences collected at 2.0 $W/cm^2$ (validation data). The validation sets were selected to be at the highest intensity since this is the condition more difficult in terms of temperature estimation, i.e. where a larger temperature variation was observed.

In the same way as for the past RBFNN-based structures, MOGA was applied for the selection of proper inputs and number of neurons. The input variables were the features referred previously plus the past temperature values (8 input variables). For each variable, 20 past lags were considered. MOGA was allowed to select structures with a number of inputs and of neurons between [2,20]. These values were selected after several test considering other possibilities. These limits on the structure parameters give a number of possible models of approximately $3.3E26$. The generic RBFNN structure is presented in Figure 6.15. To be noticed that this structure, unlike the previous ones, considers the feedback of the past

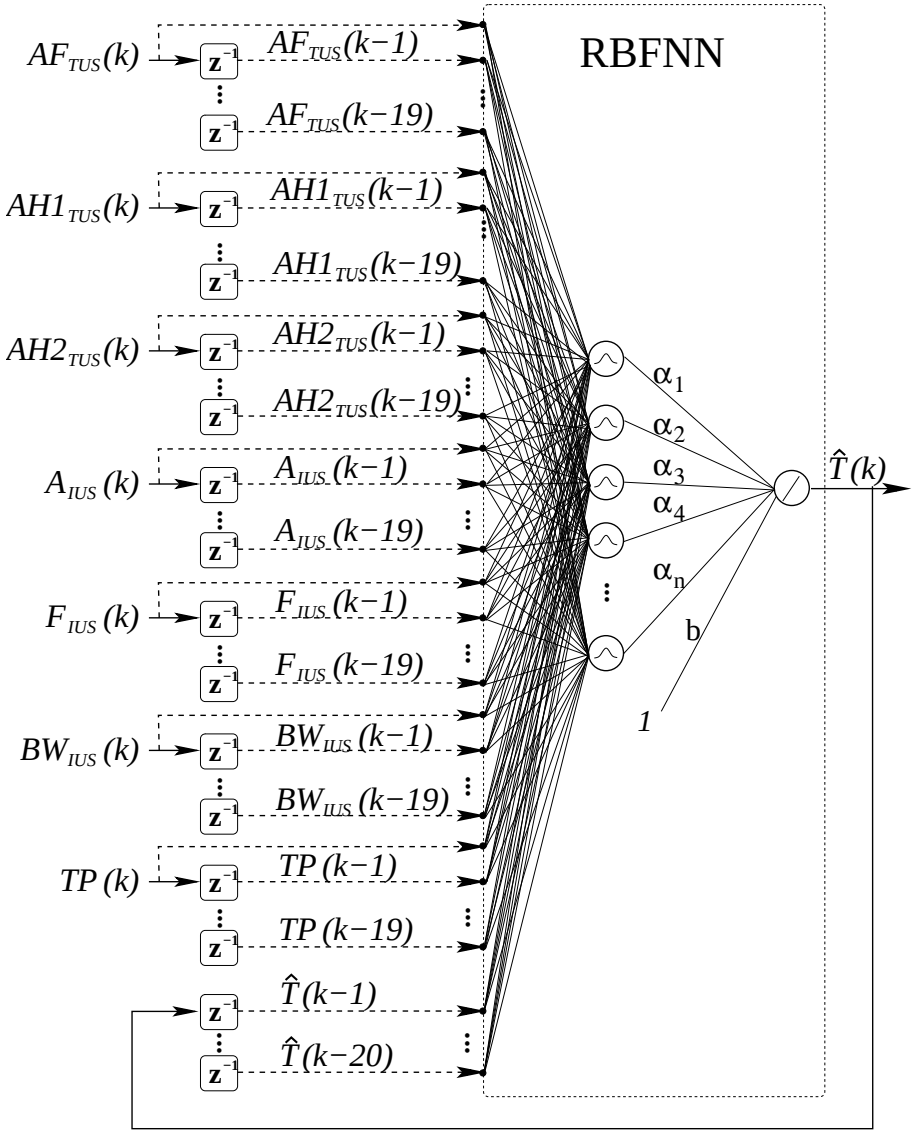


**Figure 6.15:** *Generic structure based on RBFNN, applied for single-point non-invasive estimation on liquid media. The dashed arrows represent inputs that should be selected. The symbol* $\mathbf{z}^{-1}$ *represents the ideal unit-delay operator.*

estimated temperature values. This means that it was optimised for multi-step-ahead estimation, as desired for real-world non-invasive temperature estimators. The chromosome of this structure is like the one showed previously for the RBFNN-based structures. The difference is that a lookup table considering 160 indexes (8 variables $\times$ 20 lags) were used.

The training of each structure, during the MOGA optimisation process was performed by the training methodology so far explained. This methodology involves: the initial determination of the centre using the optimal adaptive k-means clustering algorithm (OAKM); the spreads found by Equation 6.2; the optimisation of the centres and spreads using the minimisation of the criterion referred in Equation 2.33 by the Levenberg Marquardt algorithm; the values of the linear weights found by linear least squares; and the stopping of both linear and non-linear parameters using the "early-stopping" criterion.

For this structure the performance descriptors (MOGA objectives) considered were:

- root mean square error in the training set–$RMSE_{TR}$;
- root mean square error in the test set–$RMSE_{TE}$;
- maximum root mean square error in all the estimation steps–$MRMSE_{ES}$;
- linear weights norm–$LWN$;
- number of parameters–$NP$;
- model-validity tests.

The $MRMSE_{ES}$ is an essential performance descriptor, given that it discriminated the multi-step-ahead behaviour of a given model. As said previously, proper multi-step-ahead estimators are a fundamental point for non-invasive estimation. The $MRMSE_{ES}$ computation is explained in Figure 6.16.

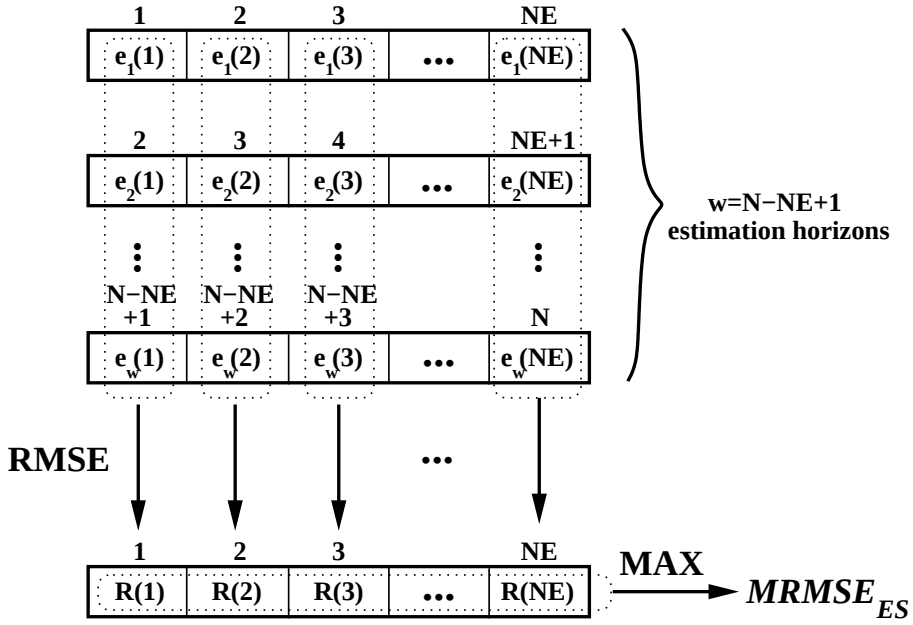


**Figure 6.16:** *$MRMSE_{ES}$ computation.* **N** *is the size of the test sequence, and* **NE** *is the number of steps-ahead considered.*

Considering a test sequence with **N** samples, and a prediction horizon of **NE** steps (i.e. **NE**-steps-ahead), the $MRMSE_{ES}$ is computed as follow:

1. by considering the past estimated temperature values, compute the estimated temperature values during **NE** steps, starting by considering the first test sequence sample;

2. by comparison with the measured temperature values, compute the associated error vector with dimensions $1\times$ **NE**;

3. starting in the second sample of the test sequence, compute the estimated temperature values during **NE** steps, and compute the associated error vector;

4. step 3 is repeated until the complete test sequence is considered, i.e. the last **NE** samples are taken into account;

5. afterwards, the computed error vectors are aggregated in a single matrix, and the root mean square error computed for each column;

6. a RMSE vector, denoting the error in each of the **NE** estimation steps is obtained.

7. Finally, the $MRMSE_{ES}$ is the maximum of this RMSE vector.

The minimisation of this performance descriptor enables the attainment of proper multi-step-ahead estimators, given that the reduction of the highest error in all the estimation steps is intended. This performance descriptor like the one presented previously was proposed in [83] for greenhouse climate prediction, where consistent results were obtained. In this work, 60 estimation steps (i.e. estimation during 10 minutes) were found appropriate given the proper results obtained. The entire model-validity tests are exposed in Equation 6.4. In this part of the work, as in the first invasive estimation attempt, only the tests involving the first order correlations ($R_{ee}$ and $R_{ue}$) were used. This was because results considering all the tests were not better. Another reason is the reduction of the objective space in six dimensions, turning more relevant the minimisation of what really matters: in this case, the model errors and complexity (number of parameters). However, for the estimation environment considered in this part of the work, the considered model-validity tests seemed to bring some advantages, given that excluding all the tests resulted in poor performance. The linear weights norm is defined as:

$$LWN = \sqrt{\sum_{i=1}^{n} \alpha_i^2 + b^2}, \tag{6.9}$$

where $\{\alpha_i\}_{i=1}^{n}$ is the number of neurons and $b$ is the bias value. Models with a high $LWN$ are bad conditioned models. They are usually specialised in the training data, and when considering other data sets they tend to present an exacerbated error, thus the importance of minimising this model feature. The number of parameters is obtained in the same way as expressed in Equation 6.5. The goals and priorities defined

**Table 6.2:** *Goals and priorities defined for the objectives applied in the optimisation of RBFNN and linear-based structures: non-invasive single-point estimation.*

| | $RMSE_{TR}$ | $RMSE_{TE}$ | $MRMSE_{ES}$ | $LWN$ | $NP^{\dagger}$ | $R_{\text{ee}}$ | $R_{\text{ue}}$ |
|---|---|---|---|---|---|---|---|
| **Goal** | -(0.004$^{\ddagger}$) | 0.002 | 0.003 | 2 | 100 | 0.0741 | 0.0741 |
| **Priority** | 0(1$^{\ddagger}$) | 2 | 2 | 1 | 1 | 1 | 1 |

†–Only defined for RBFNN-based structures

‡–Applied in the comparison between the linear and RBFNN-based structures.

for each one of the objectives are described in Table 6.2. For the $RMSE_{TR}$ in some estimation trials involving RBFNN-based structures, no goal was defined (priority 0) and the MOGA was just allowed to minimise this objective. In some situations, it was found that if no goal was defined, the MOGA after fulfilling the goals for the other objectives, was focusing only on the minimisation of $RMSE_{TR}$ as most as possible. This resulted in a search directed to models specialised only in the training data. Although the generalisation goals were already fulfilled, this specialisation on the training data can result in bad performance in other real-world data. The definition of a goal makes this objective equal to the other priority-1 objectives, meaning that after fulfilling the priority-2 objectives, MOGA will try to equally minimise all the other objectives, preventing the undesired search for good models in training. Goals for $RMSE_{TR}$ were defined for the runs used to compare the performance of the RBFNN-based structures, against the performance of the linear structures. In addition, they are applied in the remaining multi-point temperature estimation trials, presented in the next section. In order to promote the selection of models with a high generalisation capacity, the $RMSE_{TE}$ and $MRMSE_{ES}$ were defined as high priority objectives (priority = 2), and with a goal value of 0.002 and 0.003, respectively. To note that the goal values defined for the error objectives are related to the normalised data. The maximum of the correlation tests was defined with a goal value of $CI = 1.96/\sqrt{P} = 1.96/\sqrt{721 - 20} = 0.074$, and with priority 1. The goal value for the $LWN$ was based on the normalisation employed, and in the maximum number of neurons considered. The goal for the number of parameters

was set having in mind the structure limitations imposed and the previously values defined for the other RBFNN- and RBFLIC-based structures. The generic linear structure is shown in Figure 6.17. From this figure it can be seen that the same input information was considered for the RBFNN-based structures and for this linear structure. In Sub-section 6.2.1, a linear structure (ARX-based) was applied for invasive temperature estimation. The search for proper structures was iteratively performed using Algorithm 2, while the proper RBFNN-based structures for the same estimation environment were found using the MOGA. For single-point non-invasive estimation both the proper RBFNN-based structures and linear structures were found using the MOGA. As expected, the linear structures are represented in the MOGA by a chromosome that differs from the one applied for the RBFNN-based structures in the first position (which discriminates the number of neurons). This means that the chromosome of the linear structures is formed only by indexes to the 160 available input terms. The maximum number of inputs was 20, as in the RBFNN case. The training of one linear structure was performed by computing the parameters $[b_1,\cdots,b_m]$, using the linear least squares strategy. The same objectives (performance descriptors) and associated goals and priorities used for RBFNN-based structures were applied for these linear structures, with exception of the number of parameters ($NP$). This is because the number of parameters is the same as the number of inputs, being 20 in the maximum, which is a very low value.

## 6.3 Models for estimation in time and space

### 6.3.1 Single intensity

The normal evolution of the previously reported model structures is to consider estimations in both time and space. The structures explained before for single-point non-invasive temperature estimation consider different models for different points.

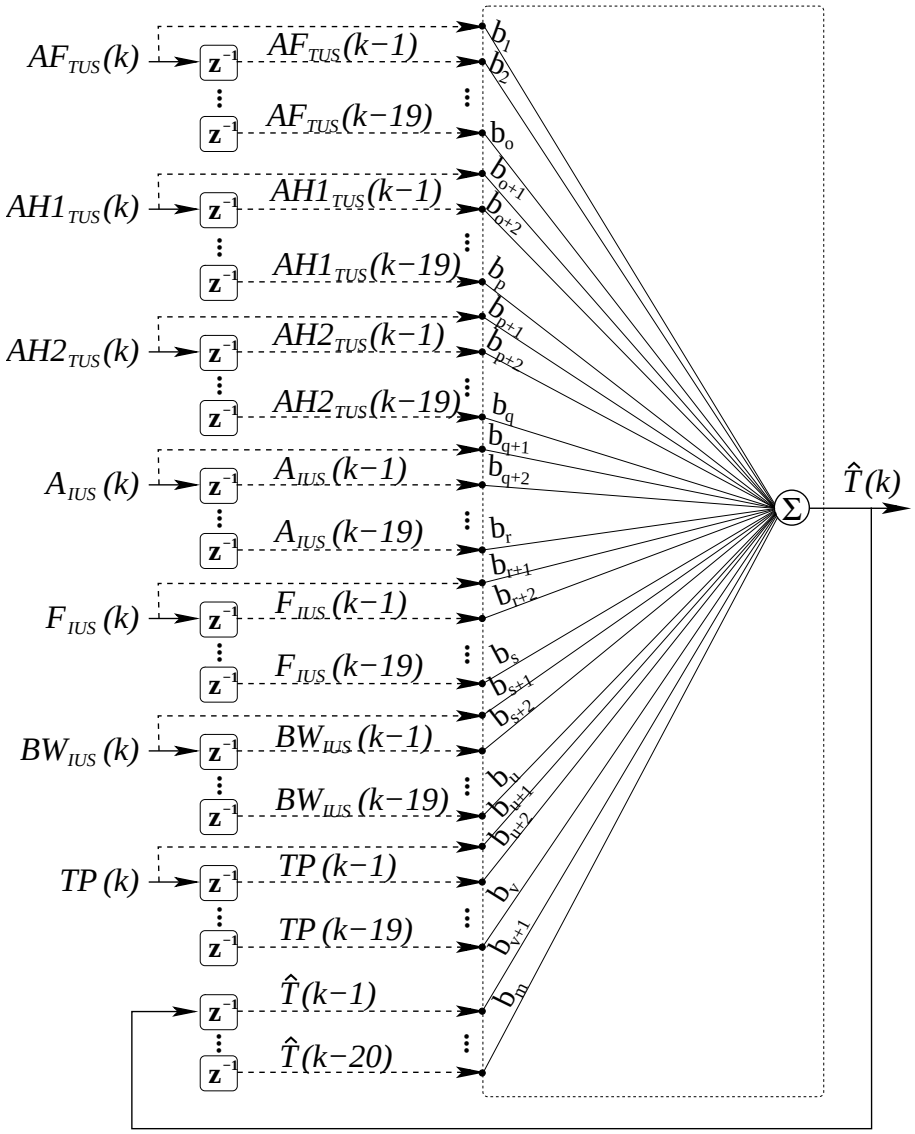


**Figure 6.17:** *Generic linear structure, applied for single-point non-invasive estimation on liquid media. The dashed arrows represent inputs that should be selected. The symbol* $\mathbf{z}^{-1}$ *represents the ideal unit-delay operator. The indexes associated with the weights are such that:* $0<o<p<q<r<s<u<v<m$.

Now, by aggregating both information extracted from the data collected at the two points in the experimental setup presented in Section 5.3, single RBFNN models for two-point estimation can be developed. The training data were obtained by randomly selecting data from the six (3 intensities $\times$ 2 points) measured sets (1/3 from each set). In this way, the models were trained to perform well in the two spatial points and for the three applied intensities. The two complete data sequences collected at 1.5 $W/cm^2$ were used for test. After the training and structure optimisation, the best-fitted structures were validated in the complete data sequences collected at 2.0 $W/cm^2$ . The generic model structure is shown in Figure 6.18. As in the other RBFNN-based models, the MOGA was again applied in the search for proper structures. Just like for single-point non-invasive estimation, the applied structure for two-point estimation considers the same input information. In addition, an extra input ($P(k)$) was assigned to discriminate between spatial points. In Figure 6.18 the dashed arrows represent connections that may or not exist, i.e. those which were or not selected by the MOGA. The extra input considered is connected to the network with a full arrow, meaning that it is always present (not selected by the MOGA). The permanent presence of this input resulted in an increase in performance. When the temperature at 24 mm was to be estimated, $P(k)$ assumed the value "0", otherwise the value "1". For this structure, the limitations defined were: a number of neurons in the range [10, 25], a number of inputs in the range [2,20], and a maximum lag for the input variables of 25. The ranges for the number of inputs and neurons were defined after several attempts considering other values. The value for the maximum lag was based on the time constants of the measured temperature signals. The analysis of the time-constants gives us an idea about short- and long-term change rate of the temperature signals. After an exponential fitting of the form:

$$\hat{T}_{exp} = C_1 e^{-a_1 t} + C_2 e^{-a_2 t}, \tag{6.10}$$

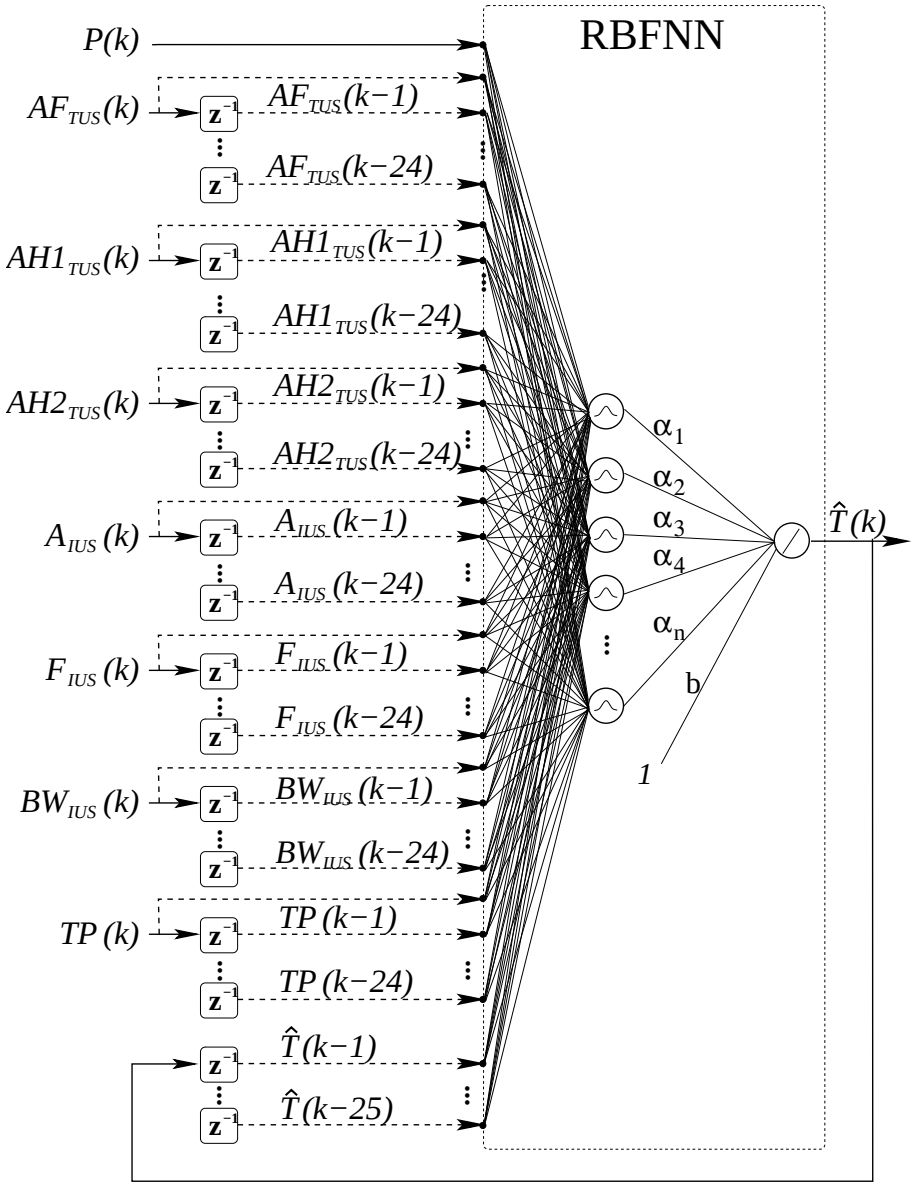


**Figure 6.18:** *Generic structure based on RBFNN, applied for two-point non-invasive estimation on liquid media. The dashed arrows represent inputs that should be selected during the structure optimisation process, while the full-arrow represent an input that is present in all the structures. The symbol* $\mathbf{z}^{-1}$ *represents the ideal unit-delay operator.*

by applying the Matlab® function "lsqnonlin.m", the values of $a_1$ and $a_2$ were found. The related time constants ($\tau_1 = 1/a_1$ and $\tau_2 = 1/a_2$) were determined for all the rising and falling parts of the temperature signals. Among those time constants, the one presenting higher values is called the dominant time-constant, and is related with the slowest mode of the signal. The non-dominant (the smallest-one), is related with the fastest mode and is the one which brings useful information for the computation of the maximum lag for the input variables. For each temperature signal two non-dominant time-constants exist (one for rising and other for falling). The smallest one was selected because it discriminates the fastest mode existent in a complete signal. All the temperature signals present non-dominant time-constants inferior to 227 seconds, except one signal which presents an exacerbated value for the non-dominant time constant. This was due to bad fitting, thus excluded in these calculations. Considering the sample period of 10 s, then the number of lags presented in 227 s is approximately 22. The maximum lag was defined as 25, in order to give a little more freedom to the MOGA search.

The training of each structure was performed using the methodology already explained for the RBFNN-based structures. The objectives taken into account for this two-point estimation attempt were:

- root mean square error in the training set–$RMSE_{TR}$;
- root mean square error in the test data collected at 24 mm– $RMSE24_{TE}$;
- root mean square error in the test data collected at 48 mm– $RMSE48_{TE}$;
- maximum root mean square error in all the estimation steps for the test sequence collected at 24 mm– $MRMSE24_{ES}$;
- maximum root mean square error in all the estimation steps for the test sequence collected at 48 mm– $MRMSE48_{ES}$;

**Table 6.3:** *Goals and priorities defined for the objectives applied in the optimisation of RBFNN-based structures for two-point temperature estimation in liquid medium.*

| Objective | Goal | Priority |
|---|---|---|
| $RMSE_{TR}$ | 0.004 | 1 |
| $RMSE24_{TE}$ | 0.002 | 2 |
| $RMSE48_{TE}$ | 0.002 | 2 |
| $MRMSE24_{ES}$ | 0.002 | 2 |
| $MRMSE48_{ES}$ | 0.002 | 2 |
| $R_{ee}$ | 0.052 | 1 |
| $R_{ue}$ | 0.052 | 1 |
| $LWN$ | 2.0 | 1 |
| $NP$ | 400 | 1 |

- model-validity tests–$R_{ee}$ and $R_{ue}$;
- linear weights norm–$LWN$;
- number of parameters–$NP$.

These objectives are identical to the ones presented previously for single-point estimation. The difference is that in the two-point situation, a single model must estimate temperature at both points, and separate objectives (related with the generalisation capacity (test errors)) were considered. In Table 6.3, the goals and priorities for each objective are presented. The error goals are related with the normalised data. Importance is given to a good generalisation in one-step-ahead and multi-step-ahead, so the test errors were defined with priority 2 and with a goal value of 0.002. The goal for the maximum of the correlation tests is $CI = 1.96/\sqrt{(2 \times 721) - 20} = 0.052$. The $LWN$ as in the single-point approach, was defined with priority 1 and with a goal value of 2.0. The goal for the number of parameters increased from 100 in the single-point to 400 in the two-points attempt. This is because a single model to estimate temperature at both points must have a larger processing capacity, and therefore a larger complexity.

### 6.3.2 Multiple intensity

Real-world temperature estimators should address not only single- and two-point temperature estimation, but also multi-point temperature estimation. In addition, multi-intensity estimation capabilities is an essential aspect concerning future therapeutic instrumentation control. The development of such estimators was possible by processing the data collected using the experimental setup presented in Section 5.4 (homogeneous phantom) and Section 5.5 (non-homogeneous phantom). From these experimental setups, temperature from five points and backscattered ultrasound (BSU) signals were collected simultaneously. Four different TUS intensities were applied in the homogeneous phantom case, and eight in the non-homogeneous phantom case. Looking at the parametrisation applied for the two-point model presented previously, the goal for the number of parameters increased from 100 in the single-point case to 400 in this case. Ideally, a model should be able to estimate temperature in multiple points and at multiple intensities in a given medium without a proportional increase in complexity. Part of the problem was solved in this thesis by considering a gel-based phantom instead of a glycerine medium (that was used in the first two experimental setups). In the gel-based phantoms no convection currents exist and the temperature variation is well-behaved and reproducible. The proportional increase in complexity can also be attenuated by selecting the appropriate temperature-dependent features. Some spectral temperature-dependent features are very dependent on the transducer, such as: amplitudes, frequency variations, bandwidth, etc. This dependence is undesirable given that, for the sake of generalisation capacity, features should be only temperature-dependent as much as possible. The temporal echo-shifts or as called previously, the temporal position is a monotonic function of the temperature, and is not intrinsically dependent on the transducer. In addition, it was found that for the same experimental conditions (i.e. for the same temperature change) the temporal echo-shifts are approximately the

same. This means that for a given point in the gel-based phantoms, the same temperature change corresponds approximately to the same temporal echo-shift. Using the temporal echo-shift as the temperature-dependent feature it was possible to perform multi-point and multiple intensity estimations with approximately the same complexity as in the single-point and single-intensity case. In addition, the temporal-echo shifts were extensively applied in the literature (such as in [4]) for estimation, and enabling consistent results. This will also provide trustworthy comparisons with the proposed methodology. The problem with the temporal echo-shifts is that the medium should not move during the experiment. Any small movement originates large variations on the temporal echo-shifts, making impossible their use for estimation. This is a major problem concerning the real application in live specimens, where movements such as respiration and heart beats exist. Movement correction algorithms should be applied to make this feature suitable for estimation. In this thesis, only in-vitro laboratory experiments were performed and consequently movement correction was not needed. Another problem is the appropriate calculation of this feature. Direct computation of this feature results in an insufficient resolution. This can be seen in the temporal position shown in Figure 6.14, as the stair-like behaviour in the descending part. Accurate temperature estimations require the determination of continuous temporal echo-shifts signals from the sampled data. This means that this feature must be estimated instead of being determined directly. In the best scenario, the direct determination leads to a resolution of 20 ns, which is the BSU signals sample rate.

For subsample time-delay estimation the most popular method encompasses the computation of a pattern matching function, which is typically the normalised correlation function between the two sampled signals. Sub-sample time delay estimation is then possible by defining an analytic function based on the sampled pattern-matching function. Normally a parabola is defined in the peak of the discrete

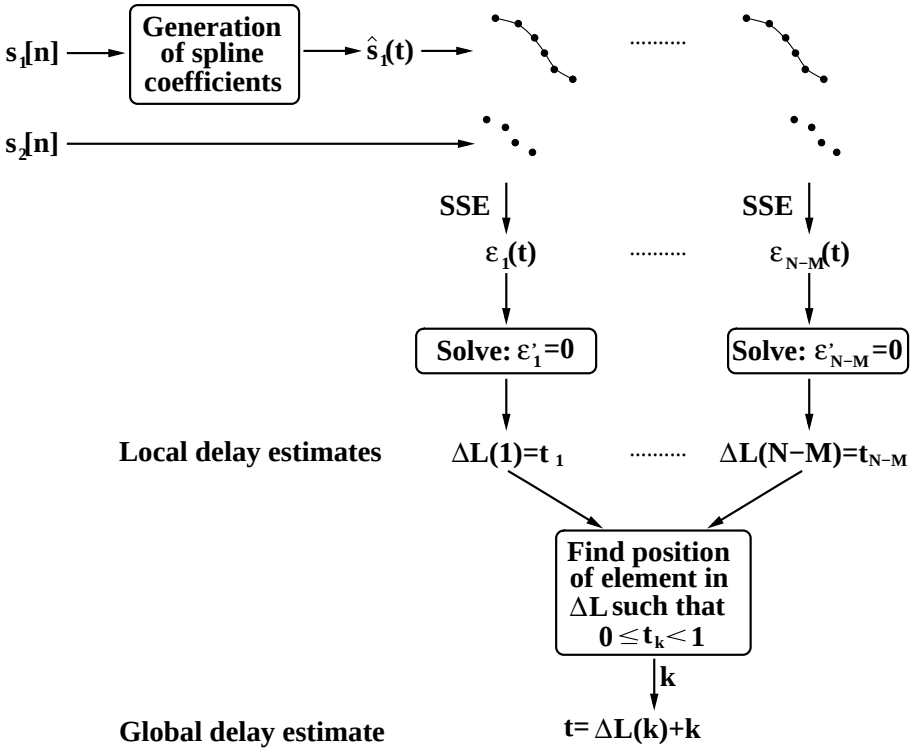


**Figure 6.19:** *Schematic representation of the algorithm applied for time-delay estimation. Where $\varepsilon_i(t)$ is the SSE function associated with the i-th overlap, $\varepsilon_i'(t)$ its correspondent derivative with respect to $t$, and $\Delta L(\cdot)$ the vector containing the local time delay-estimates ($t_i$). This figure was adapted from Fig. 2 in [15].*

pattern-matching function. After this, analytical methods, such as derivatives can be applied to the continuous pattern-matching, to determine the delay between the signals. In [15] a new strategy for time-delay estimation is presented. It is referred and we confirm in our work, that this algorithm offers excellent performance at low computational cost. It is claimed that this approach outperforms significantly other algorithms in terms of jitter and bias over a broad range of conditions. A schematic diagram of this algorithm is presented in Figure 6.19. Considering two sampled signals $s_1[n]$ and $s_2[n]$ with sizes $N$ and $M$, respectively, with $M < N$. The bigger signal $s_1[n]$ is called the reference signal, and is processed to determine an analytical representation, using cubic splines. After this, $s_2[n]$ is overlapped $N - M$ times, and a continuous pattern matching function computed for each overlap ($\epsilon_i(t)$ in Figure 6.19). In [15] it is referred that the sum of the square errors (SSE) was found par-

ticularly convenient as a pattern-matching function. In each overlap the time value that minimises the correspondent SSE function is called the local time-delay estimate. This delay is found by taking the derivative of the SSE function with respect to time, and then setting the result to zero. Concentrating all the local delays in a vector ($\Delta L$), the global time-delay estimate can be found. The global estimate is the element from $\Delta L$ that has a value between 0 and 1, indicating that the true delay is within the tested interval. It is referred in [15] that many values between 0 and 1 can occur, and the true delay is the one correspondent to the minimum SSE. As shown in Figure 6.19, the position of this element in $\Delta L$, i.e. its index, gives a discrete delay estimate and its value indicates the associated subsample delay. In this thesis, the reference signals are the echoes present in the first BSU signal in each experiment trial. The sampled delayed signals are echoes in the BSU signals, collected along each experiment trial, suffering shifts due to temperature. Since the temperature is to be estimated independently at the five points, a rectangular window was applied to isolate each echo, followed by the correspondent echo-shift computation. It was also referred in [15] that the algorithm becomes even more computationally efficient if the same reference signal is used for multiple estimates, which is the case of this thesis. The convention used to compute the temporal echo-shifts is presented in Figure 6.20 a). A temporal echo-shift is considered positive if a particular echo comes sooner in other signals than in the reference signal, and negative otherwise. An example of the computed shifts in comparison with the measured temperature change is presented in Figure 6.20 b) and c), respectively. It is possible to state that a clear, but not linear-relation exists between each other. These temperature change signals were measured using the experimental setup presented in Section 5.4, i.e. from a homogeneous gel-based phantom. For the experimental setup presented in Section 5.5 (the non-homogeneous gel-based phantoms) similar signals were measured, and then similar temporal echo-shifts computed. Figure 6.21

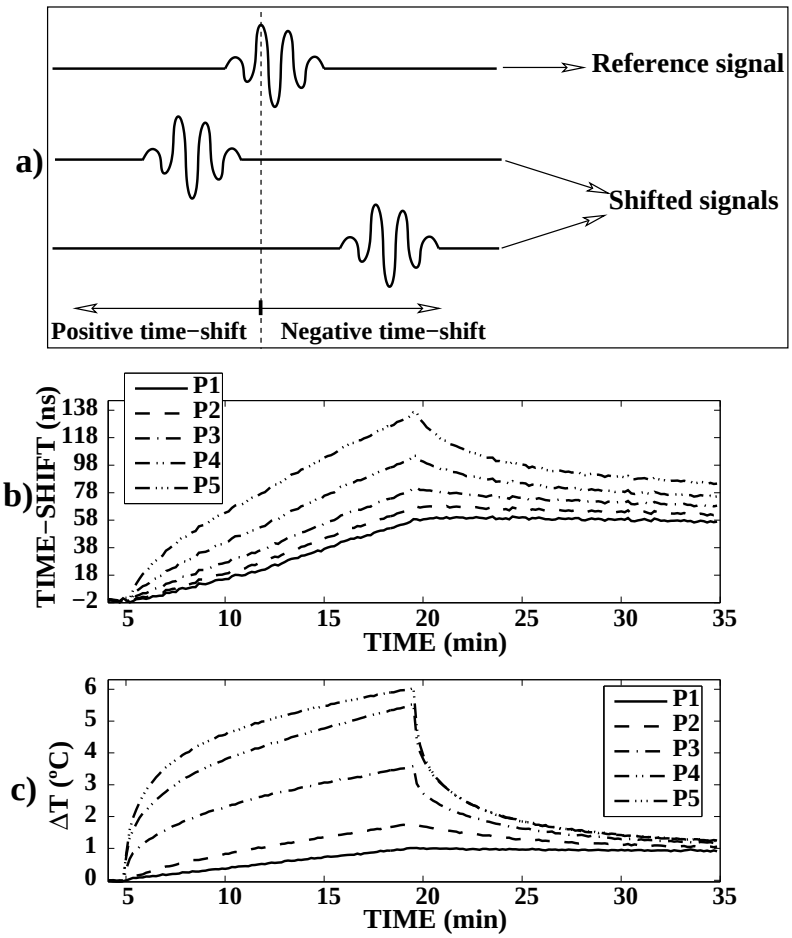


**Figure 6.20:** *Computed temporal echo-shifts in comparison with the measured temperature signals. a) temporal echo-shift computation protocol, b) computed temporal echo-shifts, and c) measured temperature change signals. P1, ..., P5 represent the different points in the medium as explained in Figure 5.10 in Section 5.4.*

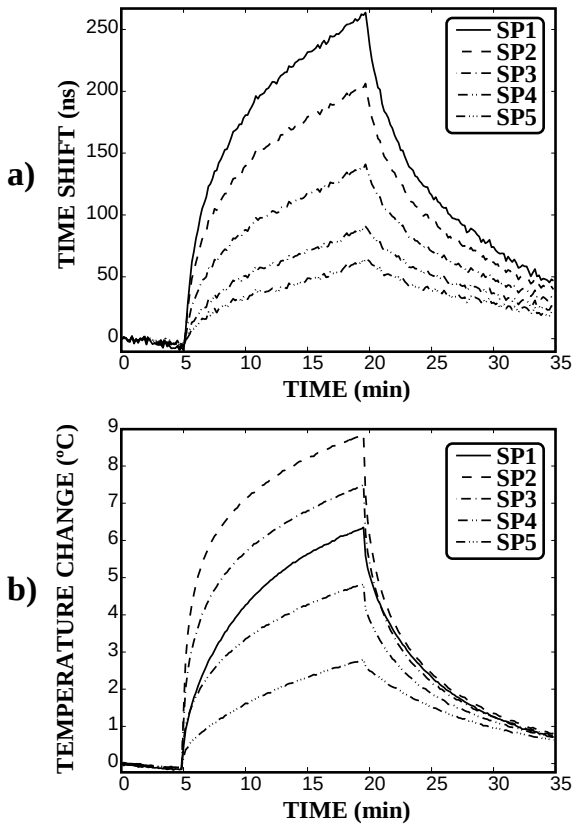


**Figure 6.21:** *Computed temporal echo-shifts in comparison with the measured temperature signals for the non-homogeneous phantom. a) computed temporal echo-shifts, and b) measured temperature change signals. SP1, ..., SP5 represent the different points in the medium as explained in Figure 5.15 in Section 5.5.*

shows the computed temporal echo-shifts, in comparison with the measured temperature for the non-homogeneous gel-based phantom. Looking at this figure, it can be said that the temporal echo-shifts signals are more similar to the temperature signals in this case than for the homogeneous phantom experiment. This is because the relative disposition of the transducers is different, and the emitted and then received acoustic waves travels along paths subjected to different heating patterns. In addition, the media differ between experimental setups. From Figure 6.21 it can be seen that the maximum shift does not match with the maximum temperature, because a cumulative temporal echo-shift was computed. This means that the shift induced in a given ultrasound pulse is dependent on the medium changes along the entire travel path. For example, the shift of the echo originated at SP1 (Figure 5.15) is dependent on the temperature along the entire travel path, and even if the temperature at SP1 does not change, the related temporal shift will be greater or equal to the other shifts on the echoes originated at locations closer to the imaging transducer. In the experiment involving the homogeneous phantom, the transducers are placed in such a way that the point (P5) more faraway from the imaging transducer corresponds to the maximum temperature, and thus to the maximum shift. The linear methods for non-invasive estimation, such as the one published in [4], compute primarily the cumulative temporal echo-shifts and then apply a difference operator along the imaging ultrasound beam path. This is done to assess the locally induced temporal echo-shifts, which are then related with the temperature. This method is explained in detail in Chapter 4.

Afterwards, the computed time-shifts and the measured temperature were smoothed using a causal low-pass Butterworth filter (cut-off frequency=1/20 of the Nyquist frequency, order=2) and normalised to values between -0.5 and 0.5. Some of the computed temporal echo-shifts curves present spurious peaks due to small movements of the experimental setup. These peaks could be removed from the signals by

filtering. The chosen parameters guarantee that the small level electronic noise and these spurious peaks are removed, maintaining the signal's fundamental behaviour. The same filter was applied to the temperature curves, which presented small electronic noise levels, to keep the temporal coherence between both the temperature and temporal echo-shifts curves. For the remaining of this thesis, the following convention was used:

- normalised and filtered temporal echo-shifts–$TES$;
- normalised and filtered temperature change–$\Delta T$.

After the temporal echo-shift computation, and consequent filtering and normalisation, the different $TES/\Delta T$ signal pairs were saved in separate files. The separation was performed according to the related intensity and spatial point. As referred in Section 5.4, six trials considering the same therapeutic ultrasound (TUS) device intensity were performed. This means that 24 (6 trials $\times$ 4 intensities) files of raw data were measured. From each file it was possible to extract five $TES/\Delta T$ signal pairs, corresponding to the five points under study. Each $TES$ and $\Delta T$ signal contains 210 samples, given that a sampling rate of 10 s was applied during 35-min experiment time. After data separation a total of 120 (24 raw data files $\times$ 5 points) files (subsets) for model's training, test and validation were obtained.

For the non-homogeneous phantom case, six trials were also performed, but eight intensities were considered instead of six, thus the number of available files was 240 (subsets). For both the homogeneous and non-homogeneous estimation environments four experimental trials were randomly selected for training, one for test, and another for validation. For the homogeneous case, a variety of studies having in mind the assessment of both the spatial and intensity generalisation performance were performed. Depending on the study, the number of points and intensities (number of subsets) considered for training varies. In the next chapter, the number

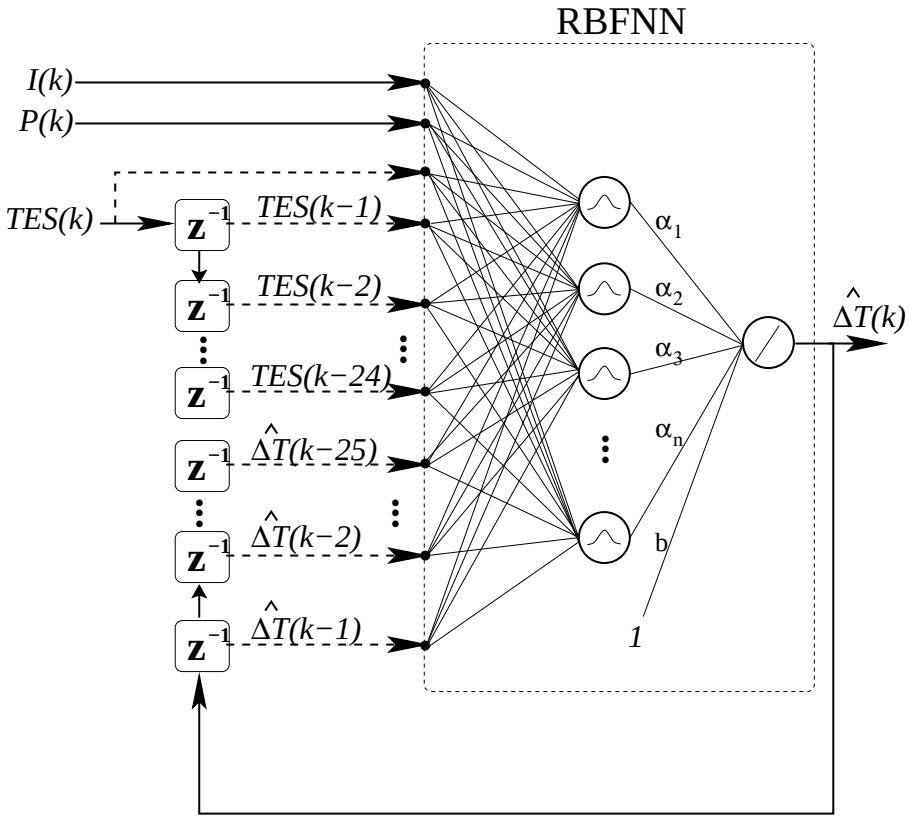


**Figure 6.22:** *Generic structure based on RBFNN, applied for multi-point and multi-intensity non-invasive estimation on gel-based media. The dashed arrows represent inputs that should be selected during the structure optimisation process, while the full-arrows represent inputs that are present in all the structures. The symbol* $\mathbf{z}^{-1}$ *represents the ideal unit-delay operator.*

of subsets employed for training, test, and validation is explained for each particular case.

Using the processed data two model structures were applied. One based on the extensively used radial-basis-functions neural networks (RBFNNs), and the other based on the adaptive-network-based fuzzy inference systems (ANFISs). The input information considered for both structures was the past lags of $TES$ and $\Delta T$. The maximum considered lag was 25, because in Sub-section 6.3.1 this value was calculated and consistent results were obtained for both estimation in liquid and gel-based media. The generic structure based on RBFNN is presented in Figure 6.22. Again the MOGA was applied to optimise this generic structure. The number of

neurons was defined as an integer in the interval [8,20], and a maximum of 20 inputs was considered. With these structure boundaries the possible number of structures is 1.5E15, justifying the application of a genetic search. As in the structure for two-point estimation, the dashed arrows represent inputs that may be selected by the MOGA, while the full arrows represent inputs present in all the models. The fixed inputs in Figure 6.22 discriminate at which intensity ($I(k)$) and spatial point ($P(k)$) the temperature was to be estimated. The training was again performed by the methodology that involves the LM and the separability of the parameters. The model performance descriptors (objectives) considered for minimisation were basically the same applied previously for RBFNN-based structures, with some adaption for multi-intensity and multi-point estimation. The objectives considered were:

- root mean square error in training–$RMSE_{TR}$;
- maximum mean square error in all the test subsets–$MRMSE_{TE}$;
- maximum of the maximum absolute multi-step-ahead error in all the test subsets–$MMAE_{TE}$;
- linear weights norm–$LWN$;
- number of parameters–$NP$;
- maximum absolute value of the error autocorrelation–$R_{ee}$;
- maximum absolute value of the cross-correlation between the inputs and the error–$R_{ue}$.

The $RMSE_{TR}$ is the standard one-step-ahead error obtained at the end of the training. In Table 6.3 two objectives related to the root mean square error in the test set were considered, one for each considered point. When multiple points and multiple intensities are considered, the number of objectives should not increase

with the number of operating points. This would result in such a high dimensional objective space turning the MOGA convergence very slow, or in the worst case impossible due to the enormous number of objectives to minimise simultaneously. Thus, in this multi-point and multi-intensity estimation attempt, the maximum of the root mean square one-step-ahead errors in the test set ($MRMSE_{TE}$) was considered to be minimised. This error is obtained by computing the $RMSE$ in all the test subsets, and then selecting the maximum. This single measure is an upper-bound, accommodating as so all the errors.

For multi-point temperature estimation the maximum root mean square error in all the estimation steps $MRMSE_{ES}$ was substituted by the maximum absolute multi-step-ahead error in the test set ($MAE_{TE}$). This error was computed by estimating a complete temperature waveform, instead of only 60 steps. Then a complete error signal was obtained and the maximum absolute value considered to be minimised. This error is a particular case of the $MRMSE_{ES}$, when the number of samples in the test sequence is equal to the number of estimation steps (N=NE). As in multi-point estimation, multiple test sequences exist (subsets), the maximum absolute multi-step-ahead errors in all the test subsets were computed and the maximum of them considered as the objective to minimise ($MMAE_{TE}$). The consideration of $MMAE_{TE}$ instead of $MRMSE_{TE}$ was to reduce the computational cost of computing a multi-step-ahead error descriptor, and to consider the commonly used error condition for hyperthermia/diathermia, which is a maximum absolute error inferior to 0.5 $^{o}$C. The other model performance descriptors are defined in the same way as done previously. It should be mentioned that for estimation in non-homogeneous media, $R_{ee}$ and $R_{ue}$ were not applied. It is reported in [13] and found in this thesis, during the development of models for the multilayer medium, that as the models were trained as one-step-ahead estimators, and the model-validity tests efficacy depends mainly in the one-step-ahead training error,

**Table 6.4:** *Goals and priorities defined for the objectives applied in the optimisation of RBFNN- and ANFIS-based structures for multi-point and multi-intensity temperature estimation in homogeneous and non-homogeneous gel-based phantoms.*

| Objective | Goal | | Priority |
|---|---|---|---|
| | (homogeneous media) | (non-homogeneous media) | |
| $RMSE_{TR}$ | 0.043 °C | 0.15 °C | 1 |
| $MRMSE_{TE}$ | 0.43 °C | 0.48 °C | 2 |
| $MMAE_{TE}$ | 0.43 °C | 0.48 °C | 2 |
| $LWN^{\dagger}$ | 2.0 | 2.0 | 1 |
| $NP$ | 200 | 200 | 1 |
| $R_{ee}$ | 2.10E-2 | ND | 1 |
| $R_{ue}$ | 2.10E-2 | ND | 1 |

ND–Not defined
†–Not defined for the ANFIS structures.

these tests bias the MOGA search towards better one-step-ahead estimators, which is not desired for non-invasive estimation. The applied objectives goals and priorities for the homogeneous and non-homogeneous phantoms are presented in Table 6.4. In the same way as for the previously reported models, the objectives related with the generalisation goals were defined with a higher priority. In this table, the error goals are related with the absolute data, in order to improve understanding. The goals defined for the $RMSE_{TR}$ envisage preventing this objective from extreme minimisation, as explained previously. The test errors were defined taking into account the accepted precision threshold defined for diathermia/hyperthermia, which is 0.5 °C. The goals are defined a little bit bellow the threshold to guaranty that, in validation, the maximum of the maximum absolute multi-step-ahead error does not exceed the threshold. Again, the $LWN$ goal was defined taking into account the normalisation employed and the maximum number of neurons; the goal for $NP$ was chosen after several attempts and observing that proper models can be obtained with the complexity inferior to 200 parameters. The goal defined for the objectives related with the model-validity tests is the confidence interval (CI) so far presented.

In addition to the MOGA structure optimisation, a simpler method was also ap-

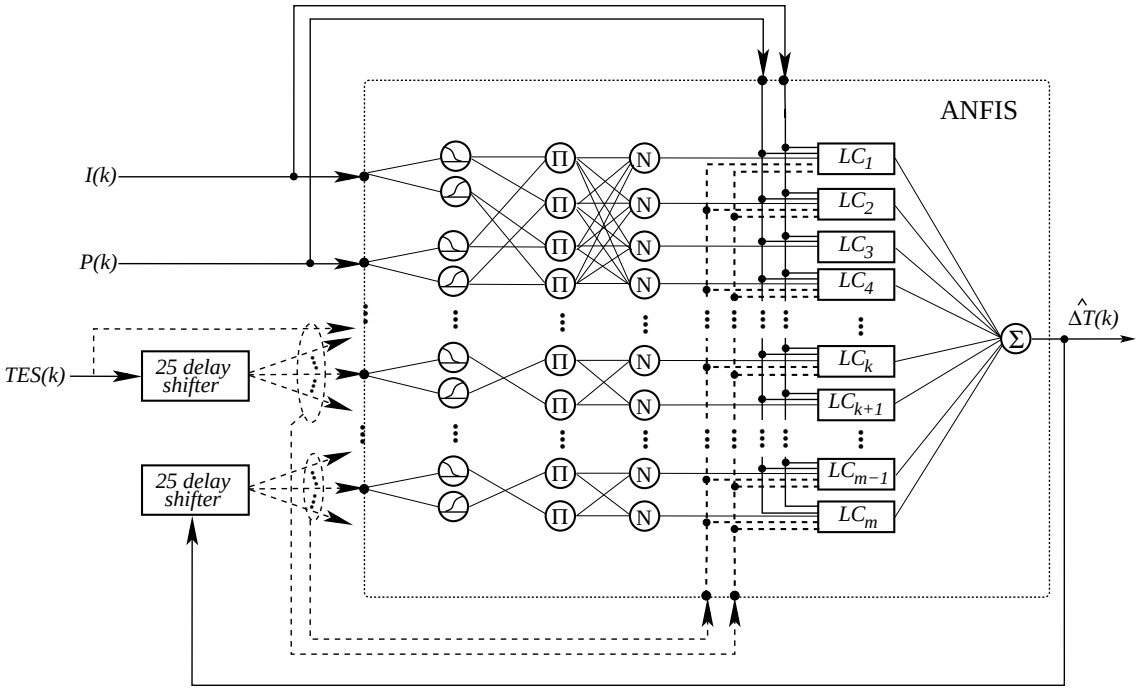


**Figure 6.23:** *Generic ANFIS-based structure. The full arrows represent permanent inputs related with the intensity and position. The dashed arrows represent inputs that may be selected by the MOGA. The "25 delay shifter" receives the signals $TES(k)$ and $\Delta T(k)$ and shifts then between 1 and 25 samples, generating inputs information for the models. The $LC_1, \cdots, LC_m$ represent linear combiners which represent the consequent part of the ANFIS models.*

plied. The method was the orthogonal least squares (OLS) [37] applied for RBFNNs training and centre selection. As this method searches only for the appropriate number of centres, the default input set was considered. This set is formed by the inputs: $I(k)$, $P(k)$, $TES(k)$, and $\Delta T(k-1)$. The maximum number of neurons was defined as 20. A $RMSE$ of 0.043 °C was defined as the goal to fulfil.

The ANFIS-based structure applied is presented in Figure 6.23. As explained in Section 2.3, this structure is a representation of a first-order Takagi–Sugeno system. The blocks $LC_1, \cdots, LC_m$ represent linear combiners that implement the consequent part of the Takagi–Sugeno model:

$$o_i = \mathbf{a}_i^T \mathbf{x} + b_i, \qquad i = 1, \cdots, m, \tag{6.11}$$

where $o_i$ is the output of the i-th linear combiner, $\mathbf{a}_i$ and $b_i$ are the linear coefficients related with the i-th rule. $\mathbf{x}$ is the input vector for a particular structure, and $m$ represents the number of rules in a particular system. The same input information, as for the RBFNN-based structures, was considered. This means that 25 past lags of the computed $TES$ signals and of the measured temperature change were considered. The number of parameters for a generic fully-connected first-order ANFIS model is:

$$NP_{ANFIS} = \underbrace{NMF^{NI} \times (NI+1)}_{\text{Linear}} + \underbrace{NI \times NMF \times NP_{fun}}_{\text{Non-linear}}, \tag{6.12}$$

where $NMF$ is the number of membership functions per input, $NI$ is the number of inputs and $NP_{fun}$ is the number of parameters needed to represent each membership function. In the particular case of this work, the standard parameters defined by Matlab® for this kind of systems were considered and include: two membership functions per input ($NMF = 2$), and the generalised "bell function" as the membership function. These functions are defined by three parameters ($NP_{fun} = 3$). To note that the number of parameters increases exponentially with the number of inputs (the well known curse of dimensionality), which limits the real application of the ANFIS models. In the same way as for the RBFNN-based structures, the MOGA was applied to select the appropriate inputs. As the MOGA is only allowed to select the proper inputs, the chromosome of each ANFIS structure is identical to the one applied for the RBFNN-based structures, but without the first position related with the number of neurons. This chromosome was applied for the linear models presented in Sub-section 6.2.2. The difference is that for this ANFIS and RBFNN-based structure, the lookup table considers 50 input term indexes related with the 25 past lags of $TES$ and $\Delta T$. The same objectives and related goals and priorities, with exception of the $LWN$, that were applied for the RBFNN-based structures in homogeneous media were applied for the ANFIS case. The $LWN$

was not minimised because it is not defined in the same way as for the RBFNNs structures, and thus its minimisation has not the same meaning. Given the dimensionality problem of these models, the maximum number of inputs was defined as six. Considering 20 as the maximum number of inputs (as in the RBFNN case), the number of parameters could be 22E6, which will make training virtually impossible. Each ANFIS structure was trained using the standard Matlab® functions which considers the separability of the parameters in linear and non-linear. The non-linear parameters were found by applying the back-propagation system, and the linear ones by using a linear least-squares strategy. The training stops in the point of maximum generalisation, i.e. by using the "early stopping" concept. Of course, the MOGA could have been used to optimise other ANFIS parameters, such as the number of membership per input, but due to the curse of dimensionality it was decided to search only for the appropriate inputs.

# Chapter 7

# Results and Discussion

## 7.1 Introduction

Using the data collected from the experimental setups presented in Chapter 5, and processed as explained in Chapter 6, models for invasive and non-invasive estimation were developed. Figure 7.1 describes the different methodologies studied during this work, indicating also the distribution of the results along this chapter. Comparisons between the extensively applied RBFNN structures optimised by the MOGA algorithm (MOGA+RBFNN) with other linear, non-linear and hybrid structures were performed. In Sub-Section 7.2.1, the MOGA+RBFNN methodology is compared with the performance of an interactively selected linear-based (ARX) structure, for invasive estimation in a liquid medium. In Sub-Section 7.2.2 the RBFNN+MOGA methodology is compared with the performance of a hybrid structure, also for invasive estimation in liquid medium. This hybrid structure is a normal RBFNN with additional linear inputs, called RBFLIC. Proper RBFLIC structures were also found by using the MOGA (MOGA+RBFLIC). In Section 7.3 the results of non-invasive temperature estimations at two points in a glycerine tank (the same liquid medium applied in Section 7.2) are presented. In Sub-section 7.3.1 the results of a two-

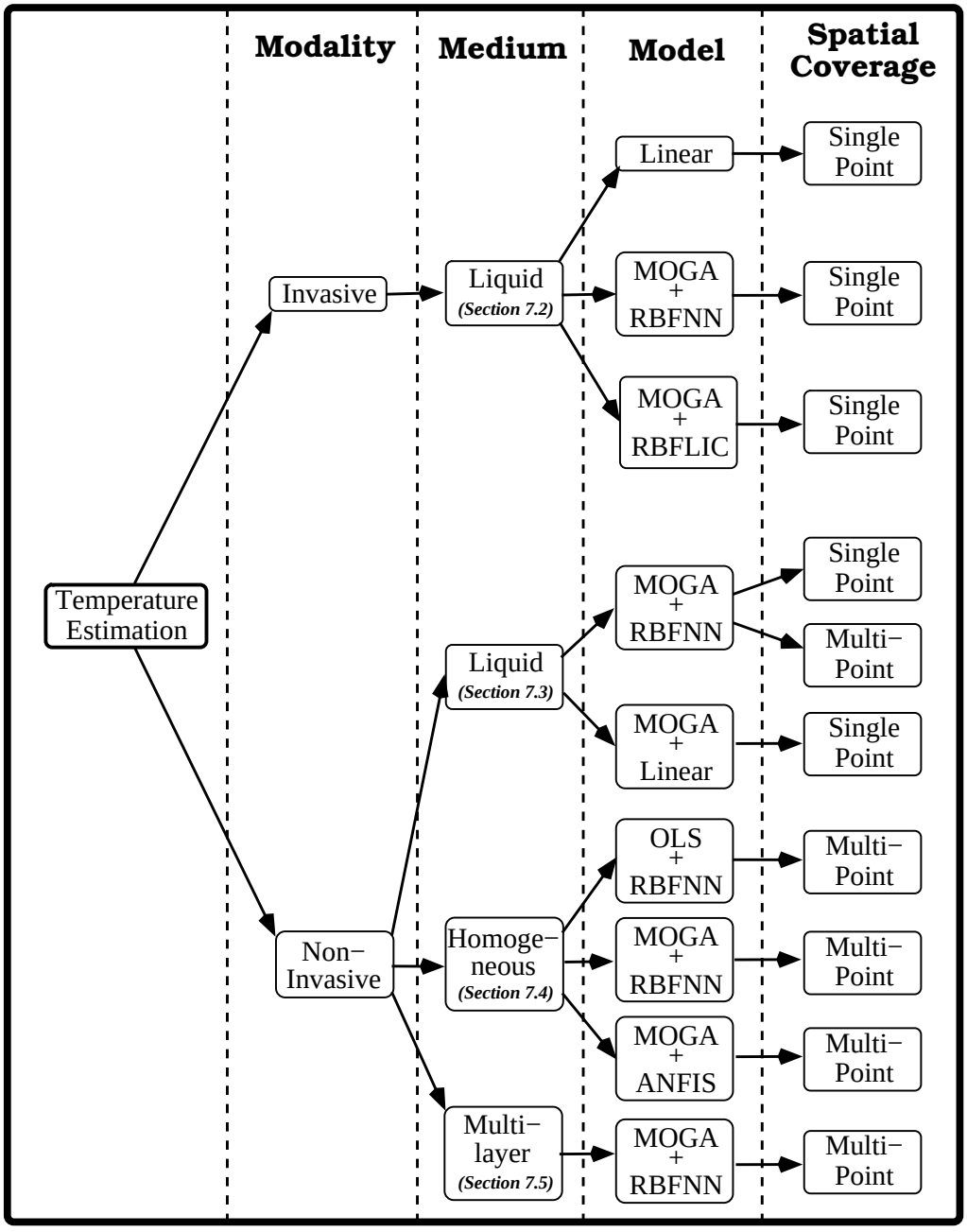


**Figure 7.1:** *Different methodologies applied for invasive and non-invasive estimation, and also the distribution of results and associated discussion in Chapter 7. MOGA–multi-objective genetic algorithms; RBFNN–radial-basis-functions neural network; RBFLIC – radial-basis-functions neural network with linear input connections; OLS–orthogonal least squares algorithm; ANFIS–adaptive-network-based fuzzy inference system; MOGA+RBFNN–RBFNN with structure optimised by MOGA; MOGA+RBFLIC–RBFLIC with structure optimised by MOGA; MOGA+Linear–Linear models with structure optimised by MOGA; OLS+RBFNN–RBFNN with structure optimised and trained by the OLS algorithm; MOGA+ANFIS–ANFIS with structure optimised by MOGA.*

model approach developed for temperature estimation at the two considered points, are presented and discussed. These results were obtained once again by applying the MOGA+RBFNN methodology. For this liquid environment, a comparison between linear (MOGA+Linear) and RBFNN-based structures was also performed, and is presented in Sub-section 7.3.2. Sub-section 7.3.3 presents the results obtained with single models developed to estimate temperature at the two points (instead of developing a model for each point, as presented in Sub-section 7.3.1). In Section 7.4 the results obtained for non-invasive temperature estimations in a homogeneous gel-based phantom, in multiple points and at multiple intensities are reported and discussed. The performance of the MOGA+RBFNN methodology is compared with two other ones: a simpler one, where RBFNNs were trained and their centre selected by applying the orthogonal least squares algorithm (OLS), and a more complex one that involved the adaptive-network-based fuzzy inference system (ANFIS) structures optimised by the MOGA (MOGA+ANFIS). In Sub-section 7.4.1, both the space and intensity generalisation capacity of RBFNN-based structures are discussed. The final results are presented in Section 7.5, which reports the performance of the MOGA+RBFNN methodology while tested for non-invasive temperature estimation in the multilayered gel-based phantom. The capacity of the best attained structures to overcome other operating situations, not used in their construction, was also evaluated and presented in Section 7.5.

To note that the assumptions made in this chapter for the best obtained structures (type of inputs, number of neurons and number of inputs), are relative to the applied MOGA parametrisation, in the runs performed, and to the experimental environment considered, discarding any attempt of generalising the results to other estimation situations. In the following sections, the selection of the best individuals from the preferable set was based on the performance attained in the validation set. This means that the best individual(s) is(are) the one(s) presenting the smallest

error in validation, when compared to other individuals in the preferable set.

## 7.2 Invasive estimation

### 7.2.1 RBFNN- and ARX-based structures

As explained in Sub-section 6.2.1, the first tests involved the application of RBFNN-based structures for invasive temperature estimation. These structures, as all the other RBFNN-based, were optimised by the MOGA. The applied MOGA parametrisation is also explained in Sub-section 6.2.1. MOGA was allowed to perform 100 generations of 100 individuals each. At the end of the 100 generations 11, preferable individuals (PIs) were obtained. The inputs selected for these individuals are presented in Table 7.1. From the analysis of this table, it is possible to realise that

**Table 7.1:** *Structure values of the preferable individuals. The inputs are represented as lags of the input variables ($A_{pc}$ and $T$). The a-priori structure limitations values (Lim.) are also presented.*

| PI | Inputs (lags of $A_{pc}$ and $T$) | | Inp. | Neu. |
|---|---|---|---|---|
| | $A_{pc}$ | $T$ | | |
| 1 | 4,21,25 | 1,3,5,14,32,39,41 | 10 | 6 |
| 2 | 0,2,4,21,27,41 | 1,5,6,11,15,22,23,29,39,46,47 | 17 | 6 |
| 3 | 32,35,36,37,40 | 1,5,6,7,14,15,17,19,20,22,31,35,39,43,45 | 20 | 15 |
| 4 | 19,22,32 | 1,6,7,20,21,28,31,35 | 11 | 4 |
| 5 | 9,32,39,43 | 1,6,12,15,20,21,22,24,35 | 13 | 13 |
| 6 | 6,32 | 1,6,20,25,29,30,34,40,43,44 | 12 | 6 |
| 7 | 0,26 | 1,3,6,9,15,20,28,31,41 | 11 | 6 |
| 8 | 0,8,20,35 | 1,3,4,6,8,9,20,28,35,40,41,46 | 16 | 10 |
| 9 | 0,10,42 | 1,4,5,6,8,9,31,40,42,47 | 13 | 6 |
| 10 | 19,45 | 1,8,13,22 | 6 | 7 |
| 11 | 1,29,34 | 1,4,6,8,13,14,18,23,29,35,38,45,46 | 16 | 4 |
| Lim. | $[0, 47]$ | $[1, 48]$ | $[2, 30]$ | $[2, 15]$ |

- $A_{pc}$–**Amplitude of the principal frequency component**;
- $T$–**Temperature.**

MOGA selects few lags of $A_{pc}$ and many lags of $T$. The input $T(k-1)$ appears in

all the PIs, demonstrating the high dependence of the present temperature on the temperature in the past 10 s. This fact indicates that MOGA converges to a set of models with a physical meaning. The temperature 6 samples in the past ($T(k-6)$), that is 1 min in the past, appears with an absolute frequency of 9, disclosing its importance. The medium lags (between 20 and 40) appear with some frequency, in special the lags 20 and 35 with an absolute frequency of 6 and 5, respectively. The dependence of $T(k)$ on its higher lags is also visible. This affirmation is based on the appearance of lags with values between 39 and 47. The presence of these lags is probably related with the thermal capacity of the glycerine tank. The information of $A_{pc}$ appears in all the PIs, showing its importance on this particular estimation environment. Short and medium term lags are basically the ones selected. The selection of few lags of $A_{pc}$, and many lags of $T$ is because the models were evolved to be well fitted for one-step-ahead estimation. This means that the past measured temperature values were considered at the inputs. The measured temperature is not contaminated by estimation errors, and thus is very useful for estimation. In multi-step-ahead estimations the past temperature values are the estimated ones which are contaminated by estimation errors. Depending on the relation with the other(s) input variables, temperature lags can be selected in equal or inferior number, as it can be seen later on this chapter (Sections 7.4 and 7.5); a constant intensity is applied during the first 60-min heating, in the remaining time the therapeutic device is switched-off and the applied intensity is zero. This means that $A_{pc}$ is approximately zero after 60 min, and the estimation is only based on the past temperatures. In terms of the number of inputs, the PIs have between 6 and 20 inputs, and the majority has between 10 and 17 inputs. The majority of the PIs has a number of neurons less than 10, 6 being the most frequent number. The appropriate choice of the a-priori defined structure limitations is justified by comparison with the obtained structures. Extreme values only appear in PI number 3 for the number of

neurons.

The obtained objectives (performance descriptors) compared with the a-priori defined goals are presented in Table 7.2. The unique model that fulfils the goal

**Table 7.2:** *Objective values presented by the preferable individuals, compared with the a-priori defined goals. (ND=Not Defined). The bold values indicate that the goal was fulfilled.*

| PI | $RMSE_{TR}$ | $RMSE_{TE}$ | $R_{ee}$ | $R_{ue}$ |
|---|---|---|---|---|
| 1 | 9.00E-4 | 3.40E-3 | 1.46E-1 | **9.03E-2** |
| 2 | 6.00E-4 | 4.70E-3 | 1.28E-1 | **5.54E-2** |
| 3 | 8.00E-4 | 1.35E-2 | **8.18E-2** | **9.90E-2** |
| 4 | 9.00E-4 | 3.20E-3 | 1.44E-1 | 1.10E-1 |
| 5 | 9.00E-4 | 7.40E-3 | 1.18E-1 | 1.13E-1 |
| 6 | 9.00E-4 | 8.60E-3 | 1.02E-1 | 1.06E-1 |
| 7 | 7.00E-4 | 3.90E-3 | 1.33E-1 | **6.09E-2** |
| 8 | 6.00E-4 | 8.10E-3 | 1.25E-1 | **6.56E-2** |
| 9 | 6.00E-4 | 4.50E-3 | 1.31E-1 | **6.47E-2** |
| 10 | 9.00E-4 | 9.00E-3 | 1.20E-1 | **7.23E-2** |
| 11 | 9.00E-4 | **2.60E-3** | 1.51E-1 | **7.63E-2** |
| Goal | ND | 3.00E-3 | 1.00E-1 | 1.00E-1 |

- $RMSE_{TR}$–**Root mean square error in the training set**;
- $RMSE_{TE}$–**Root mean square error in the test set**;
- $R_{ee}$ and $R_{ue}$–**Model-validity tests**.

defined for $RMSE_{TE}$, i.e. the objective related with the generalisation performance, is model number 11. In addition, this model also fulfils the goal defined for the $R_{ue}$. There are also models (1,2,4,6,7, and 9) that fulfil one or none of the goals defined, but those that were not fulfilled are close to the desired values, and can be considered also proper models. A common characteristic of these models is the small number of neurons (as presented in Table 7.1), showing that invasive temperature estimation in the conditions presented is well performed with low complexity models.

After the training and structure optimisation process, the preferable models must be evaluated in data never applied, called the validation data. This is a fundamental procedure, in order to evaluate the real capacities of the models, i.e. their generali-

sation performance. In Table 7.3, the root mean square error obtained in validation ($RMSE_{VL}$) is presented. As expected, this table tells that the best individual is

**Table 7.3:** *Temperature root mean square error in the validation set, presented by the preferable individuals.*

| PI | 1 | 2 | 3 | 4 | 5 | 6 | 7 | 8 | 9 | 10 | 11 |
|---|---|---|---|---|---|---|---|---|---|---|---|
| $RMSE_{VL}$ (°C) | 0.32 | 0.31 | 1.00 | 0.22 | 0.39 | 0.29 | 0.26 | 0.42 | 0.26 | 0.51 | 0.10 |

model 11, the unique that fulfilled the goal defined for the test error. This model presents a $RMSE_{VL}$ of 0.1 °C, and a maximum absolute error in validation of 0.2 °C. There are models that present a high error in validation, for example model number 3 which has a $RMSE_{VL}$ of 1.00 °C, showing its bad generalisation capacity. These models should be discarded, as they are only specialised in the training data, and can not overcome different situations. Some of these models present as a characteristic a high number of neurons, which imply more degrees of freedom, improving the possibility of overtraining (specialisation on the training data). For example, models 3 and 8 have 15 and 10 neurons, respectively; they present small $RMSE_{TR}$ values and consequently bad generalisation performance was observed.

As explained in Sub-section 6.2.1, the search for appropriate ARX models for the single-point and invasive estimation was performed in an iterative way by using Algorithm 2 (described in Sub-section 6.2.1). This algorithm iterates over the possible lags of both input variables. As for each variable 48 lags were considered, then $48^2 = 2304$ ARX structures were tested. In Figure 7.2 the percentage of agreement between the estimated temperature and the measured one, in the validation data is presented. It can be seen that the performance tends to increase as more lags are considered. The best model achieved considers 46 lags (na=46) related

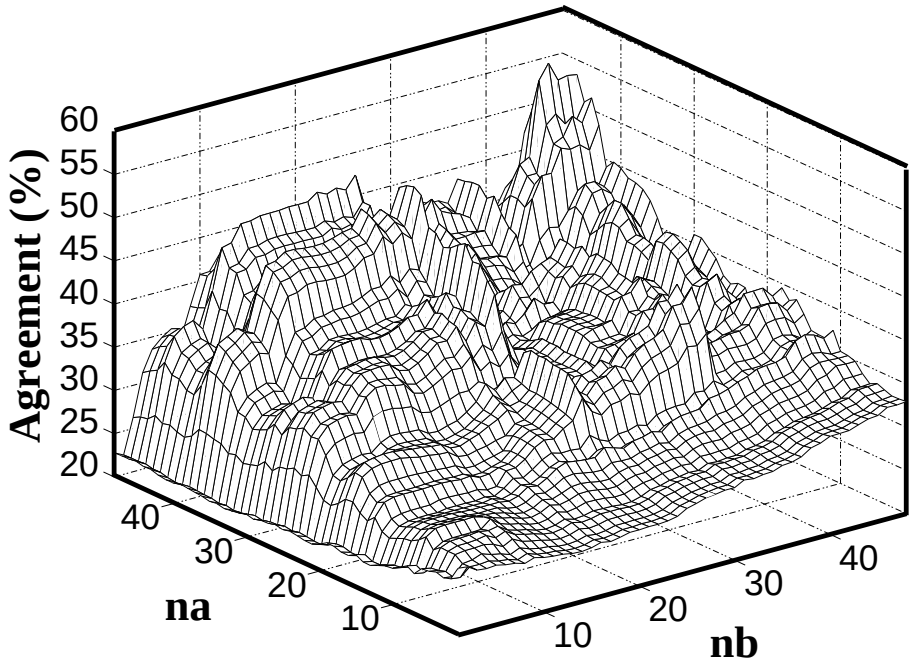


**Figure 7.2:** *Validation performance of the different ARX tested, expressed as percentage of agreement between the estimated and the desired temperature.* **na** *and* **nb** *are the number of lags associated with $T$ and $A_{pc}$, respectively.*

with temperature, and 45 (nb=45) related with $A_{pc}$. This means that the inputs of this model are: $T(k-1)$, $T(k-2)$, $\cdots$, $T(k-46)$, $A_{pc}(k)$, $A_{pc}(k-1)$, $\cdots$, $A_{pc}(k-44)$. The best ARX present a $RMSE_{VL}$ of 1.00 °C and a maximum absolute error of 2.1 °C. The measured versus the estimated temperature by both the best RBFNN- and ARX-based structures is presented in Figure 7.3. Comparing the error in validation, presented by them, and looking at Figure 7.3, it can be stated that temperature, in the environment considered for invasive estimation, could only be successfully estimated by non-linear methods, such as RBFNN-based models. The best RBFNN-based model attains an increase in performance of one order of magnitude in comparison with the best ARX. This increase justifies the time spent in the training and structure optimisation of the RBFNN-based models. Later on this chapter (in Sub-section 7.3.2) a more trustworthy comparison is presented, between RBFNN- and linear-based models for non-invasive estimation. Both model's structures were optimised by the MOGA, improving comparison.

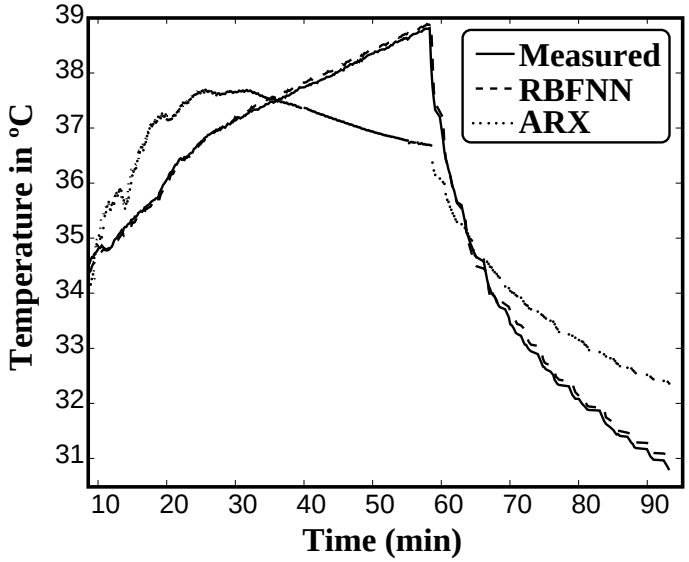


**Figure 7.3:** *Measured, and estimated temperatures by the best obtained ARX and RBFNN-based structures.*

### 7.2.2 RBFNN- and RBFLIC-based structures

As referred in Sub-section 6.2.1, radial-basis-functions neural networks (RBFNNs), and radial-basis-functions neural networks with linear input connections (RBFLICs) based structures were also applied for single-point invasive temperature estimation. The experimental conditions used were the same as in the previous section. In addition to the information of the amplitude of the principal frequency component of the intensity spectrum ($A_{pc}$), the information of its first ($A_{1h}$) and second ($A_{2h}$) harmonics was also considered. The multi-objective genetic algorithm was applied during 100 generations of 100 RBFNN- and RBFLIC-based structures.

#### RBFNN modelling

The MOGA run applied for RBFNN-based structures, yielded a preferable set of 15 individuals, i.e. 15 preferable individuals (PIs) were obtained. From these individuals, the best one presents a $RMSE_{VL}$ of 0.07 $^{o}$C, a maximum absolute error of 0.09 $^{o}$C, a mean squared error of 0.0049 ($^{o}$C)$^2$, and an average error of -0.0184 $^{o}$C. This model has 6 neurons, and a linear-weights norm of 4.76. The MOGA objectives for

**Table 7.4:** *Objective values presented by the best RBFNN and RBFLIC models. The a-priori defined goals and priorities for these objectives are also presented. The bold values mean that the associated goal was fulfilled.*

| | RBFNN | RBFLIC | Goal | Priority |
|---|---|---|---|---|
| $RMSE_{TR}$ | 9.00E-4 | 9.00E-4 | - | 0 |
| $RMSE_{TE}$ | **1.60E-3** | **1.40E-3** | 3.00E-3 | 2 |
| $NP$ | **61** | **69** | 70 | 1 |
| $R_{ee}$ | **9.21E-2** | 1.24E-1 | 9.70E-2 | 1 |
| $R_{e^2e^2}$ | **1.56E-2** | **1.54E-2** | 9.70E-2 | 1 |
| $R_{(ye)e^2}$ | 9.87E-2 | 1.07E-1 | 9.70E-2 | 1 |
| $R_{(ye)u^2}$ | **7.62E-2** | **8.48E-2** | 9.70E-2 | 1 |
| $R_{ue}$ | **8.69E-2** | **9.33E-2** | 9.70E-2 | 1 |
| $R_{u^2e^2}$ | 1.08E-1 | 1.10E-1 | 9.70E-2 | 1 |
| $R_{u^2e}$ | **7.62E-2** | **8.60E-2** | 9.70E-2 | 1 |
| $R_{e(eu)}$ | 1.05E-1 | 1.26E-1 | 9.70E-2 | 1 |

- $RMSE_{TR}$–**Root mean square error in the training set**;
- $RMSE_{TE}$–**Root mean square error in the test set**;
- $NP$–**Number of model parameters**;
- $R_{ee}$, $R_{e^2e^2}$, $R_{(ye)e^2}$, $R_{(ye)u^2}$, $R_{ue}$, $R_{u^2e^2}$, $R_{u^2e}$, and $R_{e(eu)}$ –**Model-validity tests**.

this individual are presented in Table 7.4. Looking at these values, we can state that this individual fulfils 7 out of 10 goals. However, the goals that were not fulfilled are close to the desired values. One important aspect is the fulfilment of the goal for the generalisation error ($RMSE_{TE}$), which was defined with a high priority. Another achievement is the fulfilment of both the goals defined for the generalisation performance and complexity ($NP$), meaning that it was possible to conciliate both accuracy and complexity. The inputs (nonlinear inputs) of this individual are presented in Table 7.5. Analysing this table, we can say that the information from $A_{pc}$ is not of interest for temperature modelling using RBFNNs, due to its absence in the input set. The importance of the first harmonic is marked by the presence of 2 lags. The second harmonic information is important for the temperature modelling, taking into account the great number of inputs related to this variable. The

**Table 7.5:** *Inputs of the best RBFNN and RBFLIC models, represented as lags of the input variables ($A_{pc}$, $A_{1h}$, $A_{2h}$, and $T$)*

| | RBFNN | RBFLIC | | Possible |
|---|---|---|---|---|
| | | Non-Linear | Linear | values |
| $A_{pc}$ | - | 1,7 | 1,2,6,7 | $[0, 19]$ |
| $A_{1h}$ | 1,4 | 7,9,12,15 | 6,8,12,14 | $[0, 19]$ |
| $A_{2h}$ | 5,6,15,18 | 1,3,6,13 | 6,9,17,18 | $[0, 19]$ |
| $T$ | 1,6 | 2,7,11,17 | 1,5,7,8,12,14,16,17 | $[1, 20]$ |

- $A_{pc}$–**Amplitude of the principal component**;
- $A_{1h}$–**Amplitude of the first harmonic**;
- $A_{2h}$–**Amplitude of the second harmonic**;
- $T$–**Temperature**.

past memory of the system (past temperature values) is also relevant for the model. The physical validity of the system can be demonstrated by the presence of the first lag of the temperature variable ($T(k-1)$), showing that the present temperature is dependent of the temperature in the previous 10 seconds. The temperature in the past 60 seconds is also important for the estimation of the present temperature ($T(k)$), given the presence of $T(k-6)$. The presence of this lag probably reflects the thermal capacitance of the glycerine tank.

Figure 7.4 shows the absolute frequency of the RBFNN-based structures inputs. Analysis of this figure enables stating that all the RBFNN-based structures in the preferable set do not have lags of $A_{pc}$, showing that its absence in the best individual is not accidental. The $1^{st}$ lag of $A_{1h}$ ($A_{1h}(k-1)$) appears in 13 of the 15 neural networks demonstrating its importance for the model. The $6^{th}$ lag of $A_{2h}$ ($A_{2h}(k-6)$), as well as the $1^{st}$ lag of $T$ appears in all preferable neural networks (NNs). The previous statements, and the fact that all the NNs have 6 neurons, demonstrate the MOGA convergence to a group of individuals that are proper for the estimation environment applied. The a-priori structure limitations imposed (i.e.

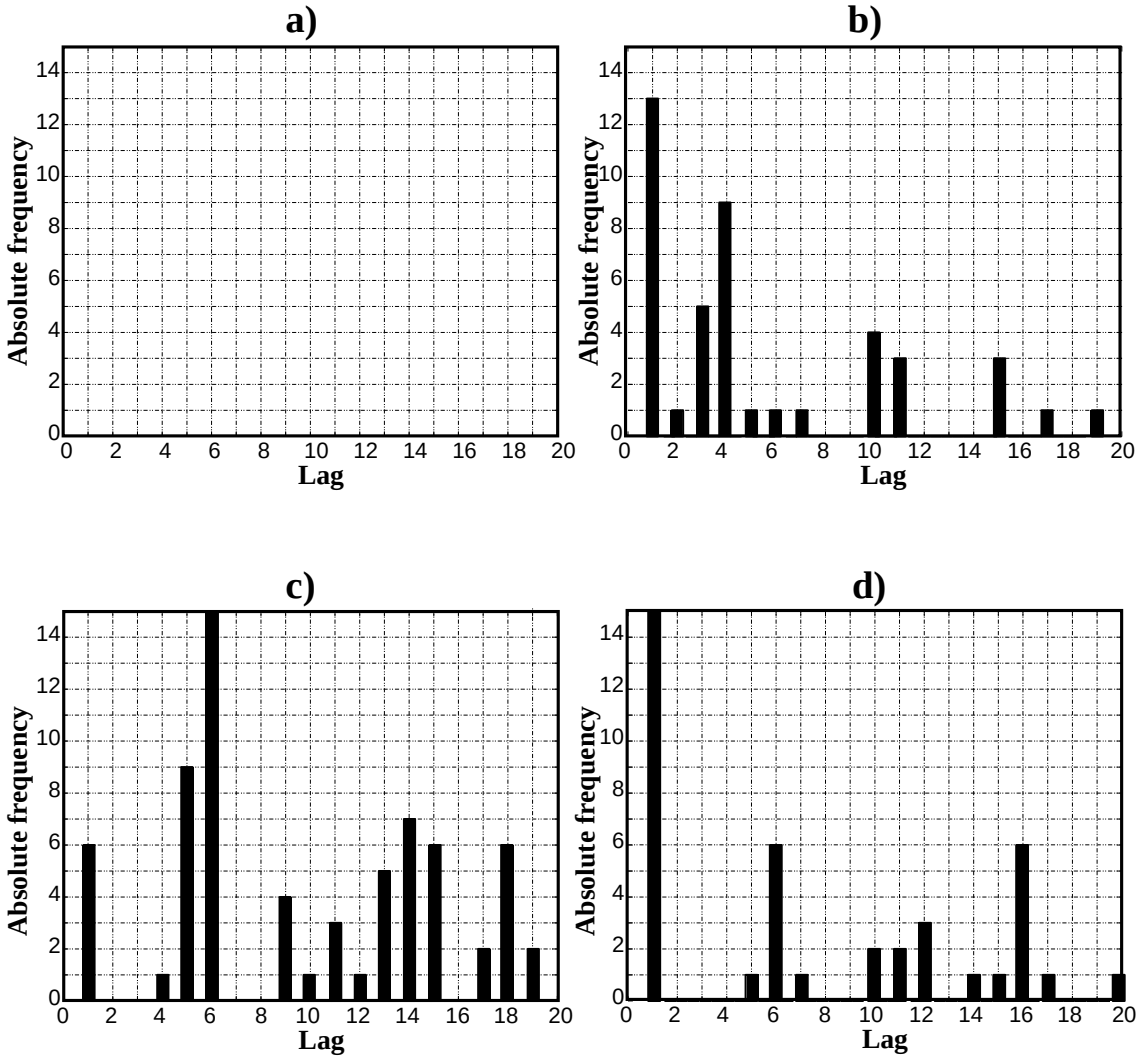


**Figure 7.4:** *Absolute frequency of the preferable RBFNN-based structures. The inputs related with $A_{pc}$ are presented in a), with $A_{1h}$ in b), with $A_{2h}$ in c), and with $T$ in d).*

the possible number of inputs and neurons, and the maximum lag for the input variables), were appropriated, given that the extreme values only appear for the maximum lag in three preferable individuals. The number of inputs and neurons never assume extreme values for the preferable models. Comparing the results with those presented in Sub-section 7.2.1 for the RBFNN-based structures, it can be said that the consideration of the amplitude of $1^{st}$ and $2^{nd}$ harmonics of the intensity spectrum, with the additional objectives introduced, leads to a reduction of the maximum absolute error from 0.2 °C to 0.09 °C. In addition, the information of the fundamental component ($A_{pc}$) is completely discarded from the preferable set in this stage of the work, reflecting that for the applied estimation environment, temperature modelling is better achieved when only information of $A_{1h}$, $A_{2h}$, and $T$ is considered as inputs.

### RBFLIC modelling

The MOGA applied to RBFLIC yielded a preferred set of 20 individuals. From these individuals, the best one presents a $RMSE_{VL}$ of 0.054 °C, a maximum absolute error of 0.12 °C, a mean squared error of 0.0032(°C)$^2$, and an average error of -0.0047 °C. This model has 3 neurons, and a weight ($||\{\alpha_i\}_{i=1}^{n} + \{\lambda_k\}_{k=1}^{m}||$) norm of 0.92. The objective values for this individual are also presented in Table 7.4. This individual fulfils 6 out of 10 objectives defined. In the same way as for RBFNN-based structures, the objectives which are not fulfilled are close to the defined goal. The linear and non-linear inputs of the best individual are presented in Table 7.5. From this table it can be stated that the information of $A_{pc}$ is of reduced importance as a non-linear input, since only two lags ($A_{pc}(k-1)$ and $A_{pc}(k-7)$) appeared, as for the RBFNN case. However, the information of this variable is more important as a linear input. The information of $A_{1h}$ has the same relevance at both nonlinear and linear inputs, given the same number of lags. In addition, those lags are in

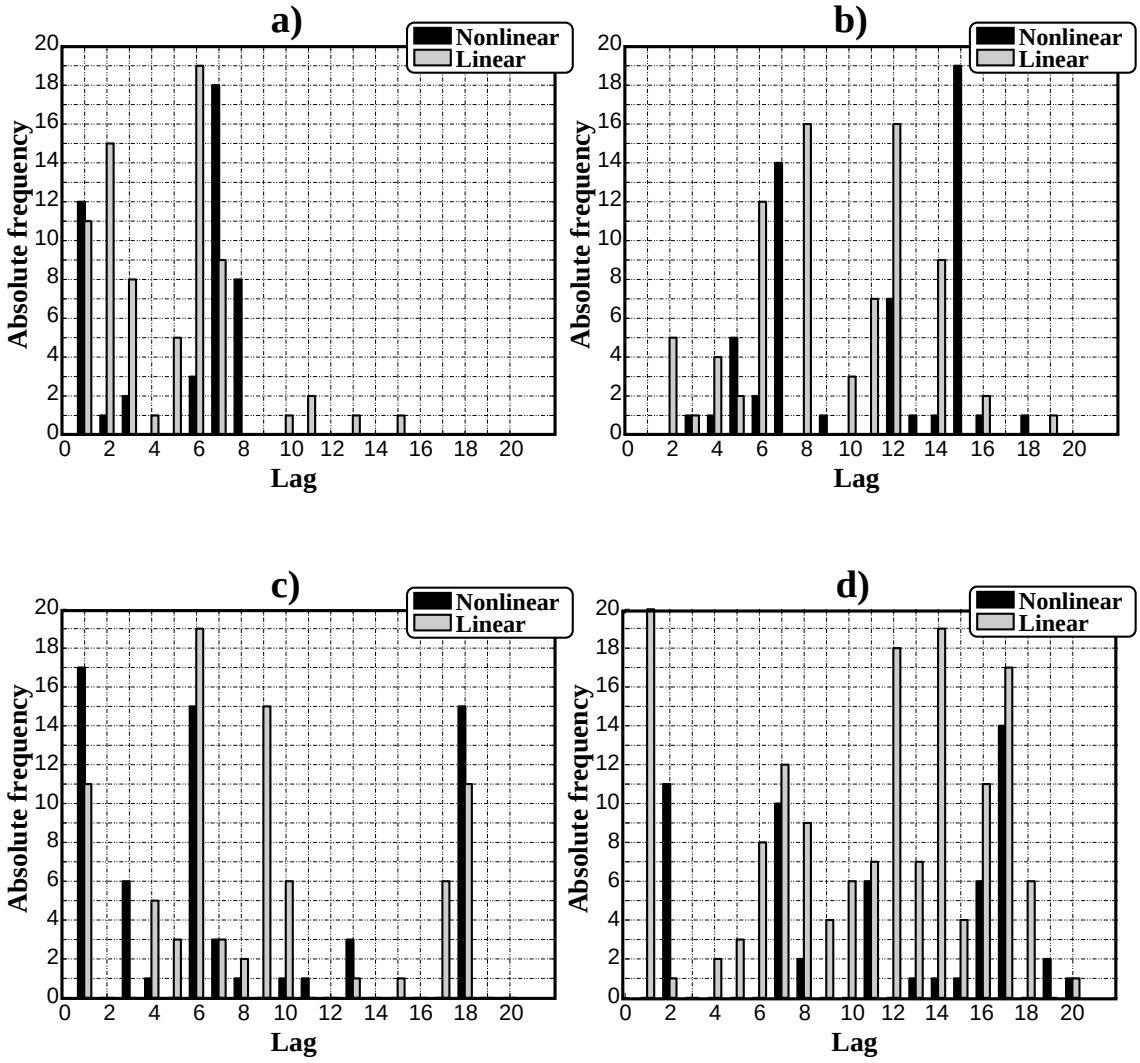


**Figure 7.5:** *Absolute frequency of the preferable RBFLIC-based structures. The inputs related with $A_{pc}$ are presented in a), with $A_{1h}$ in b), with $A_{2h}$ in c), and with $T$ in d).*

the same range, between 6 and 15, and are almost mutually exclusives. The past values of $T$ (memory of the system) appear as linear inputs in many cases. The physical validity of the best model can be viewed by the presence of the $1^{st}$ lag of $T$ (temperature value in the past 10 sec.) as a linear input, and the $2^{nd}$ lag of $T$ as a nonlinear input. The medium and higher lags of the estimated variable are also important in the models, i.e. the medium term and long term memory of the system.

Fig. 7.5 presents the absolute frequency, of the nonlinear and linear inputs assigned to the preferable RBFLIC-based structures. From the analysis of this figure it can be said that the lags between 1 and 8 of $A_{pc}$ (short lags) are of great importance for the models, specially the $6^{th}$ lag as linear input, and the $7^{th}$ lag as a nonlinear input. In the case of $A_{1h}$, the important information is related with the lags between 6 and 15, that is the medium lags. Lag 15 appears in 19 of the 20 preferable individuals as nonlinear input, indicating that the information of this variable, 150 seconds in the past, is important for the models, and it is nonlinearly related with $T(k)$. In the same way, the $6^{th}$ lag of $A_{2h}$ ($A_{2h}(k-6)$) appears also in 19 of the 20 preferable individuals as linear input. This lag is also important as a nonlinear input, given its presence in 15 preferable individuals. The lags 1 and 18 are also relevant as linear and nonlinear inputs, as well as lag 8 as linear input. The past memory of the system (lags of $T$), as expected, is of great importance as linear inputs, specially lags 1, 12, 14, and 17. The presence of 20 preferable individuals with lag 1 of $T$ proves the physical coherence of the search system. The other lags show that the temperature at 120, 140, and 170 seconds in the past is also important for the estimation of $T(k)$, once probably reflecting the thermal capacitance of the glycerine tank.

The presence of high absolute frequency values for some input terms (for example $T(k-1)$, $T(k-14)$, $A_{pc}(k-6)$, $A_{1h}(k-15)$, and $A_{2h}(k-6)$), the presence of 8 models with 3 neurons, and 6 models with 5 neurons in the preferable set, indicates that MOGA converges to a group of individuals appropriate for the task. Again the structure limitations imposed showed to be appropriate, given that extreme values only appear for 3 PI's.

**RBFNN vs RBFLIC performance**

Comparing both approaches hereby presented we may conclude that the best RBFLIC model presents an increase in performance of approximately 22%, in agreement with the $RMSE_{VL}$ attained. The mean squared error is reduced from 0.0049 $(^{o}C)^2$ in the RBFNN case to 0.0032 $(^{o}C)^2$ in the RBFLIC case. The average error is also better in the RBFLIC case, a reduction of approximately 74% is obtained. However, the maximum absolute error is better in the RBFNN case, in about 0.1 $^{o}C$. In terms of model's complexity (NP), the best RBFLIC model presents 69 parameters, against 61 in RBFNN case. As a consequence the best RBFNN is less complex than the best RBFLIC in 8 parameters. This increase in RBFLIC complexity is related to the great number of linear inputs, given the reduced number of neurons in this model. In general, RBFLIC structures reached better results for this single-point and invasive estimation trial. In fact the $RMSE_{VL}$ in the RBFLIC preferable set presents a medium value of 0.07 $^{o}C$ with variance $6.21 \times 10^{-6}$ $^{o}C$, against 0.1 $^{o}C$ with variance $9.20 \times 10^{-6}$ in the RBFNN preferable set. This implies that the results achieved with the hybrid approach are in general 28% better. The success of the hybrid approach can be explained by the direct feeding of the past measured temperature values directly at the inputs. Of course the non-linear part plays an important role, given that a pure linear structure (as presented previously) could not bring consistent results. However, the RBFLIC-based structures were only better for this initial one-step-ahead estimation trial. Their evaluation in a multi-step-ahead environment presented worse performance than the RBFNN-based models. In the RBFLIC case, the estimation error is directly fed at the output (without any processing), and it tends to assume very high values. As it will be seen later on this chapter, using RBFNN-based structures, the fed-back estimation error is non-linearly processed and the overall error assumes controlled and accepted levels.

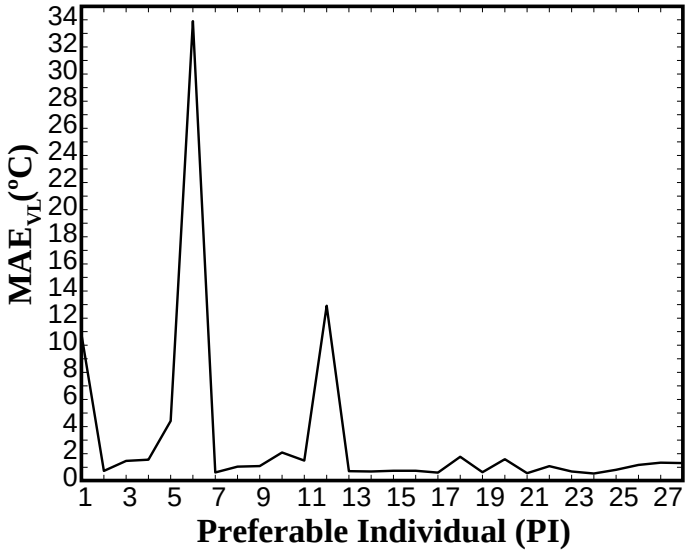


**Figure 7.6:** *Maximum absolute multi-step ahead error obtained in the validation data ($MAE_{VL}$), for the preferable individuals developed for estimation at 24-mm distance.*

## 7.3 Non-invasive estimation: liquid medium

### 7.3.1 RBFNN-based structures for single-point estimation

Using the data collected from the experimental setup presented in Figure 5.4, processed as explained in Sub-section 6.2.2, and using the generic RBFNN-based structure presented in Figure 6.15, non-invasive single-point temperature estimators were developed. Different models were developed for the data collected at 24 and 48 mm. As explained in Sub-section 6.2.2 the MOGA was applied to search for appropriate model structures for the proposed estimation environment.

The MOGA applied to the data collected at 24 mm yielded a set of 28 preferable models. As a fundamental step, the assessment of the appropriateness of these preferable individuals (PIs) was based on the performance attained in the unseen data sequence collected at 2 $W/cm^2$ , i.e. the validation data. In Figure 7.6, the maximum absolute multi-step ahead error in the validation set ($MAE_{VL}$) is presented for the PIs developed to estimate temperature at 24 mm. The $MAE_{VL}$ was obtained

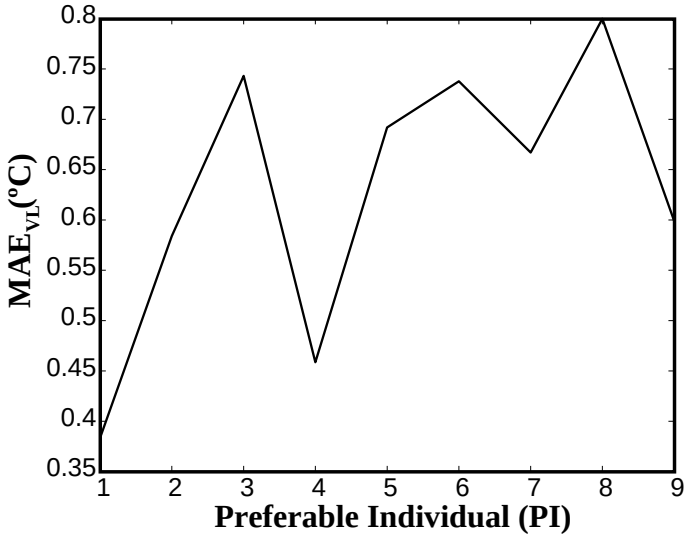


**Figure 7.7:** *Maximum absolute multi-step ahead error obtained in the validation data ($MAE_{VL}$), for the preferable individuals developed for estimation at 48-mm distance.*

by considering the estimation of the complete temperature waveform (instead of 60 steps at each time, considered for the computation of $MRMSE_{ES}$) chosen for validation, and then computing the maximum absolute value of the complete error sequence. Figure 7.6 shows that there are PIs that present a very high $MAE_{VL}$ value, demonstrating their worse generalisation capacity. From the total PI set, 14 models present a $MAE_{VL}$ inferior to 1 °C. The unique model that showed a $MAE_{VL}$ inferior to 0.5 °C was chosen as the best model. This model presents a $MAE_{VL}$ of 0.49 °C, an average error of 0.04 °C, and a mean squared error of 0.013 (°C)$^2$. On the other hand, the run applied to the data collected at 48 mm yielded a preferable set composed by 9 PIs. All of these models presented a $MAE_{VL}$ inferior to 1 °C, and two of them present a $MAE_{VL}$ inferior to 0.5 °C, as it can be seen in Figure 7.7. The best individual is PI #1 which presents a $MAE_{VL}$ of 0.38 °C, an average error of 0.0072 °C, and a mean squared error of 0.0071 (°C)$^2$. The objective values presented by the two best individuals (one for each distance), as compared with the a-priori defined goals and priorities are presented in Table 7.6. Looking at this table it is possible to realise that the best model obtained for the 24-mm distance fulfils 4

**Table 7.6:** *Objectives and related goals and priorities for the best models obtained for the two distances considered. The values in bold means that the associated goal was fulfilled.*

| Objective | Estimation distance | | Goal | Priority |
|---|---|---|---|---|
| | 24 mm | 48 mm | | |
| $RMSE_{TR}$ | 1.60E-3 | 1.10E-3 | - | 0 |
| $RMSE_{TE}$ | **1.90E-3** | **1.00E-3** | 2.00E-3 | 2 |
| $MRMSE_{ES}$ | **2.70E-3** | **1.30E-3** | 3.00E-3 | 2 |
| $LWN$ | **1.08** | **1.59** | 2 | 1 |
| $NP$ | 166 | 169 | 100 | 1 |
| $R_{ee}$ | **6.02E-2** | **7.01E-2** | 7.41E-2 | 1 |
| $R_{ue}$ | 9.29E-2 | **6.87E-2** | 7.41E-2 | 1 |

- $RMSE_{TR}$–**Root mean square error in the training set**;
- $RMSE_{TE}$–**Root mean square error in the test set**;
- $MRMSE_{ES}$–**Maximum root mean square error in the all the estimation steps**;
- $LWN$–**Linear weights norm**;
- $NP$–**Number of parameters**;
- $R_{ee}$ and $R_{ue}$–**Model-validity tests**.

out of 6 goals defined. The goals not fulfilled were the number of parameters ($NP$) and the maximum of the autocorrelation between the inputs and the error ($R_{ue}$). In spite of the fact that the goal defined for $R_{ue}$ was not fulfilled, the obtained value was close to the a-priori defined value. The best model developed for the 48-mm distance fulfils 5 out of 6 goals. Again, the goal defined for $NP$ was not fulfilled. This goal was not accomplished for both best models and in the majority of the PIs, indicating that temperature estimation in the experimental conditions applied should be performed by models with $NP > 100$. The most important aspect is that all the high priority goals were fulfilled, i.e. the ones related with the generalisation performance ($RMSE_{TE}$ and $MRMSE_{ES}$).

The inputs of the best models are presented in Table 7.7, as lags of the considered input variables. Looking at this table it is possible to analyse that the best model obtained for the data collected at 24 mm had 13 inputs. In this model the relevance of $AF_{TUS}$ for temperature estimation in the experimental conditions considered, is represented by the presence of two lags ($AF_{TUS}(k-4)$ and $AF_{TUS}(k-17)$). The importance of $AH1_{TUS}$ and $AH2_{TUS}$ is marked by the presence of the lag 3 of these variables ($AH1_{TUS}(k-3)$ and $AH2_{TUS}(k-3)$). $A_{IUS}$ relevance is marked by the presence of lags 2 and 17. For this best individual, the information of $F_{IUS}$ was completely discarded. We may not conclude that the information of this variable is not important for temperature modelling in the present conditions. This fact only indicates that for the input information considered, temperature estimation is well achieved using information from other variables. In other PIs, the information of this variable is considered. The bandwidth information contributes with three lags ($BW_{IUS}(k-3)$, $BW_{IUS}(k-6)$, and $BW_{IUS}(k-19)$). Temporal position is marked by the presence of lag 1. The past memory of the system is represented by three lags ($T(k-4)$, $T(k-16)$, and $T(k-17)$). To note that $T(k-1)$ was not considered as input, as it was for invasive estimation presented previously. This is because model

**Table 7.7:** *Inputs for the best models obtained for the two distances considered.*

| Input variables | Lags of the input variables | | Possible lags value |
|---|---|---|---|
| | 24 mm | 48 mm | |
| $AF_{TUS}$ | 4, 17 | - | |
| $AH1_{TUS}$ | 3 | 1 | |
| $AH2_{TUS}$ | 3 | - | |
| $A_{IUS}$ | 0,17 | 11,12,14 | [0,19] |
| $F_{IUS}$ | - | 1,6 | |
| $BW_{IUS}$ | 3,6,19 | 8 | |
| $TP$ | 1 | 4,13 | |
| $T$ | 4,16,17 | 10,15,17 | [1,20] |
| Number of inputs | 13 | 12 | |
| Possible number of inputs | [2,20] | | |

- $AF_{TUS}$–**Amplitude of the principal component originated by the TUS device**;
- $AH1_{TUS}$ and $AH2_{TUS}$–**Amplitude of the first and second harmonic of principal component originated by the TUS device**;
- $A_{IUS}$, $BW_{IUS}$, and $F_{IUS}$–**Amplitude, bandwidth, and central frequency of the component related with the IUS transducer**;
- $TP$–**Temporal position**;
- $T$–**Temperature**.

structures were optimised to behave well in multi-step-ahead operation, where the past estimated temperature values were considered. The past estimated temperatures introduce errors in the inputs, and the input $T(k-1)$ is the one closest to $T(k)$ which can disturb more the estimation.

The best model obtained for the 48-mm distance had 12 inputs. Analysing Table 7.7, it can be said that $AF_{TUS}$ brings no important information, once it was discarded from that best individual input set. Once again, this fact does not imply that the information of this variable is not important for temperature prediction in the conditions presented in this work; it just means that, for this arrangement of inputs, it can be discarded. On the other hand, this variable appears for all the other preferable individuals. The relevance of the amplitude of the $1^{st}$ harmonic of the fundamental component originated by the therapeutic device ($AH1_{TUS}$) is remarked by the presence of lag 1 ($AH1_{TUS}(k-1)$), showing a dependence of temperature on the information of this variable in the last 10 seconds. Nevertheless, it was discarded in virtually all the other individuals, as well as the information of the amplitude of the $2^{nd}$ harmonic of the fundamental component ($AH2_{TUS}$), reflecting that they do not add important information in the conditions of this work. On the other hand, $A_{IUS}$ bears three lags in the best individual input set, also appearing in 8 of the 9 preferable individuals, marking its importance in this temperature prediction environment. The information of $F_{IUS}$ is represented by the lags 1 and 6, being present in five of the preferable individuals. The temperature dependence on the bandwidth of the component originated by the imaging device ($BW_{IUS}$) is manifested by the presence of the input $BW_{IUS}(k-8)$; this input appears also in other six PIs, demonstrating its importance. The temporal position ($TP$) contributes with two lags for this individual. This variable is also present in eight of the preferable individuals, stating its relevance. Finally, the importance of the past temperature memory of the system is marked by the presence of $T(k-10)$, $T(k-15)$

,and $T(k-17)$. As stated previously, $T(k-1)$ and the near short-term lags of $T$ were not selected given the desired multi-step ahead behaviour. Comparing the two best individuals input sets it can be said that the number of inputs differs in one. However, the inputs chosen are very different, except for $T(k-17)$. Although the measured temperature signals for the two distances present the same behaviour, i.e. the temperature tends to increase during heating and decreases in the cooling phase, the therapeutic ultrasound beam pattern at the two distances are different, and temperature increases and decreases in different ways. This implies that for different distances different inputs are better suited for temperature modelling. In addition, genetic algorithms are based in an initial population randomly generated which are evolved in a probabilistic schema based on individual's performance. This means that for the same estimation environment different MOGA runs can lead to different preferable individuals.

It is important to say that, in all the PIs input set, the maximum lag (which is 20) appears only for the best individual obtained at 24 mm, for the $BW_{IUS}$ variable. This can be taken as an evidence that the value originally assumed for the maximum admissible lag is sufficient for the attainment of adequate estimators. The number of neurons presented by the best models is 11 and 12, and the number of inputs is 13 and 12, respectively for 24 and 48 mm. This means also that the intervals defined for these structure parameters were appropriate, given that the extreme value does not appear in the best individuals.

The estimated versus the measured temperature waveforms, as well as the associated error curve and its distribution, are presented in Figures 7.8 and 7.9, for the 24 and 48-mm distances, respectively. From these figures it can be stated that, for both experiments the estimation follows the measurement with a maximum absolute error less than 0.5 $^{o}$C, and a mean error close to 0. For the 24-mm trial, the error variance is greater than for the 48-mm trial. This can be explained by the fact that

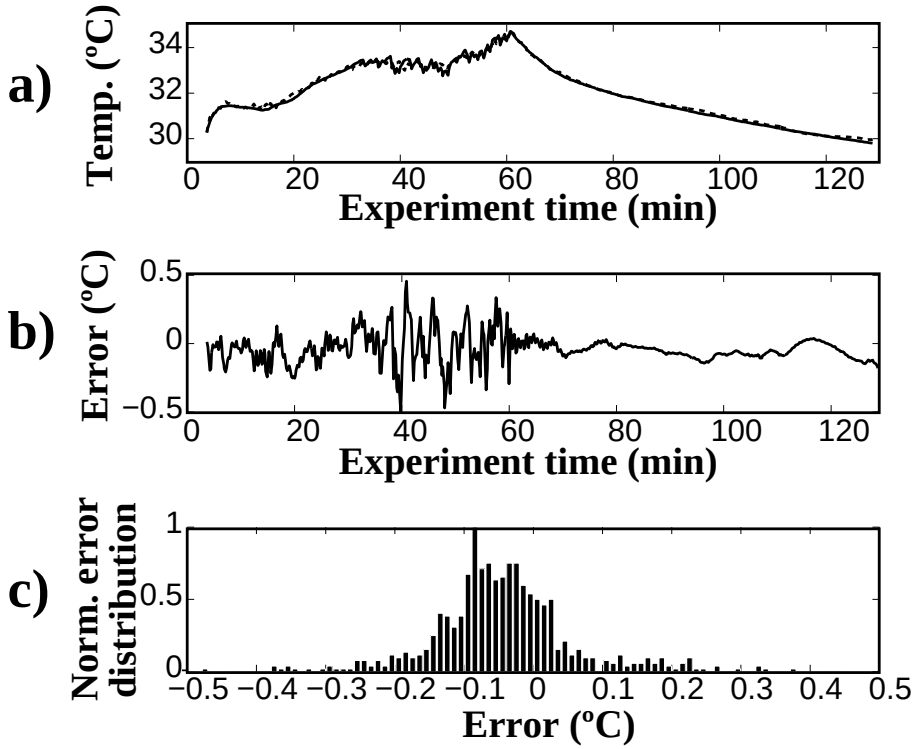


**Figure 7.8:** *Performance in the validation data for the best model obtained for the 24-mm distance. a) measured (solid-line) and estimated (dashed-line) temperatures, b) error curve, and c) error distribution.*

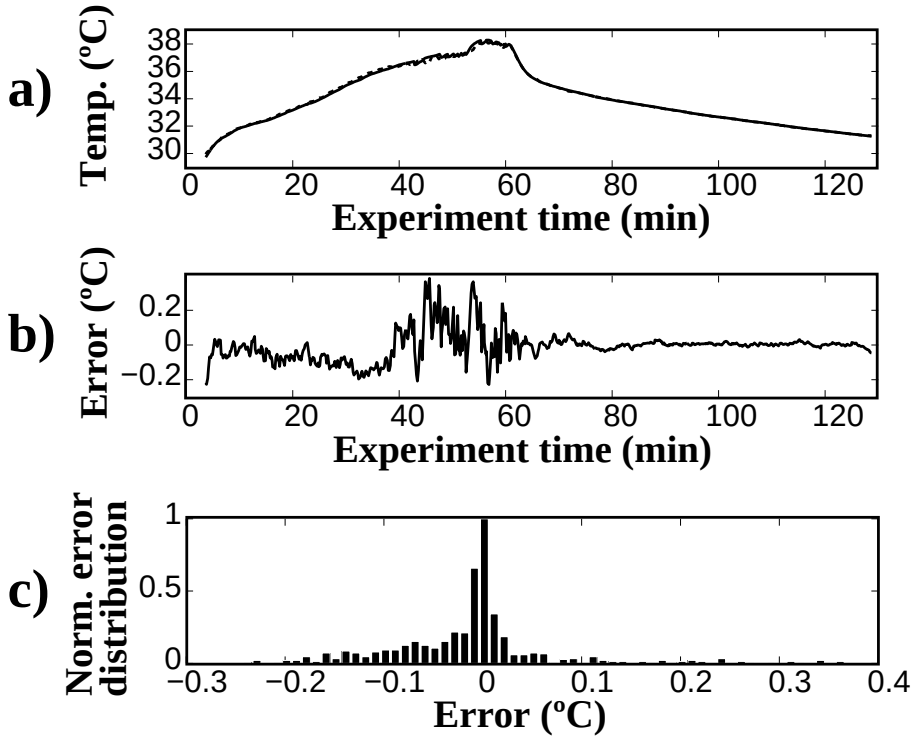


**Figure 7.9:** *Performance in the validation data for the best model obtained for the 48-mm distance. a) measured (solid-line) and estimated (dashed-line) temperatures, b) error curve, and c) error distribution.*

the point at 24 mm is within the beam near field. A point located at 48-mm distance is more in the far field (as presented in Figure 5.1), where the beam pattern is more regular, and well behaved temperature and related features can be obtained.

### 7.3.2 RBFNN- and linear-based structures

In Sub-section 7.2.1 the performance of RBFNN-based structures was compared to the performance of ARX-based models. The RBFNN structures were optimised using the MOGA algorithm, while proper ARX structures were found in an iterative way using Algorithm 2. In this sub-section both RBFNN-based structures, and linear-based structures were optimised using the MOGA, enabling more trustworthy comparisons. Using the data collected at 48 mm, the MOGA was applied using the parametrisation presented in Sub-section 6.2.2.

The MOGA applied to the linear-based models returned one preferable individual (PI). In validation, this individual presents a maximum absolute error of 2.08 $^{o}$C. The average and mean squared error obtained were: 0.22 $^{o}$C and 0.38 ($^{o}$C)$^2$, respectively. The estimated versus the measured temperature waveforms, the associated estimation error and its distribution are presented in Figure 7.10. On the other hand, the run applied to RBFNN structures obtained a set of 18 preferable individuals. The analysis of these models in validation tells us that the best one presents 9 neurons, a maximum absolute error of 0.42 $^{o}$C, an average error of -0.020 $^{o}$C, and a mean squared error of 0.0082 ($^{o}$C)$^2$. The estimated and measured temperatures, as well as the associated error and its distribution, are presented in Figure 7.11. Analysing these figures, it can be said that, for the conditions applied, the RBFNN-based structure estimates temperature non-invasively in the glycerine medium with an error much smaller than the best obtained linear model. In addition, the maximum absolute error for the RBFNN model is bellow 0.5 $^{o}$C, which is the value pointed as the borderline between an appropriate and an undesired tem-

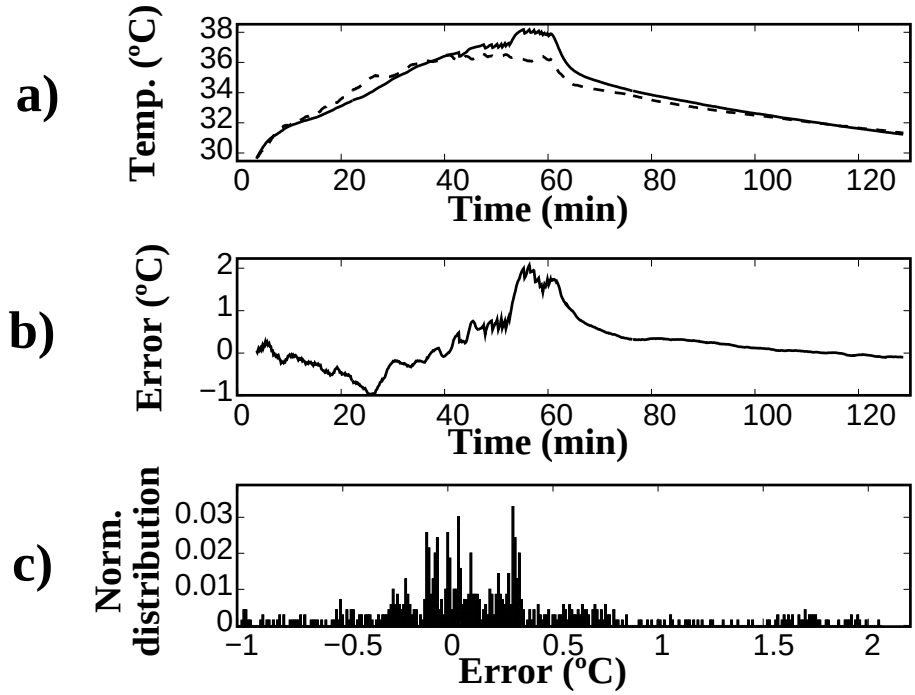


**Figure 7.10:** *Performance of the best linear structure in validation; a) measured (solid-line) and estimated (dashed-line) temperatures, b) error curve, and c) error distribution.*

perature estimator [5]. Given this threshold value, one can say that the best ARX model is an unsatisfactory estimator for single-point and non-invasive temperature estimation in the modelling conditions applied. The average error presented by the best RBFNN model is approximately one order of magnitude smaller than the value presented by the best linear model. Figures 7.10c and 7.11c show that the estimated variance produced by the RBFNN structure is smaller than in the linear model case, as expected. More precisely, the errors obtained by the NN model are practically all within the interval [-0.1 °C, 0.1 °C]. On the other hand practically all the errors committed by the linear model lie in the interval [-0.5 °C, 0.5 °C].

In Table 7.8, the inputs presented by the two best models are presented. As it can be seen, the best linear model has 20 inputs, which is the maximum possible number. Short-term lags of the extracted features ($AF_{TUS}(k)$, $AH1_{TUS}(k)$, $AH1_{TUS}(k-5)$, etc.) and of temperature ($T(k-2)$ and $T(k-4)$) were linearly related with tempera-

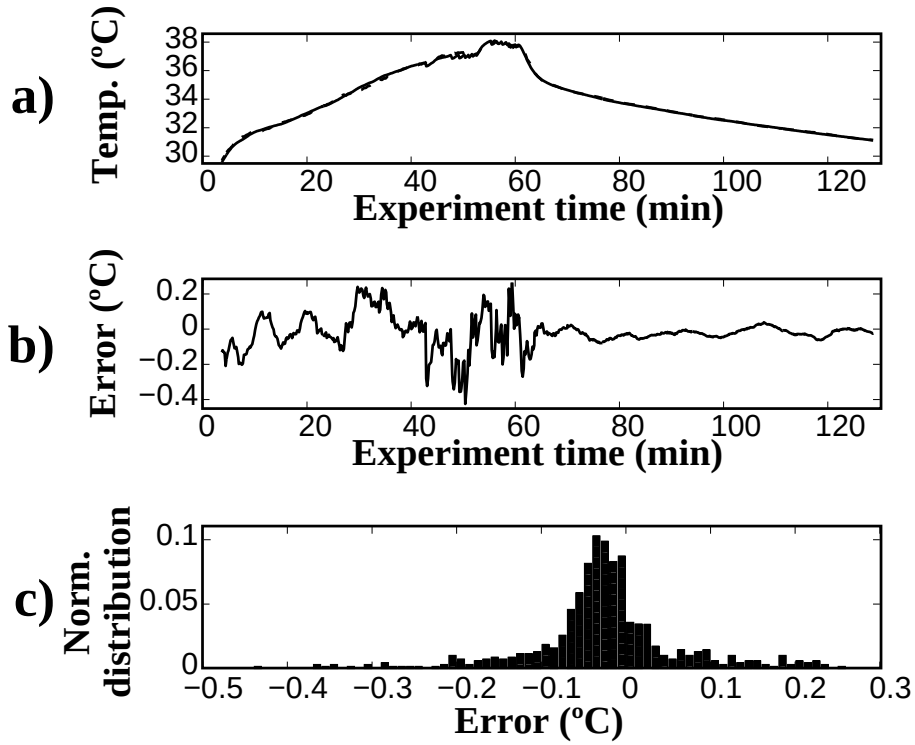


**Figure 7.11:** *Performance in the validation data for the best RBFNN-based model. a) measured (solid-line) and estimated (dashed-line) temperatures, b) error curve, and c) error distribution.*

**Table 7.8:** *Inputs for the best models obtained for the two distances considered.*

| Input variables | Lags of the input variables | | Possible lags value |
|---|---|---|---|
| | Linear | RBFNN | |
| $AF_{TUS}$ | 0,17 | - | |
| $AH1_{TUS}$ | 0,5,14 | 3 | |
| $AH2_{TUS}$ | - | 4,6 | |
| $A_{IUS}$ | 0,2,3,19 | 0,4,14 | [0,19] |
| $F_{IUS}$ | 1,5,11,18 | 16 | |
| $BW_{IUS}$ | 0,11,13,17 | 13 | |
| $TP$ | 5 | 5 | |
| $T$ | 2,4 | 4,13,19 | [1,20] |
| Number of inputs | 20 | 12 | |
| Possible number of inputs | [2,20] | | |

- $AF_{TUS}$–**Amplitude of the principal component originated by the TUS device**;
- $AH1_{TUS}$ and $AH2_{TUS}$–**Amplitude of the first and second harmonic of principal component originated by the TUS device**;
- $A_{IUS}$, $BW_{IUS}$, and $F_{IUS}$–**Amplitude, bandwidth, and central frequency of the component related with the IUS transducer**;
- $TP$–**Temporal position**;
- $T$–**Temperature**.

ture. The long-term lags of the extracted features ($AF_{TUS}(k-17)$, $A_{IUS}(k-19)$, and $F_{IUS}(k-17)$) appear also as inputs of this linear model. From Figure 6.14 and Table 7.8, it can be said that the extracted features that can be related more linearly with temperature appear in great number as inputs. These features are: $A_{IUS}$, $BW_{IUS}$, and $F_{IUS}$. The exception was the temporal position ($TP$), which contributes only with one lag. This may be because it presents some computational noise, and poor resolution. To be noticed that although $A_{IUS}$, $BW_{IUS}$ and $F_{IUS}$ can not be directly related with temperature (as it can be seen in Figure 6.14), they have some parts that were helpful for linear temperature estimation. The best obtained RBFNN model has 12 inputs, which is 6 inputs less than the best linear model. Short- and long-term lags of the extracted features are non-linearly related with temperature. The past temperature contributes with one short-term and two long-term lags. As explained in the previous sub-section, the input $T(k-1)$ is not considered in the best models input set, given that the models were developed for multi-step-ahead estimation. Comparing both structures, it can be said that the linear model uses the maximum number of inputs defined (20 inputs), expressing that it needed more information to reduce the error. On the other hand, the non-linear model obtained a much smaller error with less input information. Of course this was accomplished with an increase in complexity, required to non-linearly process the data. However, the non-linear model presents 127 parameters, which is not a heavy task for the computational power available nowadays. The maximum lag defined seems to be sufficient for the attainment of good estimators, given that it only appears in the linear model once, and does not appear in the RBFNN model inputs.

The obtained objectives for the best models, and the a-priori defined goals and priorities are presented in Table 7.9. From this table it is possible to analyse that the best linear model fulfils 3 out of 6 goals, the ones defined for $RMSE_{TR}$, $RMSE_{TE}$, and $R_{ee}$. However, the most important one is not fulfilled, which is the $MRMSE_{ES}$.

**Table 7.9:** *Objectives and related goals and priorities for the best linear and RBFNN model. The values in bold indicated that the goal was fulfilled.*

| Objective | Model type | | Goal | Priority |
|---|---|---|---|---|
| | linear | RBFNN | | |
| $RMSE_{TR}$ | **1.10E-3** | **9.0E-4** | 4.00E-3 | 1 |
| $RMSE_{TE}$ | **9.90E-4** | **1.00E-3** | 2.00E-3 | 2 |
| $MRMSE_{ES}$ | 3.10E-3 | **2.40E-3** | 3.00E-3 | 2 |
| $LWN$ | 6.68 | **1.61** | 2 | 1 |
| $NP$ | ND | 127 | 100 | 1 |
| $R_{ee}$ | **5.30E-2** | **7.40E-2** | 7.41E-2 | 1 |
| $R_{ue}$ | 1.00E-1 | 7.50E-2 | 7.41E-2 | 1 |

ND–Not defined for the linear models

- $RMSE_{TR}$–**Root mean square error in the training set**;
- $RMSE_{TE}$–**Root mean square error in the test set**;
- $MRMSE_{ES}$–**Maximum root mean square error in the all the estimation steps**;
- $LWN$–**Linear weights norm**;
- $NP$–**Number of parameters**;
- $R_{ee}$ and $R_{ue}$–**Model-validity tests**.

This objective discriminates the performance in multi-step-ahead estimation, a fundamental aspect for non-invasive estimation. The goals defined for $LWN$ and $R_{ee}$ were not fulfilled either. In particular, the value obtained for $LWN$ is very far apart from the defined goal. The best obtained RBFNN structure fulfils 5 out of 7 goals. Those not fulfilled are $NP$ and $R_{ue}$. Although these goals were not fulfilled, the obtained values are close to the a-priori defined values. In addition, this model fulfils the high priority goals ($RMSE_{TE}$ and $MRMSE_{ES}$), showing its appropriateness for non-invasive temperature estimation in the applied experimental conditions.

### 7.3.3 Single RBFNN structures for two-point estimation

In Sub-section 7.3.1, two models were obtained for estimation at two different points. However, this is impracticable for multi-point estimation, where the development of $n$ models would be necessary for $n$ points. In this way, a single model should estimate temperature at multiple points. In this sub-section single models for two-point estimation are developed. As explained in Sub-section 6.3.1, the information obtained to create both models in Sub-section 7.3.1 was aggregated, and single RBFNN-based structures optimised for estimating temperature both at 24-mm and 48-mm distance from the therapeutic transducer. The MOGA was applied using the parametrisation exposed in Sub-section 6.3.1, and a set of 75 preferable models was obtained. Once again, the selection of the best one was based on the performance attained in the validation data; in this case, it is composed by the pair of sequences collected at 2.0 $W/cm^2$ . The measured temperature for both distances, as compared with the ones estimated by the best model are presented in Figure 7.12. The maximum absolute, average and mean squared errors for this individual are presented in Table 7.10. Analysing this table it can be said that both the best single-model presented in this section, and the two best models presented in Sub-section 7.3.1, showed a maximum absolute error inferior to 0.5 $^{o}$C, which is the value pointed as the border-

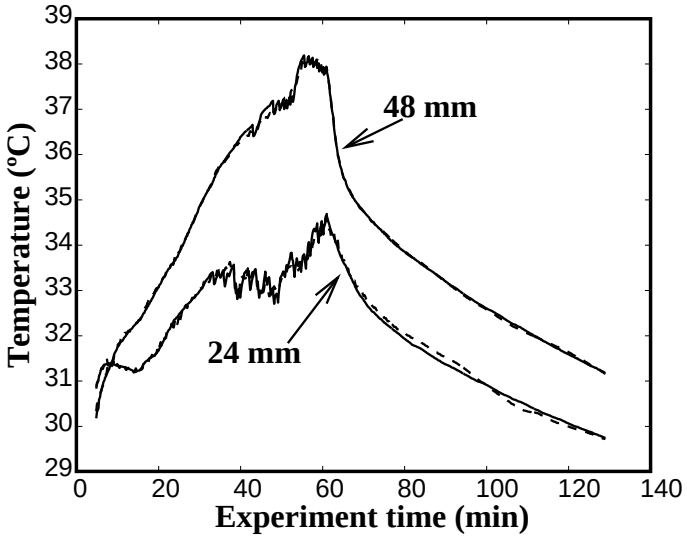


**Figure 7.12:** *Performance in the validation data for the best single-model for two-point temperature estimation in liquid media. The measured temperatures are represented by solid lines, while the estimated ones are represented by dashed lines.*

**Table 7.10:** *Errors presented by the best single-model for two-point estimation, and the errors presented by the best two separate models considered for each point, as explained in Sub-section 7.3.1.*

| | | Distance (mm) | |
|---|---|---|---|
| | | 24 | 48 |
| Two-model | Maximum absolute error (°C) | 4.9E-1 | 3.8E-1 |
| | Average Error (°C) | 4.0E-2 | 7.2E-3 |
| | Mean Squared Error $(°C)^2$ | 1.3E-2 | 7.1E-3 |
| Single-model | Maximum absolute error (°C) | 4.3E-1 | 3.4E-1 |
| | Average Error (°C) | -9.1E-3 | -3.0E-4 |
| | Mean Squared Error $(°C)^2$ | 1.3E-2 | 4.8E-3 |

line between an appropriate and an undesired temperature estimator. Comparing the single-model estimation approach with the two-model approach, it can be said that substantially better results were obtained with the best single-model. This means that a single RBFNN structure was capable to integrate the "knowledge", that was distributed between the two models in Sub-section 7.3.1. The information was integrated in such a way that better results were obtained.

The best single-model fulfils 6 out of 9 goals presented in Table 6.3. Those not fulfilled were the number of parameters ($NP$), i.e. the model complexity, and the two correlation tests. The value of $NP$ obtained was 463, which is slightly apart from the a-priori goal (which was 400). The values obtained for the maximum of the correlation tests were: $R_{ee} = 0.0746$ and $R_{ue} = 0.0707$, which are closer to the a-priori goals (values of 0.0516).

Despite the required error performance, this best model presented 22 neurons, this is approximately the double obtained in the two-model situation, where 11 and 12 neurons were obtained for each best model. In the same way, the number of inputs increased from 12 and 13 in the bi-model situation to 18 in the single-model approach. These two structure parameters are directly related with the number of parameters, which increased from 166 and 169 to 463. This is an enormous increase in complexity for just the addition of one point. In an attempt to reduce the complexity, single models were applied for multi-point temperature estimation in solid media, as described in the next section. The applied solid medium is well behaved, and the temperature-dependent feature was appropriate and computed with proper resolution, resulting in models with reduced complexity.

## 7.4 Non-invasive estimation: homogeneous phantom

Non-invasive temperature estimation should be performed at both time and space, and also in a multi-intensity fashion. In Section 5.4 the experimental setup developed for collecting data from a homogeneous gel-based phantom is presented. Temperature and backscattered ultrasound signals from five points (P1, P2, P3, P4, and P5 in Figure 5.10) inside this phantom were measured, and processed as explained in Sub-section 6.3.2. Using the obtained temporal echo-shifts($TES$)/temperature change ($\Delta T$) signal pairs, RBFNN-based structures were developed for non-invasive temperature estimation. For comparison purposes adaptive-network-based fuzzy inference system (ANFIS) based structures, and the orthogonal least squares algorithm (OLS) applied to RBFNNs training and centre selection, were used in the same estimation environment. Both RBFNN and ANFIS structures were optimised using the multi-objective genetic algorithm (MOGA). In the ANFIS case, only the inputs were selected. Both models were trained and their structure selected to estimate temperature at points P1, P3 and P5, named "trained points". The data from points P2 and P4 ("untrained points") were used to test the model spatial generalisation capacity, at the end of the training and structure selection phase, i.e. in the validation phase. In this way, the best models were tested in operational situations never "viewed" before. As referred in Sub-section 6.3.2, four experimental trials were randomly selected for training, one for test, and another for validation. In this way, 48 subsets (4 trials $\times$ 4 intensities $\times$ 3 trained points) were used for training, 12 (1 trials $\times$ 4 intensities $\times$ 3 trained points) for testing and 20 for validation (1 trials $\times$ 4 intensities $\times$ 3 trained points + (1 trials $\times$ 4 intensities $\times$ 2 untrained points)). Given that each subset contains 210 $TES/\Delta T$ samples, then 48 $\times$ 210 = 10080 patterns were available for training, 12 $\times$ 210 = 2520 for testing, and 20 $\times$

**Table 7.11:** *MOGA objectives summary for the 50 preferable individuals as compared to the a-priori defined goals.*

| Obj. | Goal | Prior. | Obtained values | | | |
|---|---|---|---|---|---|---|
| | | | Min. | Average | Max. | Std. Dev. |
| $RMSE_{TR}(^oC)$ | 4.30E-2 | 1 | 4.25E-3 | 1.32E-2 | 4.15E-2 | 6.45E-3 |
| $MRMSE_{TE}(^oC)$ | 4.30E-1 | 2 | 1.16E-2 | 3.87E-2 | 9.31E-2 | 1.72E-2 |
| $MMAE_{TE}(^oC)$ | 4.30E-1 | 2 | 3.90E-1 | 4.17E-1 | 4.28E-1 | 1.00E-2 |
| $LWN$ | 2.0 | 1 | 0.71 | 2.51 | 16.36 | 2.98 |
| $NP$ | 200 | 1 | 89 | 165.6 | 361 | 69.2 |
| $R_{ee}$ | 2.10E-2 | 1 | 8.70E-1 | 9.50E-1 | 9.77E-1 | 2.35E-2 |
| $R_{ue}$ | 2.10E-2 | 1 | 2.29E-2 | 4.89E-2 | 1.63E-1 | 2.50E-2 |

- $RMSE_{TR}$–**Root mean square error in the training set**;
- $MRMSE_{TE}$–**Maximum root mean square error in all the test subsets**;
- $MMAE_{TE}$–**Maximum of the maximum absolute multi-step-ahead error in all the test subsets**;
- $LWN$–**Linear weights norm**;
- $NP$–**Number of parameters**;
- $R_{ee}$ and $R_{ue}$–**Model-validity tests**.

$210 = 4200$ for validation.

MOGA was applied four times using the parametrisation presented in Subsection 6.3.2, and a total of 50 preferable individuals obtained. In Table 7.11, the results for the MOGA objectives in comparison with the a-priori defined goals are presented. Looking at this table, it can be said that all the individuals fulfil the goal defined for the root mean square error in training, as expected. In the same way, the goals defined for $MRMSE_{TE}$ and $MMAE_{TE}$ were also fulfilled by all the preferable individuals. These objectives are the most important ones (priority 2), given that they are related with the models' performance in new data, i.e. the models' generalisation performance. For the linear weights norm ($LWN$) there are models which presented a high value for this objective (maximum value of 16.36). In the case of this work, these models have a bad generalisation capacity. However,

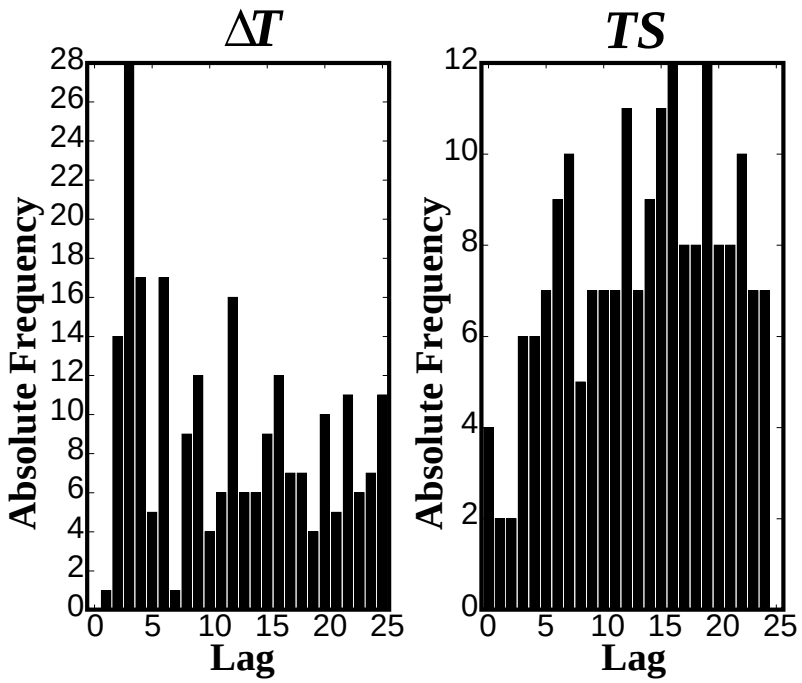


**Figure 7.13:** *Absolute frequency of the preferable individuals inputs, represented as lags of the input variables (TES and $\Delta T$).*

in average, the obtained values are close to the a-priori defined goals. In average, the goal defined for the number of parameters ($NP$) is fulfilled, and the majority of the preferable models have $NP$ bellow 200. The goals defined for model-validity tests were never fulfilled. Although the goal defined for $R_{ue}$ was never fulfilled, in average, the obtained values are close to the defined goal. On the other side, the obtained values for $R_{ee}$ are very far apart from the predefined goal. This is because the temperature waveforms are composed by two parts (an increasing and decreasing part), and the error among the 48 different data sets, which compose the total training set, tends to have a common pattern and the error autocorrelation function has high values after lag zero.

In Figure 7.13, the absolute frequency of the models' inputs is presented. Not surprisingly, the short and medium-term lags of $\Delta T$ are the most frequent in the models' input set. In particular $\Delta T(k-3)$, which appears in 28 (56%) models. As explained previously, the input $\Delta T(k-1)$ is only present in one model because

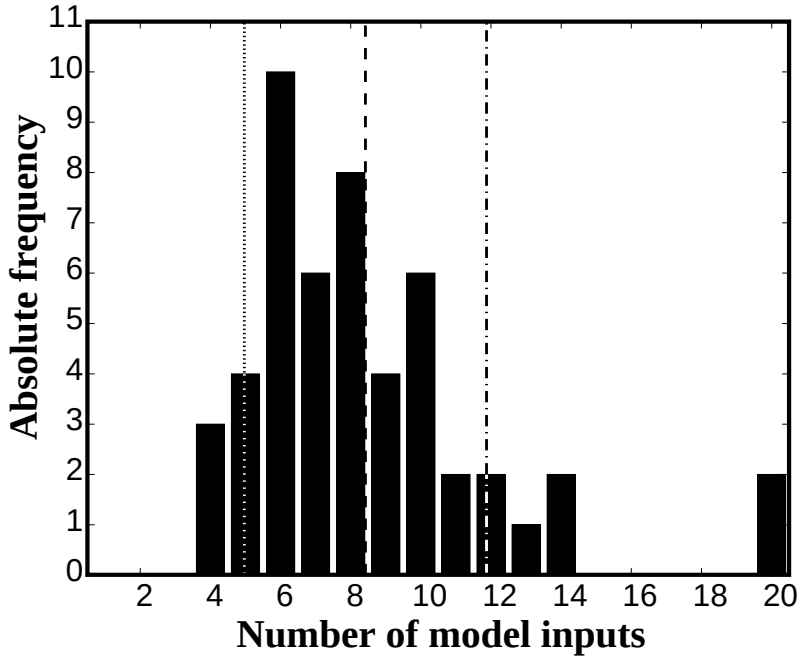


**Figure 7.14:** *Absolute frequency of the number of inputs per model. (−−) Average, (· · · ) average - standard deviation, and (− · −) average + standard deviation.*

of the required multi-step-ahead behaviour. On the other hand, the medium and long-term lags of $TES$ are the most frequent. The lags between 12 and 19 are the ones which appear in more models, in particular $TES(k-16)$ and $TES(k-19)$. In the four runs, the MOGA selected 231 inputs related with $\Delta T$ and 190 related with $TES$, i.e. 55 % of inputs related with the past temperature and 45 % related with the time-shift. This small difference shows that both variables are important for the proposed modelling environment.

The absolute frequency of the number of inputs per model is presented in Figure 7.14. The majority of the models has between 4 and 14 inputs, existing two outliers which have 20 inputs. In average, the models have approximately 9 inputs and with large probability a model picked from the 50 preferable ones has between 5 and 12 inputs.

In terms of the number of neurons (Fig. 7.15), 26 % of the models have 10 neurons, and the average has 13 neurons.

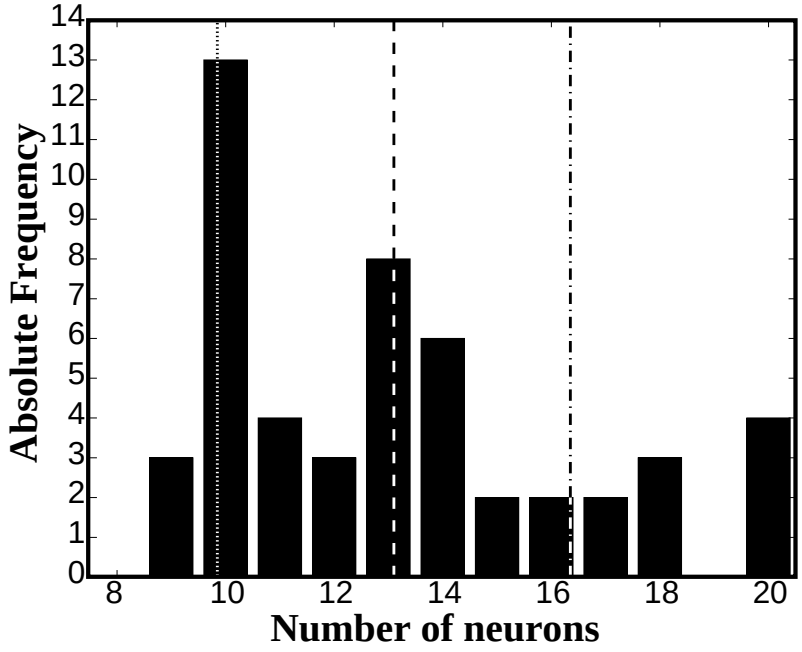


**Figure 7.15:** *Absolute frequency of the number of neurons per model. (−−) Average line, (· · · ) average - standard deviation line, and (−·−) average + standard deviation line.*

After the MOGA, the performance of the selected preferable individuals must be accessed in the validation data, i.e. data never used neither in training nor structure selection. This is an essential step to test the real capabilities of the models. The new data contain all the physical situations considered, that is, were collected at all the intensities (0.5, 1.0, 1.5 and 2.0 W/cm$^2$) and from all the considered points (P1, P2, P3, P4 and P5 in Fig. 5.10), in order to perform an effective model evaluation. As referred before, the models were trained and their structure selected for temperature estimation at points P1, P3 and P5, which are 1-cm spaced. In addition, the models were validated in points P2 and P4 which were never used either in the NNs parameters evaluation or in the structure selection.

In Table 7.12, a summary of the maximum absolute error in validation ($MMAE_{VL}$) obtained by the preferable models is presented. This error is obtained in the same way as the $MMAE_{TE}$, but using the validation data. Looking at this table, it is possible to realize that, for the trained points, the maximum absolute error is

**Table 7.12:** *Summary of the maximum absolute temperature error in estimation, for the validation set ($MMAE_{VL}$) obtained for the 50 preferable individuals, in the trained and untrained points. This summary was obtained considering all the applied intensities, i.e. 0.5, 1.0, 1.5 and 2.0 $W/cm^2$ .*

| $MMAE_{VL}$ (°C ) | | | | | |
|---|---|---|---|---|---|
| Trained points (P1, P3 and P5) | | | Untrained points (P2 and P4) | | |
| Avg. | Max. | Std. Dev. | Avg. | Max. | Std. Dev. |
| 0.49 | 0.95 | 0.11 | 3.91 | 12.80 | 2.3 |

inferior to 0.95 °C for all the models. In average, the maximum absolute error is 0.49 °C (with a standard deviation of 0.11 °C) which is less than the value required for an accurate hyperthermic/diathermic temperature estimator. For the untrained points, there are models which present a high error, being specialised in the trained points and having a bad spatial generalisation capacity. In average, the obtained models are bad in spatial generalisation, because they are tuned by the MOGA and the training algorithm to perform well in points P1, P3 and P5. However, in the four runs there was always one model which presented a maximum absolute error inferior to 1 °C. Two of these models presented a $MMAE_{VL}$ inferior to 0.5 °C in both the trained and untrained points. These models are the more realistic time-spatial non-invasive temperature estimators. The one which presents a $MMAE_{VL}$ of 0.40 °C and 0.46 °C in the trained and untrained points, respectively, was "elected" the best model. In addition, this model presents a small computational complexity ($NP = 151$) as desired for a real-time implementation. The estimated (dashed line) versus the measured temperature waveforms (solid line), for all the situations are presented in Fig. 7.16.

The performance of the RBFNN-based structures, optimised by the MOGA (MOGA+RBFNN), was tested against two other non-linear methodologies, while processing the same data. As said previously, the methodologies were: the orthogonal least squares applied to RBFNNs training and centre selection (called

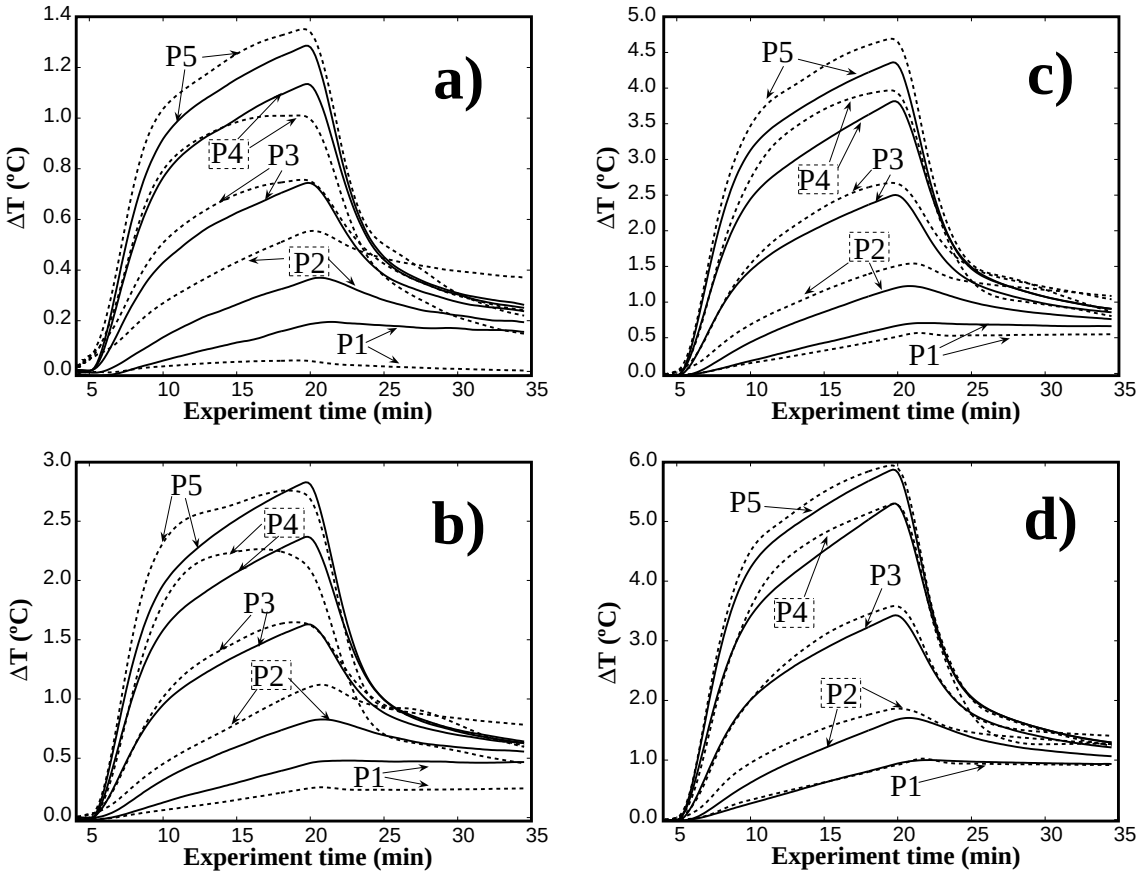


**Figure 7.16:** *Estimated (dashed lines) and measured (solid lines) temperature change by the best model, for the five considered points (P1, P2, P3, P4 and P5), and for the four applied intensities: a) 0.5 W/cm$^2$, b) 1.0 W/cm$^2$, c) 1.5 W/cm$^2$ and d) 2.0 W/cm$^2$.*

OLS+RBFNN), and ANFIS-based structures with inputs selected by the MOGA (called MOGA+ANFIS). The OLS method, with a training RMSE goal of 4.30E-2 ºC (the same value as the goal defined for the $RMSE_{TR}$ in the MOGA+RBFNN methodology), applied to the RBFNN with inputs: $I(k)$, $P(k)$, $TES(k)$ and $\Delta T(k-1)$ (see Figure 6.22), obtained a network with 20 neurons (the maximum value defined in the proposed methodology). In the validation data this network reaches a maximum absolute error of 6.6 ºC, for the spatial points included in the training (P1, P3 and P5). Such a high value invalidates the applicability of OLS for the proposed estimation environment.

MOGA was applied to the ANFIS structures, as explained in Sub-section 6.3.2, and lasted approximately one week to complete 20 generations, which is more than the time needed to complete 200 generations for the RBFNN case. Then 10 weeks (2.5 months) would be necessary to reach 200 generations. At the end of 50 generations the best attained ANFIS model reaches (in the validation data) a maximum absolute error of approximately 0.7 ºC for the trained positions (P1, P3 and P5) and greater than 3.0 ºC for the untrained ones (P2, P4).

It can be concluded that the simple method (OLS+RBFNN) could not reach the desired resolution (maximum absolute error of 0.5 ºC), probably due to its simple nature. On the other hand, the more complex methodology (MOGA+ANFIS) could not reach the desired resolution given the limitations imposed by its complexity. The proposed methodology (MOGA+RBFNN) is somewhere in between, in the sense that it is relatively simple and can achieve the required resolution faster. In fact, most of the processing time is spent in the training and structure selection. Once the best-model is identified, temperature estimation is obtained only by performing a couple of multiplications and summations, easily implemented in hardware.

**Table 7.13:** *Amount of data presented in the training, test and validation sets.*

| | Training | Test | Validation |
|---|---|---|---|
| # of experimental trials | 4 | 1 | 1 |
| # of spatial points | 3 | 3 | 5 |
| # of intensities | 3 | 3 | 4 |
| # of subsets | 36 | 9 | 20 |
| # of patterns | 7560 | 1890 | 4200 |

### 7.4.1 Space and intensity generalisation analysis

In the previous text, RBFNN-based structures were trained and optimised for estimating at three points, and then tested in other two points never applied. This means that the best obtained models were tested in terms of spatial generalisation capacity. However, proper estimators should present both a good spatial and intensity generalisation capacity. This is an important aspect concerning the application of these models for therapeutic instrumentation control. Proper generalisers have the capacity to estimate temperature at operating situations never applied, and consequently a more refined instrumentation control could be reached.

By taking the same data employed previously, the spatial and intensity generalisation capacity of RBFNN-based structures were assessed and analysed. The structures were trained and optimised using data from three points, and from three intensities; then they were validated in new data, containing information from the five points considered, and also from the four applied intensities. This means that the best obtained models (preferable models) were validated in the same situations "viewed" in training and structure selection, as well as in situations never applied related with points and intensity not considered in training and structure optimisation. This procedure enables a correct model validation and the assessment of the spatial and intensity generalisation capacity. The amount of data selected for training test and validation is presented in Table 7.13.

In order to cover all the situations, four MOGA runs were applied, corresponding

**Table 7.14:** *MOGA objectives summary for the 50 preferable individuals as compared to the a-priori defined goals.*

| Obj. | Goal | Prior. | Obtained values | | |
|---|---|---|---|---|---|
| | | | Min. | Max. | Avg. |
| $RMSE_{TR}(^oC)$ | 4.30E-2 | 1 | 4.02E-3 | 3.29E-2 | 1.06E-2 |
| $MRMSE_{TE}(^oC)$ | 4.30E-1 | 2 | 8.58E-3 | 8.02E-2 | 3.01E-2 |
| $MMAE_{TE}(^oC)$ | 4.30E-1 | 2 | 3.51E-1 | 4.30E-1 | 4.08E-1 |
| $LWN$ | 2.0 | 1 | 0.84 | 7.95 | 1.95 |
| $NP$ | 200 | 1 | 91 | 421 | 174.74 |
| $R_{ee}$ | 2.41E-2 | 1 | 8.47E-1 | 9.83E-1 | 9.46E-1 |
| $R_{ue}$ | 2.41E-2 | 1 | 2.41E-2 | 1.30E-1 | 4.25E-2 |

- $RMSE_{TR}$–**Root mean square error in the training set**;
- $MRMSE_{TE}$–**Maximum root mean square error in all the test subsets**;
- $MMAE_{TE}$–**Maximum of the maximum absolute multi-step-ahead error in all the test subsets**;
- $LWN$–**Linear weights norm**;
- $NP$–**Number of parameters**;
- $R_{ee}$ and $R_{ue}$–**Model-validity tests**.

each one to the lack of one intensity. The MOGA population size was defined as 200 individuals. After 200 generations for each run type, a set of 57 preferable individuals was obtained. The minimum, maximum, and average values, for each one of the elected objectives are presented in Table 7.14. The goals defined for the model errors were all fulfilled in average and maximum sense. In particular, the errors related with the generalisation performance ($MRMSE_{TE}$ and $MMAE_{TE}$ which have priority 2) were also fulfilled. The goal for the $LWN$ was in average fulfilled, being its maximum a moderate value. The value defined for the number of parameters was also (in average) fulfilled, meaning that for the proposed estimation environment, with great probability it is possible to obtain low complex models with good generalisation performance, as desired for real-time applications. The goal for the model-validity tests was only fulfilled by one model, for the maximum of the

correlation between the inputs and the errors ($R_{ue}$). As explained previously, the obtained values for $R_{ee}$ are very far apart from the goal, because of the nature of the temperature signals. On the other hand, the values obtained for $R_{ue}$ are in average close to the goal, being its minimum coincident with the desired value.

Figure 7.17 shows the absolute frequency of the input variable lags, selected among the preferable models. It is possible to see that lag 22 of $TES$ is the most frequent one appearing in 17 models (which is 30 % of the models). However, lags 3 and 12 are also frequent, appearing in 14 and 16 models, respectively. In Figure 7.17a, a quadratic B-spline curve (dash-dot line) traced from the central point at the top of each bar is presented. This curve enhances visual perception about the most preferable lags. It is possible to see that the most frequent $TES$ lags are organised in three clusters. The first one contains the lags between 1 and 7, the second contains the lags between 7 and 17 and the last one, the lags between 17 and 24. The MOGA chooses as relevant lags the ones around the most frequent (which are lags 3, 12 and 22), demonstrating its search coherence. In the case of the temperature lags, the most frequent is lag 3, and looking at the quadratic B-spline curve (dash-dot line), traced in the same way as in the case of $TES$, it is possible to say that the MOGA elected the short term lags of $\Delta T$, as expected.

In Figure 7.18 the absolute frequency of the number of inputs per model is presented. We may see that the majority of the preferable models has nine inputs, the average number of inputs per model being $8.68 \approx 9$. Figure 7.18 indicates also that proper models have between 3 and 17 inputs, meaning that the a-priori defined interval for the number of inputs is sufficient for the MOGA to reach the desired results.

The absolute frequency of the number of neurons per model is presented in Figure 7.19. The majority of the models has 10 neurons, being $13.70 \approx 14$ the average number. Approximately 77% of the models have a number of neurons between 9

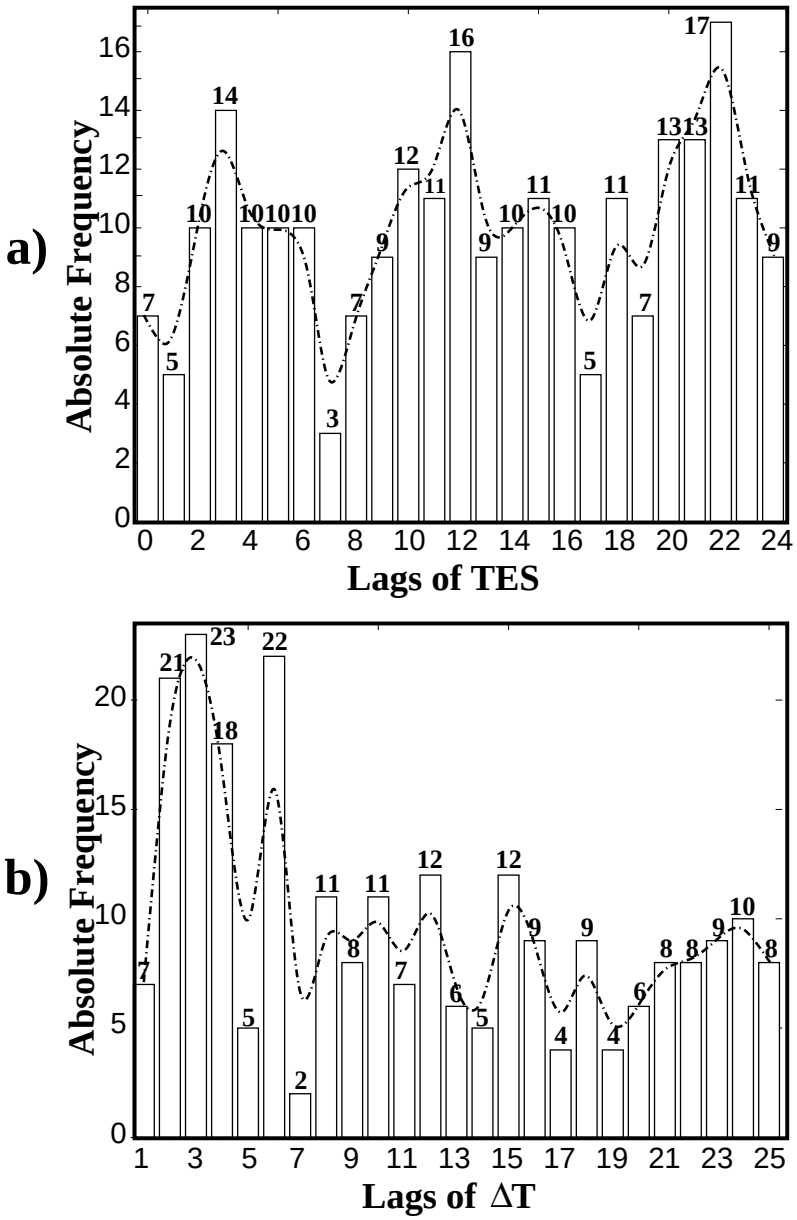


**Figure 7.17:** *Absolute frequency of the input variable lags, the dash-dotted lines are quadratic B-spline curves obtained by considering the central point at the top of each bar, these curves are used to enhance visual perception about the chosen lags. a) TES lags and b) $\Delta T$ lags.*

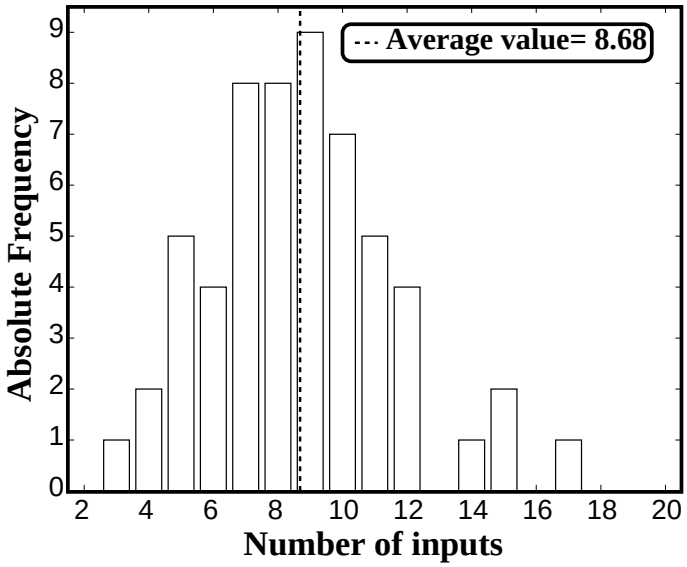


**Figure 7.18:** *Absolute frequency of the number of inputs per model.*

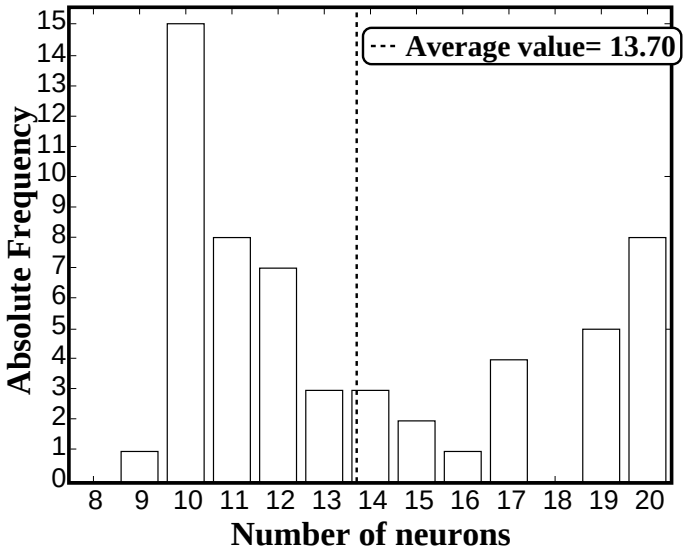


**Figure 7.19:** *Absolute frequency of the number of neurons per model.*

and 17 and only 23% have 19 and 20 neurons, meaning that the interval defined for the number of neurons is sufficient for the attainment of well-fitted estimators. The models which have 19 and 20 neurons are the result of MOGA's attempt to reach better performance by increasing the processing capacity, and normally these models violate the $NP$ goal, being undesired for real-world applications. Based on the precedent description and discussion (especially in terms of the input lags arrangement and number of inputs), it is possible to say that the MOGA converged to a type of preferable models, confirming the correct choice of the a-priori defined parametrisation.

Comparing the preferable models structures obtained in this part of the work, with the ones obtained in the beginning of this section, it can be said that they are very similar. The short-term lags of $\Delta T$ were selected in both cases. In particular, lag 2, 3, 4 and 6 are the most frequent in both situations. Comparing the $TES$ lags selected, it can be said that once more some of the most frequent ones in Figure 7.13 are also frequent in the present preferable models, for example lag 12 and 22. However, MOGA selected for the present case clusters of lags which are located around the most frequent ones. As said previously, a short-term cluster around lag 3, one medium-term cluster around lag 12, and a long-term cluster around lag 22 were selected. In Figure 7.13 it is possible to realise that MOGA selected other input arrangement for the models developed considering all the intensities, being not visible any cluster. This was probably because different goals for the model-validity tests were defined (the training set size was reduced, which increased the value of the confidence interval). This change could led to a different choice for the $TES$ lags. In average the number of neurons is approximately 9, and with large probability a model picked from the preferable ones has between 5 and 12 inputs, in both situations. As seen in Figures 7.15 and 7.19, the majority of the models has 10 neurons in both cases. The average number of neurons is approximately 14 in the

**Table 7.15:** *Maximum of the maximum absolute errors in validation ($MMAE_{VL}$) presented by the best model in the different run types.*

| Excluded intensity ($W/cm^2$) | $MMAE_{VL}$ (°C) | |
|---|---|---|
| | Trained points | Untrained points |
| 0.5 | 0.51 | 0.53 |
| 1.0 | 0.47 | 0.51 |
| 1.5 | 0.49 | 0.48 |
| 2.0 | 1.41 | 1.33 |

present preferable models and 13 in the first ones reported for this estimation environment. These structure similarities show that, although data collected at one of the intensities is not present in training and structure optimisation, MOGA selected approximately the same structure parameters since the estimation environment is the same. This fact confirms again the MOGA convergence to a set of models proper for the estimation environment applied.

At the end of the training and structure selection, the 57 MOGA preferable individuals were evaluated in new data (validation data), in order to assess their generalisation capacity. As referred previously, the validation data contain information from both trained and untrained points, and from the trained intensities and the untrained intensity. In this way, the models were evaluated in similar data, from the trained points and intensities, and in completely unseen operating situations, correspondent to the two untrained points and to one untrained intensity. In Table 7.15 the maximum absolute errors in validation ($MMAE_{VL}$) presented by the best model in each run type can be analysed. Looking at Table 7.15, it can be said that models with a maximum absolute error in the range 0.5 °C ± 10% can be obtained for the trained and untrained points, except for the training and structure selection without data from 2.0 $W/cm^2$. The good performance in the runs without data from 0.5, 1.0 and 1.5 $W/cm^2$ is because these intensities are intermediate (to mention that the null intensity at the beginning and final part of each experiment is considered to be an intensity level, which makes the 0.5 $W/cm^2$ an intermediate

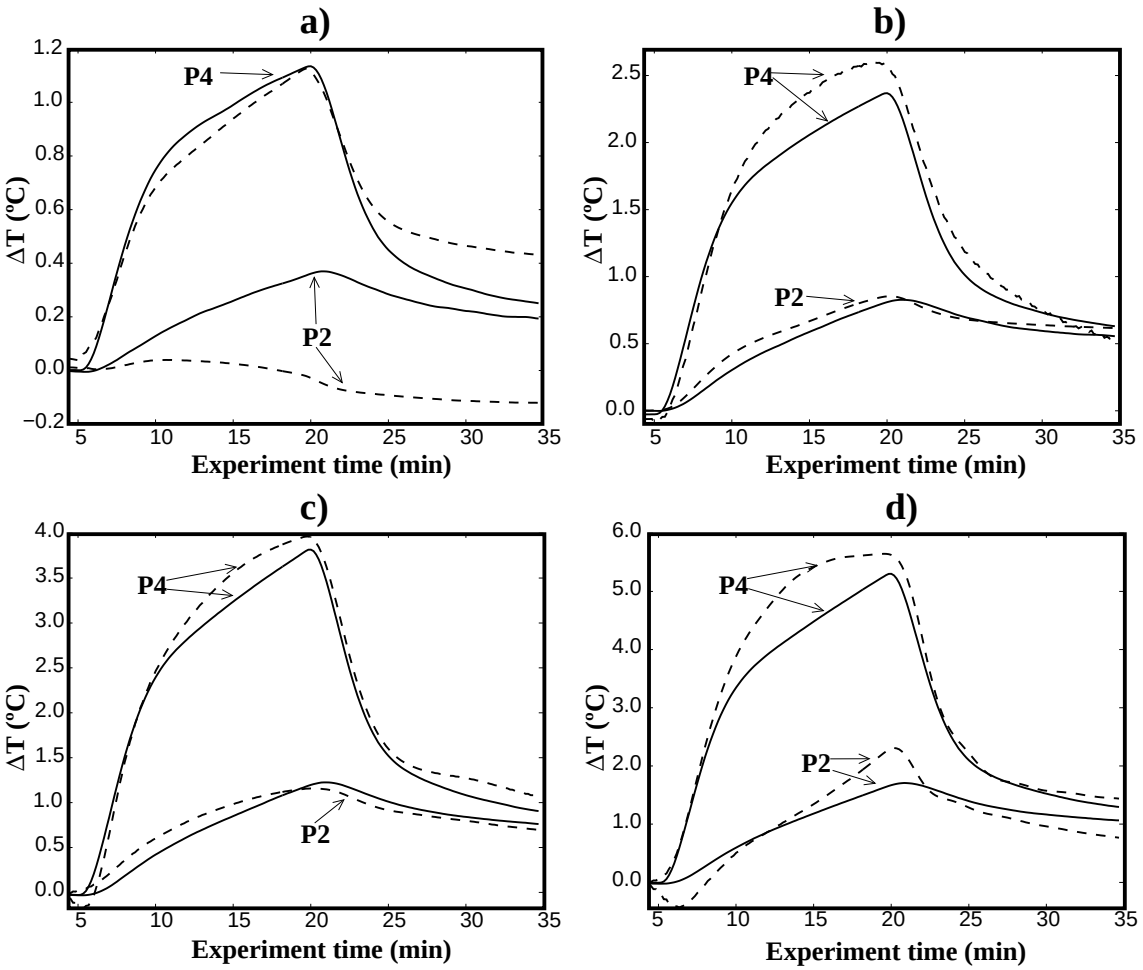


**Figure 7.20:** *Measured (full lines) versus estimated (dashed lines) temperature change signals, in the untrained points (P2 and P4) and in the untrained intensities: a) 0.5 $W/cm^2$, b) 1.0 $W/cm^2$, c) 1.5 $W/cm^2$, and d) 2.0 $W/cm^2$*

intensity), and the models can treat the lack of that data by learning from data collected at the neighbouring intensities. The 2.0 $W/cm^2$ is an extreme intensity, meaning that the temperature increase and temporal echo-shifts are also extreme. This implies that the RBFNNs parameters were found considering lower limits, and then bad performance is obtained when tested in data that is outside of the training domain. In the intermediate intensities, the models were trained knowing the data space boundaries, and generalisation inside this space were well fulfilled. The measured versus the estimated temperature changes for the best models in the untrained points and in the untrained intensities are presented in Figure 7.20. This

**Table 7.16:** *Amount of data presented in the training, test and validation sets.*

| | Training | Test | Validation |
|---|---|---|---|
| # of experimental trials | 4 | 1 | 1 |
| # of spatial points | 5 | 5 | 5 |
| # of intensities | 4 | 4 | 8 |
| # of subsets | 80 | 20 | 40 |
| # of patterns | 16800 | 4200 | 8400 |

figure shows the estimations obtained in the worst scenario that the models can be subjected to. Looking at this figure, one can see that although the best model built without data from 2.0 $W/cm^2$ presented errors over 1 $^oC$, their estimations followed the increase and decrease of the measured temperature, in a stable fashion.

## 7.5 Non-invasive estimation: multilayered phantom

Aiming a more realistic evaluation of the proposed estimation methodology, data from a multilayered phantom were obtained, as explained in Section 5.5. Data from five points (SP1, SP2, SP3, SP4, and SP5) and by applying eight intensities (0.3, 0.5, 0.7, 1.0, 1.3, 1.5, 1.7, and 2.0 $W/cm^2$ ) were collected. These data were processed as explained in Sub-section 6.3.2, and arranged in separate files for RBFNN-based structures training, test and validation. It was decided to train and optimise the structures to behave well at the five points, and at four (0.5, 1.0, 1.5 and 2.0 $W/cm^2$ ) of the applied intensities. The data collected at the other intensities were only used in the validation phase to analyse the models generalisation performance. The amount of data used for training, test and validation is presented in Table 7.16. Using the MOGA parametrisation presented in Sub-section 6.3.2, four runs were performed, considering 100 generations and a population size of 200 individuals. After all runs, a set of 82 preferable models was obtained. The statistics for the

**Table 7.17:** *Statistics of the obtained objectives for the preferable models.*

| Obj. | $RMSE_{TR}$ (°C) | $MRMSE_{TE}$ (°C) | $MMAE_{TE}$ (°C) | $LWN$ | $NP$ |
|---|---|---|---|---|---|
| Min. | 6.13E-2 | 0.10 | 0.39 | 1.18 | 64 |
| Max. | 0.15 | 0.27 | 0.48 | 1.99 | 166 |
| Avg. | 0.13 | 0.23 | 0.46 | 1.64 | 109.89 |
| Std. | 1.54E-2 | 2.98E-2 | 1.54E-2 | 0.23 | 22.96 |
| Goal | 0.15 | 0.48 | 0.48 | 2.0 | 200 |
| Priority | 1 | 2 | 2 | 1 | 1 |

- $RMSE_{TR}$–**Root mean square error in the training set**;
- $MRMSE_{TE}$–**Maximum root mean square error in all the test subsets**;
- $MMAE_{TE}$–**Maximum of the maximum absolute multi-step-ahead error in all the test subsets**;
- $LWN$–**Linear weights norm**;
- $NP$–**Number of parameters**.

obtained objectives values, presented by the preferable models can be seen in Table 7.17. Looking at this table, it is possible to notice that all the goals defined were fulfilled (in both maximum and average sense), especially the high priority goals related to $MRMSE_{TE}$ and $MMAE_{TE}$. The accomplishment of the goal defined for the $LWN$ means that all the preferable individuals are well-conditioned. Table 7.17 also indicates that the required complexity, i.e. the number of parameters, is compatible with the desired accuracy, which is an important aspect in terms of feasibility. Small standard deviations were also observed, meaning that the MOGA converged to a well defined region in the objective space.

The absolute frequency of the preferable individual inputs is presented in Fig. 7.21, where it is possible to observe that MOGA selected mainly the long-term lags of $\Delta T$. On the other hand, the short-term lags of $TES$ are the most frequent ones, more than 50 % of the models have $TES(k)$ as input. Considering all the inputs selected, 73 % are related with $TES$, and only 27 % with $\Delta T$. As explained before,

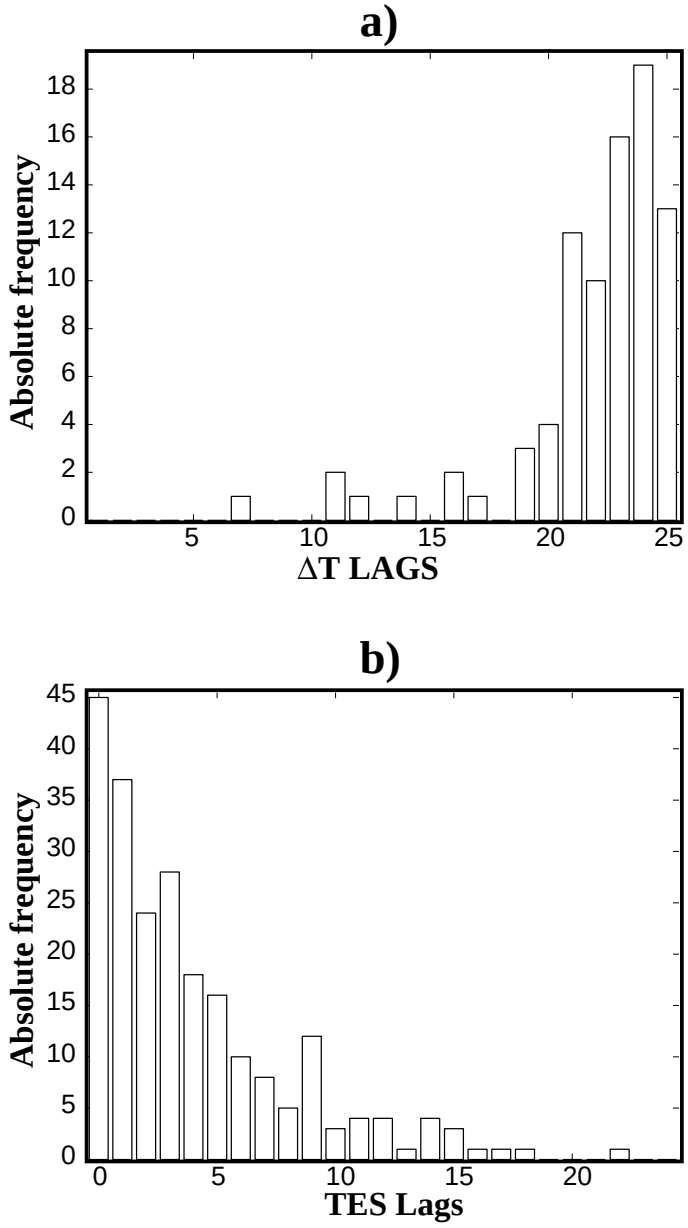


**Figure 7.21:** *Absolute frequency of the preferable model inputs, selected by the MOGA .* **a)** *inputs related with* $\Delta T$*, and* **b)** *inputs related with TES.*

this happens because the model's structure is optimised for multi-step-ahead estimation, which is possible by feeding-back the past estimated temperature values. This feedback introduces cumulative errors in the inputs, decreasing the performance. In addition, the $TES$ signals do not introduce cumulative errors, as they are obtained directly from the BSU signals at each instant. To note that for the homogeneous phantom case, the short-term lags of $\Delta T$ (with exception of lag 1) were selected. This was because the $TES$ signals obtained from the homogeneous phantom do not have the quality necessary to overcome the lack of the short-term lags of $\Delta T$. In this multi-layered phantom the backscattered ultrasound signals were collected in such a way that the short-term information of $TES$ could substitute the short-term information of $\Delta T$. Another reason for the absence of the short-term lags of $\Delta T$ is the lack of the model-validity tests as objectives. It is referred in [13] and found for this thesis, that these tests bias the search towards better one-step-ahead models, i.e. models where the short-temperature lags are important. The long-term information of $\Delta T$ seems to be important, in particular lags 23 and 24, which appears in 16 and 19 of the preferable models, respectively. In each preferable model at least one input related with temperature is present.

As it can be seen in Figure 7.22, the preferable models have between 4 and 9 inputs, most of them have 6 inputs. Figure 7.23 show that the majority of them have 11 neurons (precisely 24 models). Models with neurons between 15 and 18 were also frequent. The structure parameters selected point that MOGA converged to a class of models tuned for the proposed estimation environment ( i.e. that fulfilled the a-priori defined goals).

Again, as a fundamental step, after training and structure optimisation, the preferable models must be evaluated in new data, i.e. in the validation set. As said before, in this work RBFNN-based structures were optimised and trained to perform well in 20 operating situations (5 spatial points $\times$ 4 intensities (0.5, 1.0, 1.5 and 2.0

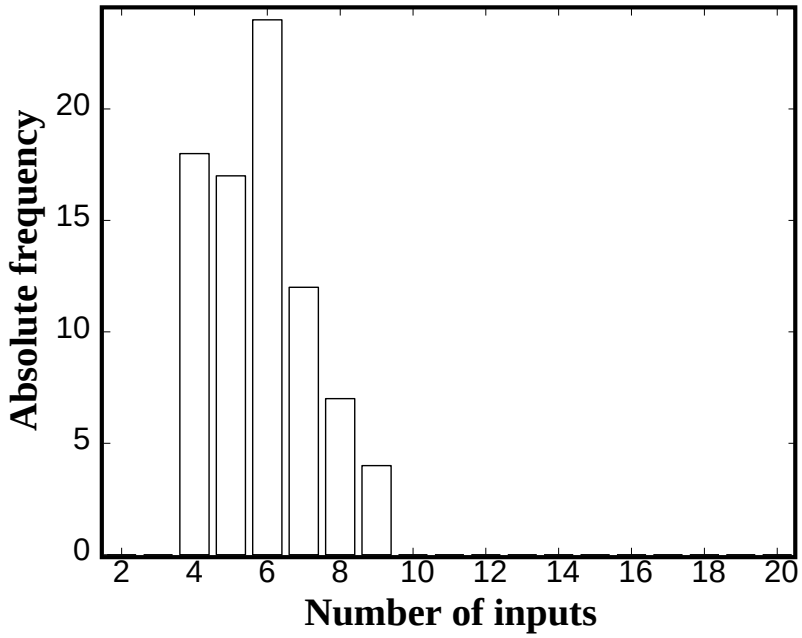


**Figure 7.22:** *Absolute frequency of the number of inputs per model. The most frequent are the models with six inputs.*

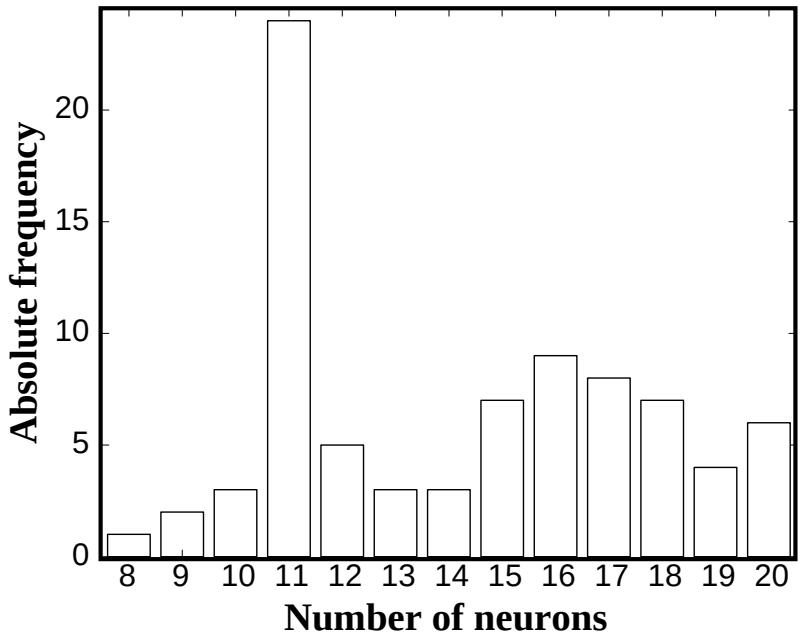


**Figure 7.23:** *Absolute frequency of the number of neurons per model. Most of the models have 11 neurons.*

**Table 7.18:** *$MMAE_{VL}$ statistics for the trained and untrained operating situations.*

| | Average | Standard dev. | Maximum |
|---|---|---|---|
| Trained | 0.49 °C | 0.048 °C | 0.66 °C |
| Untrained | 0.51 °C | 0.049 °C | 0.73 °C |

$W/cm^2$ )). However, for validation, data from the same five points but collected at eight intensities were used. Among these intensities there are the four applied in training and structure optimisation, called the "trained intensities". The other intensities (0.3, 0.7, 1.3, and 1.7 $W/cm^2$ ) never applied before were used to test how the best models can overcome different operating points, and are called the "untrained intensities". This means that the best models were validated in 40 operating situations, being 20 of them never assessed (the "untrained operating situations"). In Table 7.18, maximum, average and standard deviation values for the $MMAE_{VL}$, obtained by the preferable models, in the trained and untrained operating situations are presented. Looking at this table one can see that in average, the preferable models present a $MMAE_{VL}$, considering trained and untrained operating situations, inferior to 0.5 °C + 10%. For the trained ones, in average, the models were suited for hyperthermia/ diathermia applications, as the average $MMAE_{VL}$ is inferior to 0.5 °C. The standard deviations indicate that the majority of the preferable models present a $MMAE_{VL}$ inferior to 0.54 °C and 0.56 °C for trained and untrained situations, respectively. In the worst case, a maximum $MMAE_{VL}$ of 0.66 °C and 0.73 °C are obtained for the trained and untrained situations, respectively; which are not so high values. This table also indicates that the training and structure optimisation were successful, given that although the performance in the untrained cases is worse, in average it is very close to the value obtained for the trained situations. This means that the optimised structures "learned" the process dynamics, and they are not specialised in the training and test data, and they are good non-invasive temperature generalisers.

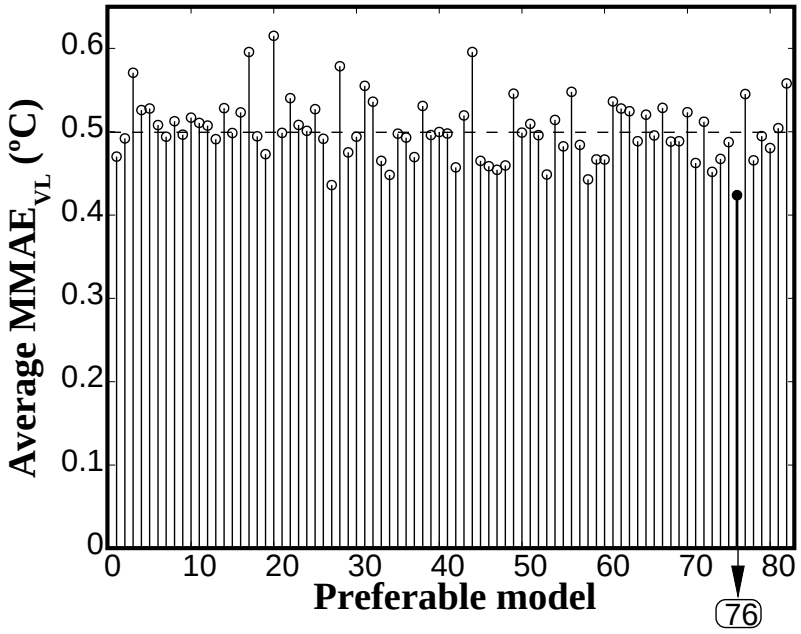


**Figure 7.24:** *Average $MMAE_{VL}$ for for each one of the preferable models. The best obtained model (the one with smallest average $MMAE_{VL}$) is the number 76. The dashed line indicates the 0.5 °C threshold.*

The choice of the best individual among the preferable set was based on both the $MMAE_{VL}$ obtained for the trained and untrained operating situations. In Figure 7.24 the average $MMAE_{VL}$ (i.e. the summation of both $MMAE_{VL}$s obtained in the trained and untrained situations divided by 2) for each individual is presented. In this figure, it is possible to say that the majority of the preferable models present an average $MMAE_{VL}$ inferior to 0.5 °C, and that the preferable model, which presents the smaller average $MMAE_{VL}$ value, is the number 76. This model presents a $MMAE_{VL}$ of 0.41 °C and 0.43 °C for the trained and untrained situations, respectively and these values are both inferior to the gold-standard value required for hyperthermia/diathermia purposes. This model has 6 inputs and 11 neurons, as the majority of the preferable models. The inputs selected for this models were: $TES(k)$, $TES(k-3)$, $TES(k-15)$, and $\Delta T(k-24)$. With the exception of $TES(k-15)$, both of this inputs are frequent on the preferable models. These points out again that MOGA returned proper structures for the applied estimation

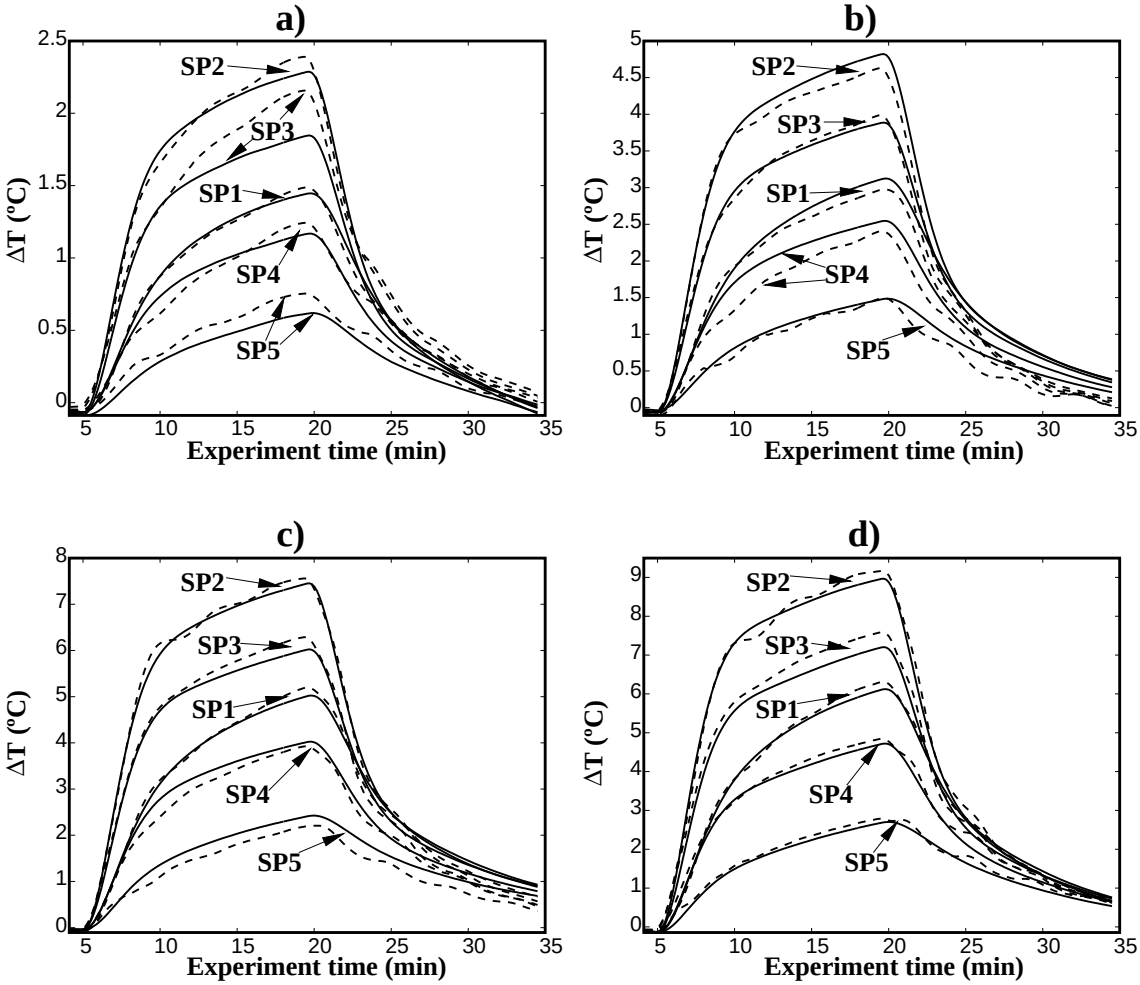


**Figure 7.25:** *Measured (solid lines) versus the estimated (dashed lines) temperature waveforms for the best preferable model in validation and in the operating situations considered in training and structure selection.* **a)** *0.5 $W/cm^2$,* **b)** *1.0 $W/cm^2$,* **c)** *1.5 $W/cm^2$, and* **d)** *2.0 $W/cm^2$.*

environment. The measured temperature changes (solid-lines) versus the estimated ones (dashed-lines) for the best model are presented in Figure 7.25 and Figure 7.26 for the trained and untrained situations, respectively. Some estimated waveforms present an oscillatory behaviour, which is the influence of the input $\Delta T(k-24)$, which feedback error to the inputs.

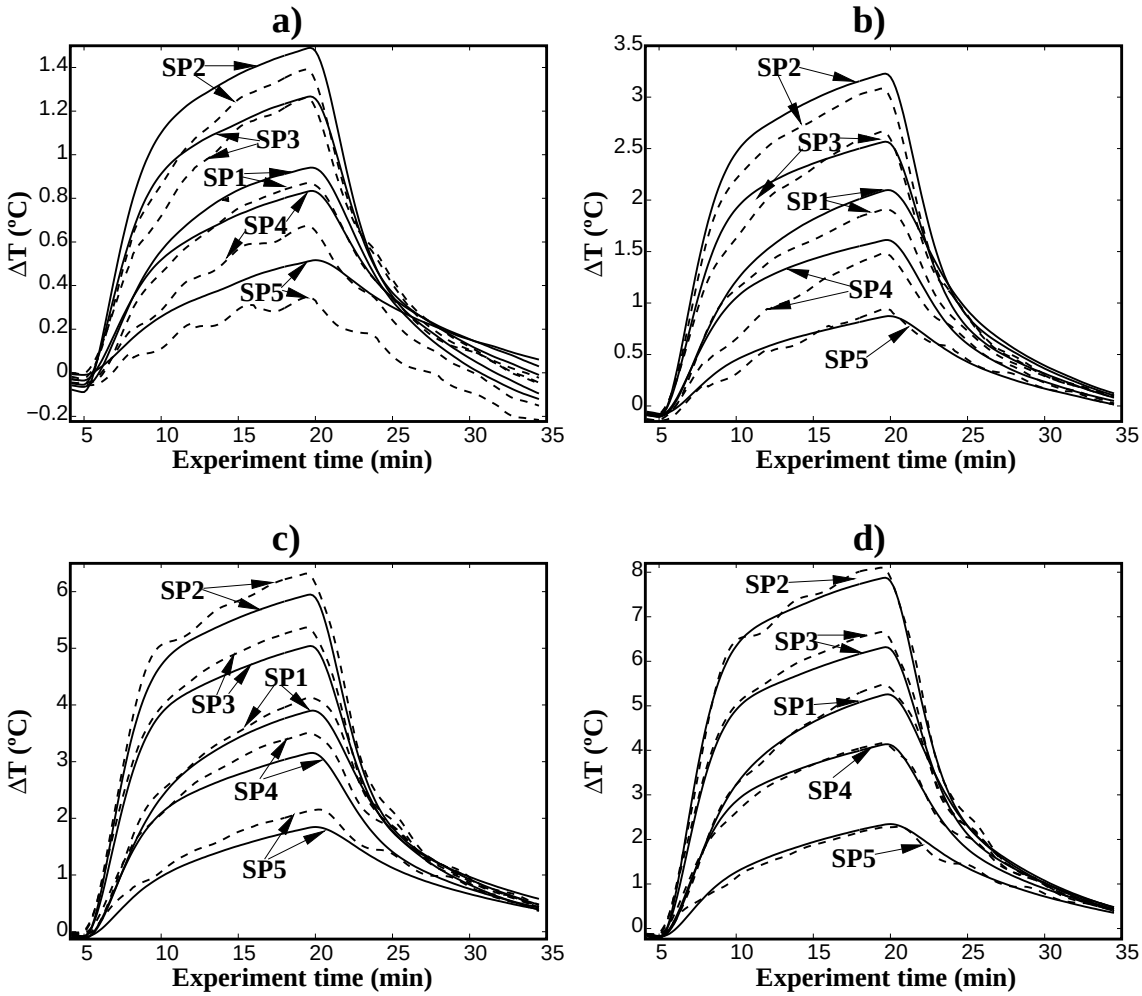


**Figure 7.26:** *Measured (solid lines) versus the estimated (dashed lines) temperature waveforms for the best preferable model in validation and in the operating situations not considered in training and structure selection.* **a)** *0.3* $W/cm^2$, **b)** *0.7* $W/cm^2$, **c)** *1.3* $W/cm^2$, *and* **d)** *1.7* $W/cm^2$.

## 7.6 General overview

In this chapter the results obtained during the thesis development are presented and discussed. The diagram in Figure 7.27 presents a general overview of the accuracies obtained in the different parts of the work. From this diagram one can see that all the methodologies based on radial-basis-functions neural networks (RBFNNs) with structure optimised by the multi-objective genetic algorithm (MOGA), reach an accuracy inferior to 0.5 °C (the pointed threshold for hyperthermia/diathermia). This accuracy was reached for invasive and non-invasive estimation trials, and for both considered media. For invasive estimation the error is much smaller than for non-invasive. This is because, invasively the past fed-back temperature values are the ones measured, while in a non-invasive trial the past temperature values (supplied at the inputs) are the estimated ones, thus contaminated with estimation errors. The other methodologies (Linear, MOGA+Linear, OLS+RBFNN, and MOGA+ANFIS) were employed for comparison purposes. One can realise that the linear models developed, for both invasive and non-invasive estimation present an inappropriate accuracy, meaning that temperature estimation should be performed by non-linear strategies. However, there were also non-linear approaches that present inappropriate accuracies. These methodologies involve the application of the orthogonal least squares for RBFNN centre selection and training, and the MOGA applied to the adaptive-network-based fuzzy inference system (ANFIS) input selection. The OLS+MOGA methodology could not reach the required accuracy given its simple nature (only search for the appropriate centres location). On the other hand, the MOGA+ANFIS could not accomplish the required goal given the course of dimensionality present in the ANFIS structures. One can realise that the MOGA+RBFNN arrangement is an intermediate solution that could fulfil the required accuracy, with proper complexity.

When compared with the so far published methodologies based on backscat-

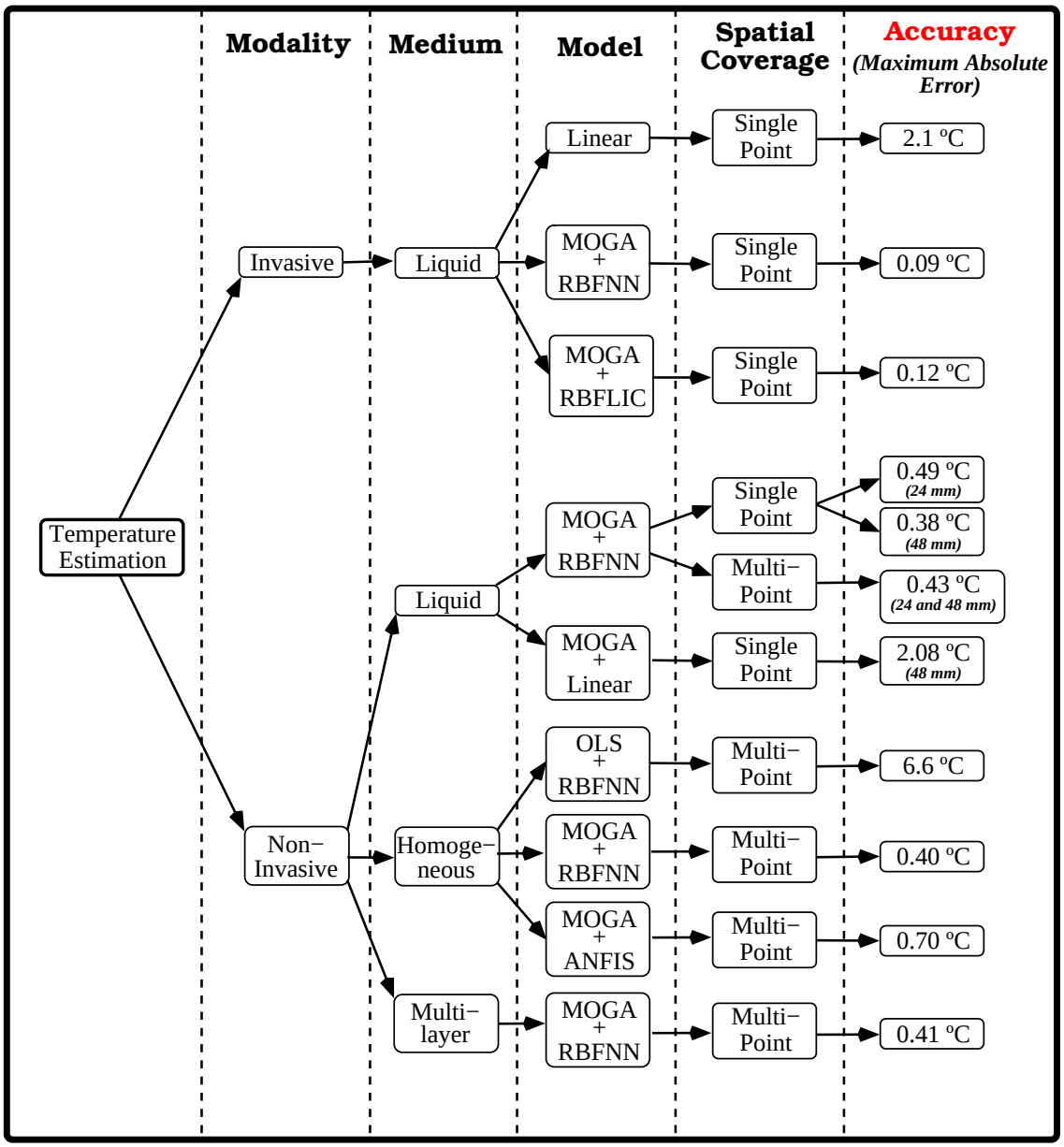


**Figure 7.27:** *Accuracies obtained for invasive and non-invasive estimation, in the applied media by the different modelling strategies. MOGA–multi-objective genetic algorithms; RBFNN–radial-basis-functions neural network; RBFLIC – radial-basis-functions neural network with linear input connections; OLS–orthogonal least squares algorithm; ANFIS–adaptive-network-based fuzzy inference system; MOGA+RBFNN–RBFNN with structure optimised by MOGA; MOGA+RBFLIC–RBFLIC with structure optimised by MOGA; MOGA+Linear– Linear models with structure optimised by MOGA; OLS+RBFNN–RBFNN with structure optimised and trained by the OLS algorithm; MOGA+ANFIS–ANFIS with structure optimised by MOGA.*

tered ultrasound for non-invasive estimation (described in Sub-section 4.3.4), the MOGA+RBFNN methodology presents better or comparable accuracies. Based on the extraction of temporal echo-shifts and in a linear model, in [4] a maximum absolute error of 0.44 °C was reported. Temperature was estimated at three points inside a rubber-phantom, and using a single intensity. Using a replication of the experimental setup used in [4], in [69] a method based on the assessment of frequency-shifts and considering also a linear model was presented, and approximately the same accuracy was pointed. In [71] the method presented in [4] was extended to three dimensions, and an accuracy of 0.24 °C pointed. However, the heating source was a nichrome heating wire (invasive source), instead of a more irregular source, such as therapeutic ultrasound. Although the two and three dimensional capabilities of the methods pointed in the previous papers, the assessment of their accuracy was performed at a maximum of three points and for a single intensity. As a major drawback, these models only can estimate temperature in homogeneous media, given that they consider only a temperature-dependent medium constant (see Equations 4.8 and 4.15 in Sub-section 4.3.4). On the other hand, the MOGA+RBFNN methodology, was extensively tested under different operating situations. More specifically, up to 40 different operating situations were applied, being some of these situations never applied in the models construction, i.e. the models were applied to estimate temperature at intensities and spatial points never used before for training and structure selection. Tests in a multilayered (non-homogeneous) phantom showed that the applied soft-computing methodology is able to estimate temperature in this type of media with proper accuracy and complexity. As the applied methodology is completely data driven, i.e. knowledge is extracted from data, the models learned the temperature evolution in different layers and interfaces by seeing similar situations during training.

# Chapter 8

# Concluding remarks

## 8.1 General conclusions

This thesis is on a new application of soft-computing methodologies, for invasive and non-invasive temperature estimation.

This work began with the extraction of appropriate temperature-dependent features. Up to 7 features of both spectral and temporal type were tested, and it was found that temporal-echo-shifts was a feature that enables by itself the development of appropriate time-spatial and non-invasive estimators, in homogeneous and multilayer media.

Several models were developed for invasive and non-invasive estimation, and the methodology involving radial-basis-functions neural networks and the multi-objective genetic algorithm (MOGA+RBFNN) was the one that reached the appropriate resolution with adequate complexity.

From the proposed goals (described in Section 1.2), the last one involving the development of a system to control the therapeutic system, was not fulfilled. The reasons for this non-compliance was in first place the time spent in a deeper analysis of the developed estimators. This analysis gave us a broader understanding

about the models behaviour, such as in situations never applied during the models training and structure selection. The second reason was the absence of therapeutic instrumentation with an interface, which would enable the control of the therapeutic instrumentation through a computer, based on the temperature estimators proposed in this thesis.

When compared with state-of-the-art methods the MOGA+RBFNN methodology equals or over-performs them, concerning the maximum absolute error. The main advantage is that the models developed in this work are able to estimate temperature in multilayered media, in a broader variety of operating situations.

The main limitation of the proposed methodologies is their high dependence on the data, given that both structure and parameters are found from data. This means that for a successful modelling, data must be representative, i.e. they must cover all possible physical situations of the estimation environment. In-vivo application in humans depends on the development of phantoms that simulate tissue acoustic and thermal properties, given that it is not feasible to measure data from a patient and then develop models. This problem is also visible in the state-of-the-art methods, since they depend on medium constants that have be found a-priori.

## 8.2 Future research lines

To date, the proposed methodologies were only tested in phantoms; next natural steps are testing them *in-vitro* with real tissue, and then in animal models.

Another point is to extend the methodology for 2D and 3D estimation. This can be performed by increasing the measurement of the backscattered ultrasound (BSU) signals to a line (for 2D) and to a plan (for 3D). This can be done by attaching the imaging transducer to a positioning system, or optimally by using a transducer array. Then features, such as, temporal echo-shifts should be extracted

for each considered point, and used in the MOGA+RBFNN methodology. However, each model structure should include additional inputs, aiming to integrate spatial information. For the 1D models developed in this work an additional input related with spatial position was included ($P(k)$), in this way for 2D and 3D two and three additional inputs should be considered.

For application in humans, a more extensive research in phantoms is a main issue. Three-layer phantoms simulating acoustic and thermal properties of bone, muscle and fat should be developed and calibrated. Future phantoms should account for blood flow perfusion, in order to approximate real tissue properties. Studies on how well models overcome variations on the media should be developed, given that each human being has its own features. The performance of the models should also be tested by using different heating sources, i.e. different therapeutic transducers.

In real environments, movements due to respiration, heart beats and deformations induced by the transducer in the application site may influence the measurements. During the computation of features, such as temporal echo-shifts, these movements are visible and introduce an interference that could lead to erroneous estimates. The consideration of algorithms that minimise (or optimally eliminate) this interferences is a main issue. They are known as *motion compensation algorithms* and were already studied and applied for non-invasive temperature estimation [84] and for HIFU therapy application [85]. In the future it is intended to extend the MOGA+RBFNN methodology to temperature estimation in media subjected to movements, by applying a motion compensation algorithm.

The quality of the estimates could be probably increased by considering information from B-Mode images. Punctual estimations could be performed by the methodology so far presented, then by B-mode image processing [86] these estimations may be extrapolated to the surrounding regions, increasing the extensibility of the local estimate.

As a main issue, the application of the developed models for therapeutic instrumentation control is planned. The temperature models enable the application of predictive controllers, which could reach better performance than the traditional control approaches (such as PID). The drawback is that non-linear models lead to a non-convex control problem, and strategies such as branch-and-bound [87] and evolutive algorithms [88] should be used.

# Bibliography

[1] K. D. Paulsen, M. J. Moskowitz, T. P. Ryan, S. E. Mitchell, and P. J. Hoopes, "Initial in vivo experience with eit as a thermal estimator during hyperthermia," *Int. J. Hyperthermia*, vol. 12, no. 5, pp. 573–591, 1996.

[2] P. M. Meaney, K. D. Paulsen, A. Hartov, and R. K. Crane, "Microwave imaging for tissue assessment: initial evaluation in multitarget tissue-equivalent phantoms," *IEEE Trans. Biomed. Eng.*, vol. 43, no. 9, pp. 878–890, 1996.

[3] K. Hynynen, A. Chung, T. Fjield, M. Buchanan, D. Daum, V. Colucci, P. Lopath, and F. Jolesz, "Feasibility of using ultrasound phased arrays for mri monitored noninvasive surgery," *IEEE Trans. Ultrason., Ferroelect., Freq. Contr.*, vol. 43, no. 6, pp. 1043–1052, 1996.

[4] C. Simon, P. VanBaren, and E. S. Ebbini, "Two-dimensional temperature estimation using diagnostic ultrasound," *IEEE Trans. Ultrason., Ferroelect., Freq. Contr.*, vol. 45, no. 4, pp. 1088–1099, 1998.

[5] R. M. Arthur, W. L. Straube, J. W. Trobaugh, and E. G. Moros, "Noninvasive temperature estimation of hyperthermia temperatures with ultrasound," *Int. J. Hyperthermia*, vol. 21, no. 6, pp. 589–600, 2005.

[6] R. Seip and E. S. Ebbini, "Noninvasive estimation of tissue temperature response to heating fields using diagnostic ultrasound," *IEEE Trans. Biomed. Eng.*, vol. 42, no. 8, pp. 828–839, 1995.

[7] S. Ueno, M. Hashimoto, H. Fukukita, and T. Yano, "Ultrasound thermometry in hyperthermia," in *Proc IEEE Ultrasonics Symposium*, vol. 3, 1990, pp. 1645–1652.

[8] R. M. Arthur, W. L. Straube, J. D. Starman, and E. G. Moros, "Noninvasive temperature estimation based on the energy of backscattered ultrasound," *Med. Phys.*, vol. 30, no. PART 6, pp. 1021–1109, 2003.

[9] C. M. Fonseca, "Multiobjective genetic algorithms with application to control engineering problems," Ph.D. dissertation, Department of Automatic Control and Systems Engineering, University of Sheffield, UK, 1995.

[10] C. M. Fonseca and P. J. Fleming, "Genetic algorithms for multi-objective optimization: Formulation, discution and generalization," in *Proc. 5th Int Conf Genetic Algorithms*, Illinois, USA, 1993, pp. 416–423.

[11] C. M. Fonseca and P. Fleming, "Multiobjective optimization and multiple constraint handling with evolutionary algorithms–part i: A unified formulation," *IEEE Trans Syst Man Cybern Part A-Syst Hum*, vol. 28, no. 1, pp. 26–37, 1998.

[12] J. C. Principe, N. R. Euliano, and W. C. Lefebvre, *Neural and adaptive systems: Fundamentals throught simulations.* New York: Jonh Wiley & Sons, 2000.

[13] A. E. Ruano, Ed., *Intelligent control systems using computational intelligence techniques.* London: IEE Press, 2005.

[14] W. R. Hedrick, D. L. Hykes, and D. E. Starchman, *Ultrasound Physics and Instrumentation*, 3rd ed. Mosby, 1995.

[15] F. Viola and W. F. Walker, "A spline-based algorithm for continuous time-delay estimation using sampled data," *IEEE Trans. Ultrason., Ferroelect., Freq. Contr.*, vol. 52, no. 1, pp. 80–93, 2005.

[16] G. ter Haar, "Therapeutic ultrasound," *Eur. J. Ultrasound*, vol. 9, no. 1, pp. 3–9, 1999.

[17] I. Rivens, A. Shaw, J. Civale, and H. Morris, "Treatment monitoring and thermometry for therapeutic focused ultrasound," *Int. J. Hyperthermia*, vol. 23, no. 2, pp. 121–139, 2007.

[18] R. Seip and E. S. Ebbini, "Invasive and non-invasive feedback for ultrasound phased array thermometry," in *Ultrasonics Symposium*. IEEE, 1994, pp. 1821–1824.

[19] R. Seip, P. VanBaren, and E. S. Ebbini, "Dynamic focusing in ultrasound hyperthermia treatments using implantable hydrophone arrays," *IEEE Trans. Ultrason., Ferroelect., Freq. Contr.*, vol. 41, no. 5, pp. 706–713, 1994.

[20] M. J. D. Powell, "Radial basis functions for multivariate interpolation: A review," in *Proc. IMA conference on algorithms for approximation of functions and data*, J. C. Mason and M. G. Cox, Eds. Shrivenham, England: Oxford University press, 1985, pp. 143–147.

[21] D. S. Broomhead and D. Lowe, "Multivariable functional interpolation and adaptive networks," *Complex Systems*, vol. 2, no. 3, pp. 321–355, 1988.

[22] P. J. Werbos, "Beyond regression: New tools for prediction and analysis in the behavioral sciences," Ph.D. dissertation, Harvard University, Cambridge, MA, 1974.

[23] D. Rumelhart, J. McClelland, and the PDP Research Group, *Parallel distributed processing*. Cambridge, MA, U. S. A.: MIT Press, 1986, vol. 1.

[24] K. Funahashi, "On the approximate realization of continuous-mappings by neural networks," *Neural Networks*, vol. 2, no. 3, pp. 183–192, 1989.

[25] K. Hornik, M. Stinchcombe, and H. White, "Multilayer feedforward networks are universal approximators," *Neural Networks*, vol. 2, no. 5, pp. 359–366, 1989.

[26] J. Park and I. W. Sandberg, "Universal approximation using radial-basis-function networks," *Neural Comput.*, vol. 3, no. 2, pp. 246–257, 1991.

[27] F. Girosi and T. Poggio, "Networks and the best approximation property," *Biological Cybernetics*, vol. 63, pp. 169–176, 1990.

[28] A. Ruano, P. Fleming, and D. Jones, "A connectionist approach to pid autotuning," in *IEE Proceedings, Part D.*, vol. 139, no. 3, 1992, pp. 279–285.

[29] S. Haykin, *Neural Networks: A comprehensive foundation.* New Jersey: Prentice Hall, 1999.

[30] J. Moody and C. J. Darken, "Fast learning in networks of locally-tuned processing units," *Neural Computation*, vol. 1, pp. 281–294, 1989.

[31] C. Chinrungrueng and C. H. Séquin, "Optimal adaptive k-means algorithm with dynamic adjustment of learning rate," *IEEE Trans. Neural Networks*, vol. 6, no. 1, pp. 157–169, 1995.

[32] K. Levenberg, "A method for the solution of certain problems in least squares," in *Quarterly Applied Mathematics*, vol. 2, 1944, pp. 164–168.

[33] D. Marquardt, "An algorithm for least-squares estimation of nonlinear parameters," *SIAM Journal of Applied Mathematics*, vol. 11, pp. 431–441, 1963.

[34] A. N. Tikhonov, "On solving incorrectly posed problems and method of regularisation," *Doklady Akademii Nauk USSR*, vol. 151, pp. 501–504, 1963.

[35] T. Poggio and F. Girosi, "Networks for approximation and learning," in *Proc. of the IEEE*, 1990, pp. 1481–1497.

[36] A. Ruano, "Applications of neural networks to control systems," Ph.D. dissertation, UCNW, UK, 1992.

[37] S. Chen, C. F. N. Cowan, and P. M. Grant, "Orthogonal least squares learning algorithm for radial basis function networks," *IEEE Trans. Neural Networks*, vol. 2, no. 2, pp. 302–309, 1991.

[38] J. Platt, "A resource-allocating network for function interpolation," *Neural Computation*, vol. 3, no. 2, pp. 213–225, 1991.

[39] P. Ferreira, E. Faria, and A. Ruano, "Neural network models in greenhouse air temperature prediction," *Neurocomputing*, vol. 43, no. 1-4, pp. 51–75, 2002.

[40] A. E. Ruano, E. M. Crispim, E. Z. E. Conceição, and M. M. J. R. Lúcio, "Prediction of building's temperature using neural networks models," *Energy Build.*, vol. 38, no. 6, pp. 682–694, 2006.

[41] C. A. Teixeira, A. E. Ruano, C. Negreira, M. G. Ruano, and W. C. A. Pereira, "Non-invasive temperature prediction of in-vitro therapeutic ultrasound signals using neural networks," *Med. Biol. Eng. Comput.*, vol. 44, no. 1-2, pp. 111–116, 2006.

[42] L. A. Zadeh, "Outline of a new approach to the analysis of complex systems and decision processes," *IEEE Trans. on Systems, Man, and Cybernetics*, vol. SMC-3, pp. 28–44, 1973.

[43] E. H. Mamdani, "Advances in the linguistic synthesis of fuzzy controllers," *International Journal of Man-Machine Studies*, vol. 8, pp. 669–678, 1976.

[44] T. Takagi and M. Sugeno, "Fuzzy identification of systems and its application to modeling and control," *IEEE Trans. Syst. Man Cybernetics*, vol. 15, no. 1, pp. 116–132, 1985.

[45] J. V. de Oliveira, "Towards neuro-linguistic modeling: constraints for optimization of membership functions," *Fuzzy Sets Syst.*, vol. 106, no. 3, pp. 357–380, 1999.

[46] J.-S. R. Jang, "Anfis: Adaptive-network-based fuzzy inference system," *IEEE Trans. Syst., Man, Cybern.*, vol. 23, no. 3, pp. 665–685, 1993.

[47] J. H. Holland, *Adaptation in natural and artificial systems.* Ann Arbor, MI: University of Michigan Press, 1975.

[48] D. E. Goldberg, *Genetic algorithms in search, optimization and machine learning.* Reading, MA: Addison-Wesley, 1989.

[49] I. Rechenberg, *Evolutionsstrategie, Optimierung technischer Systeme nach Prinzipen der biologischen Evolution.* Stuttgart: Frommann-Holzboog, 1973.

[50] H.-P. Schwefel, *Numerical optimization of computer models.* Chichester: Wiley, 1981.

[51] J. E. Baker, "Reducing bias and inefficiency in the selection algorithm," in *Proc. of the 2nd Intl Conf on GA.* Lawrence Erlbaum Associates, Inc. Mahwah, NJ, USA, 1987, pp. 14–21.

[52] P. J. B. Hancock, "An empirical comparison of selection methods in evolutionary algorithms," in *Evolutionary Computation, AISB Workshop*, 1994, pp. 80–94.

[53] A. Ben-Tal, "Characterization of pareto and lexicographic optimal solutions," in *Multiple Criteria Decision Making Theory and Application*, Fandel and Gal, Eds. Springer-Verlag, 1980, pp. 1–11.

[54] D. Dalecki, "Mechanical bioeffects of ultrasound," *Annu. Rev. Biomed. Eng.*, vol. 6, pp. 229–248, 2004.

[55] F. Foster, K. A. Haraiewicz, C. J. Pavlin, and G. R. Lockwood, "High frequency ultrasound b-scan imaging," *J. E. M. U.*, vol. 19, no. 2/3, pp. 189–194, 1998.

[56] M. Fink, G. Montaldo, and M. Tanter, "Time-reversal acoustics in biomedical engineering," *Annu. Rev. Biomed. Eng.*, vol. 5, pp. 465–497, 2003.

[57] IEC, "Iec 1390: Ultrasonics - real-time pulse-echo systems - test procedures to determine performance specifications," 1996.

[58] AIUM, "Standard methods for measuring performance of pulse-echo ultrasound imaging equipment," 1990.

[59] ——, "Methods for specifying acoustic properties of tissue mimicking phantoms and objects," 1995.

[60] E. L. Madsen, J. A. Zagzebski, R. A. Banjavie, and R. E. Jutila, "Tissue mimicking materials for ultrasound phantoms," *Med. Phys.*, vol. 5, no. 5, pp. 391–394, 1978.

[61] R. Bayford and A. Gibson, "Electrical impedance tomography," May 2007. [Online]. Available: http://www.eit.org.uk/

[62] J. Conway, "Electrical impedance tomography for thermal monitoring of hyperthermia treatment: an assessment using in-vitro and in-vivo measurements," *Clin. Phys. Physiol. Meas.*, vol. 8, no. Suppl. A, pp. 141–146, 1987.

[63] E. C. Fear, S. C. Hagness, P. M. Meaney, M. Okoniewski, and M. A. Stuchly, "Enhancing breast tumor detection with near-field imaging," *IEEE Microwave*, vol. 3, no. 1, pp. 48–56, 2002.

[64] J. T. Chang, , K. D. Paulsen, P. M. Meaney, and M. Fanning, "Noninvasive thermal assessment of tissue phantoms using an active near field microwave imaging technique," *Int. J. Hyperthermia*, vol. 14, no. 6, pp. 513–534, 1998.

[65] P. M. Meaney, K. D. Paulsen, M. W. Fanning, D. Li, and Q. Fang, "Image accuracy improvements in microwave tomographic thermometry: phantom experience," *Int. J. Hyperthermia*, vol. 19, no. PART 5, pp. 534–550, 2003.

[66] B. Quesson, J. A. de Zwart, and C. T. W. Moonen, "Magnetic resonance temperature imaging for guidance of thermotherapy," *J. Magn. Reson. Imaging*, vol. 12, no. PART 4, pp. 525–533, 2000.

[67] J. Gellermann, W. Wlodarczyk, A. Feussner, H. Fähling, J. Nadobny, B. Hildebrandt, R. Felix, and P. Wust, "Methods and potentials of magnetic resonance imaging for monitoring radiofrequency hyperthermia in a hybrid system," *Int. J. Hyperthermia*, vol. 21, no. 6, pp. 497–513, 2005.

[68] N. McDannold, "Quantitative mri-based temperature mapping based on the proton resonant frequency shift: Review of validation studies," *Int. J. Hyperthermia*, vol. 21, no. 6, pp. 533–546, 2005.

[69] A. N. Amini, E. S. Ebbini, and T. T. Georgiou, "Noninvasive estimation of tissue temperature via high-resolution spectral analysis techniques," *IEEE Trans. Biomed. Eng.*, vol. 52, no. 2, pp. 221–228, 2005.

[70] R. Seip, P. VanBaren, C. A. Cain, and E. S. Ebbini, "Noninvasive real-time multipoint temperature control for ultrasound phased array treatments," *IEEE Trans. Ultrason., Ferroelect., Freq. Contr.*, vol. 43, no. 6, pp. 1063–1073, 1996.

[71] A. Anand, D. Savéry, and C. Hall, "Three-dimensional spatial and temporal temperature imaging in gel phantoms using backscattered ultrasound," *IEEE Trans. Ultrason., Ferroelect., Freq. Contr.*, vol. 54, no. 1, pp. 23–31, 2007.

[72] M. Pernot, M. Tanter, J. Bercoff, K. R. Waters, and M. Fink, "Temperature estimation using ultrasonic spatial compound imaging," *IEEE Trans. Ultrason., Ferroelect., Freq. Contr.*, vol. 51, no. 5, pp. 606–615, 2004.

[73] W. L. Straube and R. M. Arthur, "Theoretical estimation of the temperature dependence of backscattered ultrasonic power for noninvasive thermometry," *Ultrasound Med. Biol.*, vol. 20, no. 9, pp. 915–922, 1994.

[74] R. M. Arthur, J. W. Trobaugh, W. L. Straube, E. G. Moros, and S. Sangkatumvong, "Temperature dependence of ultrasonic backscattered energy in images compensated for tissue motion," in *Proc IEEE Ultrasonics Symposium*, vol. 1, 2003, pp. 990–993.

[75] S. T. Sato, W. C. A. Pereira, and C. R. S. Vieira, "Phantom to measure displayed dynamic range at biomedical ultrasound equipments," *Brazilian J. Biomed. Eng.*, vol. 19, no. 3, pp. 157–166, 2003, in portuguese.

[76] Linux GPIB Project, "The linux gpib package homepage," May 2007. [Online]. Available: http://linux-gpib.sourceforge.net/

[77] Python Software Foundation, "Python programming language – official website," December 2007. [Online]. Available: http://www.python.org/

[78] MathWorks, Inc., "Matlab," December 2007. [Online]. Available: http://www.mathworks.com/

[79] GNOME Project and PyGTK Team, "Pygtk: Gtk+ for python," April 2006. [Online]. Available: http://www.pygtk.org/

[80] M. Haggerty, "Gnuplot.py on sourceforge.net," May 2007. [Online]. Available: http://gnuplot-py.sourceforge.net/

[81] T. Williams, L. Hecking, and H. Broeker, "Gnuplot homepage," March 2007. [Online]. Available: http://gnuplot-py.sourceforge.net/

[82] S. Billings and W. Voon, "Correlation based model validity tests for non-linear models," *Int. J. Control*, vol. 44, no. 1, pp. 235–244, 1986.

[83] P. M. Frazão, A. E. Ruano, and C. M. Fonseca, "Evolutionary multiobjective design of radial basis function networks for greenhouse environmental control," in *Proc. of the 16th Triennial IFAC World Congress*, 2005, pp. 63–68.

[84] C. Simon, P. VanBaren, and E. S. Ebbini, "Motion compensation algorithm for noninvasive two-dimensional temperature estimation using diagnostic pulse-echo ultrasound," in *Proceedings of SPIE*, vol. 3249, 1998, pp. 182–192.

[85] M. Pernot, M. Tanter, and M. Fink, "3-d real-time motion correction in high-intensity focused ultrasound therapy," *Ultrasound Med. Biol.*, vol. 30, no. 9, pp. 1239–1249, 2004.

[86] R. Xinying, W. Shuicai, and Z. Yi, "Noninvasive monitoring for hyperthermia based on ultrasonic tissue characterization of b-mode," in *The 1st International Conference on Bioinformatics and Biomedical Engineering, 2007. ICBBE 2007.*, 2007, pp. 1173–1176.

[87] J. M. Sousa, R. Babuska, and H. B. Verbruggen, "Fuzzy predictive control applied to an air-conditioning system," *Control Engineering Practice*, vol. 5, no. 10, pp. 1395–1406, 1997.

[88] M. Mahfouf and D. A. Linkens, "Non-linear generalized predictive control (nlgpc) applied to muscle relaxant anaesthesia," *Int. J. Control*, vol. 71, no. 2, pp. 239–257, 1998.